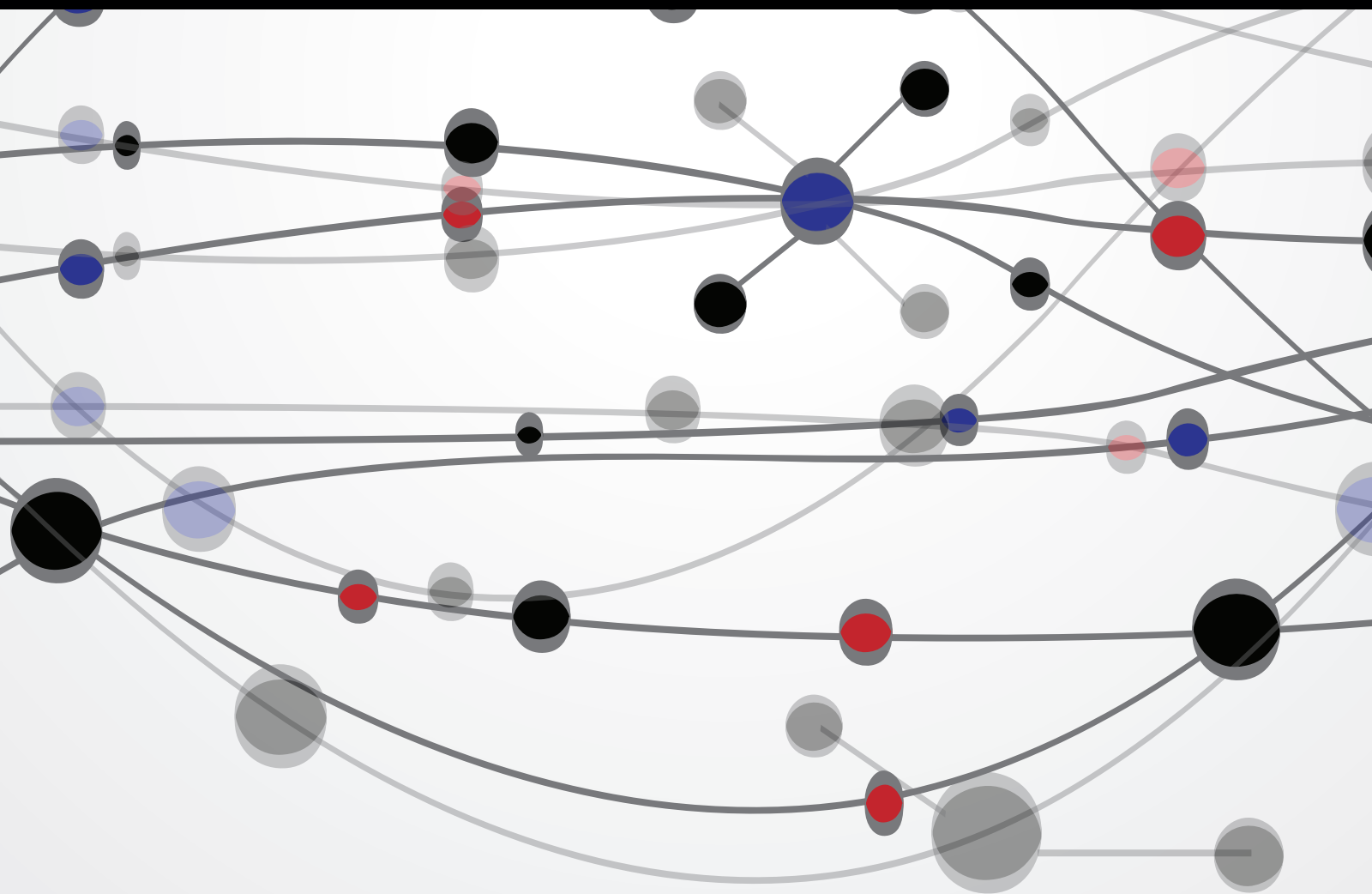


Development of Radiolabeled Compounds for Molecular Imaging and Imaging-Based Therapy

Guest Editors: Kazuma Ogawa, Masahiro Ono, Mei Tian, Masashi Ueda, and Takahiro Higuchi





Development of Radiolabeled Compounds for Molecular Imaging and Imaging-Based Therapy

The Scientific World Journal

Development of Radiolabeled Compounds for Molecular Imaging and Imaging-Based Therapy

Guest Editors: Kazuma Ogawa, Masahiro Ono, Mei Tian,
Masashi Ueda, and Takahiro Higuchi



Copyright © 2015 Hindawi Publishing Corporation. All rights reserved.

This is a special issue published in “The Scientific World Journal.” All articles are open access articles distributed under the Creative Commons Attribution License, which permits unrestricted use, distribution, and reproduction in any medium, provided the original work is properly cited.

Contents

Development of Radiolabeled Compounds for Molecular Imaging and Imaging-Based Therapy,

Kazuma Ogawa, Masahiro Ono, Mei Tian, Masashi Ueda, and Takahiro Higuchi

Volume 2015, Article ID 365418, 2 pages

Novel PET/SPECT Probes for Imaging of Tau in Alzheimer's Disease, Hiroyuki Watanabe, Masahiro Ono, and Hideo Saji

Volume 2015, Article ID 124192, 6 pages

Development of PET and SPECT Probes for Glutamate Receptors, Takeshi Fuchigami, Morio Nakayama, and Sakura Yoshida

Volume 2015, Article ID 716514, 19 pages

Theranostic Imaging Using Radiolabeled Antibodies and Tyrosine Kinase Inhibitors,

Mitsuyoshi Yoshimoto, Hiroaki Kurihara, and Hirofumi Fujii

Volume 2015, Article ID 842101, 6 pages

Iodine-131 Metaiodobenzylguanidine Therapy for Neuroblastoma: Reports So Far and Future Perspective, Daiki Kayano and Seigo Kinuya

Volume 2015, Article ID 189135, 9 pages

Multiparametric Monitoring of Early Response to Antiangiogenic Therapy: A Sequential Perfusion CT and PET/CT Study in a Rabbit VX2 Tumor Model, Jung Im Kim, Hyun-Ju Lee, Young Jae Kim,

Kwang Gi Kim, Kyung Won Lee, Jae Ho Lee, Hak Jong Lee, and Won Woo Lee

Volume 2014, Article ID 701954, 10 pages

Radiolabeled Apoptosis Imaging Agents for Early Detection of Response to Therapy,

Kazuma Ogawa and Miho Aoki

Volume 2014, Article ID 732603, 11 pages

Solid Tumor-Targeting Theranostic Polymer Nanoparticle in Nuclear Medicinal Fields,

Akira Makino and Shunsaku Kimura

Volume 2014, Article ID 424513, 12 pages

Radioimmunotherapy: A Specific Treatment Protocol for Cancer by Cytotoxic Radioisotopes Conjugated to Antibodies, Hidekazu Kawashima

Volume 2014, Article ID 492061, 10 pages

Radiolabeled Probes Targeting Hypoxia-Inducible Factor-1-Active Tumor Microenvironments,

Masashi Ueda and Hideo Saji

Volume 2014, Article ID 165461, 8 pages

Why Are We Failing to Implement Imaging Studies with Radiolabelled New Molecular Entities in Early Oncology Drug Development?, Azeem Saleem, Philip Murphy, Christophe Plisson, and Michael Lahn

Volume 2014, Article ID 269605, 9 pages

PET Quantification of Cerebral Oxygen Metabolism in Small Animals, Takashi Temma,

Kazuhiro Koshino, Tetsuaki Moriguchi, Jun-ichiro Enmi, and Hidehiro Iida

Volume 2014, Article ID 159103, 7 pages

Editorial

Development of Radiolabeled Compounds for Molecular Imaging and Imaging-Based Therapy

Kazuma Ogawa,¹ Masahiro Ono,² Mei Tian,³ Masashi Ueda,⁴ and Takahiro Higuchi⁵

¹Graduate School of Medical Sciences, Kanazawa University, Kanazawa 920-1192, Japan

²Graduate School of Pharmaceutical Sciences, Kyoto University, Kyoto 606-8501, Japan

³Department of Nuclear Medicine and Medical PET Center, The Second Hospital of Zhejiang University School of Medicine, Zhejiang, China

⁴Graduate School of Medicine, Dentistry and Pharmaceutical Sciences, Okayama University, Okayama 700-8530, Japan

⁵Molecular and Cellular Imaging, Comprehensive Heart Failure Center, Universitätsklinikum Würzburg, Würzburg 97078, Germany

Correspondence should be addressed to Kazuma Ogawa; kogawa@p.kanazawa-u.ac.jp

Received 17 November 2014; Accepted 17 November 2014

Copyright © 2015 Kazuma Ogawa et al. This is an open access article distributed under the Creative Commons Attribution License, which permits unrestricted use, distribution, and reproduction in any medium, provided the original work is properly cited.

In recent years, a companion diagnosis for prediction of the effectiveness and the side effects after administration of drugs has become very important to decide a therapeutic strategy. In USA, Food and Drug Administration (FDA) recommends the development of the companion diagnostic agent simultaneously with a new drug development. Nuclear medicine imaging using positron emission tomography (PET) or single photon emission computed tomography (SPECT), which visualizes target molecules, is able to detect biological and biochemical changes in the earlier phases of diseases differing from an anatomical imaging using X-ray computed tomography (X-ray CT) or magnetic resonance imaging (MRI). Radiolabeled tracers for the nuclear medicine have great potential to provide a lot of information about pathology of individual patients depending on characteristics of each tracer and could be the companion diagnostics. Accordingly, molecular imaging and imaging-based therapy using radiolabeled tracers must contribute to the realization of personalized medicine.

11 selected papers are published in this special issue. Most of them deal with important topics in nuclear medicine. Below is a brief introduction to some of these papers in this special issue.

In cerebral imaging, imaging of tau protein is useful for presymptomatic diagnosis and monitoring of the progression

of Alzheimer's disease because the presence of neurofibrillary tangles, composed of hyperphosphorylated tau protein, is well correlated with neurodegeneration and cognitive decline in Alzheimer's disease. H. Watanabe et al. summarized tau imaging probes for PET and SPECT.

In oncology, molecular targeted therapies using drugs, such as tyrosine kinase inhibitors and monoclonal antibodies, become the mainstream in cancer therapy. It is important to estimate the target molecule status in cancer tissues and predict therapeutic efficacy. M. Yoshimoto et al. introduced new radiolabeled tyrosine kinase inhibitors and antibodies for theragnostic imaging and their clinical application in molecular targeted therapy.

In the point of view from early detection of response to therapy, apoptosis imaging could be useful because apoptosis occur before anatomical change at posttreatment and could contribute to personalized medicine. K. Ogawa and M. Aoki introduced radiolabeled compounds for molecular imaging of apoptosis (cell death), their applications, and utility in medicine.

Hypoxic regions in tumors are known to be resistant to chemotherapy and radiotherapy. Hypoxia-inducible factor-1 (HIF-1) expressed in hypoxic regions regulates expression of genes related to tumor growth, angiogenesis, metastasis, and therapy resistance. Thus, imaging of HIF-1-active regions in

tumors is of great interest. M. Ueda and H. Saji summarized the current status of HIF-1 imaging in preclinical and clinical studies.

*Kazuma Ogawa
Masahiro Ono
Mei Tian
Masashi Ueda
Takahiro Higuchi*

Review Article

Novel PET/SPECT Probes for Imaging of Tau in Alzheimer's Disease

Hiroyuki Watanabe, Masahiro Ono, and Hideo Saji

Department of Patho-Functional Bioanalysis, Graduate School of Pharmaceutical Sciences, Kyoto University, 46-29 Yoshida Shimoadachi-cho, Sakyo-ku, Kyoto 606-8501, Japan

Correspondence should be addressed to Hiroyuki Watanabe; hwatanabe@pharm.kyoto-u.ac.jp and Hideo Saji; hsaji@pharm.kyoto-u.ac.jp

Received 25 June 2014; Revised 10 September 2014; Accepted 30 September 2014

Academic Editor: Mei Tian

Copyright © 2015 Hiroyuki Watanabe et al. This is an open access article distributed under the Creative Commons Attribution License, which permits unrestricted use, distribution, and reproduction in any medium, provided the original work is properly cited.

As the world's population ages, the number of patients with Alzheimer's disease (AD) is predicted to increase rapidly. The presence of neurofibrillary tangles (NFTs), composed of hyperphosphorylated tau protein, is one of the neuropathological hallmarks of AD brain. Since the presence of NFTs is well correlated with neurodegeneration and cognitive decline in AD, imaging of tau using positron emission tomography (PET) and single-photon emission computed tomography (SPECT) is useful for presymptomatic diagnosis and monitoring of the progression of AD. Therefore, novel PET/SPECT probes for the imaging of tau have been developed. More recently, several probes were tested clinically and evaluated for their utility. This paper reviews the current state of research on the development and evaluation of PET/SPECT probes for the imaging of tau in AD brain.

1. Introduction

Alzheimer's disease (AD) is the most common form of irreversible dementia of the elderly. The number of AD patients was estimated at 26.6 million worldwide in 2006. As the world's population ages, the prevalence of AD is predicted to grow fourfold, to 106.8 million in 2050 [1, 2]. Senile plaques (SPs), composed of β -amyloid ($A\beta$) peptides, and neurofibrillary tangles (NFTs), composed of hyperphosphorylated tau proteins, are two neuropathological hallmarks of AD brain [3, 4]. However, there is no simple and definitive diagnostic method to detect SPs and NFTs in the brain without postmortem pathological staining of brain tissue. Therefore, the quantitative evaluation of SPs and NFTs in living brain by noninvasive techniques such as positron emission tomography (PET) and single-photon emission computed tomography (SPECT) could lead to the presymptomatic detection of AD [5–7]. Much efforts have been discussed on the development of $A\beta$ imaging probes, and some of them, such as (*E*)-4-(*N*-methylamino)-4'-(2-(2-(2-[18 F]-fluoroethoxy)ethoxy)ethoxy)-stilbene ([18 F]florbetaben) [8, 9],

(*E*)-4-(2-(6-(2-(2-(2-[18 F]-fluoroethoxy)ethoxy)ethoxy)pyridin-3-yl)vinyl)-*N*-methylaniline ([18 F]florbetapir) [10–12], and 2-(3-(3-[18 F]-fluoro-4-methylaminophenyl)benzothiazol-6-yl) ([18 F]flutemetamol) [13, 14], were approved by the US Food and Drug Administration (FDA).

Although SPs are often found in the brains of both AD and healthy controls, NFTs in the hippocampus and entorhinal cortex are well correlated with neurodegeneration and cognitive decline [18, 19]. Furthermore, the formation and deposition of NFTs occur in the early stage of AD. Therefore, imaging of tau, which is the main constituent of NFTs, by PET/SPECT is useful for the presymptomatic diagnosis and monitoring of the progression of AD. 2-(1-(2-(*N*-(2-[18 F]-Fluoroethyl)-*N*-methylamino)naphthalene-6-yl)ethylidene)malononitrile ([18 F]FDDNP), which is the first PET probe to visualize AD pathology, has been demonstrated to be effective in the measurement of in vivo brain cortical accumulation of both SPs and NFTs in living subjects [20–22]. Since this probe has lower binding affinity and lack of selectivity for tau aggregates, novel probes that show high selectivity for tau aggregates have been strongly

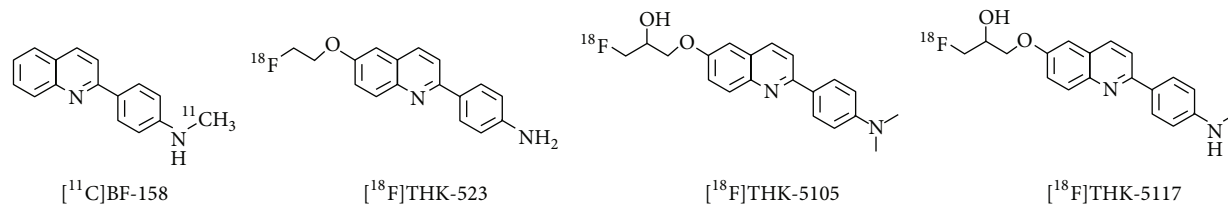


FIGURE 1: Chemical structures of quinoline derivatives for the imaging of tau [15–17].

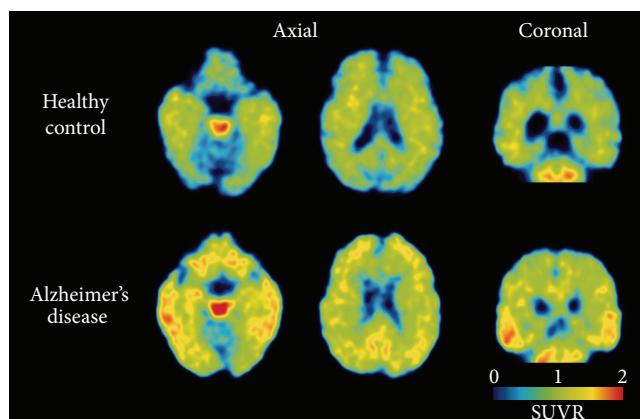


FIGURE 2: $[^{18}\text{F}]\text{THK-5105}$ PET images from 60 to 80 min after injection in a healthy control subject (72 years old, CDR 0, MMSE 29) and a patient with Alzheimer's disease (68 years old, CDR 1.0, MMSE 20). Reproduced from [23] with permission, copyright 2014 Oxford University Press.

desired. In this review, we summarize the current situation in the development of imaging probes for tau.

2. Quinoline Derivatives for Imaging of Tau

Okamura and coworkers screened >2000 small molecules in order to develop novel probes for imaging $A\beta$ and tau aggregates. In this search, they identified that the quinoline scaffold selectively binds to tau aggregates (Figure 1). Therefore, some compounds were tested for the *in vivo* imaging of tau in brain [15]. Among them, 2-[(4-methylamino) phenyl]quinoline (BF-158) showed high affinity for tau aggregates *in vitro* and clearly stained NFTs in the hippocampal section of AD brain. Furthermore, by *in vitro* autoradiography in AD brain sections, the distribution pattern of $[^{11}\text{C}]\text{BF-158}$ correlated well with tau immunostaining in the adjacent section. The authors suggested that these results indicated the binding of $[^{11}\text{C}]\text{BF-158}$ for NFTs in the AD brain. However, ^{11}C is a positron-emitting isotope with a short $t_{1/2}$ (20 min), which limits its clinical application. Therefore, they attempted to develop novel quinoline derivatives, labeled with ^{18}F , having a longer $t_{1/2}$ (110 min).

First, Fodero-Tavoletti and coworkers developed 6-(2- $[^{18}\text{F}]\text{-fluoroethoxy}$)-2-(4-aminophenyl)quinoline ($[^{18}\text{F}]\text{THK-523}$) for the quantitative imaging of tau aggregates in the human brain [16, 29]. This probe showed selective affinity for tau

aggregates *in vitro*. By *in vitro* autoradiography in AD brain sections, the distribution of $[^{18}\text{F}]\text{THK-523}$ did not conform with those of 2-(4'- $[^{11}\text{C}]\text{-methylaminophenyl}$)-6-hydroxybenzothiazole ($[^{11}\text{C}]\text{PIB}$) [30, 31] and 2-(2-[^{11}C]-dimethylaminothiazol-5-yl)ethenyl)-6-(2-[fluoro]ethoxy)benzoxazole ($[^{11}\text{C}]\text{BF-227}$) [32], which are $A\beta$ imaging probes. Furthermore, the distribution of $[^{18}\text{F}]\text{THK-523}$ in AD brain section closely resembled the findings upon Gallyas silver staining and tau immunostaining. On the basis of these results, $[^{18}\text{F}]\text{THK-523}$ was tested clinically [33]. However, the pharmacokinetics and binding characteristics of $[^{18}\text{F}]\text{THK-523}$ might not reach the necessary optimal levels for PET probes.

Therefore, Okamura and coworkers developed 6-[(3- $[^{18}\text{F}]\text{-fluoro-2-hydroxy}]\text{propoxy}$]-2-(4-dimethylaminophenyl)quinoline ($[^{18}\text{F}]\text{THK-5105}$) and 6-[(3- $[^{18}\text{F}]\text{-fluoro-2-hydroxy}]\text{propoxy}$]-2-(4-methylaminophenyl)quinoline ($[^{18}\text{F}]\text{THK-5117}$) for use as novel tau imaging PET probes (Figure 1) [17]. By *in vitro* binding assays, these compounds displayed higher affinity to tau aggregates than THK-523. By *in vitro* autoradiography in AD brain sections, the distributions of $[^{18}\text{F}]\text{THK-5105}$ and $[^{18}\text{F}]\text{THK-5117}$ coincided with Gallyas-Braak staining and tau immunostaining but not with the distribution of $[^{11}\text{C}]\text{PIB}$ and $A\beta$ immunostaining. In the biodistribution studies in normal mice, these probes showed higher uptake to mouse brain at 2 min after injection than $[^{18}\text{F}]\text{THK-523}$. In addition, the clearance of these derivatives from normal brain was also higher than that of $[^{18}\text{F}]\text{THK-523}$. These results suggest that $[^{18}\text{F}]\text{THK-5105}$ and $[^{18}\text{F}]\text{THK-5117}$ are suitable compounds for clinical application. Therefore, first, $[^{18}\text{F}]\text{THK-5105}$ was tested clinically and evaluated in terms of whether it could selectively bind to tau aggregates in living patients with AD [23]. The results of this study suggested that $[^{18}\text{F}]\text{THK-5105}$ is useful for the noninvasive evaluation of tau pathology in humans (Figure 2). In addition, clinical study of $[^{18}\text{F}]\text{THK-5117}$ is also ongoing.

3. Benzoimidazopyrimidine and Pyridoindole Derivatives for Imaging of Tau

Zhang and coworkers designed and synthesized a novel class of compounds, benzo[4,5]imidazo[1,2-a]pyrimidines, for *in vivo* imaging of tau in brain (Figure 3) [24]. Among

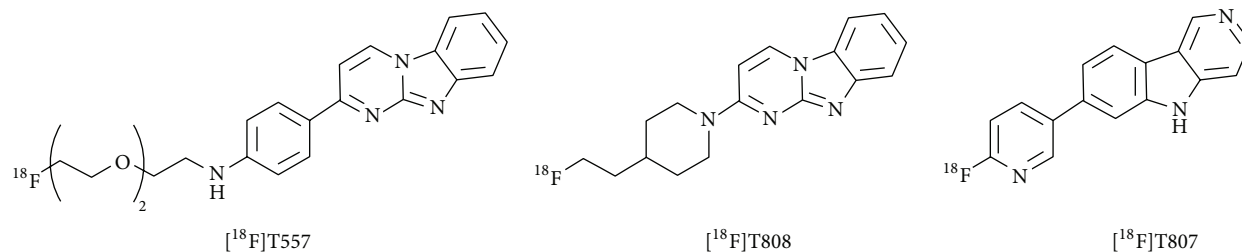


FIGURE 3: Chemical structures of benzoimidazopyrimidine and pyridoindole derivatives for the imaging of tau [24, 25].

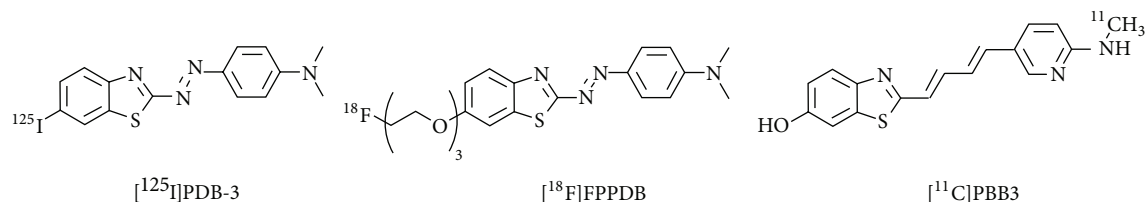


FIGURE 4: Chemical structures of benzothiazole derivatives for the imaging of tau [26–28].

numerous compounds, 4-(benzo[4,5]imidazo[1,2-*a*]pyrimidin-2-yl)-*N*-(2-(2-(2-fluoroethoxy)ethoxy)ethyl)aniline (T557) was identified as having good tau binding properties. However, imaging studies of [¹⁸F]T557 in rodents showed poor brain uptake. Therefore, they developed 2-(4-(2-(¹⁸F)-fluoroethyl)piperidin-1-yl)benzo[4,5]imidazo[1,2-*a*]pyrimidine ([¹⁸F]T808) as a novel imaging probe for tau. By in vitro autoradiography in AD brain sections, this probe localized in the tau-rich sections with considerable selectivity and specificity. Compared with [¹⁸F]T557, [¹⁸F]T808 rapidly crossed the blood brain barrier, followed by rapid clearance, suggesting little nonspecific binding in mice.

Xia and coworkers developed a novel class of 5H-pyrido[4,3-*b*]indoles and evaluated their binding affinity toward tau and their selectivity over A β aggregates (Figure 3) [25]. Through several rounds of lead optimization, 7-(6-fluoropyridin-3-yl)-5H-pyrido[4,3-*b*]indole (T807) was identified as a novel imaging probe for tau. The results of in vitro autoradiography in AD brain sections suggested that [¹⁸F]T807 bounded to NFTs of human AD brain with high specificity and weak or no interaction with SPs. In a biodistribution study in normal mice, [¹⁸F]T807 showed high brain uptake and rapid clearance from brain. In addition, [¹⁸F]T807 was metabolically stable in mice and [¹⁸F]T808 underwent slow yet acceptable de[¹⁸F]-fluorination. On the basis of these results, [¹⁸F]T807 and [¹⁸F]T808 were tested clinically. These preliminary results suggested that [¹⁸F]T807 and [¹⁸F]T808 have promise for the in vivo imaging of tau in AD patients [34, 35].

4. Benzothiazole Derivatives for Imaging of Tau

Recently, Honson and coworkers screened to determine the feasibility of distinguishing tau aggregates from A β

aggregates with a library containing 72,455 compounds [36]. They found that a phenyldiazenyl benzothiazole (PDB) derivative showed high binding affinity for tau aggregates with twofold selectivity over A β aggregates. Based on these findings, we designed novel radioiodinated PDB derivatives and evaluated their utility for the imaging of tau in AD brain (Figure 4) [26]. Among them, (*E*)-4-((6-iodobenzo[*d*]thiazol-2-yl)diazanyl)-*N,N*-dimethylaniline (PDB-3) showed high and selective binding affinity for tau aggregates in vitro. However, [¹²⁵I]PDB-3 showed poor pharmacokinetics in normal mouse brain. Therefore, we developed (*E*)-4-(((6-(2-(2-(¹⁸F)-fluoroethoxy)ethoxy)ethoxy)benzo[*d*]thiazol-2-yl)diazanyl)-*N,N*-dimethylaniline ([¹⁸F]FPPDB), which is a novel probe for the imaging of tau, to improve the in vivo pharmacokinetics of PDB-3 (Figure 4) [27]. [¹⁸F]FPPDB showed higher initial brain uptake and faster clearance from brain than [¹²⁵I]PDB-3. However, compared with PDB-3, FPPDB displayed less selectivity between tau and A β aggregates. In addition, by in vitro autoradiography in human AD brain sections, the distribution of [¹⁸F]FPPDB corresponded with that of in vitro immunohistochemical staining against phosphorylated tau, but it also matched to immunohistochemical staining against A β . Therefore, further structural optimization based on PDB scaffold is necessary to develop more useful probes for the in vivo imaging of tau in AD brains.

More recently, Maruyama and coworkers developed novel tau imaging probes, phenyl/pyridinyl-butadienyl-benzothiazole/benzothiazolium derivatives, for the imaging of tau in AD brain (Figure 4) [28]. Among them, 2-((1*E*,3*E*)-4-(6-(methylamino)pyridin-3-yl)buta-1,3-dienyl)benzo[*d*]thiazol-6-ol (PBB3) clearly stained tau aggregates in tau model mouse brain sections and human AD brain sections. By ex vivo autoradiography, PBB3 selectively labeled the brain stem and spinal cord of tau model mice harboring neuronal tau inclusions. These accumulations could be

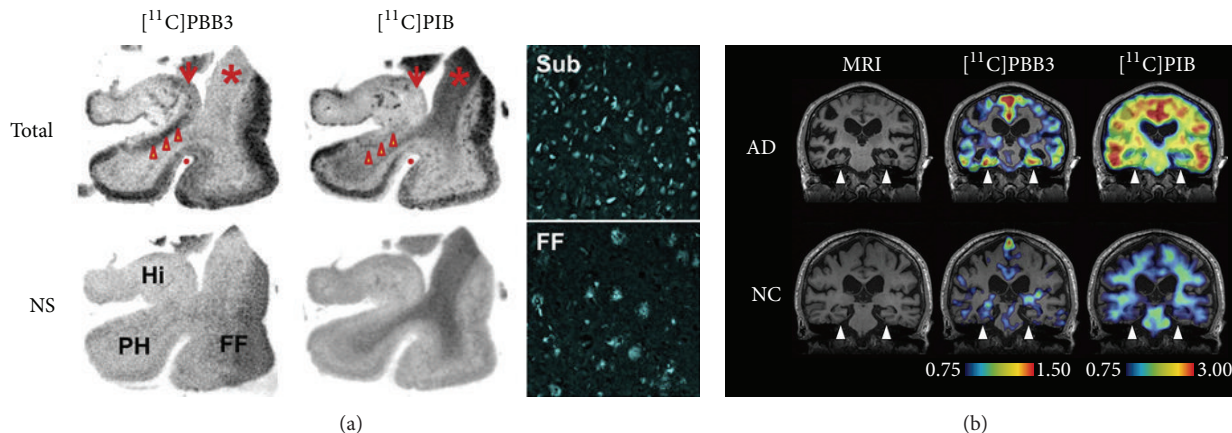


FIGURE 5: Accumulation of $[^{11}\text{C}]\text{PBB3}$ in the hippocampal formation of AD patients revealed by in vitro autoradiography (a) and in vivo PET (b). Reproduced from [28] with permission, copyright 2014 Elsevier.

detected with a micro-PET system in vivo. In addition, by in vitro autoradiography in AD hippocampus, a notable difference in the distribution between $[^{11}\text{C}]\text{PBB3}$ and $[^{11}\text{C}]\text{PIB}$ was observed in the tau-rich sections (Figure 5(a)). Since these results suggested that $[^{11}\text{C}]\text{PBB3}$ is a useful PET probe for the imaging of tau, they conducted an exploratory clinical PET study for patients with probable AD and healthy controls (Figure 5(b)). The result of this study supported the potential utility of $[^{11}\text{C}]\text{PBB3}$ for clarifying correlations between the distribution of tau deposition and the symptomatic progression of AD.

5. Other Probes for Imaging of Tau

Rojo and coworkers prepared two benzimidazole derivatives, astemizole and lansoprazole, to evaluate their interactions with tau aggregates [37]. Since these compounds showed high and specific affinity with tau aggregates, radiolabeled astemizole [38] and lansoprazole [39, 40] derivatives were reported. In particular, $[^{18}\text{F}]\text{N}$ -methyl lansoprazole is the lead compound for progression into clinical trials because this probe showed rapid brain uptake in nonhuman primates, favorable kinetics, low white matter binding, and selectivity for binding to tau aggregates over $\text{A}\beta$ aggregates. In addition, some compounds were also developed as novel PET and SPECT probes for the imaging of tau [41–44].

6. Conclusion

In the past decade, novel PET and SPECT probes for the imaging of tau were developed and evaluated for their utility. Among them, several compounds including $[^{18}\text{F}]\text{THK-523}$, $[^{18}\text{F}]\text{THK-5105}$, $[^{18}\text{F}]\text{T807}$, $[^{18}\text{F}]\text{T808}$, and $[^{11}\text{C}]\text{PBB3}$ were tested clinically. The results showed their feasibility for imaging tau aggregates for the diagnosis of AD. Therefore, we hope that further studies of these probes should lead to novel methods for presymptomatic diagnosis and monitoring of the progression of AD.

Conflict of Interests

There is no conflict of interests regarding the publication of this paper.

References

- [1] E. Johnson, R. Brookmeyer, and K. Ziegler-Graham, "Modeling the effect of Alzheimer's disease on mortality," *International Journal of Biostatistics*, vol. 3, pp. 186–191, 2007.
- [2] D. J. Selkoe, "Preventing alzheimer's disease," *Science*, vol. 337, no. 6101, pp. 1488–1492, 2012.
- [3] W. E. Klunk, "Biological markers of Alzheimer's disease," *Neurobiology of Aging*, vol. 19, no. 2, pp. 145–147, 1998.
- [4] D. J. Selkoe, "Alzheimer's disease: genes, proteins, and therapy," *Physiological Reviews*, vol. 81, no. 2, pp. 741–766, 2001.
- [5] C. A. Mathis, B. J. Lopresti, and W. E. Klunk, "Impact of amyloid imaging on drug development in Alzheimer's disease," *Nuclear Medicine and Biology*, vol. 34, no. 7, pp. 809–822, 2007.
- [6] C. A. Mathis, Y. Wang, and W. E. Klunk, "Imaging β -amyloid plaques and neurofibrillary tangles in the aging human brain," *Current Pharmaceutical Design*, vol. 10, no. 13, pp. 1469–1492, 2004.
- [7] A. Nordberg, "PET imaging of amyloid in Alzheimer's disease," *Lancet Neurology*, vol. 3, no. 9, pp. 519–527, 2004.
- [8] C. C. Rowe, U. Ackerman, W. Browne et al., "Imaging of amyloid β in Alzheimer's disease with ^{18}F -BAY94-9172, a novel PET tracer: proof of mechanism," *The Lancet Neurology*, vol. 7, no. 2, pp. 129–135, 2008.
- [9] W. Zhang, S. Oya, M.-P. Kung, C. Hou, D. L. Maier, and H. F. Kung, "F-18 Polyethyleneglycol stilbenes as PET imaging agents targeting $\text{A}\beta$ aggregates in the brain," *Nuclear Medicine and Biology*, vol. 32, no. 8, pp. 799–809, 2005.
- [10] C. M. Clark, J. A. Schneider, B. J. Bedell et al., "Use of florbetapir-PET for imaging β -amyloid pathology," *The Journal of the American Medical Association*, vol. 305, no. 3, pp. 275–283, 2011.
- [11] S. R. Choi, G. Golding, Z. Zhuang et al., "Preclinical properties of ^{18}F -AV-45: a PET agent for $\text{A}\beta$ plaques in the brain," *Journal of Nuclear Medicine*, vol. 50, no. 11, pp. 1887–1894, 2009.
- [12] D. F. Wong, P. B. Rosenberg, Y. Zhou et al., "In vivo imaging of amyloid deposition in Alzheimer disease using the radioligand

- ¹⁸F-AV-45 (flobetapir F18),” *Journal of Nuclear Medicine*, vol. 51, no. 6, pp. 913–920, 2010.
- [13] M. Koole, D. M. Lewis, C. Buckley et al., “Whole-body biodistribution and radiation dosimetry of ¹⁸F-GE067: a radioligand for in vivo brain amyloid imaging,” *Journal of Nuclear Medicine*, vol. 50, no. 5, pp. 818–822, 2009.
- [14] D. A. Wolk, I. D. Grachev, C. Buckley et al., “Association between in vivo fluorine 18-labeled flutemetamol amyloid positron emission tomography imaging and in vivo cerebral cortical histopathology,” *Archives of Neurology*, vol. 68, no. 11, pp. 1398–1403, 2011.
- [15] N. Okamura, T. Suemoto, S. Furumoto et al., “Quinoline and benzimidazole derivatives: candidate probes for in vivo imaging of tau pathology in Alzheimer’s disease,” *Journal of Neuroscience*, vol. 25, no. 47, pp. 10857–10862, 2005.
- [16] M. T. Fodero-Tavoletti, N. Okamura, S. Furumoto et al., “¹⁸F-THK523: a novel *in vivo* tau imaging ligand for Alzheimer’s disease,” *Brain*, vol. 134, no. 4, pp. 1089–1100, 2011.
- [17] N. Okamura, S. Furumoto, R. Harada et al., “Novel ¹⁸F-labeled arylquinoline derivatives for noninvasive imaging of Tau pathology in Alzheimer disease,” *Journal of Nuclear Medicine*, vol. 54, no. 8, pp. 1420–1427, 2013.
- [18] P. Giannakopoulos, F. R. Herrmann, T. Bussière et al., “Tangle and neuron numbers, but not amyloid load, predict cognitive status in Alzheimer’s disease,” *Neurology*, vol. 60, no. 9, pp. 1495–1500, 2003.
- [19] T. Gomez-Isla, R. Hollister, H. West et al., “Neuronal loss correlates with but exceeds neurofibrillary tangles in Alzheimer’s disease,” *Annals of Neurology*, vol. 41, no. 1, pp. 17–24, 1997.
- [20] E. D. Agdeppa, V. Kepe, J. Liu et al., “Binding characteristics of radiofluorinated 6-dialkylamino-2-naphthylethylidene derivatives as positron emission tomography imaging probes for beta-amyloid plaques in Alzheimer’s disease,” *The Journal of Neuroscience*, vol. 21, no. 24, article RC189, 2001.
- [21] G. W. Small, V. Kepe, L. M. Ercoli et al., “PET of brain amyloid and tau in mild cognitive impairment,” *The New England Journal of Medicine*, vol. 355, no. 25, pp. 2652–2663, 2006.
- [22] J. Shin, V. Kepe, J. R. Barrio, and G. W. Small, “The merits of FDDNP-PET imaging in Alzheimers Disease,” *Journal of Alzheimer’s Disease*, vol. 26, no. 1, pp. 135–145, 2011.
- [23] N. Okamura, S. Furumoto, M. T. Fodero-Tavoletti et al., “Non-invasive assessment of Alzheimer’s disease neurofibrillary pathology using ¹⁸F-THK5105 PET,” *Brain*, vol. 137, no. 6, pp. 1762–1771, 2014.
- [24] W. Zhang, J. Arteaga, D. K. Cashion et al., “A highly selective and specific PET tracer for imaging of tau pathologies,” *Journal of Alzheimer’s Disease*, vol. 31, no. 3, pp. 601–612, 2012.
- [25] C. F. Xia, J. Arteaga, G. Chen et al., “[¹⁸F]T807, a novel tau positron emission tomography imaging agent for Alzheimer’s disease,” *Alzheimer’s and Dementia*, vol. 9, no. 6, pp. 666–676, 2013.
- [26] K. Matsumura, M. Ono, S. Hayashi et al., “Phenyldiazanyl benzothiazole derivatives as probes for *in vivo* imaging of neurofibrillary tangles in Alzheimer’s disease brains,” *Med-ChemComm*, vol. 2, no. 7, pp. 596–600, 2011.
- [27] K. Matsumura, M. Ono, H. Kimura et al., “¹⁸F-labeled phenyldiazanyl benzothiazole for in vivo imaging of neurofibrillary tangles in Alzheimer’s disease brains,” *ACS Medicinal Chemistry Letters*, vol. 3, no. 1, pp. 58–62, 2012.
- [28] M. Maruyama, H. Shimada, T. Suhara et al., “Imaging of tau pathology in a tauopathy mouse model and in Alzheimer patients compared to normal controls,” *Neuron*, vol. 79, no. 6, pp. 1094–1108, 2013.
- [29] R. Harada, N. Okamura, S. Furumoto et al., “Comparison of the binding characteristics of [¹⁸F]THK-523 and other amyloid imaging tracers to Alzheimer’s disease pathology,” *European Journal of Nuclear Medicine and Molecular Imaging*, vol. 40, no. 1, pp. 125–132, 2013.
- [30] C. A. Mathis, Y. Wang, D. P. Holt, G.-F. Huang, M. L. Debnath, and W. E. Klunk, “Synthesis and evaluation of ¹¹C-labeled 6-substituted 2-arylbenzothiazoles as amyloid imaging agents,” *Journal of Medicinal Chemistry*, vol. 46, no. 13, pp. 2740–2754, 2003.
- [31] W. E. Klunk, H. Engler, A. Nordberg et al., “Imaging brain amyloid in Alzheimer’s disease with Pittsburgh Compound-B,” *Annals of Neurology*, vol. 55, no. 3, pp. 306–319, 2004.
- [32] Y. Kudo, N. Okamura, S. Furumoto et al., “2-(2-[2-Dimethylaminothiazol-5-yl]ethenyl)-6-(2-[fluoro]ethoxy)benzoxazole: a novel PET agent for in vivo detection of dense amyloid plaques in Alzheimer’s disease patients,” *Journal of Nuclear Medicine*, vol. 48, no. 4, pp. 553–561, 2007.
- [33] V. L. Villemagne, S. Furumoto, M. T. Fodero-Tavoletti et al., “In vivo evaluation of a novel tau imaging tracer for Alzheimer’s disease,” *European Journal of Nuclear Medicine and Molecular Imaging*, vol. 41, no. 5, pp. 816–826, 2014.
- [34] D. T. Chien, A. K. Szardenings, S. Bahri et al., “Early clinical PET imaging results with the novel PHF-tau radioligand [F18]-T808,” *Journal of Alzheimer’s Disease*, vol. 38, no. 1, pp. 171–184, 2014.
- [35] D. T. Chien, S. Bahri, A. K. Szardenings et al., “Early clinical PET imaging results with the novel PHF-tau radioligand [F-18]-T807,” *Journal of Alzheimer’s Disease*, vol. 34, no. 2, pp. 457–468, 2013.
- [36] N. S. Honson, R. L. Johnson, W. Huang, J. Inglese, C. P. Austin, and J. Kuret, “Differentiating Alzheimer disease-associated aggregates with small molecules,” *Neurobiology of Disease*, vol. 28, no. 3, pp. 251–260, 2007.
- [37] L. E. Rojo, J. Alzate-Morales, I. N. Saavedra, P. Davies, and R. B. MacCioni, “Selective interaction of lansoprazole and Astemizole with tau polymers: potential new clinical use in diagnosis of Alzheimer’s disease,” *Journal of Alzheimer’s Disease*, vol. 19, no. 2, pp. 573–589, 2010.
- [38] P. J. Riss, L. Brichard, V. Ferrari et al., “Radiosynthesis and characterization of astemizole derivatives as lead compounds toward PET imaging of τ -pathology,” *MedChemComm*, vol. 4, no. 5, pp. 852–855, 2013.
- [39] X. Shao, G. M. Carpenter, T. J. Desmond et al., “Evaluation of [¹¹C]N-methyl lansoprazole as a radiopharmaceutical for PET imaging of tau neurofibrillary tangles,” *ACS Medicinal Chemistry Letters*, vol. 3, no. 11, pp. 936–941, 2012.
- [40] M. V. Fawaz, A. F. Brooks, M. E. Rodnick et al., “High affinity radiopharmaceuticals based upon lansoprazole for PET imaging of aggregated tau in Alzheimer’s disease and progressive supranuclear palsy: synthesis, preclinical evaluation, and lead selection,” *ACS Chemical Neuroscience*, vol. 5, no. 8, pp. 718–730, 2014.
- [41] M. Ono, S. Hayashi, K. Matsumura et al., “Rhodanine and thiohydantoin derivatives for detecting tau pathology in Alzheimer’s brains,” *ACS Chemical Neuroscience*, vol. 2, no. 5, pp. 269–275, 2011.
- [42] T. Tago, S. Furumoto, N. Okamura et al., “Synthesis and preliminary evaluation of 2-arylhydroxyquinoline derivatives

for tau imaging,” *Journal of Labelled Compounds and Radiopharmaceuticals*, vol. 57, no. 1, pp. 18–24, 2014.

- [43] K. Matsumura, M. Ono, M. Yoshimura et al., “Synthesis and biological evaluation of novel styryl benzimidazole derivatives as probes for imaging of neurofibrillary tangles in Alzheimer’s disease,” *Bioorganic and Medicinal Chemistry*, vol. 21, no. 11, pp. 3356–3362, 2013.
- [44] H. Watanabe, M. Ono, H. Kimura et al., “Synthesis and biological evaluation of novel oxindole derivatives for imaging neurofibrillary tangles in Alzheimer’s disease,” *Bioorganic and Medicinal Chemistry Letters*, vol. 22, no. 17, pp. 5700–5703, 2012.

Review Article

Development of PET and SPECT Probes for Glutamate Receptors

Takeshi Fuchigami, Morio Nakayama, and Sakura Yoshida

Department of Hygienic Chemistry, Graduate School of Biomedical Sciences, Nagasaki University, 1-14 Bunkyo-machi, Nagasaki 852-8521, Japan

Correspondence should be addressed to Takeshi Fuchigami; t-fuchi@nagasaki-u.ac.jp

Received 28 June 2014; Accepted 29 August 2014

Academic Editor: Masahiro Ono

Copyright © 2015 Takeshi Fuchigami et al. This is an open access article distributed under the Creative Commons Attribution License, which permits unrestricted use, distribution, and reproduction in any medium, provided the original work is properly cited.

L-Glutamate and its receptors (GluRs) play a key role in excitatory neurotransmission within the mammalian central nervous system (CNS). Impaired regulation of GluRs has also been implicated in various neurological disorders. GluRs are classified into two major groups: ionotropic GluRs (iGluRs), which are ligand-gated ion channels, and metabotropic GluRs (mGluRs), which are coupled to heterotrimeric guanosine nucleotide binding proteins (G-proteins). Positron emission tomography (PET) and single photon emission computed tomography (SPECT) imaging of GluRs could provide a novel view of CNS function and of a range of brain disorders, potentially leading to the development of new drug therapies. Although no satisfactory imaging agents have yet been developed for iGluRs, several PET ligands for mGluRs have been successfully employed in clinical studies. This paper reviews current progress towards the development of PET and SPECT probes for GluRs.

1. Introduction

L-Glutamate is the primary endogenous excitatory neurotransmitter and glutamate receptors (GluRs) are implicated in a range of neurological functions within the mammalian central nervous system (CNS). Two distinct groups of GluRs have been identified: ionotropic receptors (iGluRs) and metabotropic receptors (mGluRs). iGluRs form ligand-gated ion channels and are classified into three subtypes based on their pharmacological properties: NMDA (*N*-methyl-D-aspartate receptors, NMDARs), AMPA (α -amino-3-hydroxy-5-methylisoxazole-4-propionic acid) receptors, and kainate receptors [1]. mGluRs are coupled to heterotrimeric guanosine nucleotide binding proteins (G-proteins) and include eight receptor subtypes, classified into three groups according to their sequence homology, signal transduction, and pharmacological profiles; group I includes mGluR1 and mGluR5, group II includes mGluR2 and mGluR3, and group III includes mGluR4, mGluR6, mGluR7, and mGluR8 [2]. Impaired regulation of GluRs may be involved in the pathophysiology of various brain disorders [3, 4]. Positron

emission tomography (PET) and single photon emission computed tomography (SPECT) imaging for GluRs are considered to be powerful tools for the evaluation of excitatory neurotransmission in the living brain, the study of the pathophysiology of related neurological disorders, and the quantification of GluR drug occupancy *in vivo*. To date, no specific radioligands for *in vivo* visualization of iGluRs have been identified. In contrast, there are several promising clinically useful PET ligands for mGluRs. This review summarizes current progress towards the development of PET and SPECT probes for GluRs, with a particular focus on NMDARs and mGluRs.

2. NMDARs

The NMDARs are iGluRs that play key roles in processes involving excitatory neurotransmission, including learning, memory, and synaptic plasticity [5, 6]. Dysregulation of NMDARs has been identified in various neurological diseases, including epilepsy, ischemia, stroke, Parkinson's disease, Alzheimer's disease, Huntington's disease, and

schizophrenia [4, 7, 8]. Activation of these receptors requires binding of glutamate and glycine and removal of Mg^{2+} blockade by membrane depolarization. NMDAR channel opening results in calcium influx into cells, followed by Ca^{2+} -dependent signal transduction cascades that modulate many aspects of neuronal function [1, 9]. Functional NMDARs are composed of two NR1 subunits, together with either two NR2 subunits or a combination of NR2 and NR3 subunits [10–12]. NR1 subunits are ubiquitously distributed throughout the brain. There are four types of the NR2 subunit (NR2A, NR2B, NR2C, and NR2D), with distinct distributions in the brain [13]. NR3 subunits can be activated by glycine alone. NR3A is expressed in the cortex and brainstem, while NR3B is distributed in the forebrain and cerebellum [14]. The glutamate binding site is present on the NR2 subunit, whereas the glycine binding site is located on NR1 or NR3 [11, 15, 16]. Polyamines are allosteric potentiators of NMDARs containing NR2B subunits, presumably through recognition of the NR1 and NR2B dimer interface [17]. It is known that aliphatic cyclic amine groups strongly inhibit NMDAR activity in a noncompetitive and voltage-dependent manner [18, 19]. Negative modulators of NR2B, including ifenprodil and its derivatives, have been found to bind at the interface between the NR1 and NR2B subunits [20]. The main strategy for development of PET and SPECT ligands is the structural modification of NMDA receptor antagonists, including channel blockers, glycine site antagonists, and NR2B negative modulators. Because most competitive antagonists of the glutamate binding site have shown low selectivity and poor blood-brain barrier (BBB) permeability [1, 21], there are no reported radioligands interacting with this region of the NMDAR.

2.1. Imaging Probes for the NMDAR Channel Blocker Binding Site. Open channel blockers of NMDARs, such as (+)-10, 11-dihydro-5-methyl-5H-dibenzo[a,d] cyclohepten-5,10-diylidammonium maleate (MK-801) and phencyclidine (PCP) derivatives, have been reported to bind to NMDARs in an activation-dependent manner [22, 23]. Thus, numerous *in vivo* imaging agents have been developed to interact with the PCP binding site, as this enables evaluation of the distribution of functional NMDARs in the brain under normal and pathological states. These agents include PCP, MK-801, ketamine, memantine, and diarylguanidine derivatives. [^{18}F]1 (Figure 1), a PCP derivative with an IC_{50} of 61 nM for the ion channel site, showed an *in vivo* distribution that was consistent with NMDAR expression. Furthermore, coinjection of 1.7 $\mu\text{mol/kg}$ of the high-affinity ion channel blocker, *cis*-2-hydroxymethyl-*r*-1-(*N*-piperidyl)-1-(2-thienyl)cyclohexane (*cis*-HPTC), resulted in a reduction in the regional cerebral distribution of [^{18}F]1. However, this tracer was unsuitable for use as an NMDAR PET radioligand because of its high nonspecific binding in the brain [24]. A 3- ^{11}C cyano analog of MK-801 (^{11}C]MKC, Figure 1) has been reported as a PET ligand with excellent affinity for the channel blocker site ($K_d = 8.2$ nM). This tracer showed highly specific binding and heterogeneous *in vitro* distribution in rat brain slices that was similar to the expression of NMDARs.

In PET studies, [^{11}C]MKC showed a rapid and high uptake into the brains of rhesus monkeys, with higher accumulation in the frontal cortex than in the cerebellar cortex. However, these distribution patterns correlated closely with regional cerebral blood flow and blocking with NMDAR antagonists did not affect the regional brain distribution of this tracer [25]. PCP and MK-801 analogs showed high nonspecific *in vivo* binding, probably due to their high lipophilicity. Diarylguanidines have been identified as highly potent NMDAR channel blockers, with less hydrophobicity than PCP and MK-801. Therefore, several radiolabeled diarylguanidine analogs have been reported as PET or SPECT ligands. *N*-(1-naphthyl)-*N'*-(3-iodophenyl)-*N'*-methylguanidine (CNS 1261, Figure 1) has been developed as a high-affinity SPECT ligand for the ion channel site ($K_i = 4.2$ nM) with moderate lipophilicity ($\log D = 2.19$). In *ex vivo* autoradiographic studies, [^{125}I]CNS 1261 showed 2.4–2.9-fold higher uptake by the hippocampus than by the cerebellum in normal rat brains. This accumulation pattern was consistent with the pattern of NMDAR expression. In addition, investigation of [^{125}I]CNS 1261 binding in a mouse model of cerebral ischemia revealed that [^{125}I]CNS 1261 showed 2-fold higher uptake by the caudate nucleus in the ischemic hemisphere, as compared to the same region of the nonischemic hemisphere (Figure 2). This suggested that [^{125}I]CNS 1261 bound selectively to activated NMDARs [26]. Based on this positive result, several clinical SPECT studies employing [^{123}I]CNS 1261 have been performed. In healthy volunteers, no significant difference in the total distribution volume (V_T) was observed between the NMDAR-rich regions (striatum, hippocampus, and frontal cortex) and the NMDAR-poor cerebellum [27, 28]. Numerous reports have suggested that hypofunction of NMDARs is associated with the pathophysiology of schizophrenia [29, 30]. It is reported that drug-free patients with schizophrenia showed reduced binding of [^{123}I]CNS 1261 in the left hippocampus relative to the whole cortex, compared with healthy controls [31]. In contrast, a separate study demonstrated that V_T values of [^{123}I]CNS 1261 in drug-free or typical antipsychotic-treated schizophrenia patients did not differ significantly from those observed in the control group [32]. Therefore, these reports did not provide evidence to support the proposal that NMDARs could be imaged by SPECT using [^{123}I]CNS 1261. *N*-(2-chloro-5-thiomethylphenyl)-*N'*-(3- ^{11}C]methoxy-phenyl)-*N'*-methylguanidine [^{11}C]GMOM (Figure 1) is a ^{11}C -labeled diarylguanidine derivative with a high affinity for the ion channel site ($K_i = 5.2$ nM). In PET studies conducted in baboons, [^{11}C]GMOM showed BBB permeability. However, brain distribution of [^{11}C]GMOM was almost homogeneous and preadministration of MK801 did not significantly change the regional V_T [33]. Another diarylguanidine derivative, *N*-(2-chloro-5-(methylmercapto)phenyl)-*N'*- ^{11}C]methylguanidine monohydrochloride (^{11}C]CNS 5161, Figure 1), had excellent affinity for the ion channel site ($K_i = 1.9$ nM). [3H]CNS 5161 showed a heterogeneous *in vivo* distribution in rat brain and a cortex/cerebellum ratio of 1.4. Pretreatment with

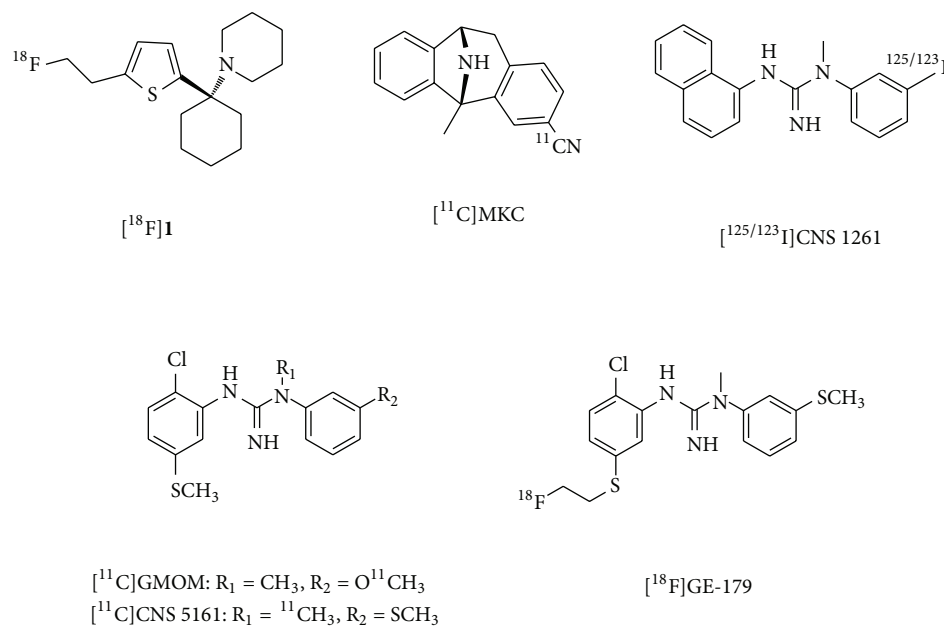


FIGURE 1: Chemical structure of imaging probes for channel blocker binding site of NMDARs.

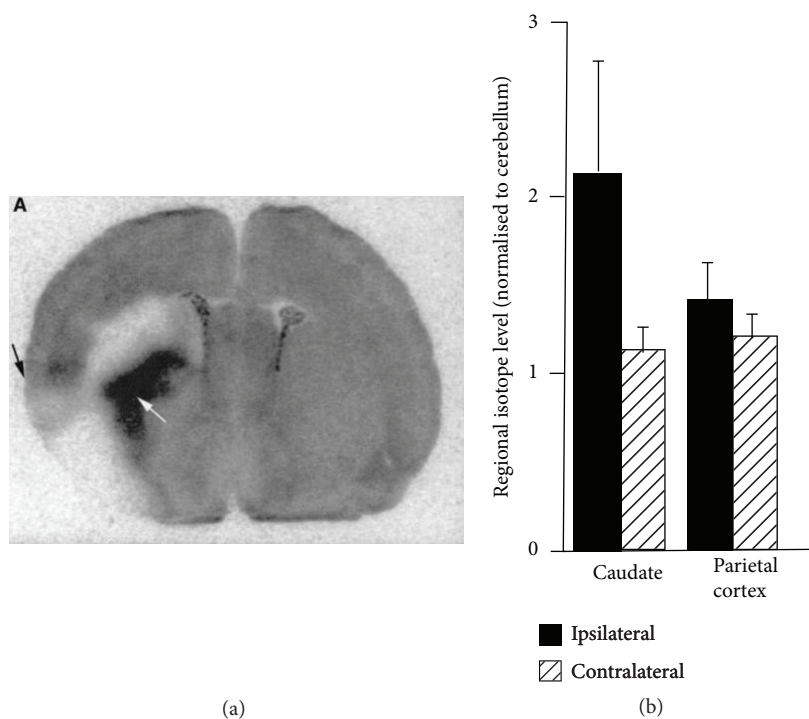


FIGURE 2: *Ex vivo* autoradiograms of $[^{125}\text{I}]\text{CNS } 1261$ in the caudate nucleus (white arrow) and cerebral cortex (black arrow) of rat brain (a). Quantified regional isotope levels normalized to cerebellum (b). The animals were injected with $[^{125}\text{I}]\text{CNS } 1261$ 15 min after permanent occlusion of the middle cerebral artery (left hemisphere) and sacrificed 120 min later [26].

NMDA increased the hippocampus/cerebellum ratio to 1.6–1.9, while MK801 reduced the ratios to close to 1.0 [34]. Clinical PET studies using $[^{11}\text{C}]\text{CNS } 5161$ indicated that the largest uptake occurred in the putamen and thalamus and the lowest uptake was observed in the cerebellum, but

relatively low levels of radioactivity were detected in the NMDAR-rich hippocampus [35]. Further investigations are necessary in order to provide consistent evidence that these diarylguanidines can be used as PET or SPECT radioligands for the channel blocker binding site of the NMDAR. Recently,

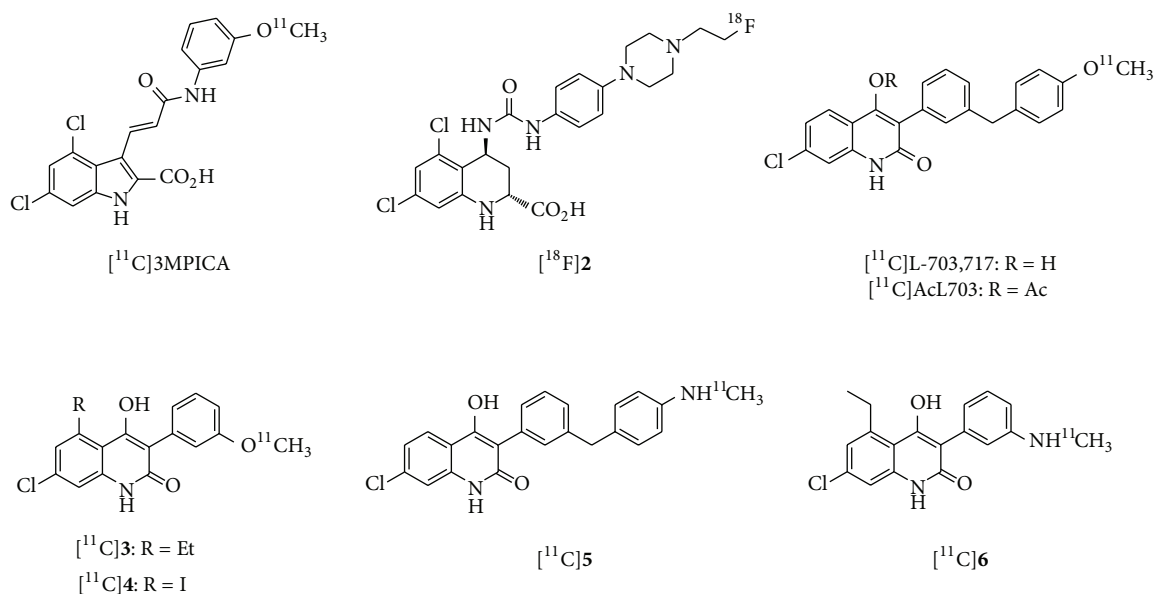


FIGURE 3: Chemical structure of imaging probes for glycine binding site of NMDARs.

$[^{18}\text{F}]GE-179$ (Figure 1), a high-affinity channel blocker ($K_i = 2.4 \text{ nM}$) [36], was radiolabeled and used for PET imaging in healthy human subjects. Although this tracer showed high brain uptake, the V_T of each region was correlated to cerebral blood flow rather than the levels of NMDAR expression. Further characterization of $[^{18}\text{F}]GE-179$ may be necessary with *in vivo* PET studies using NMDAR-activated models [37].

2.2. Imaging Probes for the NMDAR Glycine Binding Site. A number of antagonists of the NMDAR glycine binding site have been developed as anticonvulsant and neuroprotective drugs [38]. Several radiolabeled cyclic amino acid derivatives, such as $[^{11}\text{C}]3$ -[2-[(3-methoxyphenylamino) carbonyl]ethenyl]-4,6-dichloroindole-2-carboxylic acid ($[^{11}\text{C}]3\text{MPICA}$, Figure 3) and $[^{18}\text{F}]2$, have excellent binding affinities for the glycine binding site ($K_i = 4.8$ and 6.0 nM , resp.). However, they showed poor *in vivo* BBB permeability and had brain accumulation patterns that were inconsistent with those of the NMDAR [39, 40]. Since the low brain uptake of the cyclic amino acid derivatives was due to the highly polar charged carboxylate group, 4-hydroxyquinolones (4-HQs), which are carboxylic bioisosteres, have been investigated as high-affinity antagonists of the glycine binding site. 3-[3-(4- $[^{11}\text{C}]$ methoxybenzyl)phenyl]-4-hydroxy-7-chloroquinolin-2(1H)-one ($[^{11}\text{C}]L-703,717$, Figure 3) has been developed as one of the most potent glycine site antagonists with a 4-HQ backbone ($IC_{50} = 4.5 \text{ nM}$ versus $[^3\text{H}]L-689,560$) [41, 42]. *In vivo* experiments in mice showed poor initial brain uptake of $[^{11}\text{C}]L-703,717$ {0.32–0.36 percent injected dose per gram of tissue (% ID/g) at 1 min} and high levels of radioactivity in the blood. Since warfarin administration caused a dose-dependent enhancement of the initial brain uptake of $[^{11}\text{C}]L-703,717$, this tracer may have a

high affinity for plasma protein warfarin binding sites. The accumulation of $[^{11}\text{C}]L-703,717$ in the cerebrum was lower than that observed in the cerebellum at 30 min (0.20% ID/g versus 0.65% ID/g). This distribution pattern was inconsistent with that of NMDAR expression. It should be noted that treatment with nonradioactive L-703,717 (2 mg/kg) only led to a significant reduction in the accumulation of $[^{11}\text{C}]L-703,717$ in the cerebellum [43]. In order to improve the BBB permeability of $[^{11}\text{C}]L-703,717$, an acetyl derivative of L-703,717 ($[^{11}\text{C}]AcL703$, Figure 3) was developed as a prodrug radioligand. Initial brain uptake of $[^{11}\text{C}]AcL703$ at 1 min was 2-fold higher than that of $[^{11}\text{C}]L-703,717$. In rat brain tissues, approximately 80% of $[^{11}\text{C}]AcL703$ had been metabolized to $[^{11}\text{C}]L-703,717$ by 20 min after injection. In *ex vivo* studies, $[^{11}\text{C}]AcL703$ showed higher uptake in the cerebellum than in the cerebrum, consistent with the findings using $[^{11}\text{C}]L-703,717$ [44]. Although a clinical PET study of $[^{11}\text{C}]AcL703$ was performed in healthy volunteers, cerebellar NMDARs could not be visualized by PET due to poor BBB penetration [45]. Other radiolabeled 4-HQs (3 and 4, Figure 3) with lower lipophilicity than $[^{11}\text{C}]L-703,717$ have been developed as high-affinity radioligands for the glycine site ($K_i = 7.2$ and 10.3 nM). However, $[^{11}\text{C}]3$ and $[^{11}\text{C}]4$ did not exhibit a significant increase in brain uptake, as compared with $[^{11}\text{C}]L-703,717$ [46]. The 4-HQs are acidic ($pK_a \leq 5$) [42] and this may result in strong binding affinity for serum albumin and low BBB penetration. Thus, several amino 4-HQ derivatives with lower pK_a values were synthesized and evaluated as new PET radioligands for the glycine site. Methylamino derivatives of 4-HQs, 5 and 6 (Figure 3), showed high affinity for the glycine site ($K_i = 11.7 \text{ nM}$ and 11.8 nM , resp.). Although the amine derivatives showed a much lower plasma protein binding ratio than

the methoxy analogs, [¹¹C]6 still displayed poor uptake into the brain [47]. Further structure-activity relationship studies are necessary to develop PET ligands for the glycine site with significantly improved BBB penetration. Furthermore, the brain distribution of imaging agents interacting with the glycine site can be greatly influenced by endogenous agonists. The NMDAR coagonists, glycine and D-serine, are present in the brain at micromolar levels. Glycine is ubiquitously distributed in the brain, while D-serine is predominantly found in the forebrain [48, 49]. Levels of D-serine are reportedly very low level in the cerebellum, because of the high expression level of an enzyme (D-amino acid oxidase, DAO) that can degrade D-serine [50]. Consistent with the above reports, the [¹¹C]L-703,717 signal in the cerebellum was diminished in mutant ddY/DAO-mice, which have high cerebellar D-serine levels (Figure 4). The refore, the low accumulation of [¹¹C]L-703,717 in forebrain regions may reflect the strong inhibition caused by the high level of endogenous D-serine. Similarly, the higher uptake of [¹¹C]L-703,717 in the cerebellum might be due to reduced binding inhibition by D-serine [51].

2.3. Imaging Probes for the NR2B Negative Modulator Binding Site. NMDARs containing the NR2B subunit play a key role in various diseases, such as Parkinson's disease, Alzheimer's disease, and neuropathic pain. NR2B negative modulators have been developed for the treatment of these conditions [17, 52]. Ligands targeting NR2B, including ifenprodil, are thought to bind at the interlobe cleft of the NR2B subunit [53]. CP-101,606 is a potent NMDAR antagonist that is highly selective for NR2B subunit-containing receptors, with K_d values of 10 nM [54]. Because CP-101,606 was identified as a potent NR2B negative modulator ($K_i = 10$ nM), a ¹¹C-labeled CP-101,606 derivative ([¹¹C]7, Figure 5) was developed as a PET ligand for the NR2B subunit [55]. *In vitro* binding of [¹¹C]7 in rat brain slices was extremely high in the forebrain regions and very low in the cerebellum, with excellent specific binding (Figures 6(a) and 6(b)). This distribution pattern matched the NR2B subunit expression pattern [56]. However, *in vivo* studies in mice and monkeys demonstrated that this tracer showed homogeneous brain distribution and no specific binding of [¹¹C]7 was observed (Figure 6(c)) [55]. A benzylpiperidine derivative, [¹¹C]8 (Figure 5), has been developed as a selective high-affinity PET ligand for NR2B-containing NMDARs ($IC_{50} = 5.3$ nM). An *in vivo* study in rats showed poor brain uptake of [¹¹C]8 and a localization that was inconsistent with the NR2B expression pattern [57]. [¹¹C]EMD-95885 (Figure 5), a benzylpiperidine derivative with a high affinity for NR2B ($IC_{50} = 3.9$ nM), has been synthesized and evaluated. *In vivo* experiments in rats showed 59-fold higher brain uptake of [¹¹C]EMD-95885 than of [¹¹C]8. Although [¹¹C]EMD-95885 displayed homogeneous binding in brain tissues, a substantial reduction in brain uptake of [¹¹C]EMD-95885 was observed in the presence of nonradioactive 8 or ifenprodil, suggesting that some specific binding may occur in the brain. However, these blocking effects were observed in both NR2B-rich and NR2B-poor regions

[58]. The benzimidazole derivatives, 9 and 10 (Figure 5), have been identified as having high affinity for the NR2B subunit, with K_i values of 7.3 nM and 5.8 nM, respectively. Both [¹²⁵I]9 and [¹²⁵I]10 showed localizations consistent with NR2B subunit expression in rat brain slices. *In vivo* studies in mice found moderate brain uptake of [¹²⁵I]9 and [¹²⁵I]10 and distribution that was inconsistent with known NR2B expression patterns. However, treatment with nonradioactive 9 or the NR2B ligand, [(±)-(R*, S*)]-α-(4-hydroxyphenyl)-β-methyl-4-(phenylmethyl)-1-piperidine propanol (Ro 25-6981), caused 34% and 59% reduction in the brain/blood ratio of [¹²⁵I]9, respectively. This tracer may therefore show partially specific binding to the NR2B subunit *in vivo* [59]. Further structural modification of 9 may contribute to the development of more promising imaging probes for the NR2B subunit. [2-(3,4-Dihydro-1H-isoquinolin-2-yl)-pyridin-4-yl]-[¹¹C]dimethylamine ([¹¹C]Ro-647312, Figure 5) has been evaluated as a member of a different class of PET ligands with high affinity for the NR2B subunit ($K_i = 8.0$ nM). However, *in vivo* biodistribution of [¹¹C]Ro-647312 was almost homogeneous in the brain [60]. Several benzylamidines, such as [¹¹C]11 (Figure 5), have been developed as high-affinity PET ligands for NR2B ($K_i = 5.7$ nM for 11). *In vitro*, [¹¹C]11 showed excellent specific binding and a similar localization to that of NR2B. However, [¹¹C]11 is an unsuitable imaging agent due to metabolic instability [61]. (3S,4R)-4-Methylbenzyl 3-fluoro-4-((pyrimidin-2-ylamino)methyl) piperidine-1-carboxylate (MK-0657) was developed as a highly potent NR2B antagonist ($IC_{50} = 3.6$ nM) for the treatment of neuropathic pain, Parkinson's disease, and major depression [17, 62]. Two radiofluorinated diastereoisomers of MK-0657 ([¹⁸F]*trans*-MK-0657 and [¹⁸F]*cis*-MK-0657, Figure 5) exhibited a localization pattern consistent with that of NR2B expression and very high specific binding for the NR2B modulator binding site. However, no further *in vivo* evaluations of these potential imaging agents have been reported [63].

3. mGluRs

mGluRs are widely expressed though the CNS and their activation leads to various effects on neuronal synaptic transmission via regulation of ion channels and signaling proteins. Dysregulation of mGluRs has been observed in various conditions affecting the CNS, such as anxiety [64], depression [65], Alzheimer's disease [66], schizophrenia [67], Parkinson's disease [68], and epilepsy [69]. Positive and negative modulators of mGluRs have therefore been developed for the treatment of these neurological diseases. Nuclear medicine imaging of mGluRs can be used for the investigation of a range of diseases, in addition to monitoring receptor occupancy by therapeutic agents. Thus, a considerable number of PET imaging probes for mGluRs have been reported. PET ligands for group I mGluRs (mGluR1 and 5) have been developed extensively and several of these have been confirmed as promising ligands in clinical studies. Recently, potential PET probes for mGluR2 (group II) have also been reported and have proceeded to phase I studies. No

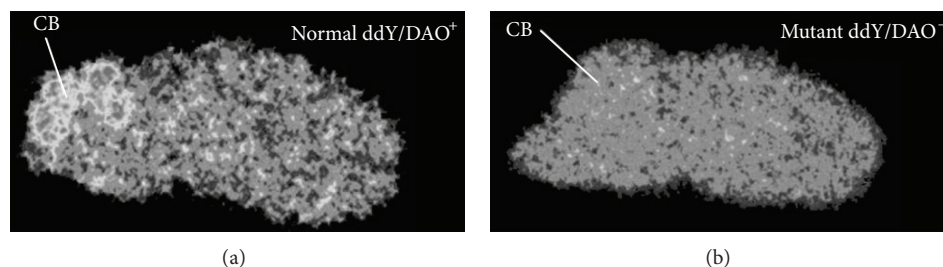


FIGURE 4: *Ex vivo* autoradiograms of [^{11}C]L-703,717 in the brain of normal ddY/DAO+ (a) and mutant ddY/DAO- mice (b) 30 min after injection of [^{11}C]L-703,717 and warfarin (60 mg/kg) [51].

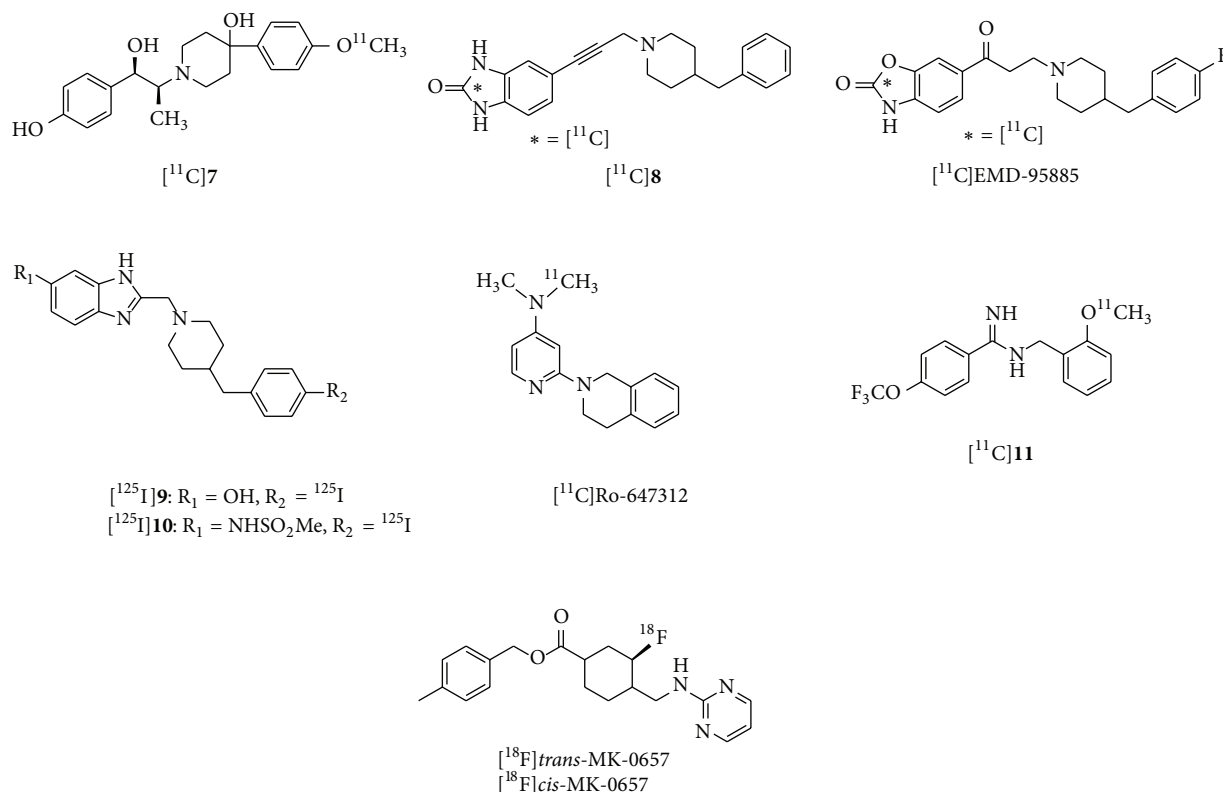


FIGURE 5: Chemical structure of imaging probes for NR2B negative modulator binding site of NMDARs.

clinically useful PET ligands for group III mGluRs have been published, due to a lack of selectivity over other mGluRs.

3.1. Imaging Probes for Group I mGluRs

3.1.1. Physiology of Group I mGluRs. Group I mGluRs (mGluR1 and mGluR5) are predominantly expressed in the postsynaptic neuron. Their activation leads to increased neuronal excitability and they are involved in modulation of synaptic plasticity at glutamatergic synapses. They are coupled to G_q/G11 and upregulate inositol triphosphate and diacylglycerol levels via phospholipase C activation, triggering calcium mobilization, and activation of protein kinase C (PKC). In addition, group I mGluRs have been reported to be implicated in the mitogen-activated protein kinase (MAPK)/extracellular signal-regulated kinase

(ERK) and mammalian target of rapamycin (mTOR)/p70 S6 kinase pathways, which can regulate synaptic plasticity [70]. Complementary expression of mGluR1 and mGluR5 has been observed in the rodent brain. mGluR1 are found extensively throughout the brain, but are highly expressed in the cerebellar cortex, hippocampus, and thalamus. mGluR5 expression has been observed in the cerebral cortex, hippocampus, accessory olfactory bulbs, and nucleus accumbens [71]. mGluR1 antagonists have shown promising anxiolytic and antidepressant effects, whereas positive modulators of mGluR1 have been reported to be useful for the treatment of schizophrenia. Negative modulators of mGluR5 can be effective in the treatment of anxiety, fragile X syndrome, chronic pain, and depression [72]. In contrast, positive modulators of this receptor have potential for the treatment of schizophrenia [73].

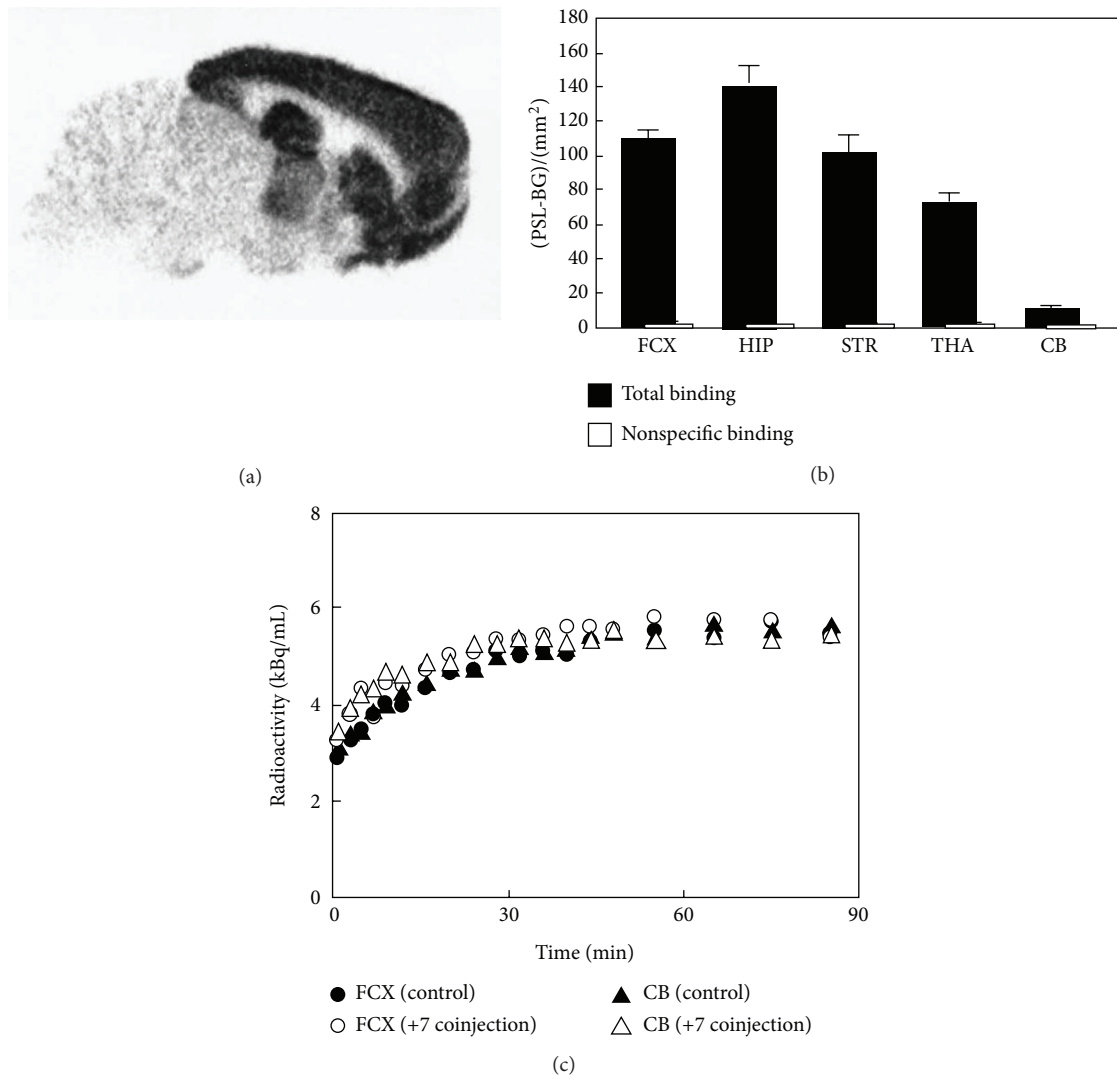


FIGURE 6: *In vitro* autoradiogram of $[^{11}\text{C}]7$ (a) and quantified values of the autoradiogram in frontal cortex (FCX), hippocampus (HIP), striatum (STR), thalamus (THA), and cerebellum (CB) (b). Nonspecific binding was determined in the presence of (+) CP-101,606 (10 μM). (c) Time radioactivity curves in the monkey brain after administration of $[^{11}\text{C}]7$. Nonradioactive 7 (2 mg/kg) was coinjected with $[^{11}\text{C}]7$ into the same monkey [55].

3.1.2. *Development of Imaging Probes for mGluR1.* (3-Ethyl-2- $[^{11}\text{C}]$ methyl-6-quinolinyloxy)-*cis*-4-methoxycyclohexylmethanone ($[^{11}\text{C}]$ JNJ-16567083, Figure 7) has been developed as a high-affinity, selective mGluR1 ligand ($K_i = 4.41$ nM for rat mGluR1, 13.3 nM for human mGluR1) [74]. *Ex vivo* studies using this ligand showed good brain uptake and a localization pattern consistent with mGluR1 expression. In addition, over 80% of the accumulation of $[^{11}\text{C}]$ JNJ-16567083 in the cerebellum was blocked by selective mGluR1 antagonists, while treatment with a selective mGluR5 antagonist produced no marked inhibition of its binding, indicating selectivity for mGluR1. In PET studies, it showed high specific binding in regions expressing mGluR1, indicating that $[^{11}\text{C}]$ JNJ-16567083 is bound to mGluR1 in the living rat brain [74]. An ^{18}F -labeled JNJ-16567083 derivative ($[^{18}\text{F}]12$, Figure 7) was also reported to have a high affinity for mGluR1 ($K_i =$

1.77 nM for rat mGluR1 and 24.4 nM for human mGluR1). The *in vivo* localization of $[^{18}\text{F}]12$ in rats was similar to that of $[^{11}\text{C}]$ JNJ-16567083. The *in vivo* accumulation of $[^{18}\text{F}]12$ in the cerebellum was inhibited by pretreatment with a selective mGluR1 antagonist, but not by an mGluR2 antagonist (LY341495) or an mGluR5 antagonist (MPEP), indicating selectivity for mGluR1 in the living rat brain. However, PET studies in baboons found that $[^{11}\text{C}]$ JNJ-16567083 and $[^{18}\text{F}]12$ produced low brain signals, probably due to a lower receptor density in baboon brain than in rat brain [75]. These results suggested that less lipophilic and/or higher affinity mGluR1 ligands are necessary for successful imaging in the primate brain.

N-Cyclohexyl-6- $\{[N-(2\text{-methoxyethyl})-N\text{-methylamino}]methyl\}$ -*N*-methylthiazolo [3,2-*a*]benzimidazole-2-carboxamide (YM-202074, Figure 7) has been reported as a

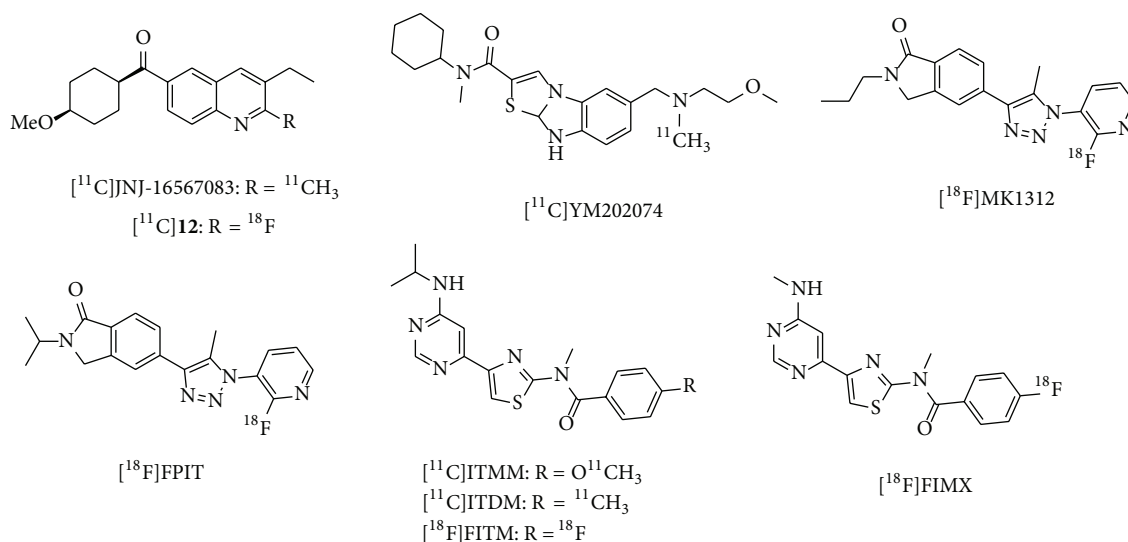
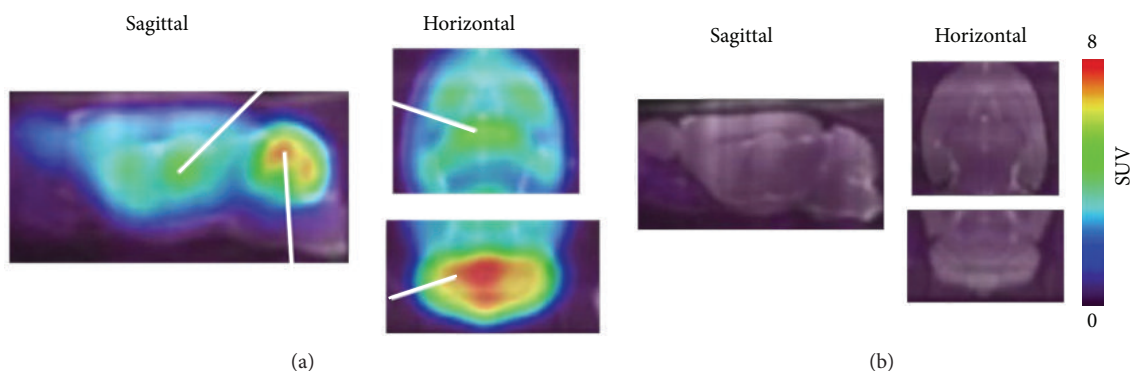


FIGURE 7: Chemical structure of imaging probes for mGluR1.

FIGURE 8: Sagittal PET images (0–60 min) of $[^{11}\text{C}]\text{ITMM}$ in wild-type (a) and mGluR1 knockout (b) mice brains [83].

high-affinity, selective mGluR1 ligand ($K_i = 4.8$ nM for rat mGluR1) with lower lipophilicity than JNJ-16567083 ($\log D = 2.7$ versus 3.38). Although $[^{11}\text{C}]\text{YM-202074}$ showed *in vitro* accumulation consistent with mGluR1 expression in the rat brain, PET studies in rats using this ligand demonstrated a low brain uptake and localization that was inconsistent with mGluR1-rich regions. These findings may be attributed to rapid ligand metabolism and the subsequent influx of radiometabolites into the brain [76]. 1-(2-Fluoro-3-pyridyl)-4-(2-propyl-1-oxoisoindoline-5-yl)-5-methyl-1H-1,2,3-triazole (MK-1312, Figure 7) has been developed as a potent mGluR1 ligand ($\text{IC}_{50} = 4.3$ nM for human mGluR1), with high selectivity and moderate lipophilicity ($\log P = 2.3$). $[^{18}\text{F}]\text{MK-1312}$ displayed similar *in vitro* localization to that of mGluR1 and highly selective binding. PET studies of this ligand in rhesus monkeys demonstrated rapid uptake kinetics, with no significant defluorination in brain. In addition, binding was inhibited by the mGluR1 antagonist, MK-5435, in a dose-dependent manner [77]. Although these results indicated that $[^{18}\text{F}]\text{MK-1312}$ may be a promising PET ligand for mGluR1, no further clinical studies have been

reported to date. 1-(2-Fluoro-3-pyridyl)-4-(2-isopropyl-1-oxoisoindoline-5-yl)-5-methyl-1H-1,2,3-triazole (FPIT, Figure 7), an MK-1312 derivative, has been reported as a selective mGluR1 ligand with an IC_{50} of 5.4 nM for human mGluR1 [77]. $[^{18}\text{F}]\text{FPIT}$ showed similar *in vitro* distribution to mGluR1 in both rat and monkey brains. In addition, its accumulation was selectively blocked by an mGluR1 ligand, indicating excellent specific binding (95%). PET/magnetic resonance imaging (MRI) studies of this ligand in rats and monkeys demonstrated a distribution that was consistent with that observed *in vitro*. Brain accumulation of $[^{18}\text{F}]\text{FPIT}$ was significantly inhibited by nonradioactive FPIT and by the mGluR1-selective ligand JNJ-16259865 [78]. Although $[^{18}\text{F}]\text{FPIT}$ has been demonstrated to be a prospective PET probe for mGluR1, further clinical studies have not yet been performed, probably due to the slow pharmacokinetics, and the influx of small levels of radiometabolites into the brain. 4-Fluoro-N-[4-[6-(isopropylamino)pyrimidin-4-yl]-1,3-thiazol-2-yl]-N-methylbenzamide (FITM, Figure 7) was developed as a potent mGluR1 antagonist ($\text{IC}_{50} = 5.1$ nM) with high selectivity [79] and low lipophilicity ($\log D = 1.46$)

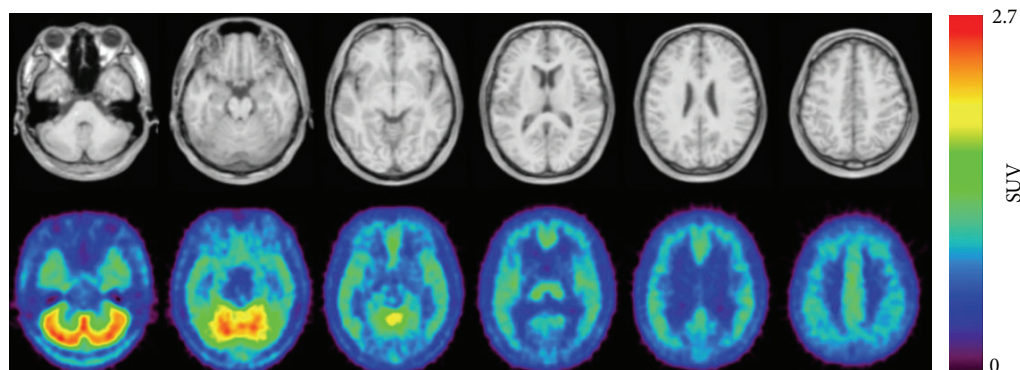


FIGURE 9: PET/MRI images of [^{11}C]ITMM (40–60 min) obtained from 5 healthy human subjects. Upper: MR image and lower: averaged [^{11}C]ITMM PET image [85].

[80]. *In vitro* and *ex vivo* binding of [^{18}F]FITM matched the distribution of mGluR1, with high specific binding in mGluR1-rich regions [80]. [^{18}F]FITM showed high brain uptake (>7% ID/g in mice) and metabolic stability, with 95% intact [^{18}F]FITM detected in the rat brain 120 min after injection. Rat and monkey PET studies demonstrated a radioactive signal distribution consistent with that of the mGluR1, with very high specific binding. Kinetic analysis showed that the calculated V_T values of [^{18}F]FITM were also consistent with the localization of mGluR1 [81]. PET studies of [^{18}F]FITM in rat brain that included blocking experiments determined B_{\max} and K_d values in several brain regions with moderate mGluR1 expression, such as the thalamus, hippocampus, striatum, and cingulate cortex, consistent with the density of mGluR1 in these regions. However, because of its relatively slow kinetics, B_{\max} and K_d values of [^{18}F]FITM could not be measured in the mGluR1-rich cerebellum [82]. Although these findings have shown that [^{18}F]FITM is a prospective PET radiotracer for mGluR1, no further clinical PET studies have been reported in the literature. It is reported that [^{18}F]FITM could be prepared in poor radiochemical yields ($14 \pm 3\%$), probably due to using the 4-nitrobenzamide precursor [80]. It is suggested that optimized methods for radiosynthesis of [^{18}F]FITM should be developed. *N*-[4-[6-(Isopropylamino)pyrimidin-4-yl]-1,3-thiazol-2-yl]-4-methoxy-*N*-methylbenzamide (ITMM, Figure 7) has been reported to be a highly potent and selective PET probe for mGluR1, with a K_i value of 12.6 nM (rat brain homogenate) and a $\log D$ value of 2.57. *In vitro* binding of [^{11}C]ITMM was consistent with mGluR1 distribution, with high specific binding in mGluR1-rich regions. A PET study in rats found that [^{11}C]ITMM displayed high brain uptake, with the highest uptake (in the cerebellum) being over 3.0 of the SUV (standardized uptake value). The *in vivo* distribution of [^{11}C]ITMM was consistent with the *in vitro* data. The heterogeneous localization of [^{11}C]ITMM was abolished by treatment with nonradioactive ITMM and an mGluR1-selective ligand. In addition, a PET study of [^{11}C]ITMM in the mGluR1 knockout mouse demonstrated quite low uptake and homogeneous distribution of radioactivity in the brain (Figure 8) [83]. Furthermore, [^{11}C]ITMM showed reduced

accumulation in the ischemic brain and treatment with the neuroprotective agent, minocycline, which may inhibit mGluR1 activation, abolished this decrease of mGluR1 in the brain [84]. Because [^{11}C]ITMM has been demonstrated to be a promising PET tracer for mGluR1, the first human PET studies have been performed. [^{11}C]ITMM uptake increased gradually in the cerebellar cortex and V_T in this brain region was 2.61, while V_T was 0.53 in the mGluR1-poor pons. The rank order of [^{11}C]ITMM uptake was consistent with mGluR1 expression levels in the human brain (Figure 9). Because [^{11}C]ITMM showed relatively low uptake in the brain regions with a modest expression of mGluR1, such as the thalamus, hippocampus, and cerebral cortex, the [^{11}C]ITMM signal in regions outside the cerebellum could be difficult to assess and this would make it hard to examine localization changes in these regions [85]. Nevertheless, [^{11}C]ITMM could be used to evaluate alterations in cerebellar mGluR1 under pathological conditions. Further clinical studies may be needed to assess the usefulness of [^{11}C]ITMM as a PET ligand for quantification of mGluR1.

N-[4-[6-(Isopropylamino)pyrimidin-4-yl]-1,3-thiazol-2-yl]-*N*-methyl-4- ^{11}C -methylbenzamide ([^{11}C]ITDM, Figure 7), an analog of ITMM, also has high affinity for mGluR1 ($K_i = 13.6$ nM) and moderate lipophilicity ($\log D = 1.74$). PET studies of [^{11}C]ITDM in the monkey brain showed localization consistent with known mGluR1 expression, fast kinetics, and a very low level of binding in the mGluR1-poor pons [86]. After detailed kinetic studies, [^{11}C]ITDM was considered superior to [^{11}C]ITMM because of its higher regional V_T values in the monkey brain [87]. Global reduction of [^{11}C]ITDM binding was observed in the mGluR1-expressing brain regions of the R6/2 mouse model of Huntington's disease. The change in the radioactive signal correlated with the expression of mGluR1 in the brains of these R6/2 mice [88]. Thus, [^{11}C]ITDM has been confirmed as a promising PET ligand for monitoring changes in mGluR1 availability in the brain. To our knowledge, clinical PET studies with [^{11}C]ITDM have not yet been published. [^{18}F]4-Fluoro-*N*-methyl-*N*-(4-(6-(methylamino)pyrimidin-4-yl)thiazol-2-yl)benzamide ([^{18}F]FIMX, Figure 7) has been shown to have a high affinity for mGluR1 ($\text{IC}_{50} = 1.8$ nM) with high

selectivity against a wide range of other human receptors [79, 89]. [^{18}F]FIMX was successfully synthesized by the radiofluorination of the diaryliodonium salts precursor. FIMX has moderate lipophilicity, with a $\log D$ value of 2.25. PET studies of [^{18}F]FIMX in rhesus monkey demonstrated high BBB permeability and maximal uptake in the mGluR1-rich cerebellum ($\text{SUV} = 5.3$ at 12 min). The distribution of radioactivity in the brain matched mGluR1 expression, and accumulation was abolished by treatment with nonradioactive FIMX or the mGluR1-selective ligand JNJ-1625968553 (3 mg/kg, resp.). In contrast, an mGluR5-selective ligand (MTEP) did not affect [^{18}F]FIMX binding in the monkey brain [89]. Apparently, [^{18}F]FIMX is a prospective PET radioligand for imaging of mGluR1. Recently, an initial clinical PET imaging study using [^{18}F]FIMX was performed. The mGluR1-rich cerebellum had the highest uptake (SUV ; 1.8 at 120 min), whereas mGluR1-poor regions ranged from SUV values of 0.3–1 at 120 min [90]. PET imaging of patients with a range of CNS disorders using [^{18}F]FITM, [^{11}C]ITMM, [^{11}C]ITDM, and [^{18}F]FIMX could help to elucidate the relationship between these disorders and mGluR1.

3.1.3. Development of Imaging Probes for mGluR5. Several diaryl alkyne derivatives have been reported as high-affinity, selective mGluR5 antagonists that could be used as *in vivo* imaging probes. 3-Fluoro-5-(2-pyridinylethynyl) benzonitrile (FPBE, Figure 10) has been reported to have an excellent affinity for mGluR5, with a K_i value of 0.2 nM (rat brain cortex) and a moderate $\log P$ value of 2.8. Autoradiography of rhesus monkey brain demonstrated high accumulation in mGluR5-rich regions, such as the cortex, caudate, putamen, amygdala, hippocampus, and most thalamic nuclei, and a low signal in the mGluR5-poor cerebellar layers. In addition, the heterogeneous binding of [^{18}F]FPBE was abolished in the presence of the mGluR5-selective ligand, MPEP, indicating that the radiotracer bound specifically to mGluR5 *in vitro* [91]. PET studies of [^{18}F]FPBE in rhesus monkey and rat showed similar localization to mGluR5 and displacement by mGluR5 ligands (Figure 11) [91, 92]. Building on these promising preclinical studies of [^{18}F]FPBE, an initial clinical PET study was performed to assess the usefulness of this radiotracer for PET imaging of mGluR5. The regional brain distribution of [^{18}F]FPBE in the healthy adult brain matched the known expression of mGluR5 and showed high reproducibility, suggesting that [^{18}F]FPBE is a suitable PET radioligand for mGluR5 in the human brain [93].

3-(6-Methyl-pyridin-2-ylethynyl)-cyclohex-2-enone-O- ^{11}C -methyl-oxime ([^{11}C]ABP688, Figure 10) has been reported as a highly selective and potent radiotracer for the mGluR5 allosteric site, with a K_d value of 1.7 nM in rat brain homogenates. *Ex vivo* autoradiography of [^{11}C]ABP688 demonstrated high accumulation of this radiotracer in mGluR5-rich brain regions, such as the cingulate cortex, striatum, and hippocampus. Treatment with M-MPEP (1 mg/kg), an mGluR5-selective antagonist, abolished the heterogeneous localization of [^{11}C]ABP688. PET studies

using [^{11}C]ABP688 in normal rats demonstrated a similar distribution to that observed in *ex vivo* experiments (Figure 12). In addition, accumulation of this radiotracer was almost homogeneous in mGluR5-knockout mice, indicating that [^{11}C]ABP688 was highly specific for mGluR5 in the living brain [94]. A clinical PET study of [^{11}C]ABP688 in human brain demonstrated high accumulation in mGluR5-rich brain regions but low levels in the mGluR5-poor regions, consistent with the results of rat PET studies. Its specific distribution volume in the brain regions ranged from 5.45 (anterior cingulate) to 1.91 (cerebellum), and the rank order of these values was consistent with the known mGluR5 density. These results suggested that [^{11}C]ABP688 could be used for PET quantification of mGluR5 in the human brain [95]. It has also been reported that [^{11}C]ABP688 can be used for monitoring mGluR5 drug occupancy. AZD2066, a highly potent mGluR5-selective ligand, dose-dependently displaced [^{11}C]ABP688 binding in the human brain (Figure 13). In this study, the dose of AZD2066 required to produce 50% mGluR5 occupancy was estimated to be 13.5 mg [96]. On the other hand, there are two geometrical isomers of [^{11}C]ABP688 and the *E*-isomer has a much higher binding affinity for mGluR5 than the *Z*-isomer ($K_d = 5.7$ nM versus 140 nM). In a rat PET study of [^{11}C]ABP688, the *E*-isomer showed high brain uptake and distribution that was consistent with mGluR5 expression. In contrast, the *Z*-isomer showed low brain retention and homogeneous binding throughout the brain [97]. Although [^{11}C]ABP688 could be synthesized with an *E*-isomer to *Z*-isomer ratio of > 10 : 1 [94], it has been suggested that *E*-[^{11}C]ABP688 should be used for reproducible imaging of mGluR5 receptors in clinical studies. 3-Fluoro-5-[2-[2-(^{18}F)fluoromethyl]thiazol-4-yl]ethynyl]benzonitrile ([^{18}F]SP203, Figure 10) has been developed as a negative allosteric modulator with excellent affinity (40 pM) for mGluR5. PET studies using [^{18}F]SP203 demonstrated high uptake in mGluR5-rich regions and the signal was greatly diminished by treatment with the mGluR5-selective ligand MPEP (5 mg/kg) [98]. One disadvantage of [^{18}F]SP203 is the ease of its defluorination by glutathione *S*-transferase in the rat brain [99]. However, because primates have much lower levels of glutathione *S*-transferase [100], initial PET studies were conducted with [^{18}F]SP203 in healthy human subjects. PET images showed high brain uptake of [^{18}F]SP203 (Figure 14) with little defluorination and brain uptake could be calculated as V_T in humans. [^{18}F]SP203 had high BBB permeability (% SUV; ~580) and the rank order of V_T values in the brain regions was as follows: neocortex (20–26) > thalamus (15) \approx cerebellum (14), consistent with the levels of mGluR5 in the human brain [101]. Therefore, despite the issue of defluorination, [^{18}F]SP203 can be used for quantification of mGluR5 by PET.

3.1.4. mGluR5-Selective PET Imaging in Diseases. Cocaine exposure has been reported to reduce mGluR5 expression in the rodent brain [102]. Clinical PET studies were conducted with [^{11}C]ABP688 in cocaine-addicted participants, in comparison with healthy control subjects. [^{11}C]ABP688 binding in the striatum was reduced by approximately 20%

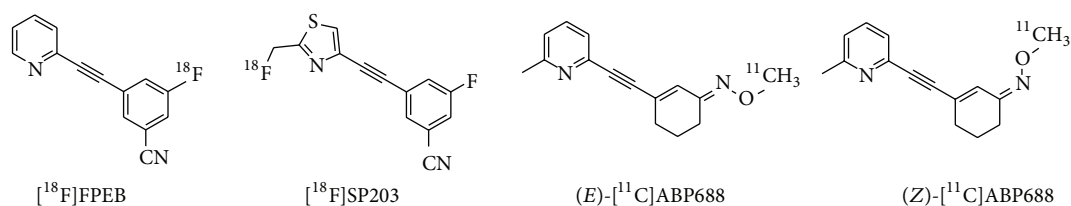
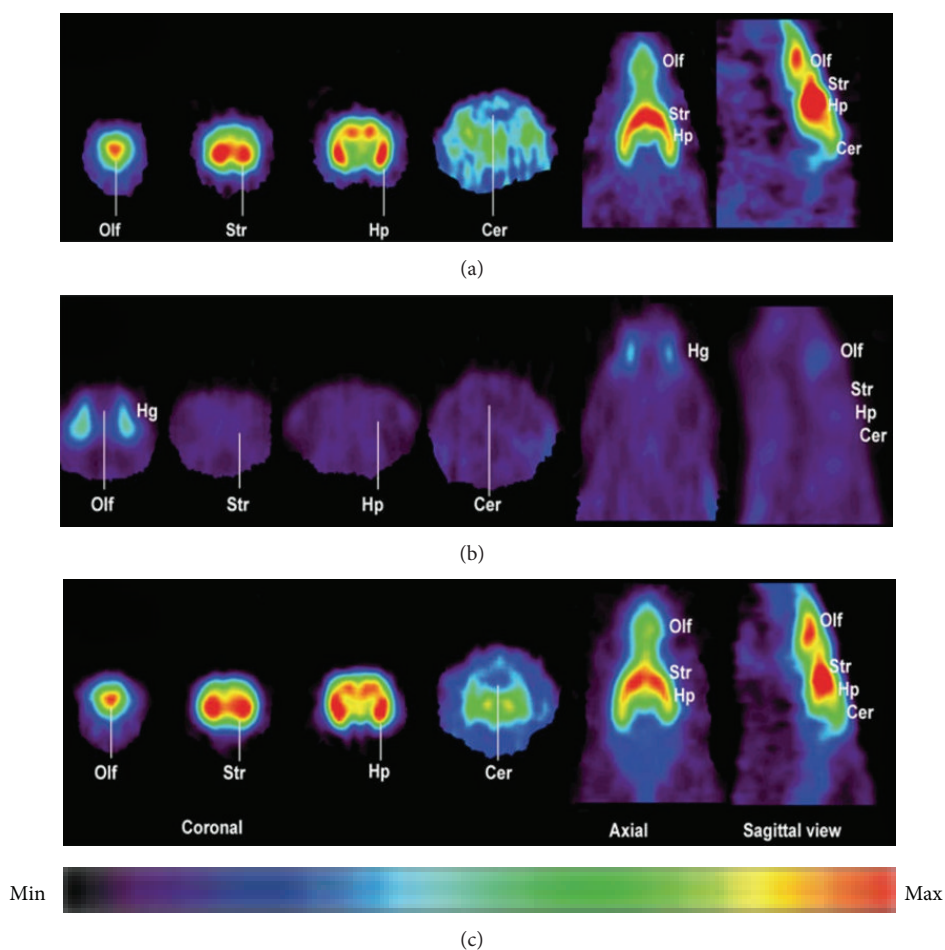


FIGURE 10: Chemical structure of imaging probes for mGluR5.

FIGURE 11: PET images of $[^{18}\text{F}]$ FPEB (20–25 min) in rat brain without drug treatment (a), treatment of mGluR5-selective ligand MTEP treatment (10 mg/kg) (b), and treatment of mGluR1-selective YM-298198 (10 mg/kg) [92].

in cocaine-addicted participants [103]. Another clinical PET study with $[^{11}\text{C}]$ ABP688 demonstrated that mGluR5 availability in cocaine-dependent subjects was inversely proportional to the duration of cocaine abstinence [104]. These studies indicated that distribution of mGluR5 was decreased in the striatum of the living brain in cocaine-abstinent individuals, information that could inform novel strategies for the control of cocaine addiction *via* mGluR5. Preclinical studies have demonstrated that mGluR5 antagonists potently reduced self-administration of nicotine [105, 106]. In a PET study, a significant reduction in $[^{11}\text{C}]$ ABP688 binding was observed in the gray matter of smokers (Figure 15), indicating

that mGluR5 could be a potential target for the treatment of nicotine dependence [107]. mGluR5 have been suggested to be involved in the pathophysiology of epilepsy [108, 109]. PET studies using $[^{11}\text{C}]$ ABP688 revealed lower levels of mGluR5 binding in the hippocampus and amygdala in rat models of chronic epilepsy, as compared to a control group. Therefore, PET imaging of mGluR5 in the temporal and spatial regions could detect dysregulated glutamatergic networks during epileptogenesis [110]. mGluR5 may also be linked to the pathophysiology of major depression [65]. Clinical PET studies using $[^{11}\text{C}]$ ABP688 showed reduced mGluR5 binding in the cortical regions, thalamus, and hippocampus of patients

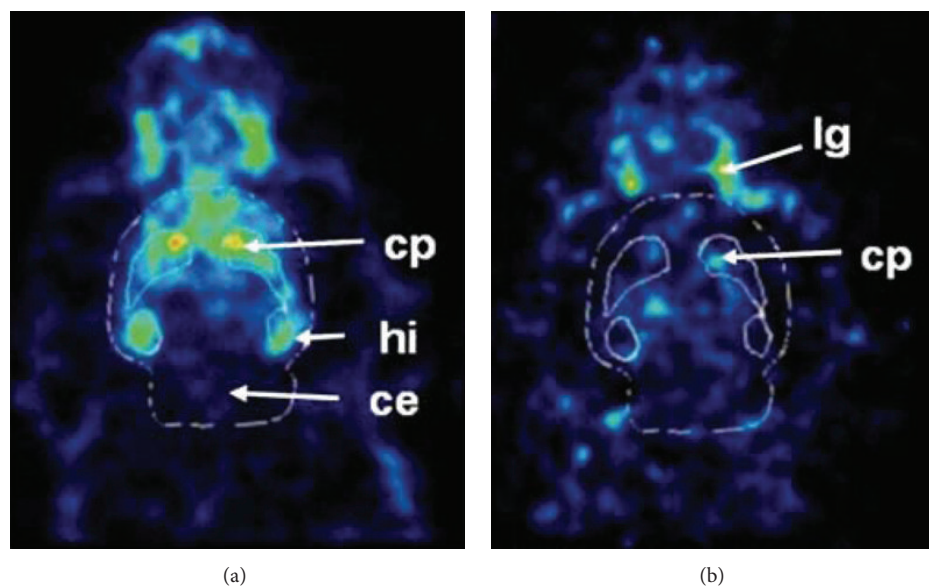


FIGURE 12: PET images of $[^{11}\text{C}]\text{ABP688}$ (0–30 min) in control rats (a) and an mGluR5-selective ligand M-MPEP (1.0 mg/kg) treated rat [94].

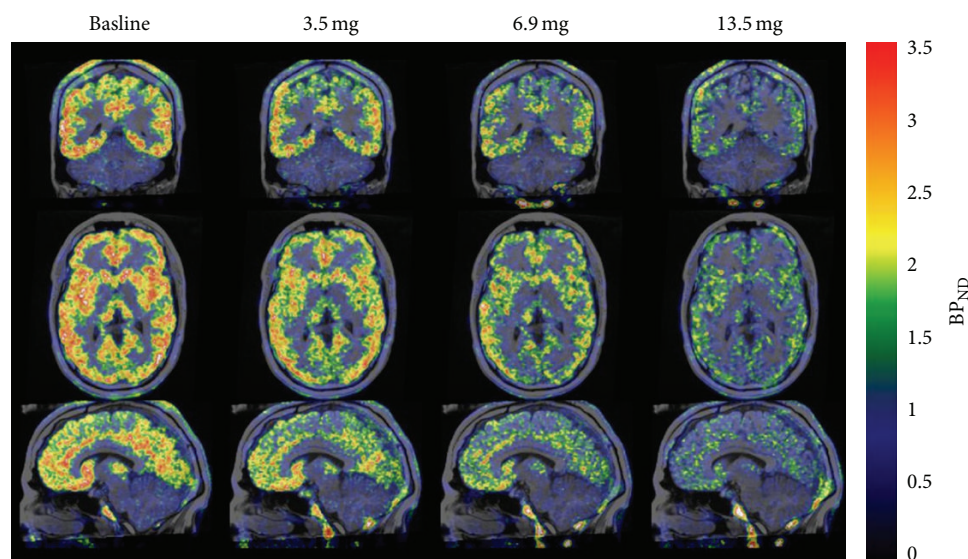


FIGURE 13: PET/MR images (0–63 min) showing the effect of AZD2066 on binding of $[^{11}\text{C}]\text{ABP688}$ [96].

with depression. Furthermore, mGluR5 availability in the hippocampus decreased with the increased severity of this disease, suggesting that changes in the availability of mGluR5 may provide a potential biomarker for the diagnosis of depression [111].

3.2. Imaging Probes for Groups II and III mGluRs

3.2.1. Physiology of Groups II and III mGluRs. Groups II (mGluR2 and mGluR3) and III (mGluR4, mGluR6, mGluR7, and mGluR8) mGluRs are primarily localized within presynaptic regions and involved in the inhibition of neurotransmitter release [70]. Groups II and III mGluRs are coupled to G_i/G_o and downregulate cAMP levels via inhibition of

adenylate cyclase. These events activate the MAPK and phosphatidylinositol 3-kinase (PI3) pathways, which regulate synaptic transmission. mGluR2 has been predominantly observed in the cerebellar cortex and olfactory bulb, while mGluR3 has been found widely throughout the brain. mGluR4 is predominantly expressed in the cerebellum. The expression of mGluR6 is restricted to the retina, whereas mGluR7 has a widespread distribution in the brain. mGluR8 is mainly expressed in the olfactory bulbs, olfactory nucleus, piriform cortex, entorhinal cortex, and medulla oblongata [71]. Agonists of group II mGluRs may be useful in the treatment of anxiety disorders and schizophrenia [73]. mGluR2/3 are involved in the pathophysiology of schizophrenia [112]. Group III mGluRs are attractive targets for the treatment

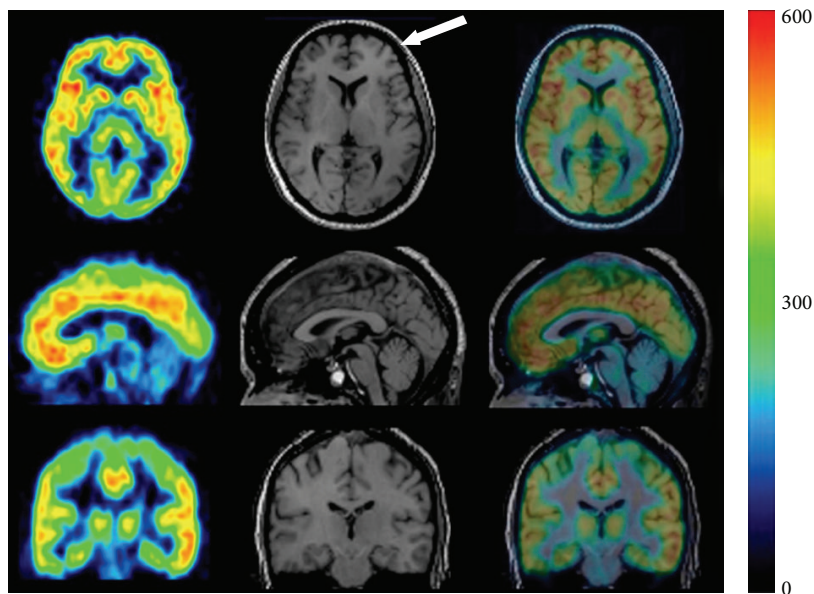


FIGURE 14: PET/MR images of $[^{18}\text{F}]\text{SP203}$ (60–180 min) in healthy subject. Arrow points to subcutaneous fat [101].

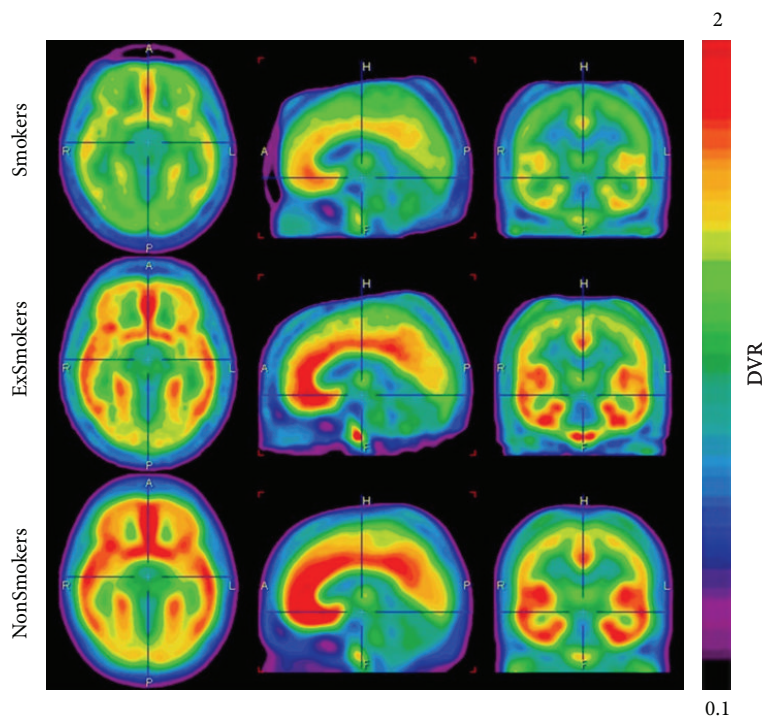


FIGURE 15: PET Images of the average mGluR5 DVR (0–40 min) using $[^{11}\text{C}]\text{ABP688}$ in the three diagnostic groups ($n = 14$) [107].

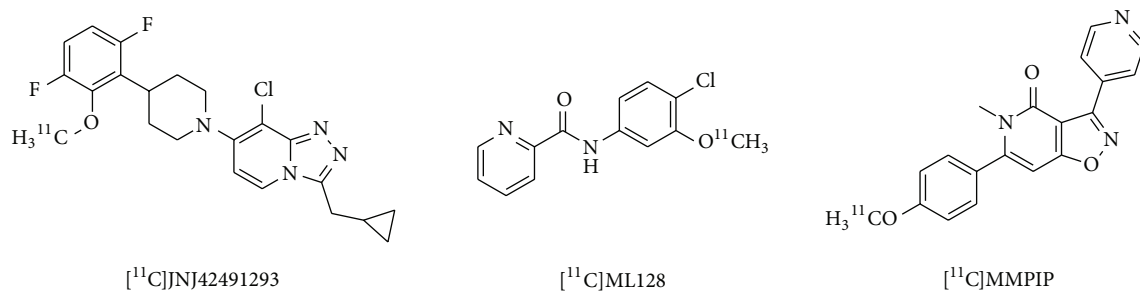


FIGURE 16: Chemical structure of imaging probes for groups II and III mGluRs.

of Parkinson's disease [113]. mGluR8 is implicated in drug addiction mechanisms [114].

3.2.2. Development of Imaging Probes for Group II mGluRs. 8-Chloro-3-(cyclopropylmethyl)-7-[4-(3,6-difluoro-2-methoxyphenyl)-1-piperidinyl]-1,2,4-triazolo[4,3-a]pyridine ($[^{11}\text{C}]\text{JNJ42491293}$, Figure 16) has been reported to act as a potent positive allosteric modulator for mGluR2, with an IC_{50} of 9.2 nM for the human mGluR2 and a high selectivity against other mGluRs. *In vivo* biodistribution and PET studies in rats demonstrated a high brain uptake of $[^{11}\text{C}]\text{JNJ42491293}$, with a signal matching the known distribution of mGluR2 that was displaced by JNJ42153605, a selective mGluR2 agonist, in all brain regions. $[^{11}\text{C}]\text{JNJ42491293}$ may be a promising PET radiotracer for the mGluR2 allosteric binding site [115]. PET studies using $[^{11}\text{C}]\text{JNJ42491293}$ in healthy male subjects demonstrated high brain uptake, which reached a maximum 30 min after treatment. Considerable $[^{11}\text{C}]\text{JNJ42491293}$ distribution was observed in the striatum and cerebellum, consistent with known mGluR2 expression patterns. $[^{11}\text{C}]\text{JNJ42491293}$ has been demonstrated to be a prospective PET radioligand for monitoring mGluR2 availability in the human brain [116].

3.2.3. Development of Imaging Probes for Group III mGluRs. *N*-(Chloro-3-methoxyphenyl)-2-picolinamide (ML128, Figure 16) has been developed as a positive allosteric modulator of mGluR4 with an EC_{50} of 110 nM for rat mGluR4 [117]. $[^{11}\text{C}]\text{ML128}$ has been synthesized and evaluated as a PET imaging probe for mGluR4. In rat PET studies, $[^{11}\text{C}]\text{ML128}$ showed high BBB penetration and localization to the hippocampus, striatum, thalamus, olfactory bulb, and cerebellum, consistent with the distribution of mGluR4. Treatment with an mGluR4 modulator led to some reduction (22–28%) in $[^{11}\text{C}]\text{ML128}$ binding in the brain. Because this radiotracer exhibited fast washout within 20 min throughout the brain, structural modification will be necessary to provide useful *in vivo* imaging probes for mGluR4 [118]. MMPIP (6-(4-methoxyphenyl-5-methyl-3-pyridin-4-ylisozazolo[4,5-c]pyridine-4(5H)-one)) is an allosteric mGluR7 antagonist with a K_b of 30 nM [119]. $[^{11}\text{C}]\text{MMPIP}$ (Figure 16) has been synthesized and evaluated as a PET radioligand for mGluR7. Although $[^{11}\text{C}]\text{MMPIP}$ showed specific *in vitro* binding in rat brain, PET studies of this radioligand in rats demonstrated low brain uptake and no specific localization to sites of mGluR7 expression.

4. Conclusion and Perspectives

Despite considerable efforts, no radioligands are currently available for human *in vivo* PET or SPECT imaging of NMDARs. There are three potential target sites for imaging agents; the channel blocker site, the glycine site, and the NR2B negative modulator site. $[^{123/125}\text{I}]\text{CNS 1261}$ is a potential imaging agent acting at the channel blocker site. However, this ligand requires further research to address its input function alteration in pathological state metabolic instability and potentially nonspecific binding. There are no radioligands for

glycine site or the NR2B negative modulator site that have shown enough promise to warrant clinical studies. Although several ligands showed localization patterns consistent with NMDAR expression and high specific binding *in vitro*, they did not show these characteristics *in vivo*. This discrepancy might be due to the dynamic properties of NMDARs. It is known that NMDAR structure is altered by binding of endogenous or exogenous ligands [1]. Importantly, the number of NMDARs on the cell surface is changed by tyrosine phosphorylation, cysteine palmitoylation of the NMDAR C-terminus, and by an alteration in subunit composition [120–122]. In addition to developing novel classes of imaging probes for NMDARs, further *in vivo* imaging studies of NMDAR models should be performed to clarify the discrepancies between the findings of *in vitro* and *in vivo* studies.

In contrast to the situation with NMDARs, several promising PET probes for mGluRs have been developed successfully. PET radioligands for mGluR1, such as $[^{18}\text{F}]\text{FITM}$, $[^{11}\text{C}]\text{ITMM}$, $[^{11}\text{C}]\text{ITDM}$, and $[^{18}\text{F}]\text{FIMX}$, have proved useful in clinical PET studies. PET imaging studies of mGluR5 with selective radiotracers ($[^{18}\text{F}]\text{FPEB}$, $[^{18}\text{F}]\text{SP203}$, and $[^{11}\text{C}]\text{ABP688}$) have enabled evaluation of mGluR5 availability in relevant disease states. $[^{11}\text{C}]\text{JNJ42491293}$ has been developed as a clinically useful prospective PET probe for mGluR2. Further PET investigations of patients with various mGluR-related diseases could make it possible to resolve the roles of mGluRs in these disorders, monitor mGluR activity, and quantify mGluR occupancy by therapeutic agents. As no clinically useful PET ligands for group III mGluRs have yet been identified, continued efforts should be made to develop high-affinity and selective ligands for these receptors.

Conflict of Interests

The authors declare that there is no conflict of interests regarding the publishing of this paper.

References

- [1] S. F. Traynelis, L. P. Wollmuth, C. J. McBain et al., "Glutamate receptor ion channels: Structure, regulation, and function," *Pharmacological Reviews*, vol. 62, no. 3, pp. 405–496, 2010.
- [2] C. M. Niswender and P. J. Conn, "Metabotropic glutamate receptors: physiology, pharmacology, and disease," *Annual Review of Pharmacology and Toxicology*, vol. 50, pp. 295–322, 2010.
- [3] D. Bowie, "Ionotropic glutamate receptors & CNS disorders," *CNS and Neurological Disorders—Drug Targets*, vol. 7, no. 2, pp. 129–143, 2008.
- [4] A. Lau and M. Tymianski, "Glutamate receptors, neurotoxicity and neurodegeneration," *Pflugers Archiv European Journal of Physiology*, vol. 460, no. 2, pp. 525–542, 2010.
- [5] G. Riedel, B. Platt, and J. Micheau, "Glutamate receptor function in learning and memory," *Behavioural Brain Research*, vol. 140, no. 1-2, pp. 1–47, 2003.
- [6] C. G. Lau and R. S. Zukin, "NMDA receptor trafficking in synaptic plasticity and neuropsychiatric disorders," *Nature Reviews Neuroscience*, vol. 8, no. 6, pp. 413–426, 2007.
- [7] J. A. Kemp and R. M. McKernan, "NMDA receptor pathways as drug targets," *Nature Neuroscience*, vol. 5, pp. 1039–1042, 2002.

- [8] L. V. Kalia, S. K. Kalia, and M. W. Salter, "NMDA receptors in clinical neurology: excitatory times ahead," *The Lancet Neurology*, vol. 7, no. 8, pp. 742–755, 2008.
- [9] R. Dingledine, K. Borges, D. Bowie, and S. F. Traynelis, "The glutamate receptor ion channels," *Pharmacological Reviews*, vol. 51, no. 1, pp. 7–61, 1999.
- [10] B. Laube, J. Kuhse, and H. Betz, "Evidence for a tetrameric structure of recombinant NMDA receptors," *Journal of Neuroscience*, vol. 18, no. 8, pp. 2954–2961, 1998.
- [11] H. Furukawa, S. K. Singh, R. Mancusso, and E. Gouaux, "Subunit arrangement and function in NMDA receptors," *Nature*, vol. 438, no. 7065, pp. 185–192, 2005.
- [12] M. H. Ulbrich and E. Y. Isacoff, "Rules of engagement for NMDA receptor subunits," *Proceedings of the National Academy of Sciences of the United States of America*, vol. 105, no. 37, pp. 14163–14168, 2008.
- [13] P. Paoletti and J. Neyton, "NMDA receptor subunits: function and pharmacology," *Current Opinion in Pharmacology*, vol. 7, no. 1, pp. 39–47, 2007.
- [14] C.-M. Low and K. S.-L. Wee, "New insights into the not-so-new NR3 subunits of N-methyl-D-aspartate receptor: localization, structure, and function," *Molecular Pharmacology*, vol. 78, no. 1, pp. 1–11, 2010.
- [15] H. Furukawa and E. Gouaux, "Mechanisms of activation, inhibition and specificity: crystal structures of the NMDA receptor NR1 ligand-binding core," *EMBO Journal*, vol. 22, no. 12, pp. 2873–2885, 2003.
- [16] Y. Yao, C. B. Harrison, P. L. Freddolino, K. Schulten, and M. L. Mayer, "Molecular mechanism of ligand recognition by NR3 subtype glutamate receptors," *The EMBO Journal*, vol. 27, no. 15, pp. 2158–2170, 2008.
- [17] L. Mony, J. N. C. Kew, M. J. Gunthorpe, and P. Paoletti, "Allosteric modulators of NR2B-containing NMDA receptors: molecular mechanisms and therapeutic potential," *British Journal of Pharmacology*, vol. 157, no. 8, pp. 1301–1317, 2009.
- [18] N. A. Anis, S. C. Berry, N. R. Burton, and D. Lodge, "The dissociative anaesthetics, ketamine and phencyclidine, selectively reduce excitation of central mammalian neurones by N-methyl-aspartate," *British Journal of Pharmacology*, vol. 79, no. 2, pp. 565–575, 1983.
- [19] A. C. Foster and E. H. F. Wong, "The novel anticonvulsant MK-801 binds to the activated state of the N-methyl-D-aspartate receptor in rat brain," *British Journal of Pharmacology*, vol. 91, no. 2, pp. 403–409, 1987.
- [20] E. Karakas, N. Simorowski, and H. Furukawa, "Subunit arrangement and phenylethanolamine binding in GluN1/GluN2B NMDA receptors," *Nature*, vol. 475, no. 7355, pp. 249–253, 2011.
- [21] J. N. C. Kew and J. A. Kemp, "Ionotropic and metabotropic glutamate receptor structure and pharmacology," *Psychopharmacology*, vol. 179, no. 1, pp. 4–29, 2005.
- [22] P. Loo, A. Braunwalder, J. Lehmann, and M. Williams, "Radioligand binding to central phencyclidine recognition sites is dependent on excitatory amino acid receptor agonists," *European Journal of Pharmacology*, vol. 123, no. 3, pp. 467–468, 1986.
- [23] E. H. F. Wong, A. R. Knight, and G. N. Woodruff, "[³H]MK-801 labels a site on the N-methyl-D-aspartate receptor channel complex in rat brain membranes," *Journal of Neurochemistry*, vol. 50, no. 1, pp. 274–281, 1988.
- [24] K. Orita, S. Sasaki, M. Maeda et al., "Synthesis and evaluation of 1-1-[5-(2'-[¹⁸F]Fluoroethyl)-2-thienyl]-cyclohexylpiperidine as a potential in vivo radioligand for the NMDA receptor-Channel complex," *Nuclear Medicine and Biology*, vol. 20, no. 7, pp. 865–873, 1993.
- [25] S. Sihver, W. Sihver, Y. Andersson et al., "In vitro and in vivo characterization of (+)-3-[¹¹C]cyano-dizocilpine," *Journal of Neural Transmission*, vol. 105, no. 2-3, pp. 117–131, 1998.
- [26] J. Owens, A. A. Tebbutt, A. L. McGregor et al., "Synthesis and binding characteristics of N-(1-naphthyl)-N'-(3-[¹²⁵I]-iodophenyl)-N'-methylguanidine ([¹²⁵I]-CNS 1261): a potential SPECT agent for imaging NMDA receptor activation," *Nuclear Medicine and Biology*, vol. 27, no. 6, pp. 557–564, 2000.
- [27] K. Erlandsson, R. A. Bressan, R. S. Mulligan et al., "Kinetic modelling of [¹²³I]CNS 1261—a potential SPET tracer for the NMDA receptor," *Nuclear Medicine and Biology*, vol. 30, no. 4, pp. 441–454, 2003.
- [28] R. A. Bressan, K. Erlandsson, R. S. Mulligan et al., "A bolus/injection paradigm for the novel NMDA receptor SPET tracer [¹²³I]CNS 1261," *Nuclear Medicine and Biology*, vol. 31, no. 2, pp. 155–164, 2004.
- [29] J. T. Kantrowitz and D. C. Javitt, "N-methyl-d-aspartate (NMDA) receptor dysfunction or dysregulation: the final common pathway on the road to schizophrenia?" *Brain Research Bulletin*, vol. 83, no. 3-4, pp. 108–121, 2010.
- [30] C. H. Lin, H. Y. Lane, and G. E. Tsai, "Glutamate signaling in the pathophysiology and therapy of schizophrenia," *Pharmacology Biochemistry and Behavior*, vol. 100, no. 4, pp. 665–677, 2012.
- [31] L. S. Pilowsky, R. A. Bressan, J. M. Stone et al., "First in vivo evidence of an NMDA receptor deficit in medication-free schizophrenic patients," *Molecular Psychiatry*, vol. 11, no. 2, pp. 118–119, 2006.
- [32] R. A. Bressan, K. Erlandsson, J. M. Stone et al., "Impact of schizophrenia and chronic antipsychotic treatment on [¹²³I]CNS-1261 binding to N-methyl-D-aspartate receptors in vivo," *Biological Psychiatry*, vol. 58, no. 1, pp. 41–46, 2005.
- [33] R. N. Waterhouse, M. Slifstein, F. Dumont et al., "In vivo evaluation of [¹¹C]N-(2-chloro-5-thiomethylphenyl)-N'-(3-methoxy-phenyl)-N'-methylguanidine ([¹¹C]GMOM) as a potential PET radiotracer for the PCP/NMDA receptor," *Nuclear Medicine and Biology*, vol. 31, no. 7, pp. 939–948, 2004.
- [34] A. Biegon, A. Gibbs, M. Alvarado, M. Ono, and S. Taylor, "In vitro and in vivo characterization of [³H]CNS-5161—a use-dependent ligand for the N-methyl-D-aspartate receptor in rat brain," *Synapse*, vol. 61, no. 8, pp. 577–586, 2007.
- [35] M. C. Asselin, A. Hammers, D. Turton, S. Osman, M. Koeppe, and D. Brooks, "Initial kinetic analysis of the in vivo binding of the putative NMDA receptor ligand [¹¹C]CNS 5161 in humans," *Neuroimage*, vol. 22, p. T137, 2004.
- [36] E. G. Robins, Y. Zhao, I. Khan, A. Wilson, S. K. Luthra, and E. Årstad, "Synthesis and in vitro evaluation of [¹⁸F]-labelled S-fluoroalkyl diarylguanidines: novel high-affinity NMDA receptor antagonists for imaging with PET," *Bioorganic and Medicinal Chemistry Letters*, vol. 20, no. 5, pp. 1749–1751, 2010.
- [37] C. J. McGinnity, A. Hammers, D. A. R. Barros et al., "Initial evaluation of [¹⁸F]-GE-179, a putative PET tracer for activated N-methyl D-aspartate receptors," *Journal of Nuclear Medicine*, vol. 55, no. 3, pp. 423–430, 2014.
- [38] W. Danyasz and C. G. Parsons, "Glycine and N-methyl-D-aspartate receptors: physiological significance and possible therapeutic applications," *Pharmacological Reviews*, vol. 50, no. 4, pp. 597–664, 1998.
- [39] R. N. Waterhouse, A. Sultana, and M. Laruelle, "In vivo evaluation of [¹¹C]-3-[2-[(3-methoxyphenylamino)carbonyl]-ethenyl]-4,6-dichloroindole-2-carboxylic acid ([¹¹C]3MPICA)

- as a PET radiotracer for the glycine site of the NMDA ion channel," *Nuclear Medicine and Biology*, vol. 29, no. 8, pp. 791–794, 2002.
- [40] M. Piel, R. Schirmacher, S. Höhnemann et al., "Synthesis and evaluation of 5,7-dichloro-4-(3-{4-[4-(2-[¹⁸F]fluoroethyl)-piperazin-1-yl]-phenyl}-ureido)-1, 2, 3, 4-tetrahydroquinoline-2-carboxylic acid as a potential NMDA ligand to study glutamatergic neurotransmission *in vivo*," *Journal of Labelled Compounds and Radiopharmaceuticals*, vol. 46, pp. 645–659, 2003.
- [41] J. J. Kulagowski, R. Baker, N. R. Curtis et al., "3'-(Arylmethyl)- and 3'-(aryloxy)-3-phenyl-4-hydroxyquinolin-2(1H)-ones: orally active antagonists of the glycine site on the NMDA receptor," *Journal of Medicinal Chemistry*, vol. 37, no. 10, pp. 1402–1405, 1994.
- [42] M. Rowley, J. J. Kulagowski, A. P. Watt et al., "Effect of plasma protein binding on *in vivo* activity and brain penetration of glycine/NMDA receptor antagonists," *Journal of Medicinal Chemistry*, vol. 40, no. 25, pp. 4053–4068, 1997.
- [43] T. Haradahira, M.-R. Zhang, J. Maeda et al., "A strategy for increasing the brain uptake of a radioligand in animals: use of a drug that inhibits plasma protein binding," *Nuclear Medicine and Biology*, vol. 27, no. 4, pp. 357–360, 2000.
- [44] T. Haradahira, M.-R. Zhang, J. Maeda et al., "A prodrug of NMDA/Glycine site antagonist, L-703,717, with improved BBB permeability: 4-acetoxy derivative and its positron-emitter labeled analog," *Chemical and Pharmaceutical Bulletin*, vol. 49, no. 2, pp. 147–150, 2001.
- [45] R. Matsumoto, T. Haradahira, H. Ito et al., "Measurement of glycine binding site of N-methyl-D-aspartate receptors in living human brain using 4-acetoxy derivative of L-703,717, 4-acetoxy-7-chloro-3-[3-(4-[¹¹C] methoxybenzyl) phenyl]-2(1H)-quinolone (AcL703) with positron emission tomography," *Synapse*, vol. 61, no. 10, pp. 795–800, 2007.
- [46] T. Fuchigami, T. Haradahira, N. Fujimoto et al., "Difference in brain distributions of carbon 11-labeled 4-hydroxy-2(1H)-quinolones as PET radioligands for the glycine-binding site of the NMDA ion channel," *Nuclear Medicine and Biology*, vol. 35, no. 2, pp. 203–212, 2008.
- [47] T. Fuchigami, T. Haradahira, N. Fujimoto et al., "Development of N-[¹¹C]methylamino 4-hydroxy-2(1H)-quinolone derivatives as PET radioligands for the glycine-binding site of NMDA receptors," *Bioorganic and Medicinal Chemistry*, vol. 17, no. 15, pp. 5665–5675, 2009.
- [48] A. Hashimoto, T. Nishikawa, T. Oka, and K. Takahashi, "Endogenous D-serine in rat brain: N-methyl-D-aspartate receptor-related distribution and aging," *Journal of Neurochemistry*, vol. 60, no. 2, pp. 783–786, 1993.
- [49] M. J. Schell, R. O. Brady Jr., M. E. Molliver, and S. H. Snyder, "D-serine as a neuromodulator: regional and developmental localizations in rat brain glia resemble NMDA receptors," *Journal of Neuroscience*, vol. 17, no. 5, pp. 1604–1615, 1997.
- [50] M. J. Schell, M. E. Molliver, and S. H. Snyder, "D-serine, an endogenous synaptic modulator: localization to astrocytes and glutamate-stimulated release," *Proceedings of the National Academy of Sciences of the United States of America*, vol. 92, no. 9, pp. 3948–3952, 1995.
- [51] T. Haradahira, T. Okauchi, J. Maeda et al., "Effects of endogenous agonists, glycine and D-serine, on *in vivo* specific binding of [¹¹C]L-703,717, a PET radioligand for the glycine-binding site of NMDA receptors," *Synapse*, vol. 50, no. 2, pp. 130–136, 2003.
- [52] K. R. Gogas, "Glutamate-based therapeutic approaches: NR2B receptor antagonists," *Current Opinion in Pharmacology*, vol. 6, no. 1, pp. 68–74, 2006.
- [53] P. Malherbe, V. Mutel, C. Broger et al., "Identification of critical residues in the amino terminal domain of the human NR2B subunit involved in the RO 25-6981 binding pocket," *Journal of Pharmacology and Experimental Therapeutics*, vol. 307, no. 3, pp. 897–905, 2003.
- [54] F. Menniti, B. Chenard, M. Collins, M. Ducat, I. Shalaby, and F. White, "CP-101,606, a potent neuroprotectant selective for forebrain neurons," *European Journal of Pharmacology*, vol. 331, no. 2-3, pp. 117–126, 1997.
- [55] T. Haradahira, J. Maeda, T. Okauchi et al., "Synthesis, *in vitro* and *in vivo* pharmacology of a C-11 labeled analog of CP-101,606, (±)threo-1-(4-hydroxyphenyl)-2-[4-hydroxy-4-(p-[¹¹C]methoxyphenyl)piperidino]-1-propanol, as a PET tracer for NR2B subunit-containing NMDA receptors," *Nuclear Medicine and Biology*, vol. 29, no. 5, pp. 517–525, 2002.
- [56] H. Mori and M. Mishina, "Structure and function of the NMDA receptor channel," *Neuropharmacology*, vol. 34, no. 10, pp. 1219–1237, 1995.
- [57] G. Roger, B. Lagnel, L. Besret et al., "Synthesis, radiosynthesis and *in vivo* evaluation of 5-[3-(4-benzylpiperidin-1-yl)prop-1-ynyl]-1,3-dihydrobenzimidazol-2-[¹¹C]one, as a potent NR1A/2B subtype selective NMDA PET radiotracer," *Bioorganic and Medicinal Chemistry*, vol. 11, no. 24, pp. 5401–5408, 2003.
- [58] G. Roger, F. Dollé, B. de Bruin et al., "Radiosynthesis and pharmacological evaluation of [¹¹C]EMD-95885: a high affinity ligand for NR2B-containing NMDA receptors," *Bioorganic and Medicinal Chemistry*, vol. 12, no. 12, pp. 3229–3237, 2004.
- [59] T. Fuchigami, H. Yamaguchi, M. Ogawa et al., "Synthesis and biological evaluation of radio-iodinated benzimidazoles as SPECT imaging agents for NR2B subtype of NMDA receptor," *Bioorganic and Medicinal Chemistry*, vol. 18, no. 21, pp. 7497–7506, 2010.
- [60] F. Dollé, H. Valette, S. Demphel et al., "Radiosynthesis and *in vivo* evaluation of [¹¹C]Ro-647312: A novel NR1/2B subtype selective NMDA receptor radioligand," *Journal of Labelled Compounds and Radiopharmaceuticals*, vol. 47, no. 13, pp. 911–920, 2004.
- [61] E. Årstad, S. Platzer, A. Berthele et al., "Towards NR2B receptor selective imaging agents for PET-synthesis and evaluation of N-[¹¹C]-(2-methoxy)benzyl (*E*)-styrene-, 2-naphthyl- and 4-trifluoromethoxyphenylamine," *Bioorganic and Medicinal Chemistry*, vol. 14, no. 18, pp. 6307–6313, 2006.
- [62] C. Addy, C. Assaid, D. Hreniuk et al., "Single-dose administration of MK-0657, an NR2B-selective NMDA antagonist, does not result in clinically meaningful improvement in motor function in patients with moderate Parkinson's disease," *Journal of Clinical Pharmacology*, vol. 49, no. 7, pp. 856–864, 2009.
- [63] R. Koudih, G. Gilbert, M. Dhilly et al., "Synthesis and *in vitro* characterization of trans- and cis-[¹⁸F]-4-methylbenzyl 4-[(pyrimidin-2-ylamino)methyl]-3-fluoropiperidine-1-carboxylates as new potential PET radiotracer candidates for the NR2B subtype N-methyl-d-aspartate receptor," *European Journal of Medicinal Chemistry*, vol. 53, pp. 408–415, 2012.
- [64] N. Pitsikas, "The metabotropic glutamate receptors: potential drug targets for the treatment of anxiety disorders?" *European Journal of Pharmacology*, vol. 723, no. 1, pp. 181–184, 2014.

- [65] S. Chaki, Y. Ago, A. Palucha-Paniewiera, F. Matrisciano, and A. Pilc, "mGlu2/3 and mGlu5 receptors: potential targets for novel antidepressants," *Neuropharmacology*, vol. 66, pp. 40–52, 2013.
- [66] H.-G. Lee, X. Zhu, M. J. O'Neill et al., "The role of metabotropic glutamate receptors in Alzheimer's disease," *Acta Neurobiologiae Experimentalis*, vol. 64, no. 1, pp. 89–98, 2004.
- [67] P. N. Vinson and P. J. Conn, "Metabotropic glutamate receptors as therapeutic targets for schizophrenia," *Neuropharmacology*, vol. 62, no. 3, pp. 1461–1472, 2012.
- [68] F. Gasparini, T. Di Paolo, and B. Gomez-Mancilla, "Metabotropic glutamate receptors for parkinson's disease therapy," *Parkinson's Disease*, vol. 2013, Article ID 196028, 11 pages, 2013.
- [69] R. T. Ngomba, I. Santolini, T. E. Salt et al., "Metabotropic glutamate receptors in the thalamocortical network: Strategic targets for the treatment of absence epilepsy," *Epilepsia*, vol. 52, no. 7, pp. 1211–1222, 2011.
- [70] F. Nicoletti, J. Bockaert, G. L. Collingridge et al., "Metabotropic glutamate receptors: from the workbench to the bedside," *Neuropharmacology*, vol. 60, no. 7–8, pp. 1017–1041, 2011.
- [71] F. Ferraguti and R. Shigemoto, "Metabotropic glutamate receptors," *Cell and Tissue Research*, vol. 326, no. 2, pp. 483–504, 2006.
- [72] A. Slassi, M. Isaac, L. Edwards et al., "Recent advances in non-competitive mGlu5 receptor antagonists and their potential therapeutic applications," *Current Topics in Medicinal Chemistry*, vol. 5, no. 9, pp. 897–911, 2005.
- [73] P. J. Conn, C. W. Lindsley, and C. K. Jones, "Activation of metabotropic glutamate receptors as a novel approach for the treatment of schizophrenia," *Trends in Pharmacological Sciences*, vol. 30, no. 1, pp. 25–31, 2009.
- [74] Y. Huang, R. Narendran, F. Bischoff et al., "A positron emission tomography radioligand for the in vivo labeling of metabotropic glutamate 1 receptor: (3-Ethyl-2-¹¹C)methyl-6-quinolinyl(cis-4-methoxycyclohexyl)methanone," *Journal of Medicinal Chemistry*, vol. 48, no. 16, pp. 5096–5099, 2005.
- [75] Y. Huang, R. Narendran, F. Bischoff et al., "Synthesis and characterization of two pet radioligands for the metabotropic glutamate 1 (mGlu1) receptor," *Synapse*, vol. 66, no. 12, pp. 1002–1014, 2012.
- [76] K. Yanamoto, F. Konno, C. Odawara et al., "Radiosynthesis and evaluation of [¹¹C]YM-202074 as a PET ligand for imaging the metabotropic glutamate receptor type 1," *Nuclear Medicine and Biology*, vol. 37, no. 5, pp. 615–624, 2010.
- [77] E. D. Hostetler, W. Eng, A. D. Joshi et al., "Synthesis, characterization, and monkey PET studies of [¹⁸F]MK-1312, a PET tracer for quantification of mGluR1 receptor occupancy by MK-5435," *Synapse*, vol. 65, no. 2, pp. 125–135, 2011.
- [78] M. Fujinaga, J. Maeda, J. Yui et al., "Characterization of 1-(2-[¹⁸F]fluoro-3-pyridyl)-4-(2-isopropyl-1-oxo-isindoline-5-yl)-5-methyl-1H-1,2,3-triazole, a PET ligand for imaging the metabotropic glutamate receptor type 1 in rat and monkey brains," *Journal of Neurochemistry*, vol. 121, no. 1, pp. 115–124, 2012.
- [79] A. Satoh, Y. Nagatomi, Y. Hirata et al., "Discovery and in vitro and in vivo profiles of 4-fluoro-N-[4-[6-(isopropylamino)pyrimidin-4-yl]-1,3-thiazol-2-yl]-N-methylbenzamide as novel class of an orally active metabotropic glutamate receptor 1 (mGluR1) antagonist," *Bioorganic and Medicinal Chemistry Letters*, vol. 19, no. 18, pp. 5464–5468, 2009.
- [80] T. Yamasaki, M. Fujinaga, Y. Yoshida et al., "Radiosynthesis and preliminary evaluation of 4-[¹⁸F]fluoro-N-[4-[6-(isopropylamino)pyrimidin-4-yl]-1,3-thiazol-2-yl]-N-methylbenzamide as a new positron emission tomography ligand for metabotropic glutamate receptor subtype 1," *Bioorganic and Medicinal Chemistry Letters*, vol. 21, no. 10, pp. 2998–3001, 2011.
- [81] T. Yamasaki, M. Fujinaga, J. Maeda et al., "Imaging for metabotropic glutamate receptor subtype 1 in rat and monkey brains using PET with [¹⁸F]FITM," *European Journal of Nuclear Medicine and Molecular Imaging*, vol. 39, no. 4, pp. 632–641, 2012.
- [82] T. Yamasaki, M. Fujinaga, K. Kawamura et al., "In vivo measurement of the affinity and density of metabotropic glutamate receptor subtype 1 in rat brain using ¹⁸F-FITM in small-animal PET," *Journal of Nuclear Medicine*, vol. 53, no. 10, pp. 1601–1607, 2012.
- [83] M. Fujinaga, T. Yamasaki, J. Yui et al., "Synthesis and evaluation of novel radioligands for positron emission tomography imaging of metabotropic glutamate receptor subtype 1 (mGluR1) in rodent brain," *Journal of Medicinal Chemistry*, vol. 55, no. 5, pp. 2342–2352, 2012.
- [84] J. Yui, L. Xie, M. Fujinaga et al., "Monitoring neuroprotective effects using positron emission tomography with [¹¹C]ITMM, a radiotracer for metabotropic glutamate 1 receptor," *Stroke*, vol. 44, no. 9, pp. 2567–2572, 2013.
- [85] J. Toyohara, M. Sakata, K. Oda et al., "Initial human PET studies of metabotropic glutamate receptor type 1 ligand ¹¹C-ITMM," *Journal of Nuclear Medicine*, vol. 54, no. 8, pp. 1302–1307, 2013.
- [86] M. Fujinaga, T. Yamasaki, J. Maeda et al., "Development of N-[4-[6-(isopropylamino)pyrimidin-4-yl]-1,3-thiazol-2-yl]-N-methyl-4-[¹¹C]methylbenzamide for positron emission tomography imaging of metabotropic glutamate 1 receptor in monkey brain," *Journal of Medicinal Chemistry*, vol. 55, no. 24, pp. 11042–11051, 2012.
- [87] T. Yamasaki, J. Maeda, M. Fujinaga et al., "PET brain kinetics studies of ¹¹C-ITMM and ¹¹C-ITDM, radioprobes for metabotropic glutamate receptor type 1, in a nonhuman primate," *The American Journal of Nuclear Medicine and Molecular Imaging*, vol. 4, pp. 260–269, 2014.
- [88] T. Yamasaki, M. Fujinaga, J. Yui et al., "Noninvasive quantification of metabotropic glutamate receptor type 1 with [¹¹C]ITDM: a small-animal PET study," *Journal of Cerebral Blood Flow and Metabolism*, vol. 34, no. 4, pp. 606–612, 2014.
- [89] R. Xu, P. Zanotti-Fregonara, S. S. Zoghbi et al., "Synthesis and evaluation in monkey of [¹⁸F]4-Fluoro-N-methyl-N-(4-(6-(methylamino)pyrimidin-4-yl)thiazol-2-yl)benzamide ([¹⁸F]FIMX): a promising radioligand for PET imaging of brain metabotropic glutamate receptor 1 (mGluR1)," *Journal of Medicinal Chemistry*, vol. 56, no. 22, pp. 9146–9155, 2013.
- [90] P. Zanotti-Fregonara, S. Zoghbi, J. S. Liow et al., "[¹⁸F]FIMX is a promising tracer to quantify metabotropic glutamate receptor 1 (mGluR1) in human brain," *Journal of Nuclear Medicine*, vol. 55, supplement 1, p. 359, 2014.
- [91] T. G. Hamill, S. Krause, C. Ryan et al., "Synthesis, characterization, and first successful monkey imaging studies of metabotropic glutamate receptor subtype 5 (mGluR5) PET radiotracers," *Synapse*, vol. 56, no. 4, pp. 205–216, 2005.
- [92] J.-Q. Wang, W. Tueckmantel, A. Zhu, D. Pellegrino, and A.-L. Brownell, "Synthesis and preliminary biological evaluation of 3-[¹⁸F] fluoro-5-(2-pyridinylethynyl)benzonitrile as a PET radiotracer for imaging metabotropic glutamate receptor subtype 5," *Synapse*, vol. 61, no. 12, pp. 951–961, 2007.
- [93] D. F. Wong, R. Waterhouse, H. Kuwabara et al., "¹⁸F-FPEB, a PET radiopharmaceutical for quantifying metabotropic glutamate 5 receptors: a first-in-human study of radiochemical

- safety, biokinetics, and radiation dosimetry," *Journal of Nuclear Medicine*, vol. 54, no. 3, pp. 388–396, 2013.
- [94] S. M. Ametamey, L. J. Kessler, M. Honer et al., "Radiosynthesis and preclinical evaluation of ^{11}C -ABP688 as a probe for imaging the metabotropic glutamate receptor subtype 5," *Journal of Nuclear Medicine*, vol. 47, no. 4, pp. 698–705, 2006.
- [95] S. M. Ametamey, V. Treyer, J. Streffer et al., "Human PET studies of metabotropic glutamate receptor subtype 5 with ^{11}C -ABP688," *Journal of Nuclear Medicine*, vol. 48, no. 2, pp. 247–252, 2007.
- [96] M. Kågedal, Z. Cselényi, S. Nyberg et al., "A positron emission tomography study in healthy volunteers to estimate mGluR5 receptor occupancy of AZD2066—estimating occupancy in the absence of a reference region," *NeuroImage*, vol. 82, pp. 160–169, 2013.
- [97] K. Kawamura, T. Yamasaki, K. Kumata et al., "Binding potential of (*E*)- ^{11}C ABP688 to metabotropic glutamate receptor subtype 5 is decreased by the inclusion of its ^{11}C -labelled Z-isomer," *Nuclear Medicine and Biology*, vol. 41, no. 1, pp. 17–23, 2014.
- [98] F. G. Siméon, A. K. Brown, S. S. Zoghbi, V. M. Patterson, R. B. Innis, and V. W. Pike, "Synthesis and simple ^{18}F -labeling of 3-fluoro-5-(2-(2-(fluoromethyl)thiazol-4-yl)ethynyl)benzotrile as a high affinity radioligand for imaging monkey brain metabotropic glutamate subtype-5 receptors with positron emission tomography," *Journal of Medicinal Chemistry*, vol. 50, no. 14, pp. 3256–3266, 2007.
- [99] H. U. Shetty, S. S. Zoghbi, F. G. Simeon et al., "Radiode-fluorination of 3-fluoro-5-(2-(2- ^{18}F)(fluoromethyl)-thiazol-4-yl)ethynyl)benzotrile (^{18}F)SP203, a radioligand for imaging brain metabotropic glutamate subtype-5 receptors with positron emission tomography, occurs by glutathionylation in rat brain," *Journal of Pharmacology and Experimental Therapeutics*, vol. 327, pp. 727–735, 2008.
- [100] J. J. P. Bogaards, J. C. Venekamp, F. G. C. Salmon, and P. J. Van Bladeren, "Conjugation of isoprene monoepoxides with glutathione, catalyzed by α , μ , π and θ -class glutathione S-transferases of rat and man," *Chemico-Biological Interactions*, vol. 117, no. 1, pp. 1–14, 1999.
- [101] A. K. Brown, Y. Kimura, S. S. Zoghbi et al., "Metabotropic glutamate subtype 5 receptors are quantified in the human brain with a novel radioligand for PET," *Journal of Nuclear Medicine*, vol. 49, no. 12, pp. 2042–2048, 2008.
- [102] Y. Hao, R. Martin-Fardon, and F. Weiss, "Behavioral and functional evidence of metabotropic glutamate receptor 2/3 and metabotropic glutamate receptor 5 dysregulation in cocaine-escalated rats: factor in the transition to dependence," *Biological Psychiatry*, vol. 68, no. 3, pp. 240–248, 2010.
- [103] D. Martinez, M. Slifstein, N. Nabulsi et al., "Imaging glutamate homeostasis in cocaine addiction with the metabotropic glutamate receptor 5 positron emission tomography radiotracer [^{11}C]ABP688 and magnetic resonance spectroscopy," *Biological Psychiatry*, vol. 75, no. 2, pp. 165–171, 2014.
- [104] M. S. Milella, L. Marengo, K. Larcher et al., "Limbic system mGluR5 availability in cocaine dependent subjects: a high-resolution PET [^{11}C]ABP688 study," *NeuroImage*, vol. 98, pp. 195–202, 2014.
- [105] N. E. Paterson and A. Markou, "The metabotropic glutamate receptor 5 antagonist MPEP decreased break points for nicotine, cocaine and food in rats," *Psychopharmacology*, vol. 179, no. 1, pp. 255–261, 2005.
- [106] M. I. Palmatier, X. Liu, E. C. Donny, A. R. Caggiula, and A. F. Sved, "Metabotropic glutamate 5 receptor (mGluR5) antagonists decrease nicotine seeking, but do not affect the reinforcement enhancing effects of nicotine," *Neuropsychopharmacology*, vol. 33, no. 9, pp. 2139–2147, 2008.
- [107] F. Akkus, S. M. Ametamey, V. Treyer et al., "Marked global reduction in mGluR5 receptor binding in smokers and ex-smokers determined by [^{11}C]ABP688 positron emission tomography," *Proceedings of the National Academy of Sciences of the United States of America*, vol. 110, no. 2, pp. 737–742, 2013.
- [108] L. R. Merlin, "Differential roles for mGluR1 and mGluR5 in the persistent prolongation of epileptiform bursts," *Journal of Neurophysiology*, vol. 87, no. 1, pp. 621–625, 2002.
- [109] T. Kirschstein, M. Bauer, L. Müller et al., "Loss of metabotropic glutamate receptor-dependent long-term depression via down-regulation of mGluR5 after status epilepticus," *The Journal of Neuroscience*, vol. 27, no. 29, pp. 7696–7704, 2007.
- [110] H. Choi, Y. K. Kim, S. W. Oh et al., "In vivo imaging of mGluR5 changes during epileptogenesis using [^{11}C]ABP688 PET in pilocarpine-induced epilepsy rat model," *PLoS ONE*, vol. 9, no. 3, Article ID e92765, 2014.
- [111] A. Deschwanden, B. Karolewicz, A. M. Feyissa et al., "Reduced metabotropic glutamate receptor 5 density in major depression determined by [^{11}C]ABP688 PET and postmortem study," *The American Journal of Psychiatry*, vol. 168, no. 7, pp. 727–734, 2011.
- [112] M. J. Fell, D. L. McKinzie, J. A. Monn, and K. A. Svensson, "Group II metabotropic glutamate receptor agonists and positive allosteric modulators as novel treatments for schizophrenia," *Neuropharmacology*, vol. 62, no. 3, pp. 1473–1483, 2012.
- [113] M. Amalric, S. Lopez, C. Goudet et al., "Group III and subtype 4 metabotropic glutamate receptor agonists: discovery and pathophysiological applications in Parkinson's disease," *Neuropharmacology*, vol. 66, pp. 53–64, 2013.
- [114] N. K. Parelkar and J. Q. Wang, "Upregulation of metabotropic glutamate receptor 8 mRNA expression in the rat forebrain after repeated amphetamine administration," *Neuroscience Letters*, vol. 433, no. 3, pp. 250–254, 2008.
- [115] J. I. Andrés, J. Alcázar, J. M. Cid et al., "Synthesis, evaluation, and radiolabeling of new potent positive allosteric modulators of the metabotropic glutamate receptor 2 as potential tracers for positron emission tomography imaging," *Journal of Medicinal Chemistry*, vol. 55, no. 20, pp. 8685–8699, 2012.
- [116] K. V. Laere, M. Koole, J. Hoon et al., "Biodistribution, dosimetry and kinetic modeling of [^{11}C]JNJ-42491293, a PET tracer for the mGluR2 receptor in the human brain," *Journal of Nuclear Medicine*, vol. 53, supplement 1, article 355, 2012.
- [117] D. W. Engers, C. M. Niswender, C. D. Weaver et al., "Synthesis and evaluation of a series of heterobiaryl amides that are centrally penetrant metabotropic glutamate receptor 4 (mGluR4) positive allosteric modulators (PAMs)," *Journal of Medicinal Chemistry*, vol. 52, no. 14, pp. 4115–4118, 2009.
- [118] K.-E. Kil, Z. Zhang, K. Jokivarsi et al., "Radiosynthesis of *N*-(4-chloro-3- ^{11}C)methoxyphenyl)-2-picolinamide (^{11}C)ML128 as a PET radiotracer for metabotropic glutamate receptor subtype 4 (mGlu4)," *Bioorganic and Medicinal Chemistry*, vol. 21, no. 19, pp. 5955–5962, 2013.
- [119] M. Nakamura, H. Kurihara, G. Suzuki, M. Mitsuya, M. Ohkubo, and H. Ohta, "Isoxazopyridone derivatives as allosteric metabotropic glutamate receptor 7 antagonists," *Bioorganic and Medicinal Chemistry Letters*, vol. 20, no. 2, pp. 726–729, 2010.
- [120] M. L. Vallano, B. Lambalez, E. Audinat, and J. Rossier, "Neuronal activity differentially regulates NMDA receptor subunit expression in cerebellar granule cells," *Journal of Neuroscience*, vol. 16, no. 2, pp. 631–639, 1996.

- [121] K. W. Roche, S. Standley, J. McCallum, C. Dune Ly, M. D. Ehlers, and R. J. Wenthold, "Molecular determinants of NMDA receptor internalization," *Nature Neuroscience*, vol. 4, no. 8, pp. 794–802, 2001.
- [122] T. Hayashi, G. M. Thomas, and R. L. Huganir, "Dual palmitoylation of NR2 subunits regulates NMDA receptor trafficking," *Neuron*, vol. 64, no. 2, pp. 213–226, 2009.

Review Article

Theragnostic Imaging Using Radiolabeled Antibodies and Tyrosine Kinase Inhibitors

Mitsuyoshi Yoshimoto,¹ Hiroaki Kurihara,² and Hirofumi Fujii¹

¹*Division of Functional Imaging, National Cancer Center Hospital East, 6-5-1, Kashiwanoha, Kashiwa, Chiba 277-8577, Japan*

²*Diagnostic Radiology, National Cancer Center Hospital, 5-1-1 Tsukiji, Chuo-ku, Tokyo 104-0045, Japan*

Correspondence should be addressed to Mitsuyoshi Yoshimoto; miyoshim@ncc.go.jp

Received 23 June 2014; Revised 22 August 2014; Accepted 22 August 2014

Academic Editor: Kazuma Ogawa

Copyright © 2015 Mitsuyoshi Yoshimoto et al. This is an open access article distributed under the Creative Commons Attribution License, which permits unrestricted use, distribution, and reproduction in any medium, provided the original work is properly cited.

During the past decade, the efficacy of new molecular targeted drugs such as tyrosine kinase inhibitors (TKIs) and monoclonal antibodies has been proven worldwide, and molecular targeted therapies have become the mainstream in cancer therapy. However, clinical use of these new drugs presents unexpected adverse effects or poor therapeutic effects. Therefore, we require diagnostic tools to estimate the target molecule status in cancer tissues and predict therapeutic efficacy and adverse effects. Although immunohistochemical, polymerase chain reaction (PCR) and fluorescence in situ hybridization (FISH) analyses of biopsy samples are conventional and popular for this diagnostic purpose, molecular imaging modalities such as positron emission tomography (PET) and single photon emission computed tomography (SPECT) are also useful for noninvasive estimation of gene and protein expression and drug pharmacokinetics. In this review, we introduce new radiolabeled TKIs, antibodies, and their clinical application in molecular targeted therapy and discuss the issues of these imaging probes.

1. Introduction

New observations regarding carcinogenesis and signal transduction pathways that regulate tumor growth, differentiation, angiogenesis, invasion, and metastasis have led to the identification of potential therapeutic targets and have accelerated molecular targeted drug development. In particular, the success of imatinib in chronic myeloid leukemia (CML) patients has strongly promoted the development of small-molecule tyrosine kinase inhibitors (TKIs). Since the United States Food and Drug Administration's approval of rituximab (Rituxan; anti-CD20 antibody) and imatinib (Gleevec; Bcr-Abl TKI), several anticancer drugs have been approved each year in the US, European Union, and Japan [1].

The antitumor mechanisms triggered by molecular targeted drugs differ from those of conventional chemotherapeutic agents. Therefore, the estimation of target molecule expression in entire tumor is required to predict therapeutic efficacy. Target molecule and target gene expressions can be evaluated using immunohistochemical, polymerase chain reaction (PCR) and fluorescence in situ hybridization (FISH)

analyses of biopsy samples. However, biopsy samples contain tissues from limited regions only, whereas tumor tissue is heterogeneous. Thus, it is possible that the expression observed in biopsy samples is not representative of that in entire tumor [2, 3]. This can lead to a misunderstanding with respect to tumor characterization. Moreover, expression levels of key molecules and gene mutations require modulation during treatment. The consequent repetitive biopsies are invasive and represent a significant burden on patients.

Molecular imaging modalities such as positron emission tomography (PET) and single photon emission computed tomography (SPECT) are suitable for noninvasive estimation of gene and protein expressions and drug pharmacokinetics [4, 5]. Molecular imaging also enables detection of changes in gene and protein expressions in response to treatment in the entire tumor and could overcome the issues associated with biopsy. Therefore, PET and SPECT are the best tools in treatment strategies that combine therapeutics with diagnostics, also known as "theragnostics."

Theragnostic imaging by using radiolabeled molecular targeted drugs provides new important insights into drug

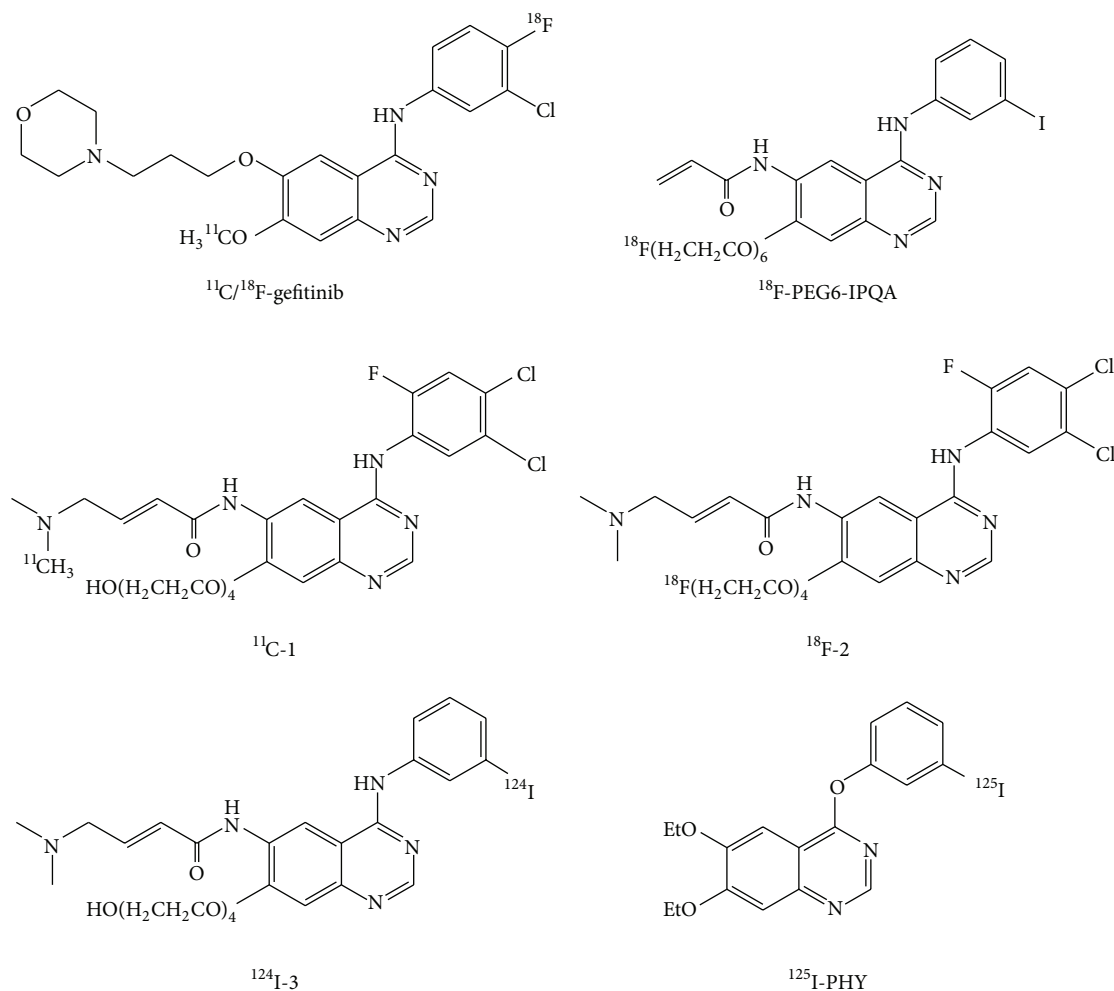


FIGURE 1: Chemical structures of the EGFR-TK imaging probes.

development and cancer treatment. For instance, theragnostic imaging reveals pharmacokinetics of drugs in individual patients. This allows stratification of the patients who would benefit from the drugs and identification of modified status of target molecules (expression levels and mutation status). Moreover, understanding of the pharmacokinetics is helpful to select candidate drugs in the process of drug development, resulting in reduction of development cost.

2. Development of Imaging Agents for Epidermal Growth Factor Receptor-Tyrosine Kinase (Figure 1)

The small molecule epidermal growth factor receptor (EGFR)-TKIs gefitinib and erlotinib have been approved for the treatment of non-small-cell lung cancer (NSCLC) and have exhibited dramatic antitumor activities. These therapeutic agents have been found to be effective primarily in patients with mutant EGFR-TK [6–8]. However, gefitinib treatment has also led to serious side effects such as interstitial lung disease [9]. In addition, the gefitinib treatment will result in

acquisition of resistance usually within a year, half of whose mechanism is secondary T790M mutation of the EGFR gene [10]. These clinical findings demonstrate the need to detect mutation status of the target molecule.

The simplest strategy for estimation of gefitinib sensitivity and mutation status is the use of radiolabeled gefitinib (Figure 1) [11, 12]. However, a discrepancy in specificity of radiolabeled gefitinib exists between ^{18}F -gefitinib and ^{11}C -gefitinib. Su et al. reported that ^{18}F -gefitinib uptake *in vitro* and *in vivo* did not correlate with EGFR expression because of nonspecific binding caused by its high lipophilicity [11]. An *in vitro* uptake study indicated that high and specific ^{18}F -gefitinib uptake was observed only in H3255 with mutant EGFR, but not in U87-EGFR. Unlike ^{18}F -gefitinib, specific ^{11}C -gefitinib uptake was observed in mice bearing murine fibrosarcoma (NFSa) [12]. However, a biodistribution study has shown that ^{11}C -gefitinib uptake was low in A431 cells which exhibit high EGFR expression. Thus, radiolabeled gefitinib may not estimate EGFR expression or mutation status.

A reduction in lipophilicity might be a simple solution to overcome the nonspecific binding of an imaging probe.

However, a certain level of imaging probe lipophilicity is essential for passage through the cell membrane and binding to the ATP binding pocket in the TK domain of the target molecule. A recent PET study indicated the failure of EGFR-expressing U-87MG cells to take up polyethylene glycol(PEG)-ylated anilinoquinazoline derivatives (^{11}C -1, ^{18}F -2, and ^{124}I -3) [13]. However, PET using 4-[(3-iodophenyl) amino]-7-(2-[2-(2-[2-(2-(^{18}F -fluoroethoxy)-ethoxy)-ethoxy)-ethoxy]-ethoxy)-quinazoline-6-yl-acrylamide) (^{18}F -PEG6- IPQA) could delineate tumors with high EGFR expression [14]. These inhibitors are irreversible (Figure 1). Although the affinities (K_D) of these compounds for EGFR-TK are not clear, an understanding of the relationships between lipophilicity, affinity, and the binding mode (reversible or irreversible) might lead to a breakthrough in the development of TK imaging probes.

3. Estimation of the Mutation Status Using EGFR-TK Imaging Probes

Monitoring of EGFR-TKI sensitivity and mutation status of the target molecule is of particular interest to the field of molecular imaging. We previously reported a correlation between the tumor uptake of 4-(3- ^{125}I -iodo-phenoxy)-6,7-diethoxy-quinazoline (^{125}I -PHY, Figure 1) and gefitinib sensitivity [15]. However, differences in tumor uptake were due partly to differences in EGFR expression and partly to non-specific binding. Unfortunately, ^{125}I -PHY could not estimate differences in mutation statuses. Yeh et al. attempted to detect a gefitinib-sensitive mutation (L858R) using ^{18}F -PEG6-IPQA which selectively and irreversibly binds to mutant EGFR-TK (L858R) [14]. An *in silico* docking study revealed that the acrylamide moiety of F-PEG6-IPQA can form a covalent bond with Cys773 in the active conformation of L858R mutant kinase domain. A PET study involving ^{18}F -PEG6-IPQA demonstrated high uptake in H3255 cells harboring the L858R mutation.

Memon et al. reported high and sustained ^{11}C -erlotinib uptake in HCC827 cells harboring a delE746-750 mutations as compared with A549 and NCI358 cells [16]. This difference was caused by different affinities of erlotinib to EGFR-TKs [17]. A recent clinical study has supported these basic research findings. A PET study involving ^{11}C -erlotinib was conducted in patients with wild-type (WT) and Exon19 deletion mutation. Although patients harboring the common L858R mutation were not included, the uptake of ^{11}C -erlotinib was higher in tumors with the deletion mutation than those with WT [18]. Moreover, these ^{11}C -erlotinib studies suggest that reversible inhibitors are efficient imaging probes for estimating the mutation status based on differences in binding affinity.

Unfortunately, this study has some limitation. Only a small number of patients (5 with and 5 without a mutation) were involved. Patients with other mutation (L858R and L858R/T790M) were not included. Further investigation is needed to demonstrate that ^{11}C -erlotinib PET is as efficient as the conventional mutation test using the biopsied samples.

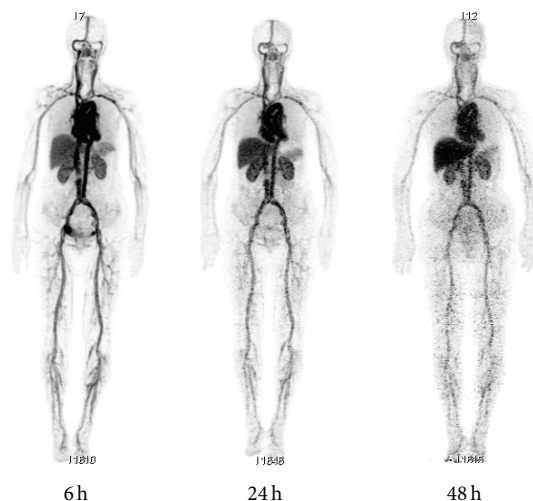


FIGURE 2: Whole-body ^{64}Cu -DOTA-trastuzumab PET images at 6, 24, and 48 h after injection.

4. Human Epidermal Growth Factor Receptor 2 (HER2) Imaging

Anti-HER2 therapy with trastuzumab, a monoclonal antibody, is now well established in HER2-positive breast cancer patients [19, 20]. Although HER2 expression is estimated using immunohistochemical or FISH analyses of biopsy samples, core needle biopsy is not possible for some lesions [21]. In addition, HER2 status can change during disease progression and over the course of the treatment [22, 23].

There have been many reports of the use of radiolabeled trastuzumab in animal and human studies (Figure 2) [24–28]. McLarty et al. reported that the tumor uptake of ^{111}In -DTPA-trastuzumab, after correcting for nonspecific IgG accumulation and circulating radioactivity, exhibited strong nonlinear associations with the HER2 density in a mouse model of breast cancer [29]. PET with ^{89}Zr -trastuzumab could detect downregulation of HER2 expression in response to afatinib treatment in a gastric cancer xenograft model [30]. Moreover, the first-in-human study of ^{89}Zr -trastuzumab PET resulted in tumor visualization and quantitative tracer uptake in HER2-positive tumors [24].

A long duration of antibody circulation leads to a high background signal, and therefore a long period of time is needed to decrease the radioactivity in the blood and acquire specific images of the target tissues. Although metal radionuclides with long half-lives such as ^{111}In and ^{89}Zr (67.9 h and 78.4 h, resp.) are appropriate for *in vivo* imaging with radiolabeled antibodies, the use of these radionuclides results in high levels of radiation exposure. Tamura et al. reported that ^{64}Cu -DOTA-trastuzumab could delineate HER2-positive lesions including brain metastases in breast carcinoma patients; further, the use of ^{64}Cu (half-life = 12.7 h) could reduce the radiation exposure to 4.5 mSv versus the 18 mSv from ^{89}Zr -trastuzumab [24, 28]. This effective dose is similar to that of ^{18}F -FDG (0.019 mSv/MBq) [31].

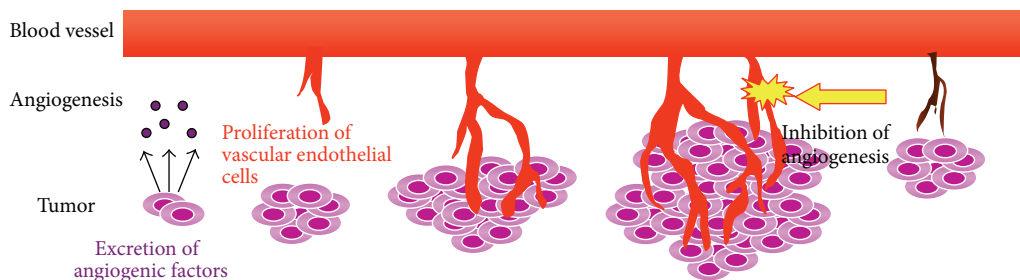


FIGURE 3: Depiction of tumor angiogenesis. Angiogenesis is an important tumor growth factor. Vascular endothelial cell proliferation is essential for the development of new blood vessels.

5. Vascular Endothelial Growth Factor (VEGF) Imaging

Antiangiogenic therapy is a cancer treatment strategy [32, 33]. Angiogenesis consists of various processes such as the secretion of angiogenic factors and the proliferation of vascular endothelial cells (ECs; Figure 3). Bevacizumab is a monoclonal anti-VEGF antibody that inhibits VEGF-stimulated EC proliferation [34, 35]. Vandetanib, a VEGFR-TK inhibitor, directly inhibits EC proliferation because VEGF expression is upregulated within tumor tissues [36, 37]. Antiangiogenic drugs directly or indirectly inhibit EC proliferation followed by tumor suppression. Therefore, to decide the therapeutic plan using antiangiogenic drugs, we should estimate the expression level of the target molecule, but not the biological activity of tumor cells.

Molecular imaging could be a powerful tool for estimating the VEGF content within tumor tissues. Enzyme-linked immunosorbent assays of tissue samples measure not only extracellular but also intracellular VEGF content. The first clinical study of ^{89}Zr -bevacizumab PET conducted in breast cancer patients indicated a correlation between the maximum standard uptake values of the tracer and VEGF-A expression in the tumors [38]. Chang et al. reported that ^{64}Cu -NOTA-bevacizumab could be used to evaluate a decrease in the expression of VEGF caused by everolimus, a mammalian target of rapamycin inhibitor [39].

6. Other Kinase Imaging with Radiolabeled Small Molecules

New kinase inhibitors have been labeled with ^{11}C or ^{18}F ; these include ^{11}C -vandetanib, ^{18}F -SKI696 (an analogue of imatinib), and ^{18}F -sunitinib [40–46]. However, their chemical structures must be modified for compatibility with the imaging probes. The biodistribution of ^{11}C -sorafenib indicated high radioactivity in the liver and slow blood clearance [46]. The tumor uptake of ^{11}C -sorafenib was lower than its radioactivity level in blood. In view of selectivity, we could not deduce which kinases contribute to tumor uptake because sorafenib is a multikinase inhibitor. The properties of the oral drugs that are high bioavailability and high blood concentration may be unfavorable for imaging

probes. Therefore, optimization of chemical structures would be required for use of kinase inhibitors for imaging probes. The use of radiolabeled kinase inhibitors may be limited to the purpose of estimating pharmacokinetics and drug concentrations.

7. Conclusion

Targeted therapy is becoming the mainstream in the field of cancer therapy, and the development of new targeted drugs is increasing. However, the therapeutic effects of the agents remain limited, and patients who benefit from targeted therapy represent a fraction of all patients. Molecular imaging plays two roles in targeted therapy. The first role is the estimation of features of the target molecules such as the expression level and mutation status, thus allowing patient stratification. The second role is the elucidation of pharmacokinetics and measurement of drug concentrations in the tissues. Drug radiolabeling is sufficient for the latter purpose, whereas the former requires imaging probes for the acquisition of informative images. We should readily try to optimize the chemical structures of kinase inhibitors for use as imaging probes instead of antibodies. We believe that advances in imaging probes will contribute to our understanding of pharmacokinetics/pharmacodynamics, drug development, and therapy planning.

Conflict of Interests

The authors declare that there is no conflict of interests regarding the publication of this paper.

References

- [1] G. Walsh, "Biopharmaceutical benchmarks," *Nature Biotechnology*, vol. 28, no. 9, pp. 917–924, 2010.
- [2] A. P. Dei Tos and I. Ellis, "Assessing epidermal growth factor receptor expression in tumours: what is the value of current test methods?" *European Journal of Cancer*, vol. 41, no. 10, pp. 1383–1392, 2005.
- [3] A. Crockford, M. Jamal-Hanjani, J. Hicks, and C. Swanton, "Implications of intratumour heterogeneity for treatment stratification," *The Journal of Pathology*, vol. 232, pp. 264–273, 2014.

- [4] E. G. E. de Vries, T. H. O. Munnink, M. A. T. M. van Vugt, and W. B. Nagengast, "Toward molecular imaging-driven drug development in oncology," *Cancer Discovery*, vol. 1, no. 1, pp. 25–28, 2011.
- [5] M. L. Thakur, "Genomic biomarkers for molecular imaging: predicting the future," *Seminars in Nuclear Medicine*, vol. 39, no. 4, pp. 236–246, 2009.
- [6] T. J. Lynch, D. W. Bell, R. Sordella et al., "Activating mutations in the epidermal growth factor receptor underlying responsiveness of non-small-cell lung cancer to gefitinib," *The New England Journal of Medicine*, vol. 350, no. 21, pp. 2129–2139, 2004.
- [7] H. Linardou, I. J. Dahabreh, D. Bafaloukos, P. Kosmidis, and S. Murray, "Somatic EGFR mutations and efficacy of tyrosine kinase inhibitors in NSCLC," *Nature Reviews Clinical Oncology*, vol. 6, no. 6, pp. 352–366, 2009.
- [8] J. G. Paez, P. A. Jänne, J. C. Lee et al., "EGFR mutations in lung cancer: correlation with clinical response to gefitinib therapy," *Science*, vol. 304, no. 5676, pp. 1497–1500, 2004.
- [9] A. Inoue, Y. Saijo, M. Maemondo et al., "Severe acute interstitial pneumonia and gefitinib," *The Lancet*, vol. 361, no. 9352, pp. 137–139, 2003.
- [10] S. Kobayashi, T. J. Boggon, T. Dayaram et al., "EGFR mutation and resistance of non-small-cell lung cancer to gefitinib," *The New England Journal of Medicine*, vol. 352, no. 8, pp. 786–792, 2005.
- [11] H. Su, Y. Seimbille, G. Z. Ferl et al., "Evaluation of [¹⁸F]gefitinib as a molecular imaging probe for the assessment of the epidermal growth factor receptor status in malignant tumors," *European Journal of Nuclear Medicine and Molecular Imaging*, vol. 35, no. 6, pp. 1089–1099, 2008.
- [12] M.-R. Zhang, K. Kumata, A. Hatori et al., "[¹¹C]Gefitinib ([¹¹C]Iressa): radiosynthesis, *in vitro* uptake, and *in vivo* imaging of intact murine fibrosarcoma," *Molecular Imaging and Biology*, vol. 12, no. 2, pp. 181–191, 2010.
- [13] M. A. Pantaleo, E. Mishani, C. Nanni et al., "Evaluation of modified PEG-anilinoquinazoline derivatives as potential agents for EGFR imaging in cancer by small animal PET," *Molecular Imaging and Biology*, vol. 12, no. 6, pp. 616–625, 2010.
- [14] H. H. Yeh, K. Ogawa, J. Balatoni et al., "Molecular imaging of active mutant L858R EGF receptor (EGFR) kinase-expressing non-small cell lung carcinomas using PET/CT," *Proceedings of the National Academy of Sciences of the United States of America*, vol. 108, no. 4, pp. 1603–1608, 2011.
- [15] M. Yoshimoto, M. Hirata, Y. Kanai et al., "Monitoring of gefitinib sensitivity with radioiodinated PHY based on EGFR expression," *Biological and Pharmaceutical Bulletin*, vol. 37, pp. 355–360, 2014.
- [16] A. A. Memon, S. Jakobsen, F. Dagnaes-Hansen, B. S. Sorensen, S. Keiding, and E. Nexø, "Positron emission tomography (PET) imaging with [¹¹C]-labeled erlotinib: a micro-PET study on mice with lung tumor xenografts," *Cancer Research*, vol. 69, no. 3, pp. 873–878, 2009.
- [17] K. D. Carey, A. J. Garton, M. S. Romero et al., "Kinetic analysis of epidermal growth factor receptor somatic mutant proteins shows increased sensitivity to the epidermal growth factor receptor tyrosine kinase inhibitor, erlotinib," *Cancer Research*, vol. 66, no. 16, pp. 8163–8171, 2006.
- [18] I. Bahce, E. F. Smit, M. Lubberink et al., "Development of [¹¹C]erlotinib positron emission tomography for *in vivo* evaluation of EGF receptor mutational status," *Clinical Cancer Research*, vol. 19, no. 1, pp. 183–193, 2013.
- [19] I. Kümler, M. K. Tuxen, and D. L. Nielsen, "A systematic review of dual targeting in HER2-positive breast cancer," *Cancer Treatment Reviews*, vol. 40, no. 2, pp. 259–270, 2014.
- [20] D. J. Slamon, B. Leyland-Jones, S. Shak et al., "Use of chemotherapy plus a monoclonal antibody against HER2 for metastatic breast cancer that overexpresses HER2," *The New England Journal of Medicine*, vol. 344, no. 11, pp. 783–792, 2001.
- [21] A. Lebeau, A. Turzynski, S. Braun et al., "Reliability of human epidermal growth factor receptor 2 immunohistochemistry in breast core needle biopsies," *Journal of Clinical Oncology*, vol. 28, no. 20, pp. 3264–3270, 2010.
- [22] C. Xiao, Y. Gong, E. Y. Han, A. M. Gonzalez-Angulo, and N. Sneige, "Stability of HER2-positive status in breast carcinoma: a comparison between primary and paired metastatic tumors with regard to the possible impact of intervening trastuzumab treatment," *Annals of Oncology*, vol. 22, no. 7, pp. 1547–1553, 2011.
- [23] E. A. Mittendorf, Y. Wu, M. Scaltriti et al., "Loss of HER2 amplification following trastuzumab-based neoadjuvant systemic therapy and survival outcomes," *Clinical Cancer Research*, vol. 15, no. 23, pp. 7381–7388, 2009.
- [24] E. C. Dijkers, T. H. Oude Munnink, J. G. Kosterink et al., "Biodistribution of ⁸⁹Zr-trastuzumab and PET imaging of HER2-positive lesions in patients with metastatic breast cancer," *Clinical Pharmacology and Therapeutics*, vol. 87, no. 5, pp. 586–592, 2010.
- [25] M. N. Lub-de Hooge, J. G. W. Kosterink, P. J. Perik et al., "Pre-clinical characterisation of ¹¹¹In-DTPA-trastuzumab," *British Journal of Pharmacology*, vol. 143, no. 1, pp. 99–106, 2004.
- [26] T. H. Oude Munnink, M. A. D. Korte, W. B. Nagengast et al., "⁸⁹Zr-trastuzumab PET visualises HER2 downregulation by the HSP90 inhibitor NVP-AUY922 in a human tumour xenograft," *European Journal of Cancer*, vol. 46, no. 3, pp. 678–684, 2010.
- [27] P. J. Perik, M. N. Lub-De Hooge, J. A. Gietema et al., "Indium-111-labeled trastuzumab scintigraphy in patients with human epidermal growth factor receptor 2-positive metastatic breast cancer," *Journal of Clinical Oncology*, vol. 24, no. 15, pp. 2276–2282, 2006.
- [28] K. Tamura, H. Kurihara, K. Yonemori et al., "⁶⁴Cu-DOTA-trastuzumab PET imaging in patients with HER2-positive breast cancer," *Journal of Nuclear Medicine*, vol. 54, pp. 1869–1875, 2013.
- [29] K. McLarty, B. Cornelissen, D. A. Scollard, S. J. Done, K. Chun, and R. M. Reilly, "Associations between the uptake of ¹¹¹In-DTPA-trastuzumab, HER2 density and response to trastuzumab (Herceptin) in athymic mice bearing subcutaneous human tumour xenografts," *European Journal of Nuclear Medicine and Molecular Imaging*, vol. 36, no. 1, pp. 81–93, 2009.
- [30] Y. Y. Janjigian, N. Viola-Villegas, J. P. Holland et al., "Monitoring afatinib treatment in HER2-positive gastric cancer with ¹⁸F-FDG and ⁸⁹Zr-trastuzumab PET," *Journal of Nuclear Medicine*, vol. 54, no. 6, pp. 936–943, 2013.
- [31] D. Delbeke, R. E. Coleman, M. J. Guiberteau et al., "Procedure guideline for tumor imaging with ¹⁸F-FDG PET/CT 1.0," *Journal of Nuclear Medicine*, vol. 47, no. 5, pp. 885–895, 2006.
- [32] N. Ferrara and T. Davis-Smyth, "The biology of vascular endothelial growth factor," *Endocrine Reviews*, vol. 18, no. 1, pp. 4–25, 1997.
- [33] J. Folkman, "Tumor angiogenesis: therapeutic implications," *The New England Journal of Medicine*, vol. 285, no. 21, pp. 1182–1186, 1971.
- [34] L. G. Presta, H. Chen, S. J. O'Connor et al., "Humanization of an anti-vascular endothelial growth factor monoclonal antibody

- for the therapy of solid tumors and other disorders,” *Cancer Research*, vol. 57, no. 20, pp. 4593–4599, 1997.
- [35] C. G. Willett, Y. Boucher, E. di Tomaso et al., “Direct evidence that the VEGF-specific antibody bevacizumab has antivascular effects in human rectal cancer,” *Nature Medicine*, vol. 10, pp. 145–147, 2004.
- [36] F. Ciardiello, R. Bianco, R. Caputo et al., “Antitumor Activity of ZD6474, a vascular endothelial growth factor receptor tyrosine kinase inhibitor, in human cancer cells with acquired resistance to antiepidermal growth factor receptor therapy,” *Clinical Cancer Research*, vol. 10, no. 2, pp. 784–793, 2004.
- [37] S. R. Wedge, D. J. Ogilvie, M. Dukes et al., “ZD6474 inhibits vascular endothelial growth factor signaling, angiogenesis, and tumor growth following oral administration,” *Cancer Research*, vol. 62, no. 16, pp. 4645–4655, 2002.
- [38] S. B. M. Gaykema, A. H. Brouwers, M. N. L.-D. Hooge et al., “⁸⁹Zr-bevacizumab PET imaging in primary breast cancer,” *Journal of Nuclear Medicine*, vol. 54, no. 7, pp. 1014–1018, 2013.
- [39] A. J. Chang, R. Sohn, Z. H. Lu, J. M. Arbeit, and S. E. Lapi, “Detection of rapalog-mediated therapeutic response in renal cancer xenografts using ⁶⁴Cu-bevacizumab immunoPET,” *PLoS ONE*, vol. 8, no. 3, Article ID e58949, 2013.
- [40] T. Kniess, R. Bergmann, M. Kuchar, J. Steinbach, and F. Wuest, “Synthesis and radiopharmacological investigation of 3-[4'-[¹⁸F]fluorobenzylidene]indolin-2-one as possible tyrosine kinase inhibitor,” *Bioorganic and Medicinal Chemistry*, vol. 17, no. 22, pp. 7732–7742, 2009.
- [41] Z. Peng, D. S. Maxwell, D. Sun et al., “Imatinib analogs as potential agents for PET imaging of Bcr-Abl and c-KIT expression at a kinase level,” *Bioorganic & Medicinal Chemistry*, vol. 22, pp. 623–632, 2014.
- [42] M. Gao, C. M. Lola, M. Wang, K. D. Miller, G. W. Sledge, and Q.-H. Zheng, “Radiosynthesis of [¹¹C]Vandetanib and [¹¹C]chloro- Vandetanib as new potential PET agents for imaging of VEGFR in cancer,” *Bioorganic and Medicinal Chemistry Letters*, vol. 21, no. 11, pp. 3222–3226, 2011.
- [43] J.-Q. Wang, K. D. Miller, G. W. Sledge, and Q.-H. Zheng, “Synthesis of [¹⁸F]SU11248, a new potential PET tracer for imaging cancer tyrosine kinase,” *Bioorganic and Medicinal Chemistry Letters*, vol. 15, no. 19, pp. 4380–4384, 2005.
- [44] E. Samén, J.-O. Thorell, L. Lu, T. Tegnebratt, L. Holmgren, and S. Stone-Elander, “Synthesis and preclinical evaluation of [¹¹C]PAQ as a PET imaging tracer for VEGFR-2,” *European Journal of Nuclear Medicine and Molecular Imaging*, vol. 36, no. 8, pp. 1283–1295, 2009.
- [45] A. P. Glekas, N. K. Pillarsetty, B. Punzalan, N. Khan, P. Smith-Jones, and S. M. Larson, “In vivo imaging of Bcr-Abl overexpressing tumors with a radiolabeled imatinib analog as an imaging surrogate for imatinib,” *Journal of Nuclear Medicine*, vol. 52, no. 8, pp. 1301–1307, 2011.
- [46] A. J. Poot, B. van der Wildt, M. Stigter-van Walsum et al., “[¹¹C]Sorafenib: radiosynthesis and preclinical evaluation in tumor-bearing mice of a new TKI-PET tracer,” *Nuclear Medicine and Biology*, vol. 40, no. 4, pp. 488–497, 2013.

Review Article

Iodine-131 Metaiodobenzylguanidine Therapy for Neuroblastoma: Reports So Far and Future Perspective

Daiki Kayano and Seigo Kinuya

Department of Nuclear Medicine, Kanazawa University Hospital, 13-1 Takara-machi, Kanazawa, Ishikawa 920-8641, Japan

Correspondence should be addressed to Daiki Kayano; kayano@nmd.m.kanazawa-u.ac.jp

Received 24 June 2014; Accepted 1 August 2014

Academic Editor: Takahiro Higuchi

Copyright © 2015 D. Kayano and S. Kinuya. This is an open access article distributed under the Creative Commons Attribution License, which permits unrestricted use, distribution, and reproduction in any medium, provided the original work is properly cited.

Neuroblastoma, which derives from neural crest, is the most common extracranial solid cancer in childhood. The tumors express the norepinephrine (NE) transporters on their cell membrane and take in metaiodobenzylguanidine (MIBG) via a NE transporter. Since iodine-131 (I-131) MIBG therapy was firstly reported, many trails of MIBG therapy in patients with neuroblastoma were performed. Though monotherapy with a low dose of I-131 MIBG could achieve high-probability pain reduction, the objective response was poor. In contrast, more than 12 mCi/kg I-131 MIBG administrations with or without hematopoietic cell transplantation (HCT) obtain relatively good responses in patients with refractory or relapsed neuroblastoma. The combination therapy with I-131 MIBG and other modalities such as nonmyeloablative chemotherapy and myeloablative chemotherapy with HCT improved the therapeutic response in patients with refractory or relapsed neuroblastoma. In addition, I-131 MIBG therapy incorporated in the induction therapy was proved to be feasible in patients with newly diagnosed neuroblastoma. To expand more the use of MIBG therapy for neuroblastoma, further studies will be needed especially in the use at an earlier stage from diagnosis, in the use with other radionuclide formations of MIBG, and in combined use with other therapeutic agents.

1. Introduction

Neuroblastoma derives from neural-crest tissues and arises mostly from adrenal medulla or paraspinal ganglia. The tumor is the most common extracranial solid cancer in childhood. The annual incidence is 10.2 cases per million children under 15 years of age [1]. More than one-third of the patients are diagnosed younger than one-year-old and the median age at diagnosis is 17 months [2]. More than half of patients have metastases at diagnosis. Main metastatic sites are regional lymph nodes, liver, bone, and bone marrow [3]. Age, stage, and MYCN status are considered as consensus determinants of prognosis. Age greater than 12 or 18 months at diagnosis and patients with an advanced primary lesion or metastases and patients with MYCN amplification have worse outcomes [2–4]. Five-year survival rates of neuroblastoma have remained approximately over 80% for infants and improved for older children from approximately 40% before 1985 to 65% in around 2000 [5]. Nevertheless, the prognosis of

high-risk patients with neuroblastoma remains poor in spite of forcible multimodality therapies.

Since metaiodobenzylguanidine (MIBG) was reported as the adrenomedullary imaging agent in the early 1980s [6–8], iodine-131 (I-131) MIBG and iodine-123 (I-123) MIBG were widely used for detecting neuroendocrine tumors such as pheochromocytoma, neuroblastoma, and medullary thyroid cancer [9]. Because of emitting a beta ray with cytotoxic effects, I-131 MIBG was used with the aim of treatment for neuroendocrine tumors from early after the development of MIBG. The first therapy with I-131 MIBG was applied to pheochromocytoma patients [10]. In 1986, I-131 MIBG therapy for neuroblastoma was reported for the first time [11]. Since then, many trials of I-131 MIBG therapy in patients with neuroblastoma have been done.

In this paper, we detail the development of I-131 MIBG therapy in patients with neuroblastoma from the last decades to the future.

2. Mechanism of MIBG Uptake in Neuroblastoma Cells

MIBG is an aralkylguanidine which is structurally similar to the neurotransmitter norepinephrine (NE) and the ganglionic blocking drug guanethidine. The uptake of MIBG in neuroendocrine cells such as normal adrenomedullary cells, neuroblastoma, and pheochromocytoma cells is similar to the uptake of NE. MIBG enters neuroendocrine cells by two pathways, a specific uptake system (uptake-one) and a nonspecific uptake system. Uptake-one is an active process via a NE transporter and is energy-requiring, sodium-dependent, temperature-dependent, and low-capacity and has a high affinity for MIBG. The nonspecific uptake is an energy-independent passive diffusional mechanism [12–14]. In the clinical setting, uptake-one is the predominant uptake system for MIBG [15, 16].

Once taken up into neuroendocrine cells, the majority of MIBG remains within the cells. MIBG is not decomposed by enzymes and is not bound to postsynaptic adrenergic receptors [17]. Most neuroendocrine cells like pheochromocytoma cells store MIBG in the neurosecretory granules. By contrast, neuroblastoma cells typically have a paucity of the neurosecretory granules and most MIBGs are stored in the cytoplasm and mitochondria, rather than in the neurosecretory granules [18, 19].

3. Indications and Contraindications

The indications and contraindications of I-131 MIBG therapy for neuroblastoma are stated in the European Association of Nuclear Medicine procedure guidelines [20]. The indication is Stage III or IV neuroblastoma with MIBG-avid lesions at diagnostic I-123 MIBG or I-131 MIBG scintigraphy before I-131 MIBG therapy. Because neuroblastoma arises from neural-crest tissues, most lesions express NE transporters on their cell surfaces and they take in and store radiolabeled MIBG. If radiolabeled MIBG does not accumulate in the lesions of neuroblastoma at pretherapy diagnostic study, I-131 MIBG therapy should not be performed. The aims of I-131 MIBG therapy are to achieve complete remission, to inhibit tumor progression, and to alleviate symptoms from primary or metastatic lesions. Absolute contraindications are renal failure requiring dialysis and expected life less than 3 months unless in case of refractory bone pain. Relative contraindications are provided as uncontrollable medical risk and urinary incontinence by isolation and decreased renal function by glomerular filtration rate (GFR) less than 30 mL/min.

In the guideline draft of I-131 MIBG therapy for neuroblastoma from our country, life expectancy less than not 3 months but one month and decreased renal function by GFR less than 30 mL/min are defined as absolute contraindications [21].

4. Toxicity of I-131 MIBG Therapy

Typical acute toxicities usually seen within two or three days after I-131 MIBG administration are nausea and vomiting.

TABLE 1: Acute toxicities in 40 patients with refractory or relapsed neuroblastoma treated with I-131 MIBG at a mean dose of 10.5 mCi/kg in our institution.

Toxicity	Grade (<i>n</i> = 40)			
	1	2	3	4
Anorexia	16	1	1	0
Nausea	12	1	1	0
Vomiting	2	2	0	0
Sialadenitis	2	7	0	0
Fatigue	3	1	0	0
Fever	2	1	0	0
Stomatitis	2	0	0	0

Toxicity is graded by the common terminology criteria for adverse events version 4.0.

These toxicities occur in approximately 10 to 20% of treated patients. In a recent report, nausea and vomiting are observed in 11% and 21% of 66 therapies treated with upfront I-131 MIBG therapy at a dose of 4.2 to 21.7 mCi/kg for newly diagnosed neuroblastoma [22]. Sialadenitis is seen with a relatively high frequency. Five of 10 patients (9 neuroblastoma and 1 malignant pheochromocytoma) had bilateral parotid swelling within 24 hours after 12 to 18 mCi/kg I-131 MIBG injections [23]. Table 1 shows acute toxicities in 40 patients with refractory or relapsed neuroblastoma treated with I-131 MIBG at a mean dose of 10.5 mCi/kg in our institution. Though anorexia, nausea, and sialadenitis are seen with a relatively high frequency, severe acute toxicities are rare. A recent study investigated blood pressure (BP) changes within 48 hours after I-131 MIBG infusion [24]. BP-related adverse events were seen in 4 of 50 patients. One of them had a hypertensive encephalopathy. Another study reported that antihypertensive drugs were required in 2.8% of 218 I-131 MIBG administrations [25]. Though clinically relevant BP changes after I-131 MIBG therapy is rare, BP changes should be monitored at least within 48 hours after I-131 MIBG injections.

The most important toxicity is hematological with dose dependency usually appears a few weeks after MIBG therapy. Hematological toxicity is more noticeable in patients with bone marrow metastases and received higher whole-body radiation doses [26]. Hematopoietic cell transplantation (HCT) was required in about one-third of patients treated with 18 mCi/kg I-131 MIBG. In contrast, all patients treated with less than 12 mCi/kg of I-131 MIBG did not need HCT [26–28]. To date, a dose of 12 mCi/kg is considered as the maximum tolerated dose of I-131 MIBG therapy without HCT. Therefore, hematopoietic cell support should be arranged when more than 12 mCi/kg of I-131 MIBG was administered to the patient.

Venoocclusive liver disease (VOLD) is an important early complication in patients received I-131 MIBG therapy followed by myeloablative chemotherapy and HCT. The new approaches to neuroblastoma therapy (NANT) consortium reported that 6 of 22 patients had VOLDs after the therapies and an apparently high rate of VOLD was seen in the patients

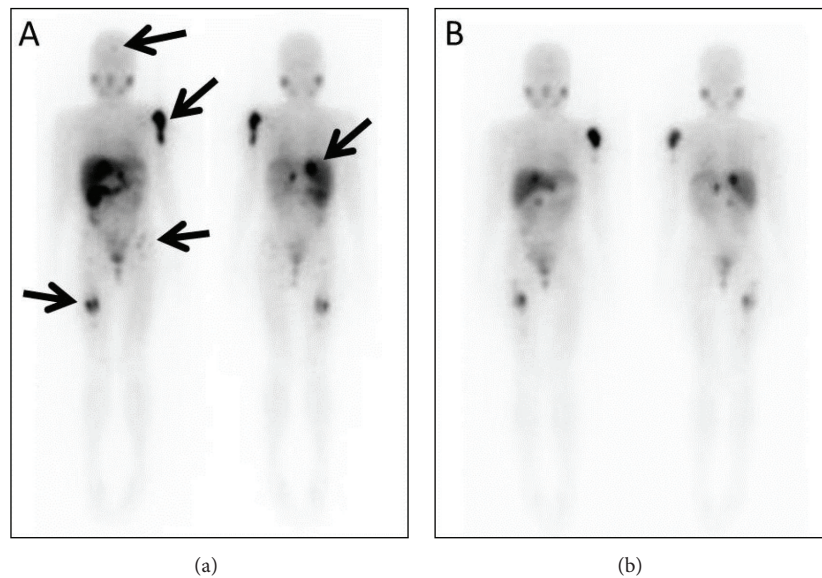


FIGURE 1: A 13-year-old female with relapsed neuroblastoma. She received the first I-131 MIBG therapy at a dose of 5.0 mCi/kg. Multiple accumulations are seen in a right retroperitoneal recurrence and multiple bone metastases ((a), arrows). The second I-131 MIBG therapy at a dose of 4.9 mCi/kg was performed 4 months after the first therapy. A scintigram after the second therapy shows a disappearance of femoral uptake and decreasing uptakes in other lesions especially in a right retroperitoneum recurrence and a left humeral bone metastasis (b). Though the objective response at the first therapy was stable by the response evaluation criteria in solid tumors, she became free of pain in the lower extremity after the first therapy. Unfortunately, she died of progressive disease 14 months after the first I-131 MIBG therapy.

with a low GFR [29]. In contrast, no VOLD was seen in patients receiving double infusions of high-dose I-131 MIBG without chemotherapy [30]. The decreased clearance of the chemotherapeutic agents was considered a major cause of VOLD.

Hypothyroidism is a major late side effect, despite the use of potassium iodine for the thyroid blockage. A Dutch group investigated the late side effect on the thyroid gland after I-131 MIBG therapy [31]. At a median follow-up time of 1.4 years after I-131 MIBG therapy, 5 of 16 survivors had TSH elevations. After a median follow-up time of 15.5 years, 8 of the 16 survivors developed hypothyroidism needed with thyroxin. In addition, papillary thyroid cancers were found in 2 of 9 survivors with thyroid nodules. Despite the protection with potassium iodine, only 3 of 16 survivors maintained normal thyroid function without any thyroid nodules. The incidence of thyroid disorders is high and increases as time advances. Papillary thyroid cancers may occur with a rather high frequency.

Second malignancies without thyroid cancers arise in less than 5%. In a report from Italy, 2 leukemia, one angiomatoid fibrous histiocytoma, one schwannoma, and one rhabdomyosarcoma occurred in 119 patients with neuroblastoma after I-131 MIBG therapy [32]. The University of California, San Francisco (UCSF) group described that leukemia was observed in 3 of 95 patients with refractory neuroblastoma at 7, 11, and 12 months after I-131 therapy [33]. It was difficult to clarify the main factor of the second malignancies, because all patients received several intensive therapies including chemotherapy and I-131 MIBG therapy.

5. Monotherapy with I-131 MIBG

Since the first I-131 MIBG therapy for neuroblastoma were reported in 1986 [11], many monotherapy trials with I-131 MIBG for refractory or relapsed neuroblastoma were reported and obtained objective responses (partial or complete response) in 0 to 66% [27, 28, 34–42]. In a report from Germany, the objective response rate was 66% in 12 evaluable patients with refractory or relapsed neuroblastoma with a mean dose of 10.3 mCi/kg of I-131 MIBG per each therapy [37]. Compared with higher doses of I-131 MIBG, lower doses tend to achieve lower objective responses. For instance, an Italian group treated 42 patients with refractory or relapsed neuroblastoma with 75 to 162 mCi of I-131 MIBG per each therapy [39]. The objective response rate was 16.7%. Five of 7 patients with objective responses survived more than 2 years without further chemotherapy. In the phase II study by a French group, 26 patients with refractory or relapsed neuroblastoma were treated with 30 to 108 mCi of I-131 MIBG per each therapy [34]. Though pain reduction was seen in 50% of patients, no patients had any objective response. In a recent report from Israel, I-131 MIBG therapy at a dose of 5 mCi/kg (maximum dose 150 mCi) per each therapy acquired pain palliation in 90% of the first therapies and 87.5% of the second therapies in 10 symptomatic patients with refractory neuroblastoma [43]. Lower doses of I-131 MIBG obtain a few objective responses, whereas can achieve high-probability pain reduction (Figure 1).

In a phase I study from UCSF, 30 patients with refractory or relapsed neuroblastoma were treated with I-131 MIBG at

escalating doses of 3 to 18 mCi/kg per each therapy [28]. The objective response rate was 37%. Most patients with objective responses were treated with 12 mCi or higher of I-131 MIBG.

A phase II study from a USA group reported some predictive factors affecting the therapeutic response of I-131 MIBG therapy in patients with refractory or relapsed neuroblastoma [27]. Sixteen patients without hematopoietic cell support were treated with 12 mCi/kg I-131 MIBG and 148 patients with hematopoietic cell support were treated with 18 mCi/kg I-131 MIBG. The overall objective response rates were 25% in patients treated with a dose of 12 mCi/kg and 37% in patients treated with a dose of 18 mCi/kg. The response rate was significantly higher in patients with fewer prior treatments, longer time from diagnosis, disease existed at soft tissue only or bone and bone marrow only and older age. The one-year event-free survival (EFS) and overall survival (OS) were 18% and 49%. The two-year OS was 29%. The EFS was significantly longer in patients with fewer prior treatments and older age.

6. Tandem Therapy with I-131 MIBG

Many of studies with I-131 MIBG monotherapy included patients with repetitive I-131 MIBG administrations. Each I-131 MIBG therapy was usually performed at intervals of more than 2 or 3 months because of the problems of hematologic toxicity and radiation safety.

The NANT consortium treated high-risk neuroblastoma with tandem I-131 MIBG administrations 14 days apart abrogating hematologic toxicity with autologous HCT (auto-HCT) 2 weeks after the second I-131 MIBG therapy [30]. In this dose escalation study, 20 evaluable patients received cumulative doses from 22 to 50 mCi/kg. All evaluable patients engrafted after auto-HCT and had no dose-limiting toxicity. Five of 11 patients (45.5%) with soft tissue lesions had good response. In contrast, bone marrow responses were seen in only 2 of 13 patients (15.4%). In the Children's Hospital of Philadelphia, 41 patients received repetitive I-131 MIBG therapies with auto-HCT at each dose of 18 mCi/kg [44]. The intervals of each therapy ranged from 42 to 100 days. The objective response rate after two therapies was 39%.

Though tandem therapy of I-131 MIBG with HCT is feasible, further studies are needed to improve therapeutic responses.

7. I-131 MIBG Therapy Combined with Chemotherapy

On the basis of I-131 MIBG monotherapeutic results, some groups tried the combination therapy with I-131 MIBG and chemotherapy agents act as radiosensitizers for refractory or relapsed neuroblastoma. In a report from Italy, 4 patients with refractory or relapsed neuroblastoma were administered I-131 MIBG in combination with cisplatin [45]. Two complete responses (CRs) and one partial response (PR) were observed. In addition, the same group treated 16 patients with 200 mCi I-131 MIBG plus cisplatin and cyclophosphamide with or without etoposide and vincristine

[46]. The objective response rate was 75%. The only toxicity was hematological mainly associated with chemotherapy. Regardless of relatively low dose of I-131 MIBG, these results were superior to the reports in monotherapy trials. A group of the United Kingdom investigated the feasibility of the combination therapy with I-131 MIBG and topoisomerase I inhibitor, topotecan [47]. Eight patients were treated with 12 mCi I-131 MIBG on days 1 and 15 along with topotecan on days 1–5 and 15–19. All patients received auto-HCT on days 25–27. The combination therapy was feasible without unanticipated toxicities. The response data was not shown in the study. In a phase I study from the NANT consortium, 24 patients with refractory or relapsed neuroblastoma treated with irinotecan which is another topoisomerase I inhibitor, vincristine, and I-131 MIBG at escalating doses of 8 to 18 mCi/kg [48]. The combination therapy was well tolerated at the maximum dose of 18 mCi with controllable toxicities and then a phase II randomized study by the NANT consortium is now in progress (N2011-01). Vorinostat, a histone deacetylase inhibitor, was preclinically proved to increase expression of NE transporters in neuroblastoma cells [49]. A phase I study with a combination of I-131 MIBG and vorinostat for refractory or relapsed neuroblastoma is now examined by the NANT consortium (N2007-03).

Myeloablative chemotherapy with auto-HCT was demonstrated to improve the outcome in patients with high-risk neuroblastoma [50]. Several groups reported I-131 MIBG therapy incorporated in myeloablative chemotherapy. A pilot study from the University of Michigan examined the feasibility and efficacy of the combination therapy with I-131 MIBG and myeloablative chemotherapy in 12 patients with relapsed or advanced neuroblastoma [51]. All patients were treated with 12 mCi I-131 MIBG on day -21, followed by carboplatin, etoposide, and melphalan (CEM) administered on day -7 to day -4. Auto-HCT was performed on day 0. This regimen was well tolerated. In evaluated 8 patients, 3 CRs and 2 PRs were observed. In a phase I dose escalation study by the NANT consortium, 24 patients with refractory neuroblastoma were treated with I-131 MIBG at escalating doses of 12 to 18 mCi/kg on day -21 along with CEM on day -7 to day -4 [29]. The maximum tolerated dose of I-131 MIBG was 12 mCi/kg when received in combination of CEM in patients with normal renal function. In evaluable 22 patients, one CR and 5 PRs were observed. The estimated EFS and OS at 3 years were 0.31 ± 0.10 and 0.58 ± 0.10 . A phase II study by the Children's Hospital Los Angeles using I-131 MIBG combined with CEM and auto-HCT is recently completed. The other myeloablative chemotherapy regimen using busulfan and melphalan (BuMel) with I-131 MIBG was reported form a UCSF group [52]. Eight patients with refractory neuroblastoma were treated with 18 mCi/kg I-131 MIBG on day -13 and auto-HCT on day 0. Six to eight weeks after I-131 MIBG administrations, they received busulfan on day -6 to day -2 and melphalan on day -1 and auto-HCT on day 0. I-131 MIBG therapies at doses of 18 mCi/kg were well tolerated without grade 3 or 4 nonhematologic toxicity except for one patient with sepsis. Though one patient died due to respiratory complications after the second auto-HCT, 3 CRs, and 2 PRs were observed in evaluable 7 patients. I-131

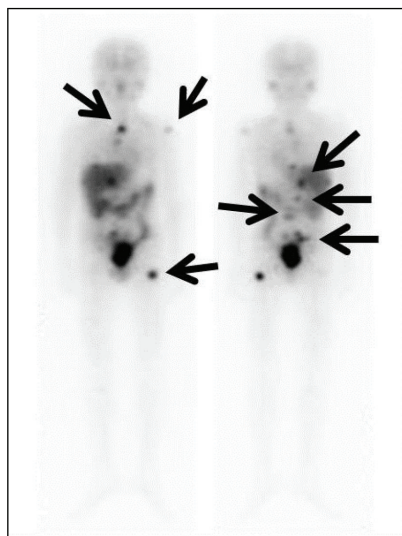


FIGURE 2: A 10-year-old male with relapsed neuroblastoma. He was treated with 16.8 mCi/kg I-131 MIBG. Multiple lymph nodes and bone metastases are detected by I-131 MIBG scintigraphy (arrows). After the treatment with chemotherapy and whole-body irradiation, he received CBSCT 4 weeks after the I-131 MIBG therapy. Complete remission has been maintained for more than 12 months.

MIBG therapy with myeloablative chemotherapy followed by auto-HCT may provide additional benefit for patients with refractory or relapsed neuroblastoma. Several further studies are now ongoing.

8. I-131 MIBG Therapy and Allogeneic Stem Cell Transplantation

Allogeneic HCT (allo-HCT) has been regarded as an alternative procedure for advanced neuroblastoma when autologous stem cells could not be obtained sufficiently [53, 54]. Some studies have recently reported the possibility to induce a graft-versus-tumor (GVT) effect against advanced neuroblastoma [55–57]. Two patients with relapsed neuroblastoma treated with I-131 MIBG and allo-HCT were reported in case reports from Japan [58, 59]. A 6-year-old female with relapsed neuroblastoma received reduced-intensity allo-HCT 21 days after I-131 MIBG therapy [59]. Though no GVT effect was observed, the patient was in CR for 3 months after allo-HCT. A 5-year-old female with relapsed neuroblastoma was executed cord blood stem cell transplantation (CBSCT) 9 days after I-131 MIBG therapy and GVT effect was observed after CBSCT [58]. Normalization of both vanillylmandelic acid and homovanillic acid for 5 months and decrease of I-123 MIBG accumulations were maintained, although the patient died 12 months after CBSCT. A 10-year-old male with relapsed neuroblastoma received I-131 MIBG therapy and CBSCT. Then, he got in remission for more than 12 months after the therapy (Figure 2). Though these reports indicate the potency of the combination therapy with I-131 MIBG and allo-HCT, prospective trials combining I-131 MIBG with allo-HCT will be required.

9. I-131 MIBG Therapy Combined with Hyperbaric Oxygen

Exposure of the neuroblastoma cells to hyperbaric oxygen (HBO) enhanced the effects of I-131 MIBG on decreasing cell proliferation and energy metabolism and increasing lipid peroxidation [60]. These effects may provide the positive effects on neuroblastoma patients treated with the combination of I-131 MIBG and HBO. A Dutch group treated 36 neuroblastoma patients with I-131 MIBG therapy alone and 27 neuroblastoma patients with a combination of I-131 MIBG therapy and 4 to 5 days HBO therapy starting 2 days after I-131 MIBG administrations [61]. The overall survival at 28 months was 32% for the I-131 MIBG and HBO combined group, compared to 12% for the group of I-131 MIBG therapy alone. Though only a few reports about the combination of I-131 MIBG and HBO therapy were shown, adding on HBO therapy may improve the effect of I-131 MIBG therapy.

10. I-131 MIBG Therapy for Newly Diagnosed Neuroblastoma

Based on the experience of I-131 MIBG therapy for refractory and relapsed neuroblastoma, several groups progressed to the new stage in evaluating the utility of I-131 MIBG therapy incorporated in the treatment for newly diagnosed neuroblastoma. A Dutch group used I-131 MIBG as an up-front agent of the induction therapy in patients with newly diagnosed stage IV neuroblastoma [62]. Two cycles of I-131 MIBG with a fixed dose of 200 mCi and 100 mCi were administered 4 to 6 weeks apart, followed by surgery or by both neoadjuvant chemotherapy and surgery. If objective responses were obtained after 2 cycles of I-131 MIBG therapy, patients proceeded to surgery. Some of them received additional I-131 MIBG therapies until surgery. If the objective responses were not obtained, patients were switched to induction chemotherapy until surgery. After surgery, all patients received myeloablative chemotherapy plus auto-HCT. Of the evaluable 41 patients, the objective response rate was 66% after two cycles of I-131 MIBG therapy. In addition, bone marrow metastases disappeared in 58%. Twenty-four patients received only I-131 MIBG and surgery. In the 24 patients, 14 patients had a CR after only I-131 MIBG plus surgery. The 5-year OS for all evaluated 41 patients was 14.6%. I-131 MIBG as an up-front use may be valuable for newly diagnosed advanced neuroblastoma.

In a German Neuroblastoma Trial (NB97), a benefit of I-131 MIBG therapy at the end of induction therapy in neuroblastoma patients with residual disease was investigated [63]. After induction therapy for newly diagnosed patients, 36 patients received I-131 MIBG therapy before auto-HCT and 30 patients did not receive I-131 MIBG therapy before auto-HCT. The 3-year EFS with or without I-131 MIBG therapy was 49% and 33%. The difference was not statistically significant; however these results might indicate the additive value of I-131 MIBG therapy after induction therapy in patients with newly diagnosed neuroblastoma. The following trial (NB2004) is now in progress.

An Italian group integrated I-131 MIBG therapy into induction chemotherapy in 13 patients with newly diagnosed advanced neuroblastoma [64]. In the pilot study, one CR and 6 very good PRs and 4 PRs were observed. These results support the feasibility of I-131 MIBG therapy as a part of induction therapy regimen. A pilot study of intensive induction chemotherapy and I-131 MIBG undergoing HCT for newly diagnosed advanced neuroblastoma by the Children's Oncology Group is currently recruiting participants.

Recently, a Dutch group reported the result of I-131 MIBG therapy in patients with unresectable localized neuroblastoma [65]. Twenty-one patients with any organ dysfunctions were treated with I-131 MIBG for unresectable localized neuroblastoma. Most patients needed additional surgery or both surgery and chemotherapy before or after I-131 MIBG therapy. As a result, 16 CRs, 3 very good PRs, and one PR were achieved. The 10-year EFS and OS were both 90.5%. I-131 MIBG therapy for unresectable localized neuroblastoma might be considerable when patients have any organ dysfunctions. To establish the validity and the utility of I-131 MIBG therapy for unresectable localized neuroblastoma, further studies are needed.

11. Other Radiopharmaceuticals in Connection with MIBG

I-131 MIBG is generally synthesized from iodine-127 MIBG by replacing stable iodine with radioiodine. Consequently, I-131 MIBG by the standard synthesis contains 1 radiolabeled I-131 MIBG molecule for 2000 nonradiolabeled MIBG molecules [66]. Nonradiolabeled MIBG competes against radiolabeled I-131 MIBG for NE transporter uptake on the cell membranes of neuroblastoma and other target organs. Some groups have synthesized no-carrier-added (NCA) I-131 MIBG and demonstrated the enhanced NCA I-131 MIBG concentrations within targets in preclinical studies [67, 68]. A phase I study about NCA I-131 MIBG showed safety in a dose escalation from 6 to 8 mCi/kg in patients with malignant pheochromocytoma or metastatic carcinoid [69]. In a phase II study by the NANT consortium, 15 patients with refractory or relapsed neuroblastoma received NCA I-131 MIBG therapy at escalation doses of 8.8 to 18.7 mCi/kg with stem cell backup [70]. Dose-limiting toxicity was not observed in all of 3, 3, and 6 patients treated with 12, 15, and 18 mCi/kg I-131 MIBG. The objective response rate was 27%, including 1 CR. NCA I-131 MIBG therapy with HCT at a dose of 18 mCi/kg is feasible without significant nonhematologic toxicity.

Because of the relatively long beta range of I-131 (0.8 mm), there is a hypothesis that I-131 fails to deliver a tumoricidal radiation dose to a small tumor less than 1 mm [71, 72]. Iodine-125 (I-125) emits very short-range Auger and conversion electrons with a high linear energy transfer and the maximum range of its emitters is about 30 μm [73, 74]. Therefore, I-125 MIBG has been considered as a potential substitute for I-131 MIBG for the treatment of neuroblastoma with microscopic disease [72, 75, 76]. In phases I and II trials by the University of Michigan, 10 patients with refractory or relapsed neuroblastoma received I-125 MIBG therapy at

a dose of 224 to 814 mCi [75]. The 1-year EFS was 50% and 4 patients were surviving 17 to 52 months after I-125 MIBG therapy. Further studies are needed, such as for macroscopic disease with a combination with I-125 MIBG and I-131 MIBG and for microscopic disease with I-125 MIBG.

Astatine-211 (At-211) generates alpha particles which are radiations of high linear energy transfer (LET) with very short-range in tissue of only a few cell diameters [77]. Because of shorter path length, higher LET, and more potent cytotoxicity, alpha particles are more suitable than beta particles for the targeted radionuclide therapy for microscopic disease. In a clinical experience, At-211-labeled antitenascin monoclonal antibodies were regionally administered in patients with malignant brain tumors [78]. This pilot study demonstrated the regional administration of At-211-labeled antitenascin antibody was feasible, safe, and effective for malignant brain tumors. MIBG analogue labeled with At-211, At-211 meta-astatobenzylguanidine (MABG) was proved to have a cytotoxic superiority to I-131 MIBG in human neuroblastoma cells which overexpressed NE transporters [79–81]. Alpha emitters hold enormous potentialities for radionuclide therapy. Further studies about At-211 MABG and other alpha emitters in both preclinical and clinical settings will be desired and will lead to future development of radionuclide therapy.

12. Conclusions

A number of studies indicate the efficacy of I-131 MIBG therapy in patients with refractory or relapsed neuroblastoma. In addition, I-131 MIBG therapy incorporated in the induction therapy is the feasible treatment strategy in patients with newly diagnosed neuroblastoma. To more expand the use of MIBG therapy for neuroblastoma, further studies will be needed especially in the use at an earlier date from diagnosis, in the use with other radionuclide formations of MIBG and in combined use with other therapeutic agents.

Conflict of Interests

The authors declare that there is no conflict of interests regarding the publication of this paper.

References

- [1] J. M. Maris, "Recent advances in neuroblastoma," *The New England Journal of Medicine*, vol. 362, no. 23, pp. 2154–2211, 2010.
- [2] W. B. London, R. P. Castleberry, K. K. Matthay et al., "Evidence for an age cutoff greater than 365 days for neuroblastoma risk group stratification in the Children's Oncology Group," *Journal of Clinical Oncology*, vol. 23, no. 27, pp. 6459–6465, 2005.
- [3] J. M. Maris, M. D. Hogarty, R. Bagatell, and S. L. Cohn, "Neuroblastoma," *The Lancet*, vol. 369, no. 9579, pp. 2106–2120, 2007.
- [4] G. M. Brodeur, J. Pritchard, F. Berthold et al., "Revisions of the international criteria for neuroblastoma diagnosis, staging, and response to treatment," *Journal of Clinical Oncology*, vol. 11, no. 8, pp. 1466–1477, 1993.

- [5] M. A. Smith, N. L. Seibel, S. F. Altekruze et al., "Outcomes for children and adolescents with cancer: challenges for the twenty-first century," *Journal of Clinical Oncology*, vol. 28, no. 15, pp. 2625–2634, 2010.
- [6] D. M. Wieland, J. I. Wu, and L. E. Brown, "Radiolabeled adrenergic neuron-blocking agents: adrenomedullary imaging with [¹³¹I]iodobenzylguanidine," *Journal of Nuclear Medicine*, vol. 21, no. 4, pp. 349–353, 1980.
- [7] M. Nakajo, B. Shapiro, J. Copp et al., "The normal and abnormal distribution of the adrenomedullary imaging agent m-[I-131]iodobenzylguanidine (I-131 MIBG) in man: evaluation by scintigraphy," *Journal of Nuclear Medicine*, vol. 24, no. 8, pp. 672–682, 1983.
- [8] D. M. Wieland, L. E. Brown, M. C. Tobes et al., "Imaging the primate adrenal medulla with [¹²³I] and [¹³¹I] meta-iodobenzylguanidine: concise communication," *Journal of Nuclear Medicine*, vol. 22, no. 4, pp. 358–364, 1981.
- [9] E. Bombardieri, F. Giammarile, C. Aktolun et al., "¹³¹I/¹²³I-Metaiodobenzylguanidine (mIBG) scintigraphy: procedure guidelines for tumour imaging," *European Journal of Nuclear Medicine and Molecular Imaging*, vol. 37, no. 12, pp. 2436–2446, 2010.
- [10] J. Sisson, B. Shapiro, W. H. Beierwaltes et al., "Treatment of malignant pheochromocytoma with a new radiopharmaceutical," *Transactions of the Association of American Physicians*, vol. 96, pp. 209–217, 1983.
- [11] J. Treuner, T. Klingebiel, U. Feine et al., "Clinical experiences in the treatment of neuroblastoma with ¹³¹I-metaiodobenzylguanidine," *Pediatric Hematology and Oncology*, vol. 3, no. 3, pp. 205–216, 1986.
- [12] S. Jaques Jr., M. C. Tobes, J. C. Sisson, J. A. Baker, and D. M. Wieland, "Comparison of the sodium dependency of uptake of meta-iodobenzylguanidine and norepinephrine into cultured bovine adrenomedullary cells," *Molecular Pharmacology*, vol. 26, no. 3, pp. 539–546, 1984.
- [13] S. Jacques Jr., M. C. Tobes, and J. C. Sisson, "Sodium dependency of uptake of norepinephrine and m-iodobenzylguanidine into cultured human pheochromocytoma cells: evidence for uptake-one," *Cancer Research*, vol. 47, no. 15, pp. 3920–3928, 1987.
- [14] J. Buck, G. Bruchelt, R. Girgert, J. Treuner, and D. Niethammer, "Specific uptake of m-[¹²⁵I]iodobenzylguanidine in the human neuroblastoma cell line SK-N-SH," *Cancer Research*, vol. 45, no. 12, pp. 6366–6370, 1985.
- [15] M. C. Tobes, S. Jaques Jr., D. M. Wieland, and J. C. Sisson, "Effect of uptake-one inhibitors on the uptake of norepinephrine and metaiodobenzylguanidine," *Journal of Nuclear Medicine*, vol. 26, no. 8, pp. 897–907, 1985.
- [16] L. A. Smets, C. Loesberg, M. Janssen, E. A. Metwally, and R. Huiskamp, "Active uptake and extravesicular storage of m-iodobenzylguanidine in human neuroblastoma SK-N-SH cells," *Cancer Research*, vol. 49, no. 11, pp. 2941–2944, 1989.
- [17] B. L. Shulkin and B. Shapiro, "Current concepts on the diagnostic use of MIBG in children," *Journal of Nuclear Medicine*, vol. 39, no. 4, pp. 679–688, 1998.
- [18] L. S. Lashford, J. P. Hancock, and J. T. Kemshead, "Metaiodobenzylguanidine (mIBG) uptake and storage in the human neuroblastoma cell line SK-N-BE(2C)," *International Journal of Cancer*, vol. 47, no. 1, pp. 105–109, 1991.
- [19] M. N. Gaze, I. M. Huxham, R. J. Mairs, and A. Barrett, "Intracellular localization of metaiodobenzyl guanidine in human neuroblastoma cells by electron spectroscopic imaging," *International Journal of Cancer*, vol. 47, no. 6, pp. 875–880, 1991.
- [20] F. Giammarile, A. Chiti, M. Lassmann, B. Brans, and G. Flux, "EANM procedure guidelines for ¹³¹I-meta-iodobenzylguanidine (¹³¹I-mIBG) therapy," *European Journal of Nuclear Medicine and Molecular Imaging*, vol. 35, no. 5, pp. 1039–1047, 2008.
- [21] M. Nakajo, K. Yoshinaga, N. Oriuchi, S. Kinuya, K. Yokoyama, and T. Yamaguchi, "Guideline draft of appropriate use of ¹³¹I-MIBG for internal radiotherapy of neuroendocrine tumors," *Kaku Igaku*, vol. 45, no. 1, supplement, pp. 1–40, 2008.
- [22] G. Bleeker, R. A. Schoot, H. N. Caron et al., "Toxicity of upfront ¹³¹I-metaiodobenzylguanidine (¹³¹I-MIBG) therapy in newly diagnosed neuroblastoma patients: a retrospective analysis," *European Journal of Nuclear Medicine and Molecular Imaging*, vol. 40, no. 11, pp. 1711–1717, 2013.
- [23] S. Modak, N. Pandit-Taskar, B. H. Kushner et al., "Transient sialoadenitis: a complication of ¹³¹I-metaiodobenzylguanidine therapy," *Pediatric Blood and Cancer*, vol. 50, no. 6, pp. 1271–1273, 2008.
- [24] M. A. Kosmin, J. B. Bomanji, N. J. Cork, A. Shankar, and M. N. Gaze, "Hypertension complicating ¹³¹I-meta-iodobenzylguanidine therapy for neuroblastoma," *European Journal of Nuclear Medicine and Molecular Imaging*, vol. 39, no. 4, pp. 597–601, 2012.
- [25] T. Wong, K. K. Matthay, W. J. Boscardin, R. A. Hawkins, P. R. Brakeman, and S. G. Dubois, "Acute changes in blood pressure in patients with neuroblastoma treated with ¹³¹I-metaiodobenzylguanidine (MIBG)," *Pediatric Blood and Cancer*, vol. 60, no. 9, pp. 1424–1430, 2013.
- [26] S. G. DuBois, J. Messina, J. M. Maris et al., "Hematologic toxicity of high-dose iodine-131-metaiodobenzylguanidine therapy for advanced neuroblastoma," *Journal of Clinical Oncology*, vol. 22, no. 12, pp. 2452–2460, 2004.
- [27] K. K. Matthay, G. Yanik, J. Messina et al., "Phase II study on the effect of disease sites, age, and prior therapy on response to iodine-131-metaiodobenzylguanidine therapy in refractory neuroblastoma," *Journal of Clinical Oncology*, vol. 25, no. 9, pp. 1054–1060, 2007.
- [28] K. K. Matthay, K. DeSantes, B. Hasegawa et al., "Phase I dose escalation of ¹³¹I-metaiodobenzylguanidine with autologous bone marrow support in refractory neuroblastoma," *Journal of Clinical Oncology*, vol. 16, no. 1, pp. 229–236, 1998.
- [29] K. K. Matthay, J. C. Tan, J. G. Villablanca et al., "Phase I dose escalation of iodine-131-metaiodobenzylguanidine with myeloablative chemotherapy and autologous stem-cell transplantation in refractory neuroblastoma: a new approaches to neuroblastoma therapy consortium study," *Journal of Clinical Oncology*, vol. 24, no. 3, pp. 500–506, 2006.
- [30] K. K. Matthay, A. Quach, J. Huberty et al., "Iodine-131-metaiodobenzylguanidine double infusion with autologous stem-cell rescue for neuroblastoma: a new approaches to neuroblastoma therapy phase I study," *Journal of Clinical Oncology*, vol. 27, no. 7, pp. 1020–1025, 2009.
- [31] S. C. Clement, B. L. van Eck-Smit, A. S. van Trotsenburg, L. C. Kremer, G. A. Tytgat, and H. M. van Santen, "Long-term follow-up of the thyroid gland after treatment with ¹³¹I-Metaiodobenzylguanidine in children with neuroblastoma: importance of continuous surveillance," *Pediatric Blood and Cancer*, vol. 60, no. 11, pp. 1833–1838, 2013.
- [32] A. Garaventa, C. Gambini, G. Villavecchia et al., "Second malignancies in children with neuroblastoma after combined treatment with ¹³¹I-metaiodobenzylguanidine," *Cancer*, vol. 97, no. 5, pp. 1332–1338, 2003.

- [33] B. Weiss, A. Vora, J. Huberty, R. A. Hawkins, and K. K. Matthay, "Secondary myelodysplastic syndrome and leukemia following ^{131}I -metaiodobenzylguanidine therapy for relapsed neuroblastoma," *Journal of Pediatric Hematology/Oncology*, vol. 25, no. 7, pp. 543–547, 2003.
- [34] J. Lumbroso, O. Hartmann, and M. Schlumberger, "Therapeutic use of [^{131}I]metaiodobenzylguanidine in neuroblastoma: a phase II study in 26 patients," *Journal of Nuclear Biology and Medicine*, vol. 35, no. 4, pp. 220–223, 1991.
- [35] R. J. Hutchinson, J. C. Sisson, B. Shapiro et al., " ^{131}I -metaiodobenzylguanidine treatment in patients with refractory advanced neuroblastoma," *The American Journal of Clinical Oncology: Cancer Clinical Trials*, vol. 15, no. 3, pp. 226–232, 1992.
- [36] K. K. Matthay, J. P. Huberty, R. S. Hattner et al., "Efficacy and safety of [^{131}I]metaiodobenzylguanidine therapy for patients with refractory neuroblastoma," *Journal of Nuclear Biology and Medicine*, vol. 35, no. 4, pp. 244–247, 1991.
- [37] T. Klingebiel, U. Feine, J. Treuner, P. Reuland, R. Handgretinger, and D. Niethammer, "Treatment of neuroblastoma with [^{131}I]metaiodobenzylguanidine: long-term results in 25 patients," *Journal of Nuclear Biology and Medicine*, vol. 35, no. 4, pp. 216–219, 1991.
- [38] A. Garaventa, O. Bellagamba, M. S. Lo Piccolo et al., " ^{131}I -metaiodobenzylguanidine (^{131}I -MIBG) therapy for residual neuroblastoma: a mono-institutional experience with 43 patients," *British Journal of Cancer*, vol. 81, no. 8, pp. 1378–1384, 1999.
- [39] F. Claudiani, A. Garaventa, L. Bertolazzi et al., "[^{131}I]metaiodobenzylguanidine therapy in advanced neuroblastoma," *Journal of Nuclear Biology and Medicine*, vol. 35, no. 4, pp. 224–227, 1991.
- [40] M. R. Castellani, A. Chiti, E. Seregni, and E. Bombardieri, "Role of ^{131}I -metaiodobenzylguanidine (MIBG) in the treatment of neuroendocrine tumours: experience of the National Cancer Institute of Milan," *Quarterly Journal of Nuclear Medicine*, vol. 44, no. 1, pp. 77–87, 2000.
- [41] T. I. Kang, P. Brophy, M. Hickeson et al., "Targeted radiotherapy with submyeloablative doses of ^{131}I -MIBG is effective for disease palliation in highly refractory neuroblastoma," *Journal of Pediatric Hematology/Oncology*, vol. 25, no. 10, pp. 769–773, 2003.
- [42] C. A. Hoefnagel, P. A. Voute, J. de Kraker, and R. A. Valdes Olmos, "[^{131}I]metaiodobenzylguanidine therapy after conventional therapy for neuroblastoma," *Journal of Nuclear Biology and Medicine*, vol. 35, no. 4, pp. 202–206, 1991.
- [43] M. W. Ben-Arush, A. B. Barak, R. Bar-Deroma et al., "Targeted therapy with low doses of ^{131}I -MIBG is effective for disease palliation in highly refractory neuroblastoma," *Israel Medical Association Journal*, vol. 15, no. 1, pp. 31–34, 2013.
- [44] K. Johnson, B. McGlynn, J. Saggio et al., "Safety and efficacy of tandem ^{131}I -metaiodobenzylguanidine infusions in relapsed/refractory neuroblastoma," *Pediatric Blood and Cancer*, vol. 57, no. 7, pp. 1124–1129, 2011.
- [45] R. Mastrangelo, A. Tornesello, R. Riccardi et al., "A new approach in the treatment of stage IV neuroblastoma using a combination of [^{131}I]meta-iodobenzylguanidine (MIBG) and cisplatin," *European Journal of Cancer*, vol. 31, no. 4, pp. 606–611, 1995.
- [46] S. Mastrangelo, A. Tornesello, L. Diociaiuti et al., "Treatment of advanced neuroblastoma: feasibility and therapeutic potential of a novel approach combining ^{131}I -MIBG and multiple drug chemotherapy," *British Journal of Cancer*, vol. 84, no. 4, pp. 460–464, 2001.
- [47] M. N. Gaze, Y. Chang, G. D. Flux, R. J. Mairs, F. H. Saran, and S. T. Meller, "Feasibility of dosimetry-based high-dose ^{131}I -meta-iodobenzylguanidine with topotecan as a radiosensitizer in children with metastatic neuroblastoma," *Cancer Biotherapy and Radiopharmaceuticals*, vol. 20, no. 2, pp. 195–199, 2005.
- [48] S. G. DuBois, L. Chesler, S. Groshen et al., "Phase I study of vincristine, irinotecan, and ^{131}I -metaiodobenzylguanidine for patients with relapsed or refractory neuroblastoma: a new approaches to neuroblastoma therapy trial," *Clinical Cancer Research*, vol. 18, no. 9, pp. 2679–2686, 2012.
- [49] S. S. More, M. Itsara, X. Yang et al., "Vorinostat increases expression of functional norepinephrine transporter in neuroblastoma in vitro and in vivo model systems," *Clinical Cancer Research*, vol. 17, no. 8, pp. 2339–2349, 2011.
- [50] F. Berthold, J. Boos, S. Burdach et al., "Myeloablative megatherapy with autologous stem-cell rescue versus oral maintenance chemotherapy as consolidation treatment in patients with high-risk neuroblastoma: a randomised controlled trial," *The Lancet Oncology*, vol. 6, no. 9, pp. 649–658, 2005.
- [51] G. A. Yanik, J. E. Levine, K. K. Matthay et al., "Pilot study of iodine-131-metaiodobenzylguanidine in combination with myeloablative chemotherapy and autologous stem-cell support for the treatment of neuroblastoma," *Journal of Clinical Oncology*, vol. 20, no. 8, pp. 2142–2149, 2002.
- [52] S. French, S. G. Dubois, B. Horn et al., " ^{131}I -MIBG followed by consolidation with busulfan, melphalan and autologous stem cell transplantation for refractory neuroblastoma," *Pediatric Blood and Cancer*, vol. 60, no. 5, pp. 879–884, 2013.
- [53] K. K. Matthay, R. C. Seeger, C. P. Reynolds et al., "Allogeneic versus autologous purged bone marrow transplantation for neuroblastoma: a report from the Childrens Cancer Group," *Journal of Clinical Oncology*, vol. 12, no. 11, pp. 2382–2389, 1994.
- [54] R. Ladenstein, C. Lasset, O. Hartmann et al., "Comparison of auto versus allografting as consolidation of primary treatments in advanced neuroblastoma over one year of age at diagnosis: report from the European Group for Bone Marrow Transplantation," *Bone Marrow Transplantation*, vol. 14, no. 1, pp. 37–46, 1994.
- [55] K. Goi, T. Inukai, H. Honna et al., "Successful tandem (autologous-cord blood) SCT in advanced neuroblastomas with highly amplified MYCN," *Bone Marrow Transplantation*, vol. 46, no. 6, pp. 835–839, 2011.
- [56] M. Inoue, T. Nakano, A. Yoneda et al., "Graft-versus-tumor effect in a patient with advanced neuroblastoma who received HLA haplo-identical bone marrow transplantation," *Bone Marrow Transplantation*, vol. 32, no. 1, pp. 103–106, 2003.
- [57] A. Marabelle, C. Paillard, A. Tchirkov et al., "Graft-versus-tumour effect in refractory metastatic neuroblastoma," *Bone Marrow Transplantation*, vol. 39, no. 12, pp. 809–810, 2007.
- [58] Y. Sato, H. Kurosawa, K. Fukushima et al., "I-131-metaiodobenzylguanidine therapy with allogeneic cord blood stem cell transplantation for recurrent neuroblastoma," *Italian Journal of Pediatrics*, vol. 38, no. 1, article 53, 2012.
- [59] H. Takahashi, A. Manabe, C. Aoyama et al., "Iodine-131-metaiodobenzylguanidine therapy with reduced-intensity allogeneic stem cell transplantation in recurrent neuroblastoma," *Pediatric Blood and Cancer*, vol. 50, no. 3, pp. 676–678, 2008.
- [60] J. Cornelissen, A. B. van Kuilenburg, L. Elzinga et al., "Hyperbaric oxygen enhances the effects of meta-iodobenzylguanidine (MIBG) on energy metabolism and lipid peroxidation in the human neuroblastoma cell line SK-N-BE(2C)," *Anticancer Research*, vol. 17, no. 1A, pp. 259–264, 1997.

- [61] P. A. Voute, A. J. van der Kleij, J. de Kraker, C. A. Hoefnagel, M. M. C. Tiel-Van Buul, and H. van Gennip, "Clinical experience with radiation enhancement by hyperbaric oxygen in children with recurrent neuroblastoma stage IV," *European Journal of Cancer A: General Topics*, vol. 31, no. 4, pp. 596–600, 1995.
- [62] J. de Kraker, K. A. Hoefnagel, A. C. Verschuur, B. van Eck, H. M. van Santen, and H. N. Caron, "Iodine-131-metaiodobenzylguanidine as initial induction therapy in stage 4 neuroblastoma patients over 1 year of age," *European Journal of Cancer*, vol. 44, no. 4, pp. 551–556, 2008.
- [63] M. Schmidt, T. Simon, B. Hero et al., "Is there a benefit of ^{131}I -MIBG therapy in the treatment of children with stage 4 neuroblastoma? A retrospective evaluation of the German Neuroblastoma Trial NB97 and implications for The German Neuroblastoma Trial NB2004," *NuklearMedizin*, vol. 45, no. 4, pp. 145–151, 2006.
- [64] S. Mastrangelo, V. Rufini, A. Ruggiero, A. Di Giannatale, and R. Riccardi, "Treatment of advanced neuroblastoma in children over 1 year of age: the critical role of ^{131}I -metaiodobenzylguanidine combined with chemotherapy in a rapid induction regimen," *Pediatric Blood & Cancer*, vol. 56, no. 7, pp. 1032–1040, 2011.
- [65] R. A. Schoot, G. Bleeker, H. N. Caron et al., "The role of ^{131}I -metaiodobenzylguanidine (MIBG) therapy in unresectable and compromising localised neuroblastoma," *European Journal of Nuclear Medicine and Molecular Imaging*, vol. 40, no. 10, pp. 1516–1522, 2013.
- [66] R. J. Mairs, S. H. Cunningham, J. Russell et al., "No-carrier-added iodine-131-MIBG: evaluation of a therapeutic preparation," *Journal of Nuclear Medicine*, vol. 36, no. 6, pp. 1088–1095, 1995.
- [67] G. Vaidyanathan and M. R. Zalutsky, "No-carrier-added synthesis of meta- ^{131}I iodobenzylguanidine," *Applied Radiation and Isotopes*, vol. 44, no. 3, pp. 621–628, 1993.
- [68] J. A. Barrett, J. L. Joyal, S. M. Hillier et al., "Comparison of high-specific-activity ultratrace $^{123/131}\text{I}$ -MIBG and carrier-added $^{123/131}\text{I}$ -MIBG on efficacy, pharmacokinetics, and tissue distribution," *Cancer Biotherapy and Radiopharmaceuticals*, vol. 25, no. 3, pp. 299–308, 2010.
- [69] R. E. Coleman, J. B. Stubbs, J. A. Barrett, M. de La Guardia, N. Lafrance, and J. W. Babich, "Radiation dosimetry, pharmacokinetics, and safety of ultratrace iobenguane I-131 in patients with malignant pheochromocytoma/paraganglioma or metastatic carcinoid," *Cancer Biotherapy and Radiopharmaceuticals*, vol. 24, no. 4, pp. 469–475, 2009.
- [70] K. K. Matthay, B. Weiss, J. G. Villablanca et al., "Dose escalation study of no-carrier-added ^{131}I - metaiodobenzylguanidine for relapsed or refractory neuroblastoma: new approaches to neuroblastoma therapy consortium trial," *Journal of Nuclear Medicine*, vol. 53, no. 7, pp. 1155–1163, 2012.
- [71] J. L. Humm, "Dosimetric aspects of radiolabeled antibodies for tumor therapy," *Journal of Nuclear Medicine*, vol. 27, no. 9, pp. 1490–1497, 1986.
- [72] J. C. Sisson, R. J. Hutchinson, B. Shapiro et al., "Iodine-125-MIBG to treat neuroblastoma: preliminary report," *Journal of Nuclear Medicine*, vol. 31, no. 9, pp. 1479–1485, 1990.
- [73] R. W. Howell, V. R. Narra, K. S. R. Sastry, and D. V. Rao, "On the equivalent dose for auger electron emitters," *Radiation Research*, vol. 134, no. 1, pp. 71–78, 1993.
- [74] W. Weber, J. Weber, and R. Senekowitsch-Schmidtke, "Therapeutic effect of m- ^{131}I - and m- ^{125}I iodobenzylguanidine on neuroblastoma multicellular tumor spheroids of different sizes," *Cancer Research*, vol. 56, no. 23, pp. 5428–5434, 1996.
- [75] J. C. Sisson, B. Shapiro, R. J. Hutchinson, B. L. Shulkin, and S. Zempel, "Survival of patients with neuroblastoma treated with ^{125}I -MIBG," *The American Journal of Clinical Oncology*, vol. 19, no. 2, pp. 144–148, 1996.
- [76] W. H. Y. Roa, G. G. Miller, A. J. B. McEwan et al., "Targeted radiotherapy of multicell neuroblastoma spheroids with high specific activity [^{125}I]meta-iodobenzylguanidine," *International Journal of Radiation Oncology, Biology, Physics*, vol. 41, no. 2, pp. 425–432, 1998.
- [77] M. Bardiès and P. Pihet, "Astatine-211-labeled radiotherapeutics: an emerging approach to targeted alpha-particle radiotherapy," *Current Pharmaceutical Design*, vol. 6, no. 14, pp. 1433–1455, 2000.
- [78] M. R. Zalutsky, D. A. Reardon, G. Akabani et al., "Clinical experience with alpha-particle-emitting ^{211}At : treatment of recurrent brain tumor patients with ^{211}At -labeled chimeric antitenascin monoclonal antibody 81C6," *Journal of Nuclear Medicine*, vol. 49, no. 1, pp. 30–38, 2008.
- [79] D. K. Strickland, G. Vaidyanathan, and M. R. Zalutsky, "Cytotoxicity of α -particle-emitting m- ^{211}At astatobenzylguanidine on human neuroblastoma cells," *Cancer Research*, vol. 54, no. 20, pp. 5414–5419, 1994.
- [80] S. H. Cunningham, R. J. Mairs, T. E. Wheldon, P. C. Welsh, G. Vaidyanathan, and M. R. Zalutsky, "Toxicity to neuroblastoma cells and spheroids of benzylguanidine conjugated to radionuclides with short-range emissions," *British Journal of Cancer*, vol. 77, no. 12, pp. 2061–2068, 1998.
- [81] M. Boyd, S. C. Ross, J. Dorrens et al., "Radiation-induced biologic bystander effect elicited in vitro by targeted radiopharmaceuticals labeled with α -, β -, and auger electron-emitting radionuclides," *Journal of Nuclear Medicine*, vol. 47, no. 6, pp. 1007–1015, 2006.

Research Article

Multiparametric Monitoring of Early Response to Antiangiogenic Therapy: A Sequential Perfusion CT and PET/CT Study in a Rabbit VX2 Tumor Model

Jung Im Kim,^{1,2} Hyun-Ju Lee,¹ Young Jae Kim,³ Kwang Gi Kim,³ Kyung Won Lee,⁴ Jae Ho Lee,⁵ Hak Jong Lee,⁴ and Won Woo Lee⁶

¹ Department of Radiology and Institute of Radiation Medicine, Seoul National University College of Medicine & Clinical Research Institute, Seoul National University Hospital, 101 Daehangno, Jongno-gu, Seoul 110-744, Republic of Korea

² Department of Radiology, Kyung Hee University Hospital at Gangdong, Kyung Hee University College of Medicine, 892 Dongnam-ro, Gangdong-gu, Seoul 134-727, Republic of Korea

³ Biomedical Engineering Branch, Division of Convergence Technology, National Cancer Center, 323 Ilsan-ro, Ilsandong-gu, Goyang-si, Gyeonggi-do 410-769, Republic of Korea

⁴ Department of Radiology, Seoul National University Bundang Hospital, Seoul National University College of Medicine, 82 Gumi-ro, 173 Beon-Gil, Bundang-Gu, Gyeonggi-do 463-707, Republic of Korea

⁵ Department of Internal Medicine, Seoul National University Bundang Hospital, Seoul National University College of Medicine, 82 Gumi-ro, 173 Beon-Gil, Bundang-Gu, Gyeonggi-do 463-707, Republic of Korea

⁶ Department of Nuclear Medicine, Seoul National University Bundang Hospital, Seoul National University College of Medicine, 82 Gumi-ro, 173 Beon-Gil, Bundang-Gu, Gyeonggi-do 463-707, Republic of Korea

Correspondence should be addressed to Hyun-Ju Lee; lee.hyunju.rad@gmail.com

Received 27 June 2014; Revised 19 August 2014; Accepted 1 September 2014; Published 15 October 2014

Academic Editor: Masashi Ueda

Copyright © 2014 Jung Im Kim et al. This is an open access article distributed under the Creative Commons Attribution License, which permits unrestricted use, distribution, and reproduction in any medium, provided the original work is properly cited.

Objectives. To perform dual analysis of tumor perfusion and glucose metabolism using perfusion CT and FDG-PET/CT for the purpose of monitoring the early response to bevacizumab therapy in rabbit VX2 tumor models and to assess added value of FDG-PET to perfusion CT. **Methods.** Twenty-four VX2 carcinoma tumors implanted in bilateral back muscles of 12 rabbits were evaluated. Serial concurrent perfusion CT and FDG-PET/CT were performed before and 3, 7, and 14 days after bevacizumab therapy (treatment group) or saline infusion (control group). Perfusion CT was analyzed to calculate blood flow (BF), blood volume (BV), and permeability surface area product (PS); FDG-PET was analyzed to calculate SUV_{max}, SUV_{mean}, total lesion glycolysis (TLG), entropy, and homogeneity. The flow-metabolic ratio (FMR) was also calculated and immunohistochemical analysis of microvessel density (MVD) was performed. **Results.** On day 14, BF and BV in the treatment group were significantly lower than in the control group. There were no significant differences in all FDG-PET-derived parameters between both groups. In the treatment group, FMR prominently decreased after therapy and was positively correlated with MVD. **Conclusions.** In VX2 tumors, FMR could provide further insight into the early antiangiogenic effect reflecting a mismatch in intratumor blood flow and metabolism.

1. Introduction

Angiogenesis is an essential component of tumor growth, invasion, and metastasis. Recently, with the continued development of antiangiogenic drugs that target the inhibition of tumor angiogenesis, techniques that can evaluate tumor angiogenesis have also been emphasized in clinical practice. In contrast to other anticancer therapies such as the use of

cytotoxic agents and irradiation, after antiangiogenic treatment, a decrease in tumor volume is not an expected treatment response [1]. Rather, quantitative computed tomography (CT) and magnetic resonance (MR) imaging kinetic parameters may be used to obtain insights into underlying tissue pathophysiologic processes of a variety of treatments, allowing prediction of treatment response or monitoring of their effects [2]. For these purposes, perfusion CT has

particularly seen increasing use as a method to quantify tumor vascularity and to monitor antiangiogenic response [3–8].

Another modality that has been used to evaluate the angiogenesis of tumors is positron emission tomography (PET). However, published data thus far have shown to be contradictory between different series [9]. Contractor and Aboagye [10] emphasized the requirement of multiphasic effect on FDG (fluorodeoxyglucose) uptake as well as dynamic analytic methods which can overcome the changes in perfusion after antiangiogenic treatment that affects any static imaging protocol. In addition, they suggested that measurement of the pharmacodynamic effects of antiangiogenic therapies with FDG at an earlier time point (within days) may be more appropriate to monitor changes in cell viability.

Another factor that has hampered the assessment of angiogenesis with PET is that standardized uptake values (SUVs) do not thoroughly provide metabolic information of the entire neoplasm although average SUV is partly associated with the tumor volume. Thus, the intratumor heterogeneity with areas of different biological activity would not sufficiently be reflected with SUV values. To compensate for this limitation, in addition to volumetric parameters including metabolic tumor volume (MTV) and total lesion glycolysis (TLG), texture analysis which estimates SUV distribution can be evaluated to characterize the aggressiveness of the tumor and the response assessment of anticancer therapy.

After the introduction of novel oncologic drugs targeted to interfere with specific aberrant biologic pathways involved in tumor development, the limitations of current structural imaging approaches have been further highlighted. Although the application of functional imaging such as FDG-PET and tumor perfusion imaging as markers of tumor response has been increasing in both research and clinical settings, these functional imaging techniques have been used in isolation [11]. There have been few studies in which both sequential perfusion and FDG uptake have been measured after antiangiogenic treatment.

Therefore, the purpose of this study was to undertake dual analysis of tumor perfusion and glucose metabolism after initiation of bevacizumab, a monoclonal antibody against the vascular endothelial growth factor, using perfusion CT and FDG-PET/CT in a VX2 tumor model in rabbits and to assess the possible added value of variable FDG-PET-derived indices to perfusion CT in monitoring early treatment response.

2. Materials and Methods

2.1. Study Design. This study was approved by the animal care committee of our institute. The rationale for selecting VX2 tumors for our experimental model is as follows: its blood supply is similar to that of human hepatocellular carcinomas, with rapid growth of the tumor, allowing it to grow relatively large and easily identified on imaging [12–14]. Twelve adult New Zealand white rabbits weighing 3.0 to 3.5 kg were used. For each rabbit, a 24-gauge medicut was inserted into an auricular vein, and anesthesia was induced with

intravenous ketamine hydrochloride (50 mg per kg of body weight; Ketamine, Yuhan, Korea) and 2% xylazine (0.1 mL/kg; Rompun, Bayer, Germany). Thereafter, the bilateral back parallel to the spine of the rabbits was shaved and sterilized, and the rabbits were put in the prone position on the table. Under ultrasound (US) guidance, a 21-gauge Chiba needle was inserted into the bilateral back muscle at the level of the kidney. Then, a VX2 tumor suspension (0.1 mL) was slowly injected into each back muscle through the Chiba needle.

On one week after tumor implantation when the tumors were expected to be round in shape with a diameter of approximately 1 cm, a baseline perfusion CT as well as PET/CT was performed for each rabbits. The rabbits were randomly allocated (6 per group) to receive serial injections of either bevacizumab (10 mg/kg; Avastin, Genentech) or the same dose of normal saline (treatment group and control group, resp.). Follow-up perfusion CT and PET/CT scans were acquired 3, 7, and 14 days after the baseline study. Each PET/CT scan was performed within 6 hours after perfusion CT scanning.

2.2. Perfusion CT and FDG-PET/CT Imaging. During CT imaging and PET/CT, animals were sedated with an intramuscular injection of 5 mg/kg of Xylazine hydrochloride (Rompun; Bayer Korea, Seoul, Korea) and 15 mg/kg of Zoletil mixture (Zoletil 50, Virbac Lab., Carros Cedex, France).

2.2.1. Perfusion CT Imaging. The rabbits were fixed on a CT board in the supine position by applying a thoracoabdominal bandage to reduce motion artifacts. The whole perfusion CT imaging was performed with a 64-detector row dual-source scanner (Siemens Definition; Siemens Medical Solutions, Erlangen, Germany). Noncontrast CT (80 kV; 120 mAs; detector configuration 20×0.6 mm; rotation time 1 second; section thickness 5.0 mm; reconstruction interval 5.0 mm; and reconstruction kernel H31s) was performed to confirm the complete coverage of the tumor. Marking of the tumor injection site provided a good guide for tumor localization. An experienced radiologist (J.L.K.) with seven years of experience in chest perfusion CT analyzed the unenhanced CT images and selected a fixed scanning range to cover the entire mass with care taken to avoid the possible exclusion of the peripheral portion of the mass during free breathing.

A total of 6.5 mL of a nonionic iodinated contrast medium (Ultravist 370, Schering, Berlin, Germany) was injected using a dual-phase injection protocol (3 mL at 0.5 mL/sec and 3.5 mL at 0.1 mL/sec followed by a 1.5 mL saline flush at 0.1 mL/sec) and a dual-head power injector (MedradStellant Dual; Medrad, Indianola, Pa). Perfusion CT scanning was started 2 seconds after injection with free breathing dynamic acquisition. The CT parameters were as follows: 120 kV, 150 mAs; detector configuration 24×1.2 mm; rotation time 0.33 seconds; section thickness 3.0 mm; reconstruction interval 2 mm; and reconstruction kernel B20f. Dynamic CT scans were obtained 40 times for each mass with a 1.5 second interval for the first 20 scans, a 3 second interval for the next 10 scans, and a 6 second interval for the remaining 10 scans; the total scanning time was 120 seconds.

2.2.2. PET/CT Imaging. All rabbits were fasted for at least 6 hours prior to intravenous injection of 37 MBq (1 mCi) of FDG. Before scanning, urinary voiding was performed with a 6-F urinary catheter. Scanning was performed 45 minutes after the injection of FDG using a dual modality PET/CT scanner (Gemini; Philips Medical Systems, Milpitas). CT was performed for attenuation correction, and an emission scan was performed in three-dimensional mode with a 256×256 matrix. PET images were reconstructed using an ordered-set expectation-maximization algorithm and CT scans were reconstructed with a section thickness of 4 mm to match the parameters of the PET scan.

2.3. Perfusion CT Data Processing. A radiologist (J.I.K., who had 8 years of experience in interpreting perfusion images) measured all perfusion parameters using commercially available software (Syngo VPCT, Siemens Healthcare, Forchheim, Germany). The measurement was performed with computerized motion correction using whole tumor coverage. Arterial input was measured by placing a circular region of interest (ROI) at the level of renal artery or within the abdominal aorta and an arterial time-enhancement curve was automatically generated with the software. A volume of interest (VOI) of the whole tumor was manually drawn around the tumor outline in all three planes (axial, coronal, and sagittal) with exclusion of the adjacent muscle. The following settings were adopted for segmentation: tissue upper and lower limits of 150 and -50 HU, respectively, reference vessel input window width and a center of 300 and 150 HU, respectively, and percentage of relative threshold inside and outside of 50 and 50, respectively.

At each measurement of perfusion CT, blood flow (BF; mL/100 mL/min), blood volume (BV; mL/100 mL), and permeability surface area product (PS; mL/100 mL/min) were obtained. With the software (Syngo VPCT, Siemens Healthcare, Forchheim, Germany), blood flow was calculated using the maximum slope method [15] and blood volume and PS were calculated using Patlak analysis [16].

2.4. PET/CT Analysis. The CT scan of the PET/CT acquisition and the thirty-first frame (time point) of the perfusion CT scan were coregistered to the same locations. Thereafter, the PET scan and coregistered perfusion CT scan were rigidly fused using in-house developed software, which uses the three-dimensional registration and color mapping hardware (Figure 1). PET and perfusion CT data were initially transferred to the software in DICOM format.

For each tumor, manually delineated ROIs were placed along the boundary of the tumor on axial fused images 3 mm in section thickness, in which the tumor was easily demarcated with guidance from coregistered perfusion CT images. Our in-house software calculated the maximum standardized uptake value (SUVmax), mean SUV (SUVmean), tumor volume (TV), and total lesion glycolysis (TLG; $TV \times SUVmean$).

All textural parameters were calculated from the manually delineated ROI as described above. Voxel values were first

resampled to yield a finite range of 128 discrete values between the minimum and maximum SUV in the tumor, using

$$R(x) = 128 * \left(\frac{I(x) - SUV_{min}}{SUV_{max} - SUV_{min} + 1} \right), \quad (1)$$

where $I(x)$ is the SUV of voxel x in the original image, SUV_{min} and SUV_{max} are the minimum and maximum SUV in the VOI, and $R(x)$ is the resampled value of voxel x [17].

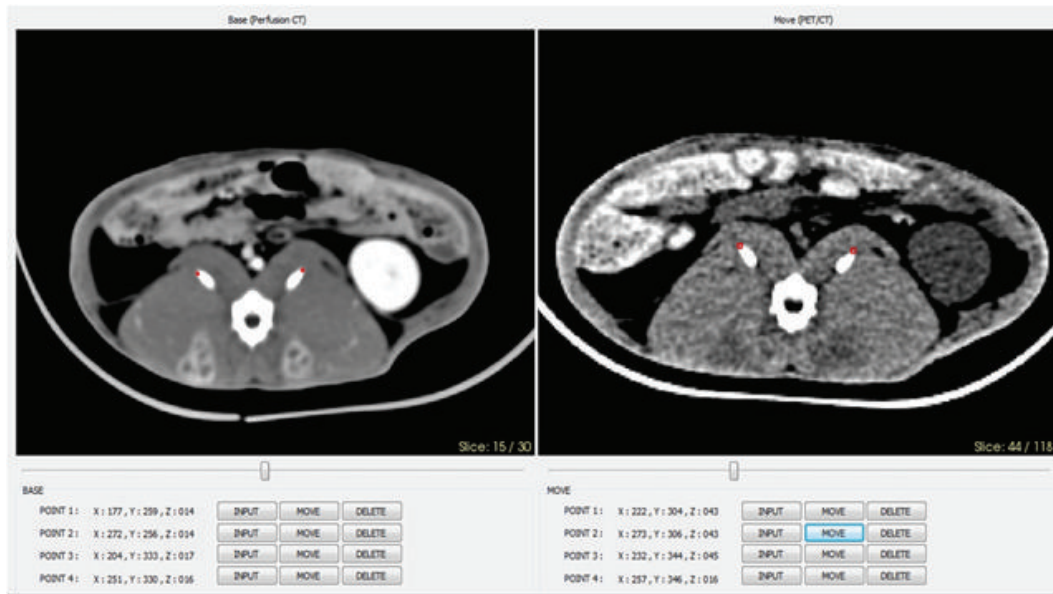
Two 3D matrices depicting texture heterogeneity were estimated from the delineated tumors. The grey level co-occurrence matrix (GLCM), describing the pair-wise arrangement of voxels is a 3D matrix related to texture heterogeneity at a local level [18].

In this study, we focused on 2 textural indices that were initially calculated: homogeneity and entropy calculated from the GLCM as defined by Haralick et al. [18], Amadasun and King [19], and Txier et al. [20]. While homogeneity measures the homogeneity of a pixel pair, entropy measures the randomness of gray-level distribution.

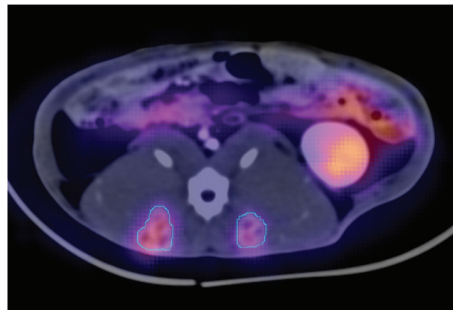
The flow-metabolic ratio (FMR, the ratio of contrast agent delivery to tumor glucose metabolism) was also determined for each patient by dividing blood flow by SUV_{max} [21]. The FMR, a combined assessment of intratumor blood flow and glucose metabolism using FDG-PET and perfusion CT, has been recently introduced as a promising parameter in clinical practice with the potential to risk-stratify patient.

2.5. Histopathologic Evaluation. After completion of serial perfusion CT scanning, all rabbits were sacrificed with an intravenous injection of a lethal amount of sodium thiopental (Pentothal) and were frozen in a refrigerator at -70°C in the same position used for CT imaging. More than 24 hours later, the rabbits were cut in the axial plane according to the guidance of the transverse line, 5 mm in thickness, marked on the skin. After each slice of the specimens was fixed with 10% phosphate-buffered formaldehyde and embedded in paraffin, pathologic specimens (approximately $5 \mu\text{m}$ thick) were obtained. For microvessel density (MVD) measurement, these pathologic slides were immunohistochemically stained specifically for the endothelial antigen CD31, which is traditionally used to evaluate tumor angiogenesis. Counterstaining with hematoxylin-eosin was performed for regular histologic characterization of the tumor.

MVD was quantified by counting the number of vessels plus immunoreactive endometrial cells per 200x high power field in four vascular "hot spots" within the malignant tumor with the mean number reported as the final MVD [22]. Hot spots were selected at low magnification (40x) and corresponded to areas that showed stronger CD31 staining and, consequently, higher vascular density than the rest of the tissue. MVD was calculated when any endothelial cell or cell cluster showed CD31 staining and was clearly separate from adjacent tissue elements [23–25]. ScanScope CS (Aperio Technologies, Inc., Vista, CA, USA) was used to scan the entire tissue sections at $\times 40$ magnification and



(a)



(b)

FIGURE 1: Coregistration of perfusion CT and PET images on day 7: rabbit number 3 in the control group. (a) A contrast-enhanced CT image from the thirty-first frame (time point) of perfusion CT and noncontrast CT image from PET/CT acquisition were coregistered to the same locations. (b) PET and coregistered perfusion CT images were rigidly fused using in-house developed software and ROIs were manually delineated throughout the whole tumor at each axial image.

Aperio ImageScope v11.0.2.782 (Aperio Technologies, Inc., Vista, CA, USA) was used for quantification of MVD.

2.6. Statistical Analysis. Within the framework of the mixed-effect model, a repeated-measure analysis was used to compare the mean change of measure parameters from baseline. In addition, measured data between the treatment and control groups were compared at each time points. Rabbit and tumor identification were both used as random effects to accommodate possible correlations between tumors from the same rabbit and measurements with the same rabbit across time.

To assess the relationship between perfusion and metabolic parameters as well as between measured parameters and CD 31 expression, Pearson's or Spearman's correlation coefficients were applied under the linear mixed effect model. All statistical analyses were performed using the *R* statistics package (v.3.1.0; <http://www.R-project.org/>) and SAS 9.2

software (SAS Institute); a two-tailed *P* value < 0.05 was considered to indicate a statistically significant difference for all statistical analyses.

3. Results

In two rabbits, perfusion CT data were incomplete: perfusion CT on day 3 of one rabbit in the control group and baseline perfusion CT of another rabbit in the treatment group were not suitable for imaging registration owing to movement during CT scanning. A baseline FDG-PET/CT data of one rabbit in the control group was also not suitable for imaging registration due to motion artifacts. In addition, two rabbits each in the control and treatment groups unexpectedly expired after imaging on day 7.

Both in the control and the treatment groups, the volume of tumors significantly increased during follow-up with no statistically significant differences between the two groups (Figure 2 and Table 1).

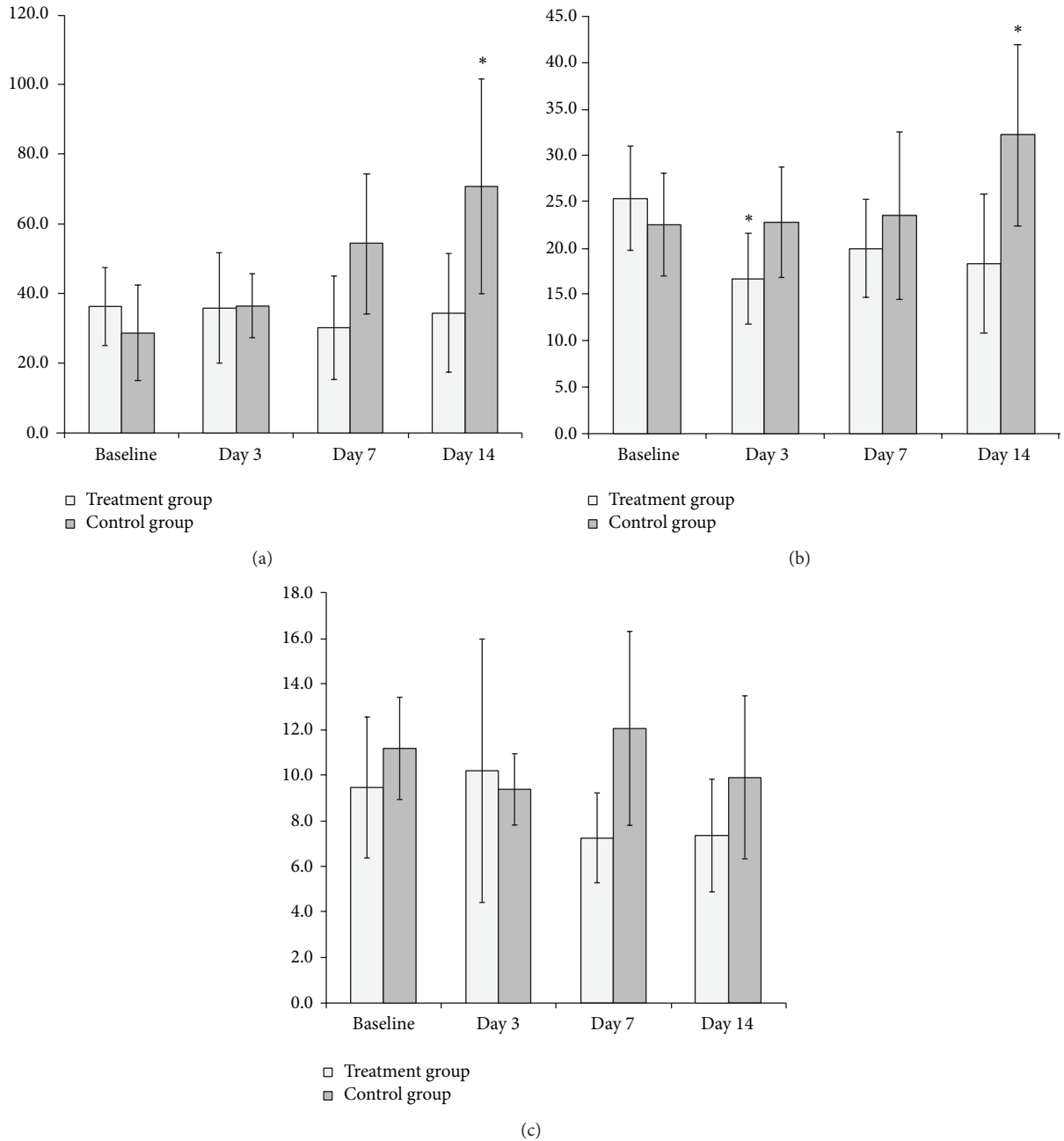


FIGURE 2: Averaged (a) BF, (b) BV, and (c) PS before and at different time points after bevacizumab therapy. In the control group, BF increased gradually and both BF and BV on day 14 demonstrated significant increases. In the treatment group, a significant decrease in BV on day 3 was observed. * is significant change compared to the baseline, BF is blood flow, BV is blood volume, and PS is permeability surface area product.

3.1. Sequential Assessment of Perfusion CT and FDG-PET/CT

3.1.1. Perfusion CT. Changes in the mean values of BF, BV, and PS over time with averaging of the parameters of the entire tumor in each group are summarized in Figure 2 and in Table 1. In the control group, BF and BV showed a trend toward an increase over time. A significant increase in BF and BV was observed on day 14 ($P < 0.05$, both), compared with the same parameters at baseline (Figure 2). In the treatment group, a significant decrease in BV was observed on day 3 and day 14 ($P < 0.05$), compared with baseline, in contrary to BF

in which changes from baseline were unnoticeable (Figure 2). Changes in the mean values of PS were minimal over time both in the control and the treatment groups (Figure 2).

3.1.2. FDG-PET/CT. Changes in the mean values of SUVmax, SUVmean, TLG, local entropy, local homogeneity, and FMR over time with averaging of the parameters of the entire tumor in each group are shown in Figure 3 and in Table 1. All parameters obtained from FDG-PET/CT except homogeneity showed a significant increase over time in both groups ($P < 0.01\sim 0.001$) (Figure 3). Particularly on day 14, a

TABLE 1: Perfusion and metabolic parameters between the treatment and the control groups at each time point.

Parameters	Before		3 D		7 D		14 D	
	Treatment	Control	Treatment	Control	Treatment	Control	Treatment	Control
Tumor volume (cm ³)	0.18 ± 0.08	0.18 ± 0.10	0.53 ± 0.32	0.43 ± 0.23	0.79 ± 0.47	0.76 ± 0.57	1.53 ± 1.11	1.88 ± 1.32
Blood flow (mL/100 mL/min)	36.16 ± 11.15	28.64 ± 13.78	35.82 ± 25.93	36.44 ± 9.22	30.05 ± 14.87	54.13 ± 30.11	34.34 ± 17.10	70.75 ± 50.65
Blood volume (mL/100 mL)	25.36 ± 5.62	22.56 ± 5.56	16.71 ± 4.91	22.81 ± 5.95	19.99 ± 5.30	23.54 ± 9.04	18.35 ± 7.48	32.20 ± 9.76
PS (mL/100 mL/min)	9.47 ± 3.09	11.18 ± 2.24	10.18 ± 5.81	9.39 ± 1.58	7.246 ± 1.97	12.06 ± 7.25	7.36 ± 2.48	9.91 ± 3.59
SUVmax	1.45 ± 0.26	1.31 ± 0.43	2.23 ± 0.65	2.21 ± 0.60	2.42 ± 0.92	2.13 ± 0.89	3.03 ± 1.36	3.73 ± 1.22
SUVmean	0.96 ± 0.18	0.84 ± 0.29	1.30 ± 0.33	1.33 ± 0.29	1.33 ± 0.40	1.27 ± 0.45	1.77 ± 0.66	2.10 ± 0.54
TLG (cm ³)	0.43 ± 0.22	0.35 ± 0.16	1.16 ± 0.63	1.20 ± 0.55	1.96 ± 1.28	1.61 ± 1.13	4.43 ± 3.63	4.78 ± 3.95
Entropy	5.95 ± 0.32	5.80 ± 0.47	6.36 ± 0.34	6.41 ± 0.35	6.58 ± 0.32	6.46 ± 0.46	6.69 ± 0.57	6.91 ± 0.34
Homogeneity	0.31 ± 0.07	0.26 ± 0.10	0.32 ± 0.06	0.30 ± 0.05	0.34 ± 0.04	0.32 ± 0.06	0.34 ± 0.05	0.33 ± 0.05
FMR	27.10 ± 12.19	25.19 ± 20.54	17.12 ± 12.80	17.33 ± 7.20	13.55 ± 6.41	29.75 ± 22.78	12.24 ± 6.92	25.87 ± 29.22

Data are presented as mean ± standard deviation.

Boldface indicates significant difference between the treatment and the control groups.

PS: permeability surface area product.

SUV: standardized uptake value.

TLG: total lesion glycolysis.

FMR: flow-metabolic ratio.

marked increase in SUVmax, SUVmean, TLG, and entropy was observed in both groups ($P < 0.001$). In contrast, changes in local homogeneity were minimal over time in both groups (Figure 3).

FMR showed a significant decrease over time in the treatment group but no significant difference over time in the control group (Figure 3). In the treatment group, a significant increase in FMR was observed on days 7 and 14 ($P < 0.05$, both), compared with baseline.

3.2. Treatment versus Control Group: Perfusion, Metabolism, and MVD. BF on day 7 of the treatment group was significantly lower than in the control group ($P < 0.05$), and the difference measured on day 14 was still significant between the two groups ($P < 0.05$) (Table 1). In addition, BV on day 3 of the treatment group was significantly lower than in the control group ($P < 0.05$), and a further significant difference was measured on day 14 ($P < 0.01$) (Table 1). None of the PET-derived parameters showed statistically significant differences between the two groups (Table 1). However, FMRs on days 7 and 14 of the treatment group were significantly lower than in the control group ($P < 0.05$) (Figure 4).

The mean MVD of the treatment group was significantly lower than the control group (8.75 ± 2.49 (range, 4~12) versus 21.50 ± 3.49 (range, 17~26), resp.; $P < 0.001$) (Figure 5).

3.3. Correlation Analysis. Both in the treatment and in the control groups, no significant correlation was demonstrated between blood flow and metabolic parameters. However, in the treatment group, BF and FMR correlated significantly with MVD ($r = 0.709$, $P < 0.05$; $r = 0.782$, $P < 0.01$, resp.). In the control group, only BF correlated significantly with MVD ($r = 0.733$, $P < 0.05$).

4. Discussion

Antiangiogenic agents have become an essential components of cancer research, and among them, bevacizumab (Avastin; Genentec) has been the most widely used antiangiogenic agent. The development and validation of biomarkers for the prediction of response to antiangiogenic therapy is an area of increasing importance, particularly given recent concerns surrounding the effectiveness of such therapies in prolonging patient survival as well as their potential effects on metastasis [26]. Perfusion CT, an advanced functional imaging biomarker, cannot provide only regional morphologic maps but also quantitative measurements of various tissue hemodynamic parameters [3]. Several previous studies have already reported the predictive values of perfusion CT in antiangiogenic therapy, considering that changes in tumor vascularity precede the changes in tumor size within days of initiating antiangiogenic therapy [3, 7, 27–29]. However, the usefulness of FDG-PET in detecting the response to antivascular endothelial growth factor (VEGF) therapies has been limited [30]. Our study evaluated the early therapeutic response to bevacizumab using serial FDG-PET/CT and perfusion CT and assessed the possible additional value of FDG-PET to perfusion CT.

We found that in the treatment group, there were no significant changes in BF and PS other than a weak declining trend over time in BV. This may have resulted from intratumor vascular normalization of early antiangiogenic effects on perfusion parameters, previously mentioned by García-Figueiras et al. [31], although BF did not show increase in our study. However, in the control group, BF and BV showed a significant increase over time implying an increase in intratumor mature vascular density [32].

To the contrary, there were no significant differences in SUVmax and SUVmean between the two groups even though

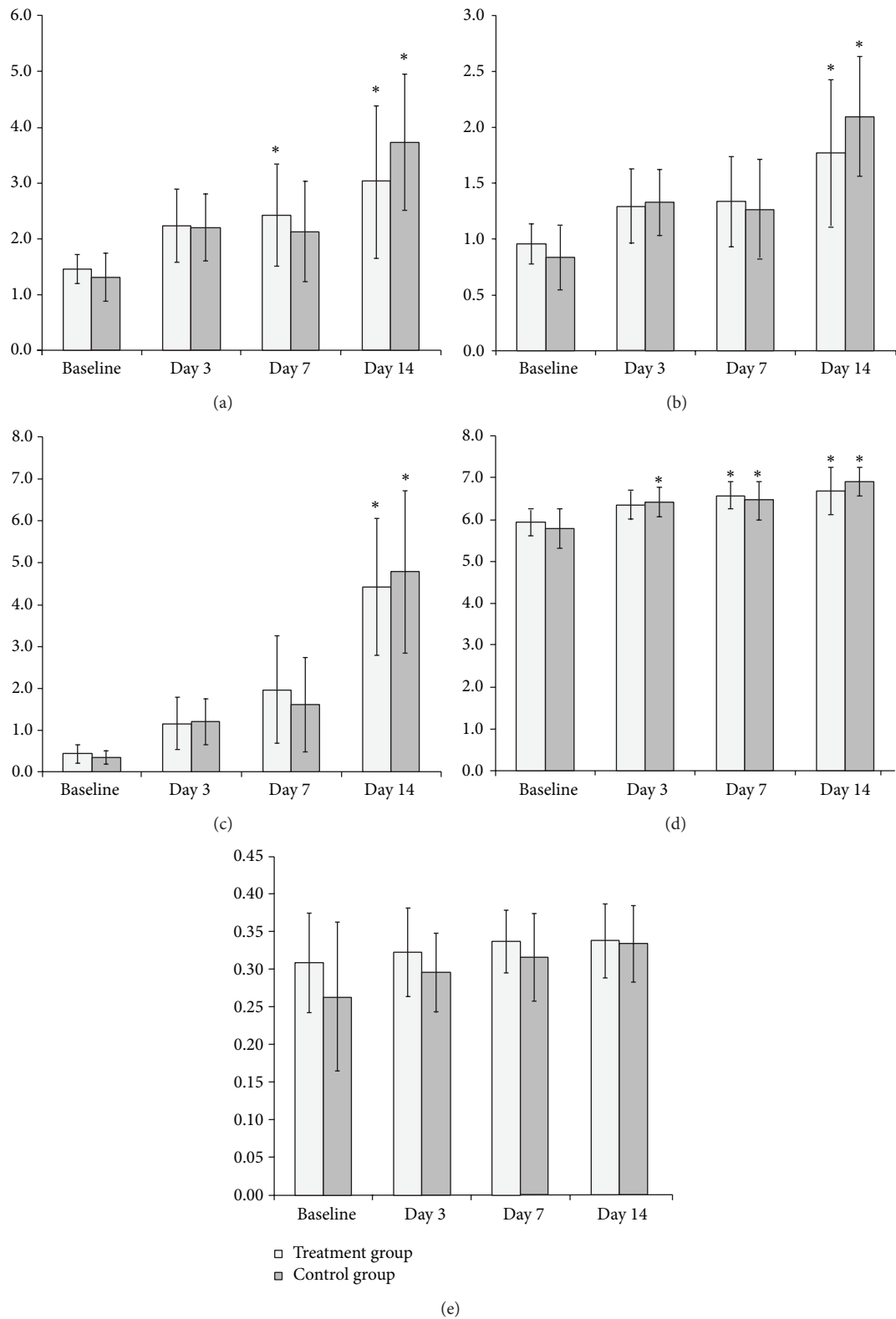


FIGURE 3: Averaged (a) SUVmax, (b) SUVmean, (c) TLG, (d) entropy, and (e) homogeneity before and at different time points after bevacizumab therapy. SUVmax, SUVmean, TLG, and entropy showed an increasing trend in both groups. * is significant change compared to the baseline, SUV is standardized uptake value, TLG is total lesion glycolysis, and FMR is flow-metabolic ratio.

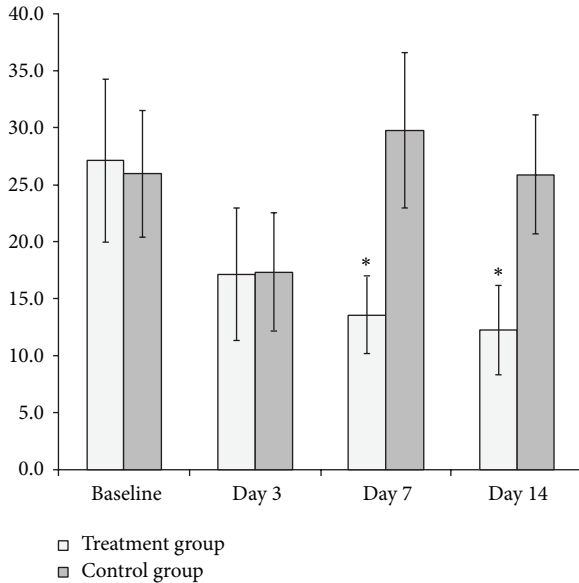
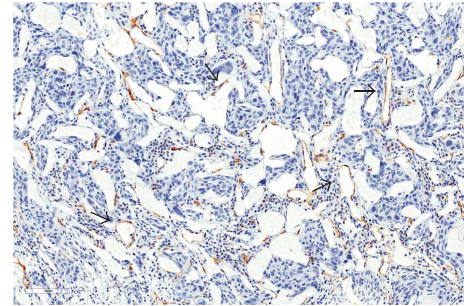


FIGURE 4: Averaged flow-metabolic ratio (FMR) before and at different time points after bevacizumab therapy. FMR showed a distinct decreasing trend in the treatment group whereas no significant change was identified in the control group. In particular, FMR on day 7 and day 14 significantly decreased compared with baseline.

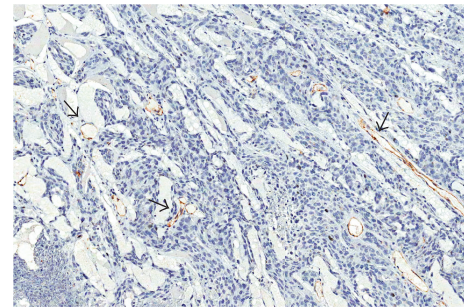
the values of the treatment group were slightly lower than in the control group. As the tumors became larger, SUVmax and SUVmean became significantly higher regardless of antiangiogenic treatment. This is comparable to the results of Miles et al.'s study [33] in which greater FDG uptake of non-small cell lung cancer (NSCLC) was linked to larger tumors and to Willett et al.'s study [4] using perfusion CT and FDG-PET reporting significant falls in perfusion but no change in glucose metabolism after bevacizumab treatment.

Recently, metabolic-volumetric variables and texture analysis have been introduced as new emerging parameters for PET/CT therapy monitoring. As SUVmax reflects the metabolic activity of the most aggressive cells and lacks prognostic significance, TLG has been suggested as a quantitative parameter for FDG-PET [34]. Indeed, a few works showed that TLG can be significant prognostic factors in various tumors [35]. However, in this study, although the tumor volume (TV) was meticulously acquired using manual delineation on coregistered perfusion CT and PET images, we could not find any statistically significant differences in TLG between the treatment and control groups. Similar with SUVmax and SUVmean, the TLG of both groups demonstrated significant sequential increase after initiation of bevacizumab. Considering that bevacizumab is not only a cytostatic agent but that SUVmax or SUVmean are dependent on tumor size, no significant differences in tumor volume and TLG between the treatment and control groups may be an appropriate result.

In addition to quantitative analysis of FDG-PET, characterization of tumor FDG distribution has been introduced as a useful resource in predicting therapeutic response.



(a)



(b)

FIGURE 5: Representative microvessel density (MVD) of (a) control and (b) treatment groups: immunostaining with CD31 antibody highlights vessels (arrows). Intratumoral MVD of the right tumor of the rabbit number 5 (control group) is 26.25 and the left tumor of the rabbit number 2 is 9.25 (original magnification, $\times 200$).

Intratumor FDG activity distribution may be assessed in a global, regional, or local fashion, allowing the assessment of corresponding global, regional, or local patterns of biologic heterogeneity [20]. Among the variable texture parameters, the valuation of local homogeneity and entropy may provide the best outcomes for characterization of local nonuniformities. In this study, however, changes in local homogeneity of the treatment group over time were minimal in both groups and the difference between the two groups was also diminutive. On the other hand, local entropy showed an increasing trend over time in both groups although the difference between the two groups was also minimal, consistent with the results of SUV and TLG.

One of our more interesting observations was that FMR had significantly decreased since bevacizumab initiation despite the fact that there was a considerable increase in SUVmax with no significant change in BF over time; FMRs on day 7 and day 14 were significantly lower, compared with baseline values. Similar observation has been reported for the antiangiogenic agent endostatin on various advanced cancers where high doses of endostatin resulted in decreased tumor perfusion but increased glucose metabolism [36]. Furthermore, in the control group, FMR did not demonstrate a noticeable change over time. This suggests that there may be a mismatch of flow and metabolism following antiangiogenic therapy, possibly indicating drug-induced hypoxia and subsequent stimulation of glucose metabolism. Although a significant decrease in FMR and BV was observed

after bevacizumab therapy, FMR showed considerably higher changes and a greater tendency to decrease compared to the changes in BV. We were also able to identify a significant positive correlation between FMR and MVD in the treatment group. Given that MVD reflects tumor angiogenesis, the degree of change in FMR may potentially indicate the degree of the antiangiogenic effect. Ultimately, FMR may provide further biologic insights into early antiangiogenic effects reflecting the mismatch between intratumor blood flow and metabolism.

Our results support the view of Miles et al.'s study in which they posit that imaging tumor blood flow and metabolism has potential applications for the noninvasive characterization of tumor aggression, allowing novel subclassification of response with opportunities for personalized cancer care [11].

There are still controversial results concerning the relationship between perfusion and glucose metabolism in the literature that can be classified as showing positive, showing negative, and showing no correlation [37]. In our study, we found no correlation between the perfusion and metabolic parameters nor among metabolic-volumetric and texture parameters. Furthermore, we also found no correlation between MVD and FDG uptake-derived parameters.

Our study has several limitations. First, subcutaneous tumor models may not accurately reflect that of real patients in the clinical setting. Secondly, our study included only a small number of tumors, and thus further studies with larger groups of patients are warranted to support our results.

5. Conclusions

The predictive value of FDG-PET was shown to be limited in monitoring the early effect of bevacizumab despite applying texture analysis and volumetric assessment. However, we found that FMR showed a significant sequential decrease over time after bevacizumab therapy which positively correlated with MVD. Thus, our study proposes a potential role of FMR in monitoring the early response to antiangiogenic therapy which will need to be confirmed from larger clinical studies in the near future.

Conflict of Interests

The authors declare that there is no conflict of interests regarding the publication of this paper.

Acknowledgments

This research was supported by National Strategic Coordinating Center for Clinical Research (H110V-0080-010013) of Korea and SNUH Research Fund (Grant no. 0520120010, 2012-1356).

References

- [1] K. Hori, S. Saito, Y. Sato et al., "Differential relationship between changes in tumour size and microcirculatory functions induced by therapy with an antivascular drug and with cytotoxic drugs: implications for the evaluation of therapeutic efficacy of AC7700 (AVE8062)," *European Journal of Cancer*, vol. 39, no. 13, pp. 1957–1966, 2003.
- [2] V. N. Harry, S. I. Semple, D. E. Parkin, and F. J. Gilbert, "Use of new imaging techniques to predict tumour response to therapy," *The Lancet Oncology*, vol. 11, no. 1, pp. 92–102, 2010.
- [3] T. Jiang, A. Kambadakone, N. M. Kulkarni, A. X. Zhu, and D. V. Sahani, "Monitoring response to antiangiogenic treatment and predicting outcomes in advanced hepatocellular carcinoma using image biomarkers, ct perfusion, tumor density, and tumor size (RECIST)," *Investigative Radiology*, vol. 47, no. 1, pp. 11–17, 2012.
- [4] C. G. Willett, Y. Boucher, E. di Tomaso et al., "Direct evidence that the VEGF-specific antibody bevacizumab has antivasular effects in human rectal cancer," *Nature Medicine*, vol. 10, no. 2, pp. 145–147, 2004.
- [5] M. I. Koukourakis, I. Mavanis, G. Kouklakis et al., "Early antivasular effects of bevacizumab anti-VEGF monoclonal antibody on colorectal carcinomas assessed with functional CT imaging," *The American Journal of Clinical Oncology*, vol. 30, no. 3, pp. 315–318, 2007.
- [6] C. S. Ng, C. Charnsangavej, W. Wei, and J. C. Yao, "Perfusion CT findings in patients with metastatic carcinoid tumors undergoing bevacizumab and interferon therapy," *The American Journal of Roentgenology*, vol. 196, no. 3, pp. 569–576, 2011.
- [7] A. X. Zhu, N. S. Holalkere, A. Muzikansky, K. Horgan, and D. V. Sahani, "Early antiangiogenic activity of bevacizumab evaluated by computed tomography perfusion scan in patients with advanced hepatocellular carcinoma," *Oncologist*, vol. 13, no. 2, pp. 120–125, 2008.
- [8] A. Vidiri, A. Pace, A. Fabi et al., "Early perfusion changes in patients with recurrent high-grade brain tumor treated with Bevacizumab: preliminary results by a quantitative evaluation," *Journal of Experimental and Clinical Cancer Research*, vol. 31, no. 1, article 33, 2012.
- [9] R. G. Figueiras, A. R. Padhani, V. J. Goh et al., "Novel oncologic drugs: what they do and how they affect images," *Radiographics*, vol. 31, no. 7, pp. 2059–2091, 2011.
- [10] K. B. Contractor and E. O. Aboagye, "Monitoring predominantly cytostatic treatment response with ¹⁸F-FDG PET," *Journal of Nuclear Medicine*, vol. 50, supplement 1, pp. 97S–105S, 2009.
- [11] K. A. Miles and R. E. Williams, "Warburg revisited: imaging tumour blood flow and metabolism," *Cancer Imaging*, vol. 8, no. 1, pp. 81–86, 2008.
- [12] S. H. Choi, J. W. Chung, H.-C. Kim et al., "The role of perfusion CT as a follow-up modality after transcatheter arterial chemoembolization: an experimental study in a rabbit model," *Investigative Radiology*, vol. 45, no. 7, pp. 427–436, 2010.
- [13] H. S. Park, J. W. Chung, H. J. Jae, and et al., "FDG-PET for evaluating the antitumor effect of intraarterial 3-bromopyruvate administration in a rabbit VX2 liver tumor model," *Korean Journal of Radiology*, vol. 8, no. 3, pp. 216–224, 2007.
- [14] C. Sun, C. Liu, X.-M. Wang, J. Chen, D. Wang, and R. Merges, "Functional CT in a rabbit model: evaluation of the perfusion characteristics before and after Ar-He cryoablation therapy," *Journal of Medical Imaging and Radiation Oncology*, vol. 52, no. 4, pp. 351–357, 2008.
- [15] K. A. Miles, "Measurement of tissue perfusion by dynamic computed tomography," *British Journal of Radiology*, vol. 64, no. 761, pp. 409–412, 1991.

- [16] C. S. Patlak, R. G. Blasberg, and J. D. Fenstermacher, "Graphical evaluation of blood-to-brain transfer constants from multiple-time uptake data," *Journal of Cerebral Blood Flow and Metabolism*, vol. 3, no. 1, pp. 1–7, 1983.
- [17] M. Soussan, F. Orlhac, M. Boubaya et al., "Relationship between tumor heterogeneity measured on FDG-PET/CT and pathological prognostic factors in invasive breast cancer," *PLoS ONE*, vol. 9, no. 4, Article ID e94017, 2014.
- [18] R. M. Haralick, K. Shanmugam, and I. H. Dinstein, "Textural features for image classification," *IEEE Transactions on Systems, Man and Cybernetics*, vol. 3, no. 6, pp. 610–621, 1973.
- [19] M. Amadasun and R. King, "Textural features corresponding to textural properties," *IEEE Transactions on Systems, Man and Cybernetics*, vol. 19, no. 5, pp. 1264–1274, 1989.
- [20] F. Tixier, C. C. le Rest, M. Hatt et al., "Intratumor heterogeneity characterized by textural features on baseline 18F-FDG PET images predicts response to concomitant radiochemotherapy in esophageal cancer," *Journal of Nuclear Medicine*, vol. 52, no. 3, pp. 369–378, 2011.
- [21] V. Goh, A. Engledow, M. Rodriguez-Justo et al., "The flow-metabolic phenotype of primary colorectal cancer: assessment by integrated 18F-FDG PET/perfusion CT with histopathologic correlation," *Journal of Nuclear Medicine*, vol. 53, no. 5, pp. 687–692, 2012.
- [22] Y. H. Kim, M. A. Kim, I.-A. Park et al., "VEGF polymorphisms in early cervical cancer susceptibility, angiogenesis, and survival," *Gynecologic Oncology*, vol. 119, no. 2, pp. 232–236, 2010.
- [23] N. Weidner, "Intratumor microvessel density as a prognostic factor in cancer," *The American Journal of Pathology*, vol. 147, no. 1, pp. 9–19, 1995.
- [24] P. B. Vermeulen, G. Gasparini, S. B. Fox et al., "Second international consensus on the methodology and criteria of evaluation of angiogenesis quantification in solid human tumours," *European Journal of Cancer*, vol. 38, no. 12, pp. 1564–1579, 2002.
- [25] N. Weidner, J. P. Semple, W. R. Welch, and J. Folkman, "Tumor angiogenesis and metastasis—correlation in invasive breast carcinoma," *The New England Journal of Medicine*, vol. 324, no. 1, pp. 1–8, 1991.
- [26] S. Mehta, N. P. Hughes, F. M. Buffa et al., "Assessing early therapeutic response to bevacizumab in primary breast cancer using magnetic resonance imaging and gene expression profiles," *Journal of the National Cancer Institute—Monographs*, no. 43, pp. 71–74, 2011.
- [27] A. Sabir, R. Schor-Bardach, C. J. Wilcox et al., "Perfusion MDCT enables early detection of therapeutic response to antiangiogenic therapy," *The American Journal of Roentgenology*, vol. 191, no. 1, pp. 133–139, 2008.
- [28] J. H. Tai, J. Tessier, A. J. Ryan, L. Hoffman, X. Chen, and T.-Y. Lee, "Assessment of acute antivasular effects of vandetanib with high-resolution dynamic contrast-enhanced computed tomographic imaging in a human colon tumor xenograft model in the nude rat," *Neoplasia*, vol. 12, no. 9, pp. 697–707, 2010.
- [29] L. S. Fournier, S. Oudard, R. Thiam et al., "Metastatic renal carcinoma: evaluation of antiangiogenic therapy with dynamic contrast-enhanced CT," *Radiology*, vol. 256, no. 2, pp. 511–518, 2010.
- [30] R. M. Stephen and R. J. Gillies, "Promise and progress for functional and molecular imaging of response to targeted therapies," *Pharmaceutical Research*, vol. 24, no. 6, pp. 1172–1185, 2007.
- [31] R. García-Figueiras, V. J. Goh, A. R. Padhani et al., "CT perfusion in oncologic imaging: a useful tool?" *The American Journal of Roentgenology*, vol. 200, no. 1, pp. 8–19, 2013.
- [32] K. A. Miles, T.-Y. Lee, V. Goh et al., "Current status and guidelines for the assessment of tumour vascular support with dynamic contrast-enhanced computed tomography," *European Radiology*, vol. 22, no. 7, pp. 1430–1441, 2012.
- [33] K. A. Miles, M. R. Griffiths, and C. J. Keith, "Blood flow-metabolic relationships are dependent on tumour size in non-small cell lung cancer: a study using quantitative contrast-enhanced computer tomography and positron emission tomography," *European Journal of Nuclear Medicine and Molecular Imaging*, vol. 33, no. 1, pp. 22–28, 2006.
- [34] S. M. Larson, Y. Erdi, T. Akhurst et al., "Tumor treatment response based on visual and quantitative changes in global tumor glycolysis using PET-FDG imaging: the visual response score and the change in total lesion glycolysis," *Clinical Positron Imaging*, vol. 2, no. 3, pp. 159–171, 1999.
- [35] G. Tomasi and L. Rosso, "PET imaging: implications for the future of therapy monitoring with PET/CT in oncology," *Current Opinion in Pharmacology*, vol. 12, no. 5, pp. 569–575, 2012.
- [36] R. S. Herbst, N. A. Mullani, D. W. Davis et al., "Development of biologic markers of response and assessment of antiangiogenic activity in a clinical trial of human recombinant endostatin," *Journal of Clinical Oncology*, vol. 20, no. 18, pp. 3804–3814, 2002.
- [37] A. W. Sauter, D. Spira, M. Schulze et al., "Correlation between [¹⁸F]FDG PET/CT and volume perfusion CT in primary tumours and mediastinal lymph nodes of non-small-cell lung cancer," *European Journal of Nuclear Medicine and Molecular Imaging*, vol. 40, no. 5, pp. 677–684, 2013.

Review Article

Radiolabeled Apoptosis Imaging Agents for Early Detection of Response to Therapy

Kazuma Ogawa and Miho Aoki

Division of Pharmaceutical Sciences, Graduate School of Medical Sciences, Kanazawa University, Kakuma-machi, Kanazawa 920-1192, Japan

Correspondence should be addressed to Kazuma Ogawa; kogawa@p.kanazawa-u.ac.jp

Received 25 June 2014; Revised 11 August 2014; Accepted 12 August 2014; Published 14 October 2014

Academic Editor: Masahiro Ono

Copyright © 2014 K. Ogawa and M. Aoki. This is an open access article distributed under the Creative Commons Attribution License, which permits unrestricted use, distribution, and reproduction in any medium, provided the original work is properly cited.

Since apoptosis plays an important role in maintaining homeostasis and is associated with responses to therapy, molecular imaging of apoptotic cells could be useful for early detection of therapeutic effects, particularly in oncology. Radiolabeled annexin V compounds are the hallmark in apoptosis imaging *in vivo*. These compounds are reviewed from the genesis of apoptosis (cell death) imaging agents up to recent years. They have some disadvantages, including slow clearance and immunogenicity, because they are protein-based imaging agents. For this reason, several studies have been conducted in recent years to develop low molecule apoptosis imaging agents. In this review, radiolabeled phosphatidylserine targeted peptides, radiolabeled bis(zinc(II)-dipicolylamine) complex, radiolabeled 5-fluoropentyl-2-methyl-malonic acid (ML-10), caspase-3 activity imaging agents, radiolabeled duramycin, and radiolabeled phosphonium cation are reviewed as promising low-molecular-weight apoptosis imaging agents.

1. Introduction

Apoptosis is known to play an important role in maintaining homeostasis; therefore, it is associated with several diseases and responses to therapy. Molecular imaging of apoptotic cells could be useful for elucidation of the diseases and early detection of therapeutic effects and could contribute to personalized medicine. In this review, we introduce radiolabeled compounds for molecular imaging of apoptosis (cell death), their applications, and utility in medicine.

2. Radiolabeled Annexin V

The lipid composition of the outer and inner leaflets of the plasma membrane is not symmetrical. Phosphatidylserine (PS) is normally retained on the intracellular face of the cell membrane. When cells undergo apoptosis, this distribution is altered, so that PS is rapidly exposed to the outside of the cell membrane. In fact, not only apoptosis but also some other forms of cell death including autophagy can externalize PS [1, 2]. Moreover, in the final stage of almost all forms

of cell death, PS on the intracellular face of the plasma membrane become accessible to PS-targeting probes in a nonspecific fashion, because of complete loss of membrane integrity. Thus, PS-targeted radiolabeled probes must not be considered specific apoptosis imaging agents, but they may be used to detect multiple forms of cell death.

In this paper, we have used the phrase “apoptosis imaging” for PS-targeted radiolabeled probes. However, to be accurate, it is “cell death imaging” and not “apoptosis imaging.” The typical compound of PS targeted carriers is annexin V, a 36 kDa human protein with a nanomolar affinity for membrane-bound PS [3–5]. Because of this property, radiolabeled annexin V compounds have been developed and evaluated as *in vivo* imaging agents for detection of cell death.

3. ^{99m}Tc -4,5-bis(thioacetamido)pentanoyl-Annexin V (^{99m}Tc -BTAP-Annexin V)

^{99m}Tc is an ideal radionuclide for scintigraphic imaging applications because of its excellent physical properties,

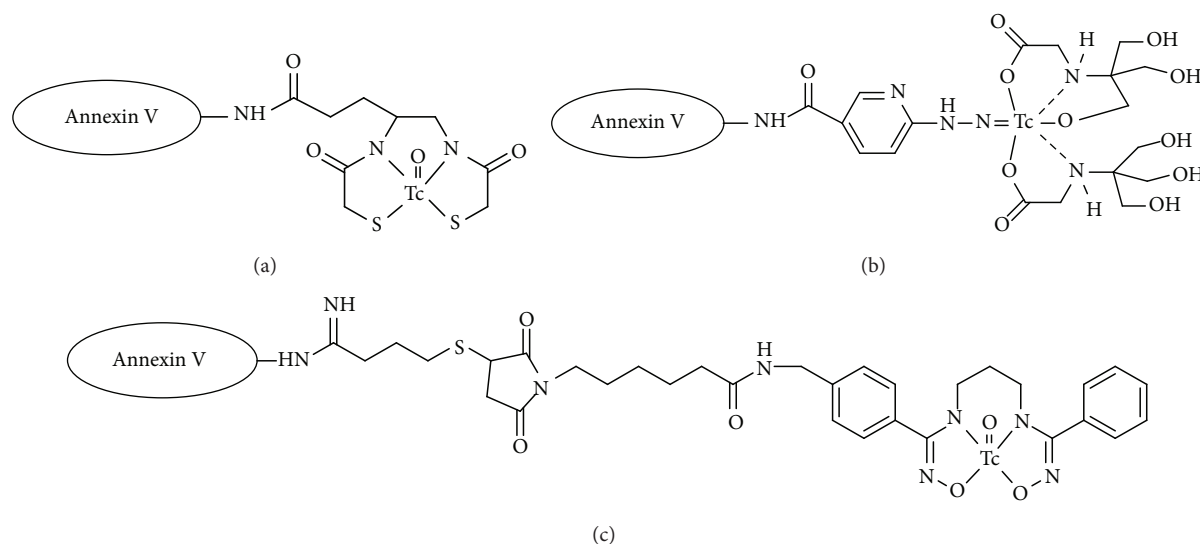


FIGURE 1: Structures of (a) ^{99m}Tc -BTAP-annexin V, (b) ^{99m}Tc -HYNIC-annexin V, and (c) ^{99m}Tc -C₃(BHam)₂-annexin V.

low cost, and ready availability as a generator-produced nuclide. Since most polypeptides do not possess binding sites allowing them to form ^{99m}Tc chelates with high *in vivo* stability, appropriate chelating molecules are incorporated into polypeptide molecules to prepare ^{99m}Tc -labeled peptides for *in vivo* applications. Tetradentate ligands, such as N₃S and N₂S₂ coordination molecules, form stable ^{99m}Tc complexes with the [Tc=O]³⁺ core. In the field of apoptosis imaging, ^{99m}Tc -4,5-bis(thioacetamido)pentanoyl(BTAP)-annexin V (Figure 1(a)) was developed as the first ^{99m}Tc -labeled annexin V compound, which is a ^{99m}Tc complex with N₂S₂ ligand-conjugated annexin V, after development of iodine-labeled annexin V. The first report of ^{99m}Tc -BTAP-annexin V use was in thrombosis imaging and not for apoptosis imaging. In that paper, Stratton et al. reported that ^{99m}Tc -BTAP-annexin V detected acute left atrial thrombi *in vivo* in swine because PS becomes exposed on the surface of activated platelets [6]. Narula et al. reported that ^{99m}Tc -BTAP-annexin V was injected into cardiac allograft recipients. Some patients who showed at least moderate transplant rejection had positive myocardial uptake of radioactivity. This study showed the clinical feasibility of ^{99m}Tc -labeled annexin V imaging for the noninvasive detection of apoptosis [7]. However, N₂S₂ ligands may require harsh conditions such as high pH or high temperature to prepare ^{99m}Tc complexes with high radiochemical yields. Accordingly, ^{99m}Tc labeling of annexin V with a N₂S₂ ligand was performed using a preformed-chelate approach. The conjugation between annexin V and ^{99m}Tc complex must be performed after the complexation reaction of ^{99m}Tc . This method requires multiple steps and purification, resulting in a 25%–30% overall radiochemical yield. For routine clinical use, ^{99m}Tc labeling of annexin V, which can be prepared by an easier labeling operation, is required.

4. ^{99m}Tc -HYNIC-Annexin V

Blankenberg et al. reported the use of ^{99m}Tc -labeled annexin V, which has hydrazinonicotinamide (HYNIC) as a ligand for technetium, for apoptosis imaging [8]. HYNIC is one of the most attractive bifunctional chelating agents for the labeling of peptides and proteins with ^{99m}Tc . It has been reported that HYNIC acts as a monodentate or bidentate ligand to form a mixed ligand ^{99m}Tc complex in the presence of appropriate coligands [9]. Tricine has been frequently used as a coligand since it provides ^{99m}Tc -HYNIC-labeled peptides and proteins with high radiochemical yields and high specific activities in a short reaction time at room temperature. ^{99m}Tc -HYNIC-annexin V (Figure 1(b)) could be prepared in high radiochemical yield without any purification after a one-step reaction. In cultures of Jurkat T-cell lymphoblasts induced to undergo apoptosis, the uptake of ^{99m}Tc -HYNIC-annexin V directly correlated with the percentage of cells labeled by FITC-labeled annexin V, which has an affinity for PS nearly identical to that of the native (unlabeled) protein, as determined by flow cytometry ($r^2 = 0.922$) [10]. In another study, the bioactivity of HYNIC-annexin V was verified by measuring its binding to erythrocyte membranes containing exposed PS. The affinity of HYNIC-annexin V was comparable with that of native annexin V. The IC₅₀ values, which were determined using a competition assay, were 10.1 ± 2.0 nmol/L and 6.8 ± 0.7 nmol/L, respectively [11]. Moreover, many studies have demonstrated that ^{99m}Tc -HYNIC-annexin V accumulates in apoptotic cells and can be used to visualize apoptosis in animal models [12–15]. ^{99m}Tc -HYNIC-annexin V can be considered as a benchmark in the field of apoptosis imaging, as the easy labeling method has made this tracer the most extensively investigated and the best characterized apoptosis-detecting radioligand [16].

5. Clinical Studies of ^{99m}Tc -Labeled Annexin V in Oncology

For evaluation of the response to cancer therapy, ^{99m}Tc -HYNIC-annexin V imaging should be performed before and after the starting point of treatment. In a clinical study reported by Kartachova et al. in 2007, ^{99m}Tc -HYNIC-annexin V imaging in 16 non-small-cell lung cancer patients was performed before and within 48 hours after the initiation of platinum-based chemotherapy [17]. All patients, displaying imaging data confirming markedly increased uptake of annexin V in tumor, showed complete or partial response. A significant correlation ($r^2 = 0.86$; $P = 0.0001$) was found between the changes of annexin V uptake in tumor and the treatment outcome.

In another clinical study reported by Rottey et al. in 2006, changes in relative ^{99m}Tc -HYNIC-annexin V tumor uptake in patients undergoing chemotherapy at baseline and at 5–7 and 40–44 hours after treatment initiation were investigated [18]. The tumor response was evaluated by response evaluation criteria in solid tumors (RECIST) and related to observed changes in the ratios of tumor activity to background activity. Responders to chemotherapy could be separated from nonresponders with a 94% accuracy (16/17 patients) by use of the sequential ^{99m}Tc -HYNIC-annexin V imaging and a 25% change threshold.

Although these studies indicated that ^{99m}Tc -HYNIC-annexin V could be a good predictor of the response to cancer therapy, the numbers of patients in these studies were small. Furthermore, further larger studies are necessary to confirm the utility of ^{99m}Tc -HYNIC-annexin V for the prediction of therapeutic effects in early stages after chemotherapy initiation.

6. Other ^{99m}Tc -Labeled Annexin V Compounds

Tait et al. reported the use of ^{99m}Tc -labeled annexin V with site-specific labeling in 2000 [11]. In this study, annexin V derivatives, containing N-terminal extensions of seven amino acids for complexation with technetium, were produced by expression in *E. coli* ($\text{NH}_2\text{Ala-Cys-Gly-Gly-Gly-His-Met-annexin V}$, $\text{NH}_2\text{Ala-Gly-Gly-Cys-Gly-His-Met-annexin V}$, and $\text{NH}_2\text{Ala-Cys-Gly-Cys-Gly-His-Met-annexin V}$). One derivative is predicted to form N_2S_2 chelation site, and two are predicted to form N_3S site. The bioactivities of the mutant proteins were verified by measuring binding activity to erythrocyte membranes with exposed PS. The mutant proteins also had the same degree of IC_{50} values (9.3 ± 0.4 , 10.3 ± 2.5 , and 10.0 ± 2.8 nmol/L), which were determined for unlabeled proteins by competition assay, as HYNIC-annexin V (10.1 ± 2.0 nmol/L). The radiochemical yields of the mutant proteins with ^{99m}Tc were approximately 90%.

Tait et al. reported another annexin V mutant-labeled with a Tc(I)-carbonyl complex in 2002 [19]. They prepared annexin V mutants with N-terminal extensions of three or six histidine residues for labeling with a Tc(I)-tricarboxyl core. Annexin V-123, which has an N-terminal extension of six histidine residues, could be superior to annexin V-122, which has

three histidine residues, because ^{99m}Tc -labeled annexin V-123 had higher radiochemical yield and radiochemical purity and experimentally demonstrated bioactivity in binding to erythrocytes.

We recently developed a novel ^{99m}Tc -labeled annexin V, $^{99m}\text{Tc-C}_3(\text{BHam})_2$ -annexin V (Figure 1(c)), using a bis(hydroxamamide) derivative [$\text{C}_3(\text{BHam})_2$] as a bifunctional chelating agent to decrease uptake and retention in nontarget tissues compared with ^{99m}Tc -HYNIC-annexin V [20]. In biodistribution experiments in normal mice, $^{99m}\text{Tc-C}_3(\text{BHam})_2$ -annexin V showed a much lower kidney accumulation of radioactivity than ^{99m}Tc -HYNIC-annexin V. In the organs for metabolism, such as liver and kidney, radioactivity after the injection of ^{99m}Tc -HYNIC-annexin V was residual for a long time. On the other hand, radioactivity after the injection of $^{99m}\text{Tc-C}_3(\text{BHam})_2$ -annexin V gradually decreased. In experiments using tumor bearing mice, $^{99m}\text{Tc-C}_3(\text{BHam})_2$ -annexin V showed significantly increased tumor uptake after 5-FU treatment. The accumulation of radioactivity in tumor correlated positively with the counts of TUNEL-positive cells.

7. ^{18}F -Labeled Annexin V

Apoptosis imaging probes for positron emission tomography (PET) are required because PET imaging has high spatial resolution and great sensitivity, and ^{18}F -labeled annexin V has been developed. In 2003, Zijlstra et al. reported the preparation of ^{18}F -labeled annexin V using N-succinimidyl 4- ^{18}F fluorobenzoate (^{18}F SFB) as a labeling reagent [21]. The decay-corrected radiochemical yield was in the range of 15–20%. The ^{18}F -labeled annexin V highly bound to apoptotic Jurkat T-cells, compared with nonapoptotic control cells. In 2004, Toretzky et al. also reported ^{18}F -labeled-annexin V via ^{18}F SFB [22]. The overall decay-corrected radiochemical yield of ^{18}F -labeled annexin V from $^{18}\text{F}^-$ was comparable ($17.6\% \pm 5.6\%$). In addition, Murakami et al. also reported ^{18}F -labeled annexin V by a similar procedure in the same year [23]. In that study, accumulation of ^{18}F -labeled annexin V in the infarct area using a rat model of myocardial ischemia and reperfusion was comparable to that of ^{99m}Tc -labeled-annexin V with site-specific labeling [11]. However, the complicated radiosynthesis procedure and the low radiochemical yield of ^{18}F -labeling (especially, in this study, approximately 10%, decay-corrected form [^{18}F]SFB) were weak points for clinical use.

8. ^{68}Ga -Labeled Annexin V

The radionuclide ^{68}Ga has great potential for clinical PET and could become an attractive alternative to ^{18}F because of its radiophysical properties, particularly as a generator-produced nuclide with a half-life ($T_{1/2}$) of 68 minutes [24]. It does not require an on-site cyclotron and can be eluted on demand. In principle, the long half-life of the parent nuclide ^{68}Ge ($T_{1/2} = 270.8$ days) provides a generator with a long

life span. Wangler et al. reported a ^{68}Ga -labeling technique for proteins using a sulfhydryl-derivatized chelator, 2,2'-(7-(1-carboxy-4-(2-mercaptoethylamino)-4-oxobutyl)-1,4,7-triazonane-1,4-diyl)diacetic acid (NODA-GA-T) in 2011 [25]. In that study, ^{68}Ga -labeled annexin V was prepared within a short time of only 15 minutes. In a PET study with an animal model, the ^{68}Ga -labeled annexin V accumulated in the apoptotic area by the myocardial infarction.

In the same year, Bauwens et al. reported site-specific ^{68}Ga -labeled annexin V compounds, ^{68}Ga -Dotamaleimide-conjugated Cys2-annexin V and ^{68}Ga -Dotamaleimide-conjugated Cys165-annexin V [26]. Cys2-annexin V and Cys165-annexin V are variants of annexin V containing a single available cysteine residue at respective positions 2 and 165. Total synthesis time was approximately 55 minutes with an end-of-synthesis yield of 25% (43% if decay-corrected) in both cases. Both compounds showed well-preserved PS binding capacity and high *in vitro* stability in buffer and in plasma. Tumor uptake of ^{68}Ga -Cys2-annexin V and ^{68}Ga -Cys165-annexin V was low but significantly increased after cyclophosphamide and radiation therapy in a tumor model.

9. Radiolabeled PS Targeted Peptides

Annexin V is best known in the field of apoptosis imaging as a carrier because it has high affinity for PS and that radiolabeled annexin V compounds have been extensively investigated and well characterized. However, the use of annexin V, a protein, imposes limitations, such as slow pharmacokinetics and potential immunogenicity. In contrast to protein-based radioligands like radiolabeled annexin V, for low-molecular-weight compounds, it is not difficult to modify chemical structures to improve their biodistribution. Accordingly, several studies have been performed in recent years to develop low-molecular-weight apoptosis imaging agents.

In 1995, Igarashi et al. reported a 14-amino acid synthetic peptide, FNFRLKAGQKIRFG (PSBP-0), derived from PS decarboxylase bound to PS effectively and specifically [27]. However, the binding affinity of PSBP-0 was not very high.

In 2011, Xiong et al. modified PSBP-0 to develop peptides with higher affinity for PS [28]. Each of the 14 residues of PSBP-0, except the endogenous alanine residue at position 8 (Ala⁸), was initially replaced with Ala to identify amino acid residues that contribute to PS affinity. The variant PSBP-6, in which Gln⁶ is replaced by Ala, showed the highest relative binding level and high stability. The binding levels of PSBP-6 were higher than those of PSBP-0. The remaining Ala-substituted peptides had lower affinity for PS than the parent PSBP-0 peptide. Next, Lys[di(2-pyridinemethyl)]-COOH, termed a single amino acid chelator (SAAC), was introduced at specific positions of PSBP-0 and PSBP-6 as a ligand for complexation with technetium. The peptide containing SAAC introduced at the N-terminus of PSBP-6 (SAAC-PSBP-6, Figure 2(a)) showed greater binding to PS than PSBP-6. Moreover, the rhenium complex, SAAC(Re)-PSBP-6 (Figure 2(b)), displayed a higher level of binding than

SAAC-PSBP-6. In a biodistribution study, SAAC($^{99\text{m}}\text{Tc}$)-PSBP-6 (Figure 2(b)) showed significantly higher accumulation in B16/F10 melanoma treated with poly(L-glutamic acid)-paclitaxel than in untreated tumor ($4.1 \pm 0.6\%$ ID/g versus $1.6 \pm 0.3\%$ ID/g).

In 2013, Song et al. compared SAAC($^{99\text{m}}\text{Tc}$)-PSBP-6 with [^{18}F]FDG for detecting apoptosis induced by chemotherapy [29]. In B16/F10 melanoma and 38Cl3 lymphoma tumor models, the uptake of SAAC($^{99\text{m}}\text{Tc}$)-PSBP-6 significantly increased on the first day after treatment, whereas [^{18}F]FDG uptake significantly decreased. The uptake of SAAC($^{99\text{m}}\text{Tc}$)-PSBP-6 negatively correlated with that of [^{18}F]FDG ($r = -0.79$, $P < 0.05$). These results indicated that the SAAC($^{99\text{m}}\text{Tc}$)-PSBP-6 could be a useful probe to evaluate early therapeutic response after chemotherapy.

10. Bis(zinc(II)-dipicolylamine) Complex

Binuclear Zn(II) complexes of 2,2'-dipicolylamine (Zn^{2+} -DPA) are known as an effective binding motif for phosphate anion [30]. Because PS is an anionic phospholipid, Zn^{2+} -DPA has a selective affinity for biomembranes enriched with PS and could have an apoptosis sensing function. In 2011, Wyffels et al. reported $^{99\text{m}}\text{Tc}$ labeled Zn^{2+} -DPA with a $^{99\text{m}}\text{Tc}$ -tricarboxyl core and via $^{99\text{m}}\text{Tc}$ -HYNIC (Figures 3(a) and 3(b)) [31]. Both compounds showed significantly higher uptake in livers of anti-Fas antibody-treated mice compared with that in livers of control mice. The increased liver uptake of $^{99\text{m}}\text{Tc}$ -labeled Zn^{2+} -DPA was comparable to that of $^{99\text{m}}\text{Tc}$ -labeled annexin V, indicating the *in vivo* affinity of $^{99\text{m}}\text{Tc}$ labeled Zn^{2+} -DPA for hepatic apoptosis.

Recently, Wang et al. reported the ^{18}F -labeled Zn^{2+} -DPA compounds, 2- ^{18}F -fluoroethyl-bis(zinc(II)-dipicolylamine) (^{18}F -FEN-DPAZn2) and 4- ^{18}F -fluoro-benzoyl-bis(zinc(II)-dipicolylamine) (^{18}F -FB-DPAZn2) (Figures 3(c) and 3(d)), as apoptosis (cell death) imaging agents [32]. Decay-uncorrected radiochemical yields of the precursors of ^{18}F -FEN-DPAZn2 and ^{18}F -FB-DPAZn2, ^{18}F -FEN-DPA2 and ^{18}F -FB-DPA2, were 8.9% and 13%, respectively. ^{18}F -FEN-DPAZn2 and ^{18}F -FB-DPAZn2 complexes were prepared from ^{18}F -FEN-DPA2 and ^{18}F -FB-DPA2 with $\text{Zn}(\text{NO}_3)_2$. The authors described that the low radiochemical yield of ^{18}F -FEN-DPA2 limited further animal experiments. *In vivo* PET imaging experiments using ^{18}F -FDG, ^{18}F -FB-DPA2, and ^{18}F -FB-DPAZn2 were performed in Hepal-6 hepatocellular carcinoma-bearing mice and adriamycin-treated tumor-bearing mice. ^{18}F -FDG and ^{18}F -FB-DPA2 showed no significant uptake change before and after chemotherapy. These results indicate that ^{18}F -FDG could lack specificity to monitor anticancer therapy and that ^{18}F -FB-DPA2 has no binding affinity to PS without zinc. In contrast, ^{18}F -FB-DPAZn2 showed significantly higher accumulation in adriamycin-treated tumors compared with that in untreated ones. However, the background uptake of ^{18}F -FB-DPAZn2 in liver and intestine was high. Optimization of the chemical

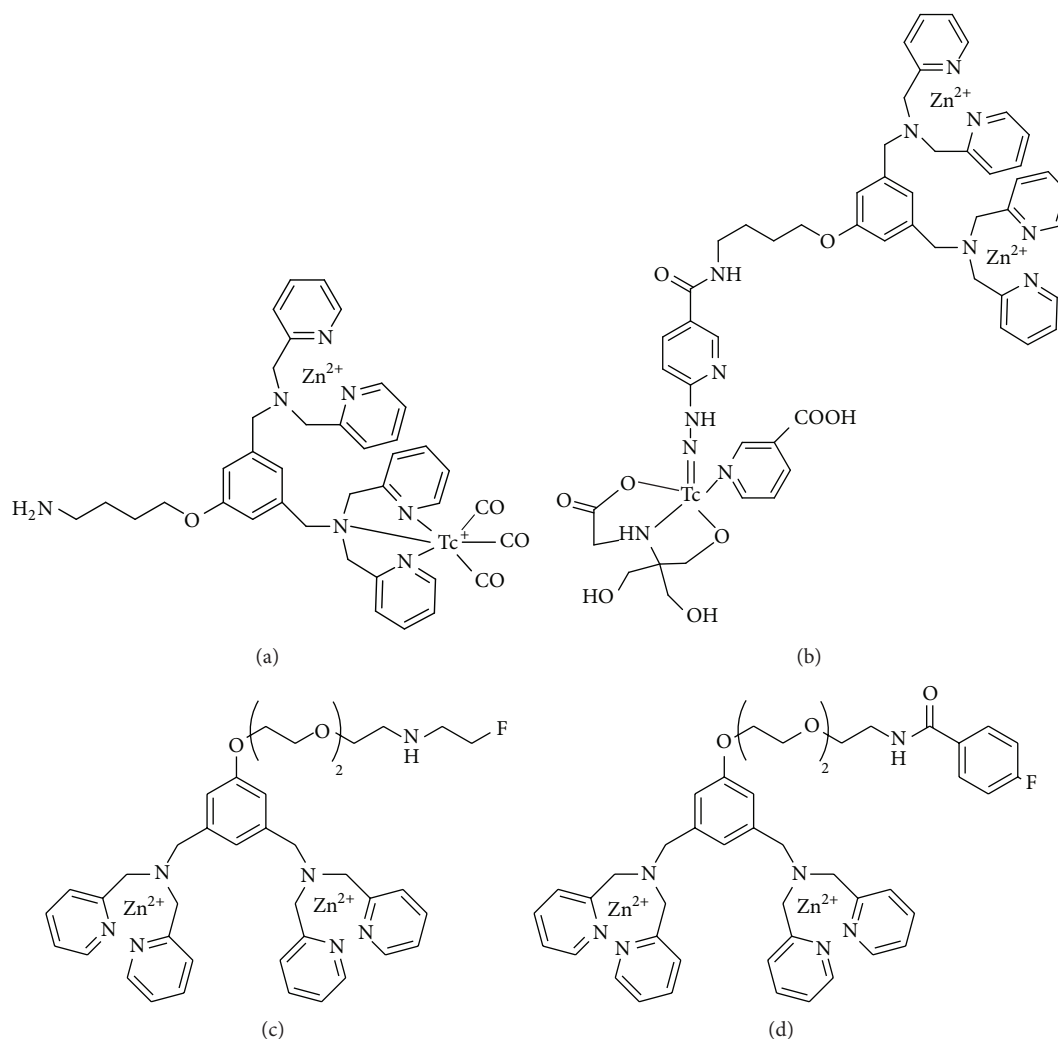


FIGURE 3: Structures of (a) ^{99m}Tc -labeled Zn^{2+} -DPA with ^{99m}Tc -tricarbonyl core, (b) ^{99m}Tc -labeled Zn^{2+} -DPA with ^{99m}Tc -HYNIC, (c) ^{18}F -FEN-DPAZn2, and (d) ^{18}F -FB-DPAZn2.

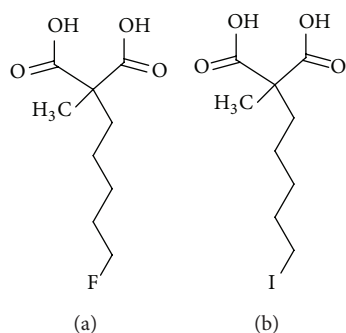


FIGURE 4: Structures of (a) ^{18}F -ML-10 and (b) ^{123}I -ML-10.

that in untreated control cells. ^3H -ML-10 crossed the cell membrane at the stage of early apoptosis and was mainly localized in the cytoplasm (60%) and in the nucleus (30%). Interestingly, ^3H -ML-10 accumulated only in apoptotic cells

and not in either untreated control cells or necrotic cells induced by freeze-thaw injury.

Recently, ^{123}I -labeled ML-10 analog as a single photon emission tomography (SPECT) tracer was reported. [^{123}I]-2-(5-iodopentyl)-2-methylmalonic acid (^{123}I -ML10, Figure 4(b)) was expected to show increased penetration in apoptotic cells because of its greater lipophilicity compared with ^{18}F -ML-10 [38]. ^{123}I -ML10 accumulated in apoptotic cells, but a clear uptake in the thyroid, resulting from *in vivo* deiodination, was observed because of its instability.

12. Caspase-3 Activity Imaging Agents

The caspases are a family of intracellular cysteine aspartate-specific proteases that play an important role in the initiation and execution of apoptosis [39]. Caspases are subdivided into three groups on the basis of homology and substrate specificity: (1) caspases involved in inflammation (caspases 1, 4, 5, and 13); (2) initiator caspases which are found at the top

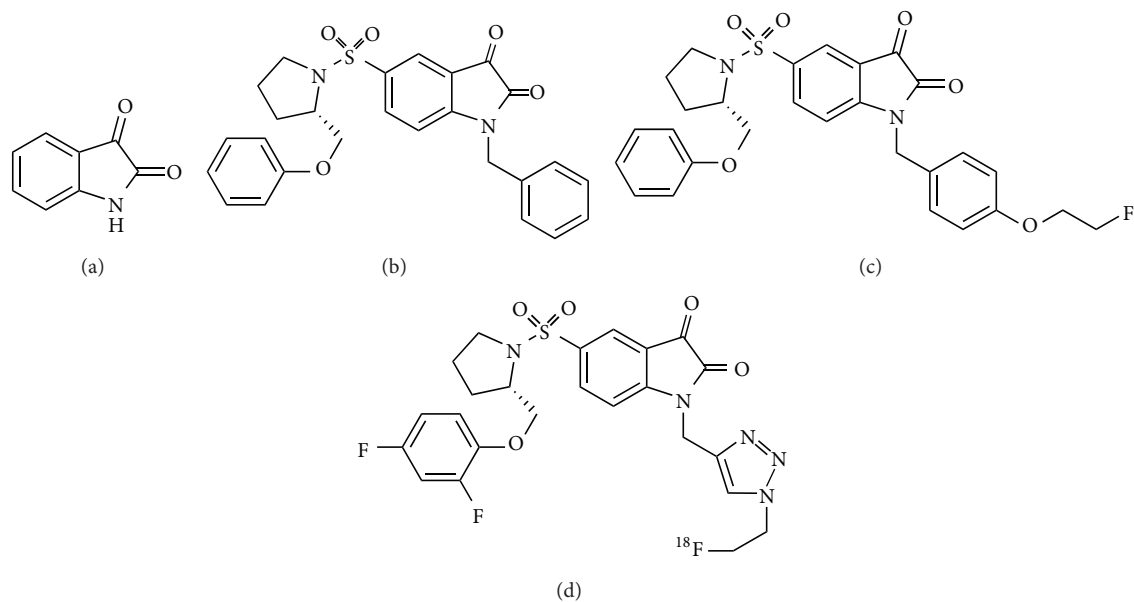


FIGURE 5: Structures of (a) Isatin, (b) (S)-1-benzyl-5-[1-[2-(phenoxy)methyl]pyrrolidinyl]sulfonyl]isatin, (c) WC-II-89, and (d) [^{18}F]ICMT-11.

of the signaling cascade (caspases 6 and 8–10), and (3) effector caspases which are activated further downstream (caspases 2, 3, and 7) [40]. Among these caspases, caspase-3 is a frequently activated death protease, catalyzing the specific cleavage of many key cellular proteins [41]. Thus, caspase-3 should be an attractive biomarker for apoptosis.

In 2001, Lee et al. determined the activity and the selectivity of a series of isatin (Figure 5(a)) analogs for caspase-3 [42]. They found that the substituent at position 5 was important and demonstrated a correlation between the electron-withdrawing ability of the substituent at position 5 and the potency of caspase-3 inhibition. The 5-dialkylaminosulfonylisatins were identified as potent inhibitors of caspases 3 and 7. Within this series, (S)-1-benzyl-5-[1-[2-(phenoxy)methyl]pyrrolidinyl]sulfonyl]isatin (Figure 5(b)) was the most promising and showed very high activity and selectivity for caspases 3 and 7.

In 2006, Zhou et al. synthesized WC-II-89 (Figure 5(c)), an isatin sulfonamide analog containing a fluorine atom that has a structure similar to that of compound 5B [43]. WC-II-89 was a highly potent inhibitor of caspases 3 and 7 and displayed high selectivity with respect to other caspases. [^{18}F]WC-II-89 was prepared via a nucleophilic substitution of the corresponding mesylate precursor with [^{18}F]fluoride ion in high radiochemical yield. In animal experiments, [^{18}F]WC-II-89 showed higher uptake in the liver of a cycloheximide-treated rat, a model for chemically induced apoptosis, compared to the untreated control. Western blot analysis confirmed that the uptake was related to caspase-3 activation.

In 2008, Smith et al. reported the synthesis and characterization of the [^{18}F]labeled isatin analog (S)-1-[[1-(2-fluoroethyl)-1H-[1,2,3]triazol-4-yl]methyl]-5-[2-(2,4-difluorophenoxy)methyl-pyrrolidine-1-sulfonyl]isatin ([^{18}F]ICMT-

11, Figure 5(d)). [^{18}F]ICMT-11 possesses the characteristic of high metabolic stability with no indication of defluorination *in vivo*, reduced lipophilicity, and subnanomolar affinity for caspase-3 [44]. “Click labeling” provided [^{18}F]ICMT-11 in 65% decay-corrected radiochemical yield from 2-[^{18}F]fluoroethylazide.

In 2009, Nguyen et al. reported the results of a detailed *in vitro* study and an animal PET study of [^{18}F]ICMT-11 [45]. *In vitro* binding of [^{18}F]ICMT-11 was increased in drug-treated cells and corresponded to higher cellular activity of caspases 3 and 7. In addition, [^{18}F]ICMT-11 binding did not increase in caspase-3 deficient MCF-7 human breast cancer cells treated with 4-hydroperoxycyclophosphamide (4-HC), compared with a control. In the PET study, the [^{18}F]ICMT-11 signal increased in up to twofold during the first 24 hours after treatment. Other papers have also recently indicated that [^{18}F]ICMT-11 could be useful as a caspase-3 imaging apoptosis tracer [46, 47].

In 2013, Challapalli et al. reported the result of a PET study in healthy human volunteers that revealed the biodistribution and internal dosimetry profiles of [^{18}F]ICMT-11 [48]. [^{18}F]ICMT-11 was shown to be a safe PET tracer with a favorable radiation dosimetry profile for clinical use. Further clinical studies of [^{18}F]ICMT-11 for apoptosis imaging are anticipated.

13. Radiolabeled Duramycin

Phosphatidylethanolamine (PE) is the second most abundant phospholipid and accounts for approximately 20% of all phospholipids in mammalian cellular membranes [49]. Similar to PS, PE is a major component of the inner leaflet of

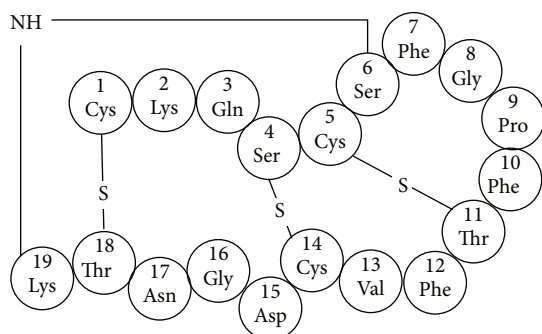


FIGURE 6: Structure of duramycin.

the cell membrane and is rare on the surface of normal viable cells [50]. When apoptosis occurs, PE is exposed onto the cell surface [51]. Thus, PE could also be a target molecule for apoptosis imaging. As a potential molecular probe candidate for PE, duramycin (2 kDa), which is produced by *Streptovercillium cinnamoneus*, is a tetracyclic peptide consisting of 19 amino acids (Figure 6) [52, 53] and binds the head group of PE with high affinity ($K_d = 11$ nM) at a molar ratio of 1:1 [54–56].

In 2008, Zhao et al. reported ^{99m}Tc -labeled duramycin, which is a novel PE-binding molecular probe, using a HYNIC ligand with tricine and phosphine as coligands [57]. In a myocardial ischemia/reperfusion injury lesion using a rat model, ^{99m}Tc -duramycin showed specific higher uptake in apoptotic cells compared with that in viable control cells. Intravenously injected ^{99m}Tc -duramycin showed favorable pharmacokinetic and biodistribution profiles. It was rapidly cleared from the circulation via the renal system with a blood half-life of less than 4 minutes in rats. Hepatic and gastrointestinal uptake was very low. In addition, ^{99m}Tc -duramycin was evaluated for ischemia/reperfusion injury in brain using the rat model of middle cerebral artery occlusion (MCAO) [58], oxidative lung injury [59], and damage in susceptible tissues after high-dose radiation exposure [60]. In all cases, ^{99m}Tc -duramycin could detect apoptotic cells and was useful for the estimation of the degree of the symptoms.

Recently, Yao et al. reported ^{18}F -labeled duramycin, [^{18}F]FPDuramycin, as a novel tracer for PET imaging of cell death [61]. [^{18}F]FPDuramycin was successful in visualizing tumor cell death after treatment with cyclophosphamide and cisplatin in tumor-bearing mice using PET. However, its pharmacokinetics was not favorable because [^{18}F]FPDuramycin showed high accumulation in the liver and spleen, which would limit detection of cell death in the upper abdomen.

14. [^{18}F]-*p*-Fluorobenzyl Triphenylphosphonium Cation (^{18}F -FBnTP)

It is known that mitochondria play an important role in an intrinsic pathway of apoptosis. Disruption of the mitochondrial membrane potential ($\Delta\Psi_m$) and mitochondrial outer membrane permeabilization, which leads to the release

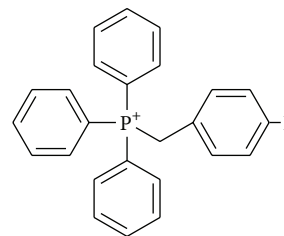


FIGURE 7: Structure of [^{18}F]-*p*-fluorobenzyl triphenylphosphonium cation (^{18}F -FBnTP).

of intermembrane proteins including cytochrome *c* and others, occurs at an early stage of apoptosis [62, 63]. The collapse of $\Delta\Psi_m$ occurs before the major morphology and biochemistry changes of apoptosis including nuclear DNA fragmentation and externalization of membranous PS [63]. Moreover, although the transient exposure of the PS allows measurement of the extent of the apoptosis during a limited time window, the loss of $\Delta\Psi_m$ is an ongoing process not limited to a time window. Thus, monitoring $\Delta\Psi_m$ could offer the information about the kinetics of the apoptotic process in the target tissue and could accordingly be an effective approach for detecting apoptosis at an early stage.

Phosphonium cations can pass through the lipid bilayer because they are sufficiently lipophilic and their positive charge is delocalized. In addition, because the membrane potential of mitochondria is the highest in cells, phosphonium cations could selectively accumulate in the interior of the mitochondria [64]. Consequently, when apoptosis causes loss of $\Delta\Psi_m$, phosphonium cations in cells would decrease.

In 2007, Madar et al. reported the ^{18}F -labeled phosphonium cation, ^{18}F -fluorobenzyl triphenylphosphonium cation (^{18}F -FBnTP, Figure 7), as a PET tracer for noninvasive assessment of $\Delta\Psi_m$ [65]. The performance of ^{18}F -FBnTP for measuring changes in membrane potential was comparable to that of ^3H -tetraphenylphosphonium (^3H -TPP), which has been used for measurement of $\Delta\Psi_m$ *in vitro*. *In vitro* experiments assessing the dependence of ^{18}F -FBnTP uptake on membrane potential showed that about 80% of total uptake was $\Delta\Psi_m$ -dependent, about 10% was plasma membrane potential ($\Delta\Psi_p$)-dependent, and remaining about 10% was independent of membrane potential, namely, nonspecific binding. Therefore, the change of radioactivity accumulation in the target tissue determined using ^{18}F -FBnTP PET imaging could mainly reflect changes in $\Delta\Psi_m$.

In 2009, Madar et al. reported *in vivo* study of ^{18}F -FBnTP [66]. Tumor uptake under anticancer treatment was evaluated in orthotropic prostate tumor-bearing mice. At 48 hours after treatment with docetaxel, ^{18}F -FBnTP and ^{18}F -FDG were intravenously administered. At 60 minutes after injection, ^{18}F -FBnTP uptake (percentage of dose per gram) in the prostate tumor of untreated mice was 1.84 ± 0.65 and that of treated mice was 0.90 ± 0.31 . In contrast, ^{18}F -FDG uptake levels in the prostate tumors of untreated mice and of treated mice were 1.31 ± 0.14 and 1.15 ± 0.54 , respectively. Treatment with docetaxel resulted in a significant decline in tumor uptake of ^{18}F -FBnTP (54.2%), but ^{18}F -FDG showed

no significant change in tumor uptake on treatment with docetaxel. Thus, the measurement of $\Delta\Psi_m$ using ^{18}F -FBnTP could be an effective strategy for the early detection of apoptosis.

15. Summary

In this review, we introduced a variety of apoptosis imaging probes. The most typical probes were radiolabeled agents that bind to PS, such as radiolabeled annexin V. Studies in model systems as well as clinical studies have demonstrated that the accumulation of PS-directed probes correlates with apoptotic cells after therapy. However, PS-directed probes accumulate not only as a result of apoptosis but also as a result of other forms of cell death. Both PS and PE are exposed onto the cell surface during apoptosis. PE-directed probes, such as radiolabeled duramycin, could also be apoptosis imaging agents using the same strategy used with PS-directed probes. Unlike PS- or PE-directed probes, caspase-3 imaging probes were expected to specifically detect apoptosis. Promising caspase-3 imaging probes have been developed, and their accumulation in apoptosis in animal models was shown to be higher than that in controls. However, the specificity of the imaging probe [^{18}F]ICMT-11, which targets caspases 3 and 7, for the detection of apoptotic cells was not shown [45]. The small-molecule ^{18}F -ML-10 (MW 206) is an apoptosis probe for PET that has simple structure derived from the ApoSense family. Although ^{18}F -ML-10 binds at apoptotic sites, the absolute uptake of ^{18}F -ML-10 in apoptotic tissue could be not enough. The probe ^{18}F -FBnTP, which is used to assess $\Delta\Psi_m$, can detect apoptosis because disruption of $\Delta\Psi_m$ occurs at an early stage of apoptosis. The loss of $\Delta\Psi_m$ is not limited to a specific time window, unlike the transient nature of PS exposure. A disadvantage of probes that assess $\Delta\Psi_m$ is that their uptake may display a negative correlation with apoptosis.

Quantitative imaging of apoptosis (cell death) provides useful information for therapeutic effects on diseases before anatomical changes of the lesion site. Selection of the appropriate therapies on the basis of the imaging data from the patients may be possible. Because the apoptosis imaging can allow evaluating the therapeutic effects of drugs under development, this modality may help the screening of novel compounds. Some promising agents have been developed in recent years as we introduced some of them in the review, but their imaging quality is not always sufficient. We hope that novel apoptosis imaging agents, showing higher S/N ratios, will be developed in the near future.

Conflict of Interests

The authors declare that there is no conflict of interests regarding the publication of this paper.

References

- [1] M. Verheij, "Clinical biomarkers and imaging for radiotherapy-induced cell death," *Cancer and Metastasis Reviews*, vol. 27, no. 3, pp. 471–480, 2008.

- [2] G. Melino, R. A. Knight, and P. Nicotera, "How many ways to die? How many different models of cell death?" *Cell Death & Differentiation*, vol. 12, no. 2, pp. 1457–1462, 2005.
- [3] P. W. Vriens, F. G. Blankenberg, J. H. Stoot et al., "The use of technetium Tc 99m annexin V for in vivo imaging of apoptosis during cardiac allograft rejection," *Journal of Thoracic and Cardiovascular Surgery*, vol. 116, no. 5, pp. 844–853, 1998.
- [4] J. F. Tait, D. Gibson, and K. Fujikawa, "Phospholipid binding properties of human placental anticoagulant protein-I, a member of the lipocortin family," *The Journal of Biological Chemistry*, vol. 264, no. 14, pp. 7944–7949, 1989.
- [5] J. H. Walker, C. M. Boustead, J. J. Koster, M. Bewley, and D. A. Waller, "Annexin V, a calcium-dependent phospholipid-binding protein," *Biochemical Society Transactions*, vol. 20, no. 4, pp. 828–833, 1992.
- [6] J. R. Stratton, T. A. Dewhurst, S. Kasina et al., "Selective uptake of radiolabeled annexin V on acute porcine left atrial thrombi," *Circulation*, vol. 92, no. 10, pp. 3113–3121, 1995.
- [7] J. Narula, E. R. Acio, N. Narula et al., "Annexin-V imaging for noninvasive detection of cardiac allograft rejection," *Nature Medicine*, vol. 7, no. 12, pp. 1347–1352, 2001.
- [8] F. G. Blankenberg, P. D. Katsikis, J. F. Tait et al., "In vivo detection and imaging of phosphatidylserine expression during programmed cell death," *Proceedings of the National Academy of Sciences of the United States of America*, vol. 95, no. 11, pp. 6349–6354, 1998.
- [9] R. C. King, M. B.-U. Surfraz, S. C. G. Biagini, P. J. Blower, and S. J. Mather, "How do HYNIC-conjugated peptides bind technetium? Insights from LC-MS and stability studies," *Dalton Transactions*, no. 43, pp. 4998–5007, 2007.
- [10] F. G. Blankenberg, P. D. Katsikis, J. F. Tait et al., "Imaging of apoptosis (programmed cell death) with ^{99m}Tc annexin V," *Journal of Nuclear Medicine*, vol. 40, no. 1, pp. 184–191, 1999.
- [11] J. F. Tait, D. S. Brown, D. F. Gibson, F. G. Blankenberg, and H. W. Strauss, "Development and characterization of annexin V mutants with endogenous chelation sites for ^{99m}Tc ," *Bioconjugate Chemistry*, vol. 11, no. 6, pp. 918–925, 2000.
- [12] T. Doue, K. Ohtsuki, K. Ogawa et al., "Cardioprotective effects of erythropoietin in rats subjected to ischemia-reperfusion injury: Assessment of infarct size with ^{99m}Tc -annexin V," *Journal of Nuclear Medicine*, vol. 49, no. 10, pp. 1694–1700, 2008.
- [13] T. Takeji, Y. Kuge, S. Zhao et al., "Time course of apoptotic tumor response after a single dose of chemotherapy: comparison with ^{99m}Tc -annexin V uptake and histologic findings in an experimental model," *Journal of Nuclear Medicine*, vol. 45, no. 12, pp. 2083–2087, 2004.
- [14] K. Ohtsuki, K. Akashi, Y. Aoka et al., "Technetium-99m HYNIC-annexin V: a potential radiopharmaceutical for the in-vivo detection of apoptosis," *European Journal of Nuclear Medicine*, vol. 26, no. 10, pp. 1251–1258, 1999.
- [15] M.-F. Guo, Y. Zhao, R. Tian et al., "In vivo ^{99m}Tc -HYNIC-annexin V imaging of early tumor apoptosis in mice after single dose irradiation," *Journal of experimental & clinical cancer research*, vol. 28, article 136, 2009.
- [16] F. G. Blankenberg, J.-L. Vanderheyden, H. W. Strauss, and J. F. Tait, "Radiolabeling of HYNIC-annexin V with technetium-99m for in vivo imaging of apoptosis," *Nature Protocols*, vol. 1, no. 1, pp. 108–110, 2006.
- [17] M. Kartachova, N. van Zandwijk, S. Burgers, H. van Tinteren, M. Verheij, and R. A. V. Olmos, "Prognostic significance of ^{99m}Tc Hynic-rh-annexin V scintigraphy during platinum-based

- chemotherapy in advanced lung cancer," *Journal of Clinical Oncology*, vol. 25, no. 18, pp. 2534–2539, 2007.
- [18] S. Rottey, G. Slegers, S. van Belle, I. Goethals, and C. van de Wiele, "Sequential ^{99m}Tc -hydrazinonicotinamide-annexin V imaging for predicting response to chemotherapy," *Journal of Nuclear Medicine*, vol. 47, no. 11, pp. 1813–1818, 2006.
- [19] J. F. Tait, C. Smith, and D. F. Gibson, "Development of annexin V mutants suitable for labeling with Tc(I)-carbonyl complex," *Bioconjugate Chemistry*, vol. 13, no. 5, pp. 1119–1123, 2002.
- [20] K. Ogawa, K. Ohtsuki, T. Shibata et al., "Development and evaluation of a novel ^{99m}Tc -labeled annexin A5 for early detection of response to chemotherapy," *PLoS ONE*, vol. 8, no. 12, Article ID e81191, 2013.
- [21] S. Zijlstra, J. Gunawan, and W. Burchert, "Synthesis and evaluation of a ^{18}F -labelled recombinant annexin-V derivative, for identification and quantification of apoptotic cells with PET," *Applied Radiation and Isotopes*, vol. 58, no. 2, pp. 201–207, 2003.
- [22] J. Toretzky, A. Levenson, I. N. Weinberg, J. F. Tait, A. Üren, and R. C. Mease, "Preparation of F-18 labeled annexin V: a potential PET radiopharmaceutical for imaging cell death," *Nuclear Medicine and Biology*, vol. 31, no. 6, pp. 747–752, 2004.
- [23] Y. Murakami, H. Takamatsu, J. Taki et al., " ^{18}F -labelled annexin V: a PET tracer for apoptosis imaging," *European Journal of Nuclear Medicine and Molecular Imaging*, vol. 31, no. 4, pp. 469–474, 2004.
- [24] K. P. Zhernosekov, D. V. Filosofov, R. P. Baum et al., "Processing of generator-produced ^{68}Ga for medical application," *Journal of Nuclear Medicine*, vol. 48, no. 10, pp. 1741–1748, 2007.
- [25] C. Wangler, B. Wangler, S. Lehner et al., "A universally applicable ^{68}Ga -labeling technique for proteins," *Journal of Nuclear Medicine*, vol. 52, no. 4, pp. 586–591, 2011.
- [26] M. Bauwens, M. de Saint-Hubert, E. Devos et al., "Site-specific ^{68}Ga -labeled Annexin A5 as a PET imaging agent for apoptosis," *Nuclear Medicine and Biology*, vol. 38, no. 3, pp. 381–392, 2011.
- [27] K. Igarashi, M. Kaneda, A. Yamaji et al., "A novel phosphatidylserine-binding peptide motif defined by an anti-idiotypic monoclonal antibody. Localization of phosphatidylserine-specific binding sites on protein kinase C and phosphatidylserine decarboxylase," *Journal of Biological Chemistry*, vol. 270, no. 49, pp. 29075–29078, 1995.
- [28] C. Xiong, K. Brewer, S. Song et al., "Peptide-based imaging agents targeting phosphatidylserine for the detection of apoptosis," *Journal of Medicinal Chemistry*, vol. 54, no. 6, pp. 1825–1835, 2011.
- [29] S. Song, C. Xiong, W. Lu, G. Ku, G. Huang, and C. Li, "Apoptosis imaging probe predicts early chemotherapy response in preclinical models: a comparative study with ^{18}F -FDG PET," *Journal of Nuclear Medicine*, vol. 54, no. 1, pp. 104–110, 2013.
- [30] T. Sakamoto, A. Ojida, and I. Hamachi, "Molecular recognition, fluorescence sensing, and biological assay of phosphate anion derivatives using artificial Zn(II)-Dpa complexes," *Chemical Communications*, no. 2, pp. 141–152, 2009.
- [31] L. Wyffels, B. D. Gray, C. Barber, J. M. Woolfenden, K. Y. Pak, and Z. Liu, "Synthesis and preliminary evaluation of radiolabeled bis(zinc(II)-dipicolylamine) coordination complexes as cell death imaging agents," *Bioorganic & Medicinal Chemistry*, vol. 19, no. 11, pp. 3425–3433, 2011.
- [32] H. Wang, X. Tang, G. Tang et al., "Noninvasive positron emission tomography imaging of cell death using a novel small-molecule probe, ^{18}F labeled bis(zinc(II)-dipicolylamine) complex," *Apoptosis*, vol. 18, no. 8, pp. 1017–1027, 2013.
- [33] G. Marino and G. Kroemer, "Mechanisms of apoptotic phosphatidylserine exposure," *Cell Research*, vol. 23, no. 11, pp. 1247–1248, 2013.
- [34] M. Damianovich, I. Ziv, S. N. Heyman et al., "ApoSense: a novel technology for functional molecular imaging of cell death in models of acute renal tubular necrosis," *European Journal of Nuclear Medicine and Molecular Imaging*, vol. 33, no. 3, pp. 281–291, 2006.
- [35] A. Reshef, A. Shirvan, R. N. Waterhouse et al., "Molecular imaging of neurovascular cell death in experimental cerebral stroke by PET," *Journal of Nuclear Medicine*, vol. 49, no. 9, pp. 1520–1528, 2008.
- [36] J. Höglund, A. Shirvan, G. Antoni et al., " ^{18}F -ML-10, a PET tracer for apoptosis: first human study," *Journal of Nuclear Medicine*, vol. 52, no. 5, pp. 720–725, 2011.
- [37] A. Cohen, A. Shirvan, G. Levin, H. Grimberg, A. Reshef, and I. Ziv, "From the gla domain to a novel small-molecule detector of apoptosis," *Cell Research*, vol. 19, no. 5, pp. 625–637, 2009.
- [38] M. Bauwens, M. de Saint-Hubert, J. Cleyhens et al., "In vitro and in vivo comparison of ^{18}F and ^{123}I -labeled ML10 with ^{68}Ga -Cys2-Anx A5 for molecular imaging of apoptosis," *Quarterly Journal of Nuclear Medicine and Molecular Imaging*, vol. 57, no. 2, pp. 187–200, 2013.
- [39] J. Li and J. Yuan, "Caspases in apoptosis and beyond," *Oncogene*, vol. 27, no. 48, pp. 6194–6206, 2008.
- [40] D. W. Nicholson and N. A. Thornberry, "Caspases: killer proteases," *Trends in Biochemical Sciences*, vol. 22, no. 8, pp. 299–306, 1997.
- [41] A. G. Porter and R. U. Jänicke, "Emerging roles of caspase-3 in apoptosis," *Cell Death & Differentiation*, vol. 6, no. 2, pp. 99–104, 1999.
- [42] D. Lee, S. A. Long, J. H. Murray et al., "Potent and selective nonpeptide inhibitors of caspases 3 and 7," *Journal of Medicinal Chemistry*, vol. 44, no. 12, pp. 2015–2026, 2001.
- [43] D. Zhou, W. Chu, J. Rothfuss et al., "Synthesis, radiolabeling, and in vivo evaluation of an ^{18}F -labeled isatin analog for imaging caspase-3 activation in apoptosis," *Bioorganic and Medicinal Chemistry Letters*, vol. 16, no. 19, pp. 5041–5046, 2006.
- [44] G. Smith, M. Glaser, M. Perumal et al., "Design, synthesis, and biological characterization of a caspase 3/7 selective isatin labeled with 2- ^{18}F fluoroethylazide," *Journal of Medicinal Chemistry*, vol. 51, no. 24, pp. 8057–8067, 2008.
- [45] Q.-D. Nguyen, G. Smith, M. Glaser, M. Perumal, E. Årstad, and E. O. Aboagye, "Positron emission tomography imaging of drug-induced tumor apoptosis with a caspase-3/7 specific ^{18}F -labeled isatin sulfonamide," *Proceedings of the National Academy of Sciences of the United States of America*, vol. 106, no. 38, pp. 16375–16380, 2009.
- [46] Q.-D. Nguyen, I. Lavdas, J. Gubbins et al., "Temporal and spatial evolution of therapy-induced tumor apoptosis detected by caspase-3-selective molecular imaging," *Clinical Cancer Research*, vol. 19, no. 14, pp. 3914–3924, 2013.
- [47] T. H. Witney, R. R. Fortt, and E. O. Aboagye, "Preclinical assessment of carboplatin treatment efficacy in lung cancer by ^{18}F -ICMT-11-positron emission tomography," *PLoS ONE*, vol. 9, no. 3, Article ID e91694, 2014.
- [48] A. Challapalli, L. M. Kenny, W. A. Hallett et al., " ^{18}F -ICMT-11, a caspase-3-specific PET tracer for apoptosis: biodistribution and radiation dosimetry," *Journal of Nuclear Medicine*, vol. 54, no. 9, pp. 1551–1556, 2013.

- [49] A. A. Spector and M. A. Yorek, "Membrane lipid composition and cellular function," *Journal of Lipid Research*, vol. 26, no. 9, pp. 1015–1035, 1985.
- [50] E. M. Bevers, P. Comfurius, D. W. C. Dekkers, and R. F. A. Zwaal, "Lipid translocation across the plasma membrane of mammalian cells," *Biochimica et Biophysica Acta: Molecular and Cell Biology of Lipids*, vol. 1439, no. 3, pp. 317–330, 1999.
- [51] K. Emoto, N. Toyama-Sorimachi, H. Karasuyama, K. Inoue, and M. Umeda, "Exposure of phosphatidylethanolamine on the surface of apoptotic cells," *Experimental Cell Research*, vol. 232, no. 2, pp. 430–434, 1997.
- [52] F. Hayashi, K. Nagashima, Y. Terui, Y. Kawamura, K. Matsumoto, and H. Itazaki, "The structure of PA48009: the revised structure of duramycin," *Journal of Antibiotics*, vol. 43, no. 11, pp. 1421–1430, 1990.
- [53] N. Zimmermann, S. Freund, A. Fredenhagen, and G. Jung, "Solution structures of the lantibiotics duramycin B and C," *European Journal of Biochemistry*, vol. 216, no. 2, pp. 419–428, 1993.
- [54] F. Märki, E. Hänni, A. Fredenhagen, and J. van Oostrum, "Mode of action of the lanthionine-containing peptide antibiotics duramycin, duramycin B and C, and cinnamycin as indirect inhibitors of phospholipase A2," *Biochemical Pharmacology*, vol. 42, no. 10, pp. 2027–2035, 1991.
- [55] K. Iwamoto, T. Hayakawa, M. Murate et al., "Curvature-dependent recognition of ethanolamine phospholipids by duramycin and cinnamycin," *Biophysical Journal*, vol. 93, no. 5, pp. 1608–1619, 2007.
- [56] J. Seelig, "Thermodynamics of lipid-peptide interactions," *Biochimica et Biophysica Acta—Biomembranes*, vol. 1666, no. 1–2, pp. 40–50, 2004.
- [57] M. Zhao, Z. Li, and S. Bugenhagen, "^{99m}Tc-labeled duramycin as a novel phosphatidylethanolamine-binding molecular probe," *Journal of Nuclear Medicine*, vol. 49, no. 8, pp. 1345–1352, 2008.
- [58] Y. Zhang, G. D. Stevenson, C. Barber et al., "Imaging of rat cerebral ischemia-reperfusion injury using ^{99m}Tc-labeled duramycin," *Nuclear Medicine and Biology*, vol. 40, no. 1, pp. 80–88, 2013.
- [59] A. V. Clough, S. H. Audi, S. T. Haworth, and D. L. Roerig, "Differential lung uptake of ^{99m}Tc-hexamethylpropyleneamine oxime and ^{99m}Tc-duramycin in the chronic hyperoxia rat model," *Journal of Nuclear Medicine*, vol. 53, no. 12, pp. 1984–1991, 2012.
- [60] S. E. Johnson, Z. Li, Y. Liu, J. E. Moulder, and M. Zhao, "Whole-body imaging of high-dose ionizing irradiation—induced tissue injuries using ^{99m}Tc-duramycin," *Journal of Nuclear Medicine*, vol. 54, no. 8, pp. 1397–1403, 2013.
- [61] S. Yao, K. Hu, G. Tang et al., "Positron emission tomography imaging of cell death with [¹⁸F]FPDduramycin," *Apoptosis*, vol. 19, no. 5, pp. 841–850, 2014.
- [62] D. R. Green and G. Kroemer, "The pathophysiology of mitochondrial cell death," *Science*, vol. 305, no. 5684, pp. 626–629, 2004.
- [63] S. A. Susin, N. Zamzami, and G. Kroemer, "Mitochondria as regulators of apoptosis: doubt no more," *Biochimica et Biophysica Acta*, vol. 1366, no. 1–2, pp. 151–165, 1998.
- [64] M. P. Murphy and R. A. J. Smith, "Drug delivery to mitochondria: the key to mitochondrial medicine," *Advanced Drug Delivery Reviews*, vol. 41, no. 2, pp. 235–250, 2000.
- [65] I. Madar, H. Ravert, B. Nelkin et al., "Characterization of membrane potential-dependent uptake of the novel PET tracer ¹⁸F-fluorobenzyl triphenylphosphonium cation," *European Journal of Nuclear Medicine and Molecular Imaging*, vol. 34, no. 12, pp. 2057–2065, 2007.
- [66] I. Madar, Y. Huang, H. Ravert et al., "Detection and quantification of the evolution dynamics of apoptosis using the PET voltage sensor ¹⁸F-fluorobenzyl triphenyl phosphonium," *Journal of Nuclear Medicine*, vol. 50, no. 5, pp. 774–780, 2009.

Review Article

Solid Tumor-Targeting Theranostic Polymer Nanoparticle in Nuclear Medicinal Fields

Akira Makino^{1,2} and Shunsaku Kimura³

¹ Biomedical Imaging Research Center (BIRC), University of Fukui, Fukui 910-1193, Japan

² Research and Education Program for Life Science, University of Fukui, Fukui 910-1193, Japan

³ Department of Material Chemistry, Graduate School of Engineering, Kyoto University, Kyoto 615-8510, Japan

Correspondence should be addressed to Akira Makino; amakino@u-fukui.ac.jp

Received 27 June 2014; Revised 8 August 2014; Accepted 11 August 2014; Published 14 October 2014

Academic Editor: Masashi Ueda

Copyright © 2014 A. Makino and S. Kimura. This is an open access article distributed under the Creative Commons Attribution License, which permits unrestricted use, distribution, and reproduction in any medium, provided the original work is properly cited.

Polymer nanoparticles can be prepared by self-assembling of amphiphilic polymers, and various types of molecular assemblies have been reported. In particular, in medicinal fields, utilization of these polymer nanoparticles as carriers for drug delivery system (DDS) has been actively tried, and some nanoparticulate drugs are currently under preclinical evaluations. A radionuclide is an unstable nucleus and decays with emission of radioactive rays, which can be utilized as a tracer in the diagnostic imaging systems of PET and SPECT and also in therapeutic purposes. Since polymer nanoparticles can encapsulate most of diagnostic and therapeutic agents with a proper design of amphiphilic polymers, they should be effective DDS carriers of radionuclides in the nuclear medicinal field. Indeed, nanoparticles have been recently attracting much attention as common platform carriers for diagnostic and therapeutic drugs and contribute to the development of nanotheranostics. In this paper, recent developments of solid tumor-targeting polymer nanoparticles in nuclear medicinal fields are reviewed.

1. Introduction

Nanoparticles have been actively examined as carriers for drug delivery system (DDS), which make it possible to improve therapeutic efficacy and to suppress side effects of the parent drug [1–5]. Among various types of nano-ordered carriers including inorganic and lipid particles, polymeric micelles and vesicles, which are prepared from self-assembling process of amphiphilic polymers, can encapsulate in general hydrophobic and hydrophilic compounds in the hydrophobic core and inner aqueous cavity regions, respectively [6–10]. Further, not only surface modification but also functionalization of these nanoparticles is possible with ease by using suitably designed amphiphilic polymers. Therefore, polymeric nanoparticles have received much attention as the DDS carriers.

Additionally, nanoparticles are originally accumulated at the region where cells are rapidly proliferating, because leakage of nanoparticles can occur through the holes on immature blood vessels. Combined with the effect of undeveloped

lymph system at tumor region, nanoparticles are retained there, leading to the passive accumulation. This phenomenon is called the enhanced permeability and retention (EPR) effect and is one of the most frequently utilized methodologies of nanoparticles for DDS [11–13]. On the basis of these reasons, polymeric nanoparticle is a suitable carrier for solid tumors-targeting DDS [8, 14]. In fact, various tumor-targeting DDS carriers have been developed, and some polymeric nanoparticles encapsulating antitumor drugs are currently under clinical trials [15].

Recently, polymeric nanoparticles are also applied as carriers for contrast agents in the field of *in vivo* imaging [16–18]. Among various modalities such as near-infrared fluorescence (NIRF) imaging, magnetic resonance imaging (MRI), positron emission tomography (PET), and single photon emission computed tomography (SPECT) systems, the *in vivo* near-infrared fluorescence (NIRF) imaging system has shown amazing progresses. This is because handling of the NIRF compounds is relatively easy and its biodistribution can be directly visualized. However, penetration depth of

TABLE 1: Representative radionuclides used for imaging and radiotherapy.

Radionuclide	Emission type	Half-life	Usage ¹
¹¹ C	β^+ (99.8%), γ (0.2%)	20.39 min	I
¹³ N	β^+ (99.8%), γ (0.2%)	9.965 min	I
¹⁵ O	β^+ (99.9%), γ (0.1%)	2.037 min	I
¹⁸ F	β^+ (96.7%), γ (3.3%)	109.8 min	I
³² P	β^- (100%)	14.24 day	T
⁶⁴ Cu	β^+ (17.4%), γ (43.6%), β^- (39.0%)	12.70 h	T/I
⁸⁹ Sr	β^- (100%)	50.53 day	T
⁹⁰ Y	β^- (100%)	64.00 h	T
^{99m} Tc	γ (>99.9%)	6.015 h	T/I
¹¹¹ In	γ (100%)	2.805 day	T/I
¹²³ I	γ (100%)	13.22 h	I
¹²⁵ I	γ (100%)	59.40 day	T/I
¹³¹ I	β^-	8.021 day	T/I
¹⁸⁶ Re	β^- , γ	3.718 day	T/I
¹⁸⁸ Re	β^- , γ	17.00 h	T
²¹¹ At	α	7.214 h	T
²¹³ Bi	α	2.14 min	T
²²⁵ Ac	α	10.0 day	T

¹Radionuclide usage for imaging and therapy are abbreviated as "I" and "T," respectively.

near-infrared light in tissue is limited to a few centimeters [19]. Therefore, the NIRF imaging system is suitable for *in vivo* experiments using small animals, but its applicative area in human clinical uses is limited to near the surface where fluorescent signal can be detectable. On the other hand, in general, sensitivity of nuclear imaging is high. Further, quantitative analyses are available by using PET images. When it comes to the quantitative performance, SPECT is less competitive than PET but has been improved by recent mechanical developments [20]. Positron emitters such as ¹¹C, ¹³N, ¹⁵O, ¹⁸F, and ⁶⁴Cu are used for PET imaging as signal sources, and γ -ray emitters such as ^{99m}Tc, ¹¹¹In, and ¹²³I are for SPECT imaging (Table 1). For preparation of nanoparticle type probes for nuclear imaging techniques, strategies on how to encapsulate these radioisotopes into nanoparticles are important. There are considerable approaches for the encapsulation, which can be classified into three categories: (1) hydrophobized radionuclides are encapsulated into the hydrophobic core region of polymeric micelle, (2) radionuclide solution is encapsulated into the inner cavity of vesicular assemblies, and (3) metal radionuclides such as ⁶⁴Cu and ^{99m}Tc can be attached to the nanoparticles as chelates by modifying constituent amphiphilic polymers with appropriate chelators. About the inner radiation therapy, β^- ray emitters, such as ⁹⁰Y and ¹³¹I, are generally used. In addition, attempts to utilize radionuclides emitting α -ray (²¹¹At, ²¹³Bi) and auger electron (^{99m}Tc, ¹¹¹In, and ¹²⁵I) are also performed (Table 1) [21–25]. Any radionuclides labeled nanoparticle can be prepared by selecting appropriate methods for encapsulation as written above.

In this review, recent research developments on solid tumor-targeting DDS using polymer nanoparticle carriers in nuclear medicinal fields are summarized.

2. Polymeric Micelles

2.1. Importance of Surface Modification with Poly(ethylene glycol) (PEG)

2.1.1. *Poly(methyl acrylate)-b-poly(acrylic acid)*. One of the initial trials to utilize polymeric micelle as a carrier for PET tracer agent was performed in 2005 by Rossin et al. [26]. Polymeric micelle was prepared from amphiphilic poly(methyl acrylate)-*b*-poly(acrylic acid) (PMA₁₆₄-*b*-PAA₉₃), which was synthesized via sequential atom transfer radical polymerization (ATRP) [27]. As illustrated in Figure 1, PMA-*b*-PAA in the micelle was cross-linked between the carboxyl acid group of PAA and the amine functionalities of 2,2'-(ethylenedioxy)diethylamine poly(acrylic acid) to form shell cross-linked (SCK) nanoparticles. Folate receptor (FR) is well-known molecular target for tumor therapies [28], and therefore, folate-poly(ethylene glycol)-amine was conjugated to the surface of the micelle. Further, 1,4,8,11-tetra-azacyclotetradecane-*N'*, *N''*, *N'''*, *N''''*-tetra-acetic acid (TETA) was also modified to the micelle surface for ⁶⁴Cu chelate formation.

Using tumor transplanted mice, biodistribution of the micelle was examined by organ harvesting method. The micelle was recognized by reticuloendothelial system (RES), which is self-defense system of living organisms, and its

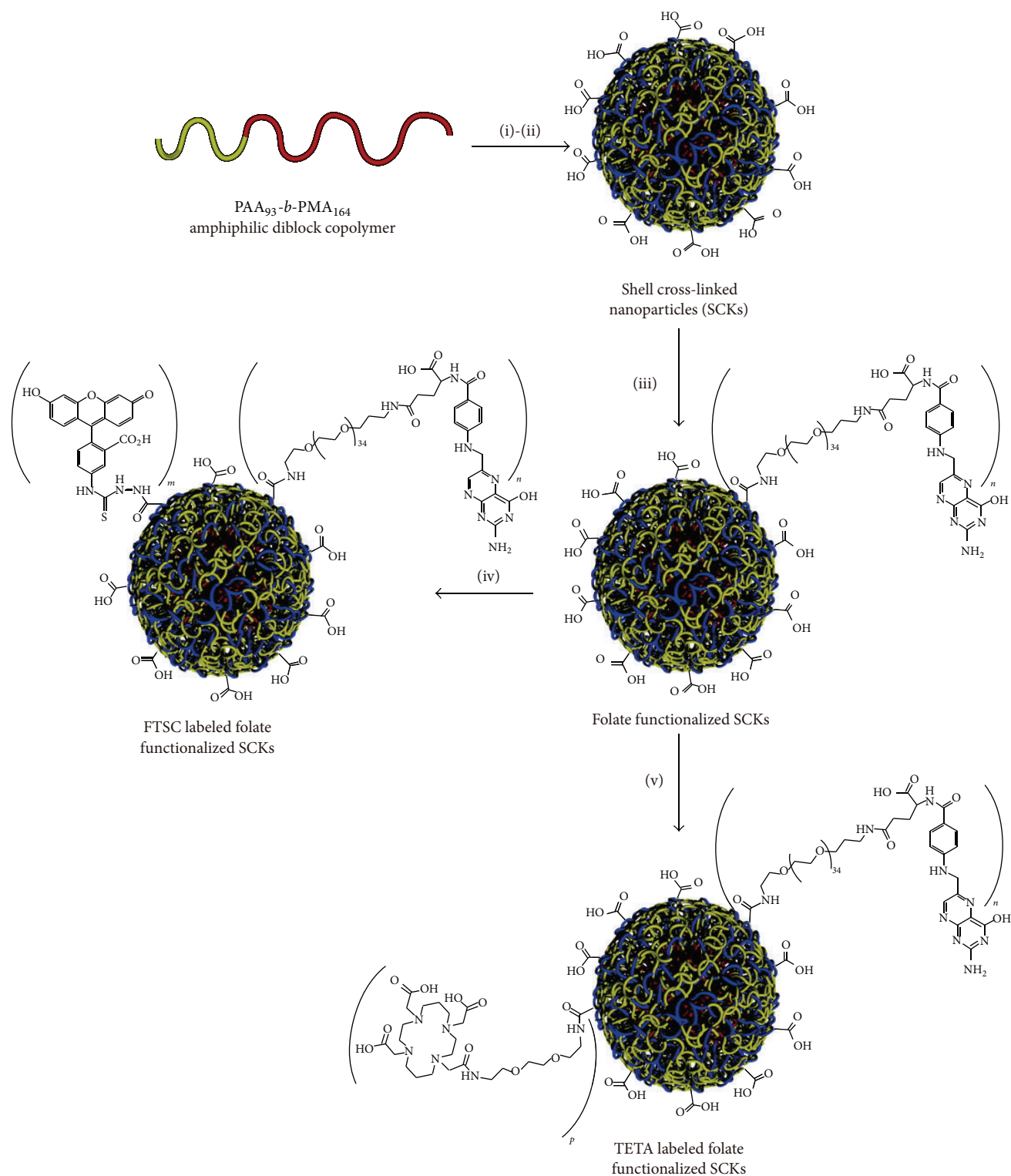


FIGURE 1: Polymeric micelle prepared from PMA-*b*-PAA. This research was originally published in JNM. R. Rossin, D. P. J. Pan, K. Qi, J. L. Turner, X. K. Sun, K. L. Wooley, and M. J. Welch. "Cu-64-labeled folate-conjugated shell cross-linked nanoparticles for tumor imaging and radiotherapy: Synthesis, radiolabeling, and biologic evaluation." J. Nucl. Med. 2005, 46, 1210-1218. The Society of Nuclear Medicine and Molecular Imaging, Inc ©.

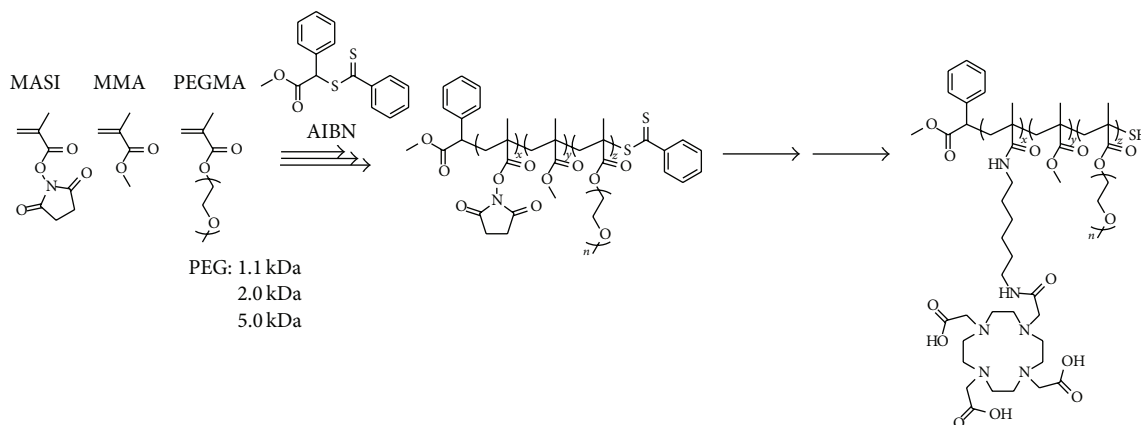


FIGURE 2: Scheme for poly(methyl methacrylate-co-methacryloxysuccinimide-graft-poly(ethylene glycol)).

undesired uptake at liver and spleen was high. However, owing to the combined effects of FR-mediated cell uptake and EPR effect, the micelle was accumulated at the tumor region with 2.1 ± 0.3 , 3.2 ± 0.7 , 6.0 ± 1.9 , and $5.6 \pm 0.9\%$ ID/g at 10 min, 1 h, 4 h, and 24 h from the administration, respectively.

2.1.2. Poly(methyl methacrylate-co-methacryloxysuccinimide-graft-poly(ethylene glycol)). To suppress undesired micelle uptake by RES, comb copolymers with branching various lengths of poly(ethylene glycol) (PEG) chains (1.1–5.0 kDa) were synthesized by standard reversible addition-fragmentation chain-transfer (RAFT) polymerization conditions [29], and to the polymer terminal end, 1,4,7,10-tetra-azacyclododecanetetra-acetic acid (DOTA) ligand was introduced as a chelator for radionuclides (Figure 2). The chelation with ^{64}Cu was carried out after preparation of polymeric micelles. Diameters of the micelles prepared from copolymers with PEG of 1.1, 2.0, and 5.0 kDa were 9.7 ± 1.1 , 17 ± 2 , and 20 ± 3 nm, respectively.

Three types of ^{64}Cu labeled micelles were injected into rats from the tail vein and their biodistribution was determined by organ harvesting method so as to evaluate the effect of PEG chain length on the micelle biodistribution. Additionally, the imaging studies were carried out using small animal PET system. The 5.0 kDa PEG micelle underwent a slow blood clearance, and $31 \pm 2\%$ of the dose was still in blood at 48 h after injection, which was almost ten times and twice higher than that of 1.1 kDa and 2.0 kDa PEG micelles, respectively. Biodistribution trend in the liver was opposite to that observed in the blood. Liver uptake of 1.1, 2.0, and 5.0 kDa PEG micelles at 24 h from the injection was decreased in this order and to be ca. 4.0, 2.8, and 1.2% ID/g, respectively. These results indicated that surface modification with PEG is important to control *in vivo* dynamics of the micelle, and prolongation of blood circulation time and low accumulation in excretory organs can be achieved by increased thickness of PEG shell.

2.1.3. Poly(lauryl methacrylate)-*b*-poly(*N*-(2-hydroxypropyl) methacrylamide). Amphiphilic copolymer consisted of

hydrophobic poly(lauryl methacrylate) (poly(LMA)) and hydrophilic poly(*N*-(2-hydroxypropyl)methacrylamide) (poly(HPMA)) blocks that was synthesized via RAFT polymerization, and PEG₂₀₀₀ was incorporated into the side chain of the hydrophilic block with 0–11% modification ratio [30]. Further, the amphiphile was covalently labeled by radionuclides of ^{18}F . Polymeric micelle was prepared from the amphiphile, and the effects of the PEGylation on micelle size, biodistribution, and cell uptake behavior were evaluated. In animal experiments using rats, polymeric micelle with diameter of 38.1 ± 2.1 nm, which was prepared from amphiphilic block copolymer with 7% PEGylation, exhibited the most favorable organ distribution pattern, showing highest blood circulation behavior as well as lowest undesired uptake at spleen and liver. Tumor cells of Walker 256 mammary carcinomas were clearly visualized by animal PET system after 2 h from the micelle dosage.

The group also synthesized random copolymers as well as block copolymers. Polymeric micelles were prepared from these copolymers, and their cellular uptake and biodistribution were evaluated using two different types of tumor models (AT1 prostate carcinoma and Walker-256 mammary carcinoma). They concluded that not only PEGylation, but also other numerous factors including molecular weight of the copolymers, polymer structure, size of the micelle, and characteristics of tumor affected the intratumor accumulation level of the micelle [31]. Therefore, preclinical screening to analyze polymer uptake for each individual patient is considered to be essential for each chemo- and radiotherapy using polymer-based DDS.

2.2. Core-Cross-Linked Type Polymeric Micelle (CCPM) for Enhanced Thermodynamic Stability. Compared with liposome, polymeric micelle is thermodynamically stable. This is because relatively long hydrophobic polymer chains can stabilize the molecular assemblies more than the hydrophobic interaction among alkyl chains of phospholipids. Aiming at further improvement of polymeric micelle stability, intermolecular cross-linking of copolymers via covalent bonds has been examined.

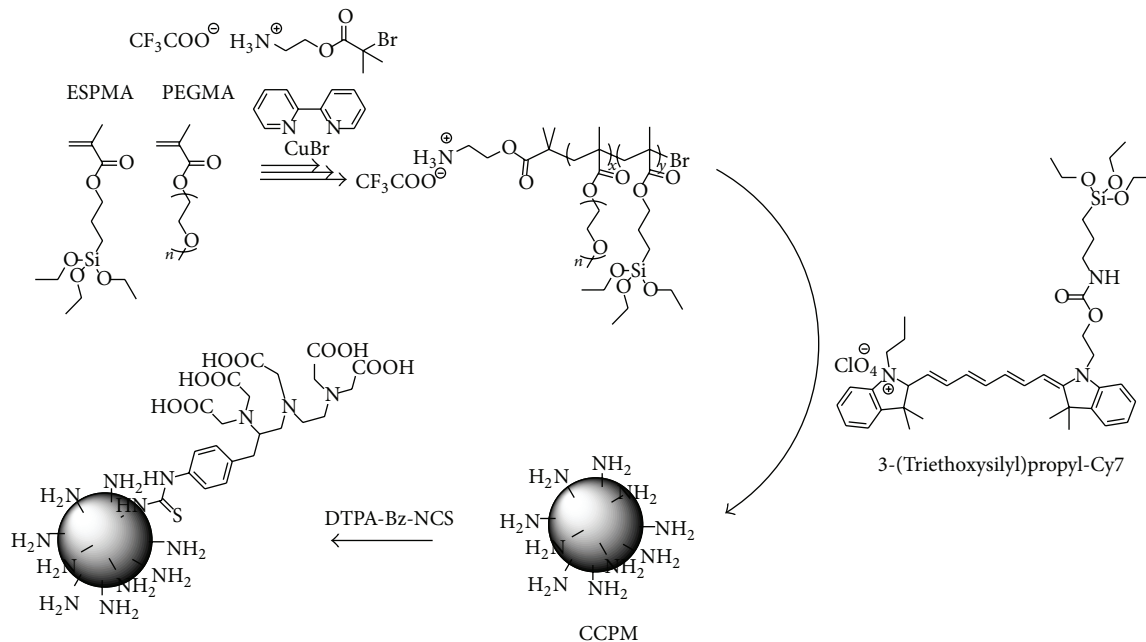


FIGURE 3: Preparation of core-cross-linked polymeric micelle (CCPM).

2.2.1. Poly(triethoxysilyl propylmethacrylate)-*b*-poly(PEG-methacrylate). Poly(triethoxysilyl propylmethacrylate)-*b*-poly(PEG-methacrylate) (PESPMA-*b*-PPEGMA) was synthesized by atom transfer radical polymerization (ATRP). From the mixture of the polymer and 3-(trimethoxysilyl)propyl-Cy7, polymeric micelle was prepared by sol-gel process upon addition of acetic acid. The acid caused rapid hydrolysis of ethoxy silane precursors and subsequent cross-link of the PESPMA core with the Cy7 derivative via Si-O bonds. Targeting the amino group, which is located at terminal end of hydrophilic block, DTPA was inserted on the surface of the core-cross-linked polymeric micelle (CCPM) and used for chelate formation with ^{111}In (Figure 3). To the breast tumor cells of MDA-MB468 transplanted mice, ^{111}In -DTPA-CCPM with diameter of 24 ± 8.9 nm was injected and γ -scintigraphy and NIRF optical imaging were performed [32]. CCPM showed prolonged blood circulation behavior ($t_{1/2,\alpha} = 1.25$ h, $t_{1/2,\beta} = 46.18$ h) and passively accumulated at the tumor region (5.5% ID/g at 48 h after injection). At 120 h from the dosage, tumor/blood and tumor/muscle signal ratios reached 4.44 and 28.0, respectively.

Characteristic point of CCPM is location of amino group on the surface, and therefore, it is possible to attach targeting ability to CCPM by ligand conjugation. For example, EphB4-binding peptide and synthetic somatostatin analogue of octreotide-conjugated CCPMs were prepared to detect EphB4-positive PC-3 M prostate and somatostatin receptor overexpressed glioblastoma U87 cells, respectively [33, 34]. When a cell undergoes apoptosis, phosphatidylserine is exposed on the cell surface. Then, annexin A5-conjugated CCPM, which binds strongly with phosphatidylserine, was also prepared [35]. Utilizing these ^{111}In labeled CCPMs, dual

SPECT and NIRF imaging of the targeted region was accomplished. Further, time for accumulation of these ligand-conjugated CCPMs to the targeted region could be shortened by specific bindings with corresponding receptors, and signal intensity ratio against background was also improved.

2.2.2. Poly(7-(2-methacryloyloxyethoxy)4-methylcoumarin)-*b*-poly(hydroxyethylmethacrylate)-*b*-poly(ethylene glycol). Copolymer consisting of one hydrophobic 7-(2-methacryloyloxyethoxy)-4-methylcoumarin (CMA) and two hydrophilic hydroxyethylmethacrylate (HEMA) and PEG blocks was also synthesized by Jensen et al. [36]. To hydroxyl groups of the HEMA block, DOTA or CB-TE2A was conjugated as a chelator for radioactive metal of ^{64}Cu . After micelle formation by using self-assembling mechanism, the micelle dispersion was irradiated by UV light so as to cross-link 4-methylcoumarin moieties in the hydrophobic core. The cross-linked micelle showed higher stability in blood and was accumulated at transplanted tumor region (U87MG) of mice. After 22 and 46 h from the dosage of ^{64}Cu labeled micelles, tumor can be visualized.

2.3. Micelle Formation from Biodegradable and Biocompatible Amphiphilic Polymers

2.3.1. Poly(ϵ -caprolactone)-*b*-poly(ethylene glycol). Polymeric micelle can be prepared from various amphiphilic polymers. From the view point that polymer nanoparticles are applied as carrier for DDS, utilization of biodegradable and biocompatible amphiphilic polymers should take priority. Then, poly(ϵ -caprolactone), which is representative biodegradable

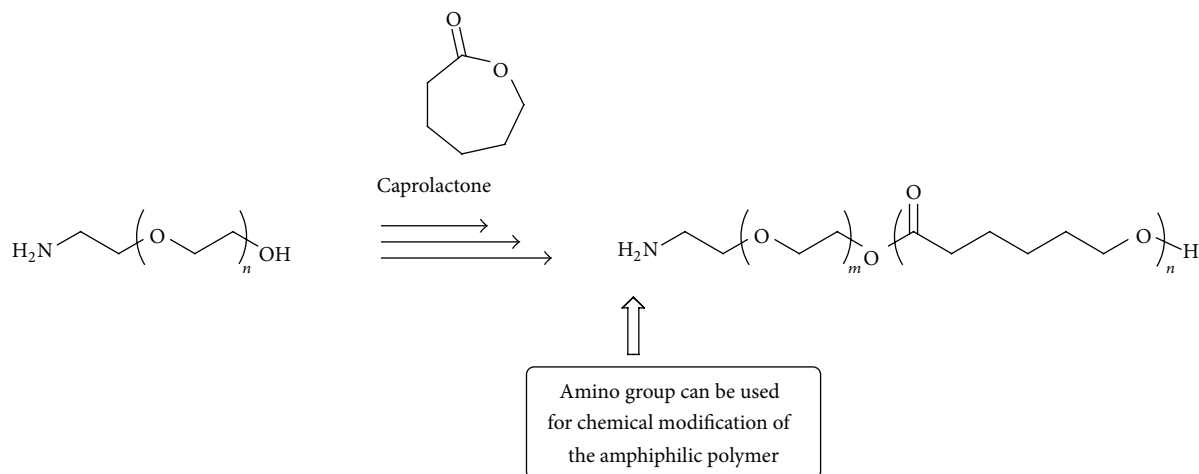


FIGURE 4: Amphiphilic poly(ϵ -caprolactone)-*b*-poly(ethylene glycol) for micelle preparation.

polymer connecting through ester linkages, was selected as hydrophobic block of the amphiphilic polymer (Figure 4) [37]. For the chelate formation with ^{111}In , terminal end of the amphiphilic polymer is modified by diethylene triamine penta-acetic acid (DTPA), which is a well-known chelator to form stable complexes with metals. From DTPA modified poly(ϵ -caprolactone)-*b*-poly(ethylene glycol) (PCL-*b*-PEG), polymer micelle was prepared and then radionuclide ^{111}In was chelated to DTPA [38]. To the tumor-bearing mice, the ^{111}In labeled micelle with diameter of ca. 60 nm was injected, and its biodistribution and pharmacokinetics were evaluated by the organ harvesting method and SPECT/CT *in vivo* imaging system. The micelle was passively accumulated at the tumor region ($9 \pm 2\%$ ID/g), and transplanted tumor could be imaged by SPECT.

On a cell surface of various types of epithelial cancers including lung and breast, epidermal growth factor receptor (EGFR) is known to be overexpressed. The micelle surface was functionalized by conjugating EGF to terminal amino group of the amphiphile so as to improve the ^{111}In labeled micelle delivering efficiency to the targeted tumor region [39]. Compared with the accumulation of the nontargeting micelle (EGF-), *in vivo* cell uptake and cell membrane binding of the EGF modified micelle (EGF+) to tumors overexpressing EGFR were significantly enhanced ($P < 0.05$).

^{111}In can be also utilized as therapeutic nucleotide as emitter of auger electrons [40]. Using the EGF modified micelle, effect of auger electron therapy against EGFR-positive breast cancer cells was performed [41]. In this research, three types of human breast cancer cell cultures of MDA-MB-468 (1×10^6 EGFR/cell), MDA-MB-231 (2×10^5 EGFR/cell), and MCF-7 (1×10^4 EGFR/cell) were used. Correlated with the density of EGFR expression level on these cancer cells, EGFR-mediated uptake of the micelle (EGF+) was increased. In *in vitro* cell survival assay, cell number of MDA-MB-468 was significantly decreased after 21 h from the treatment by 1 MBq of ^{111}In -DTPA modified micelle (EGF+). However,

the micelle showed no cytotoxicity against MCF-7 with low EGFR expression level.

On the cell surface of breast cancer, it is known to express different levels of HER2. Then, ^{111}In labeled micelle, whose surface is modified by HER2 specific antibody (trastuzumab fab) instead of the EGF sequence, was prepared, and its therapeutic performance was also evaluated [42, 43]. Targeting the gastric cancer diagnosis, glucose-regulated protein 78 (GRP78) binding peptide modified micelle was attached to the ^{111}In labeled micelle surface, and *in vivo* SPECT imaging was accomplished [44]. In short, polymeric micelle can be arranged in accordance with the intended uses.

Preparation of multifunctional micelles for photothermal therapy (PTT) is also conducted [45]. To the hydrophobic core of the micelle prepared from DTPA modified PCL-*b*-PEG, near-infrared (NIR) dye of IR-780 iodide was encapsulated as signal agent for NIRF imaging and photosensitizer for PTT. Further, ^{188}Re was chelated to DTPA as a signal source for SPECT imaging. The micelle was designed so that *in vivo* dynamics after dosage can be traced by SPECT system. Based on the real time monitoring of the micelle integration to the targeted tumor region, NIR light irradiation could be carried out.

Characters of molecular assemblies can be controlled by changing polymer architecture and its hydrophilic-hydrophobic balance. For example, thermosensitive hydrogel containing a therapeutic radionuclide (^{188}Re -Tin colloid) and a chemotherapeutic drug (liposomal doxorubicin) was prepared from PCL-*b*-PEG-*b*-PCL triblock copolymer [46]. The thermosensitive gel was intratumorally administrated to the hepatocellular carcinoma, and the therapeutic effect was evaluated. At the tumor region, liposomal doxorubicin and ^{188}Re -Tin colloid were released slowly and steadily. The therapeutic effect was greater than the cases in which either component was individually used, and the synergetic effect against tumor growth was confirmed.

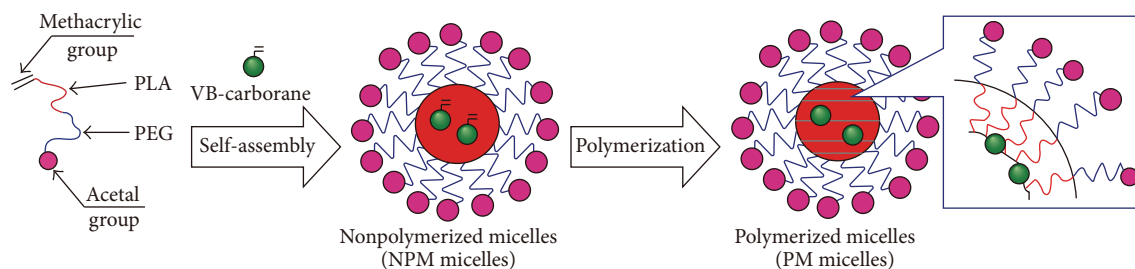


FIGURE 5: Schematic illustration of ^{10}B -enriched micelle preparation from acetal-PEG-*b*-PLA-MA and polymerizable VB-carborane. Reprinted from *Biomaterials*, 2012, 33, 3568-3577. S. Sumitani, M. Oishi, T. Yaguchi, H. Murotani, Y. Horiguchi, M. Suzuki, K. Ono, H. Yanagie, and Y. Nagasaki. "Pharmacokinetics of core-polymerized, boron-conjugated micelles designed for boron neutron capture therapy for cancer." Copyright (2012), with permission from Elsevier.

2.3.2. *Poly(ethylene glycol)-b-poly(lactic acid)*. Poly(lactic acid) (PLA) is representative biodegradable polymer connecting through ester linkage. Polymeric micelle prepared from PEG-*b*-PLA is also evaluated and used as nanoordered carriers for DDS by various research groups [47].

Nonradioactive ^{10}B is known to produce α particles and ^7Li nuclei with ca. 2.3 MeV of energy by the capture reaction of thermal neutrons, and therefore, utilization ^{10}B on boron neutron capture therapy (BNCT) is investigated. BNCT could make it possible to irradiate directly targeted tumor region with suppressing nonspecific exposure. However, restricted neutron source for the treatment is one of the major problems for practical usages. Sumitani et al. evaluated utilization of PEG-*b*-PLA micelle to improve delivering efficiency of boron derivatives to the targeted tumor region [48, 49]. In this study, polymeric micelle was prepared from amphiphilic PEG-*b*-PLA polymer derivative of acetal-PEG-*b*-PLA-MA, whose PEG and PLA terminal ends are modified by acetal and methacryloyl groups, respectively. To the micelle, 1-(4-vinylbenzyl)-*closo*-carborane (VB-carborane) and azobisisobutyronitrile (AIBN) mixtures were encapsulated, and core cross-polymerized and boron-conjugated micelles were prepared by the free radical polymerization method (Figure 5). To the tumor transplanted mice, the ^{10}B -enriched micelle was administrated, and neutron irradiation was performed after 24 h from the dosage. The ^{10}B -enriched micelle was accumulated at the tumor region and showed significant therapeutic effects after the neutron irradiation.

2.3.3. *Poly(sarcosine)-b-poly(L-lactic acid)*. Amphiphilic polydeipeptide of (sarcosine) $_{70}$ -*b*-(L-lactic acid) $_{30}$ is known to form polymeric micelle with diameter of ca. 35 nm, and the polymeric micelle was named as "Lactosome" [18, 50]. Sarcosine (Sar), *N*-methyl glycine in other words, is natural amino acid, and its homopolymer shows high solubility against aqueous solution like PEG. Therefore, polymeric micelle whose surface is covered with poly(Sar) was also expected to show a prolonged blood circulation behavior with low undesired accumulation by reticuloendothelial system (RES).

As a radionuclide for PET imaging, hydrophobized ^{18}F by attaching PLLA chain (^{18}F)SFB labeled poly(L-lactic acid)

of 30 mer) was encapsulated into the core region of the polymeric micelle by using hydrophobic interactions [51]. The ^{18}F labeled Lactosome was administrated from the tail vein to the tumor transplanted mice, and PET images were taken after 6 h from the dosage. Lactosome showed a good blood circulation behavior owing to the surface modification with hydrophilic poly(sarcosine) chains. Therefore, signal intensity at organs with high blood flows was high. However, the accumulated signal in the transplanted tumor region could be detected. Since Lactosome surface was not specifically modified by ligands, Lactosome is considered to be passively accumulated to the tumor region by the EPR effect.

As a therapeutic radionuclide, [^{131}I]SIB labeled PLLA was encapsulated into the Lactosome as β^- ray emitter by the same approach with the previous ^{18}F compound for PET imaging. To the tumor transplanted mice, which were preliminary treated with preethanol injection therapy (PEIT), ^{131}I labeled Lactosome of 200 MBq/kg was injected and time courses of tumor growth were observed [52]. As a result, ^{131}I labeled Lactosome could be delivered to the tumor region, and the tumor growth was significantly suppressed.

2.4. *Accelerated Blood Clearance (ABC) Phenomenon of Lactosome*. Lactosome is a candidate nanoordered carrier for drug and/or imaging agent delivery. On medicinal usages, nanocarriers are expected to show unaltered disposition on multiple administrations. However, production of anti-Lactosome antibody occurred after 3 days from the first Lactosome administration, and the antibody production kept high level for 6 months [53]. Lactosome on second dosage was opsonized by the anti-Lactosome antibody soon after the administration and entrapped by reticuloendothelial system (RES). This phenomenon is named as accelerated blood clearance (ABC) phenomenon of Lactosome, and resembled phenomenon is sometimes observed on PEGylated materials [54, 55].

The production amounts of the anti-Lactosome IgM were revealed to be inversely correlated with that of the first Lactosome dosage. When first Lactosome dosage is over 150 mg/kg, the Lactosome ABC phenomenon

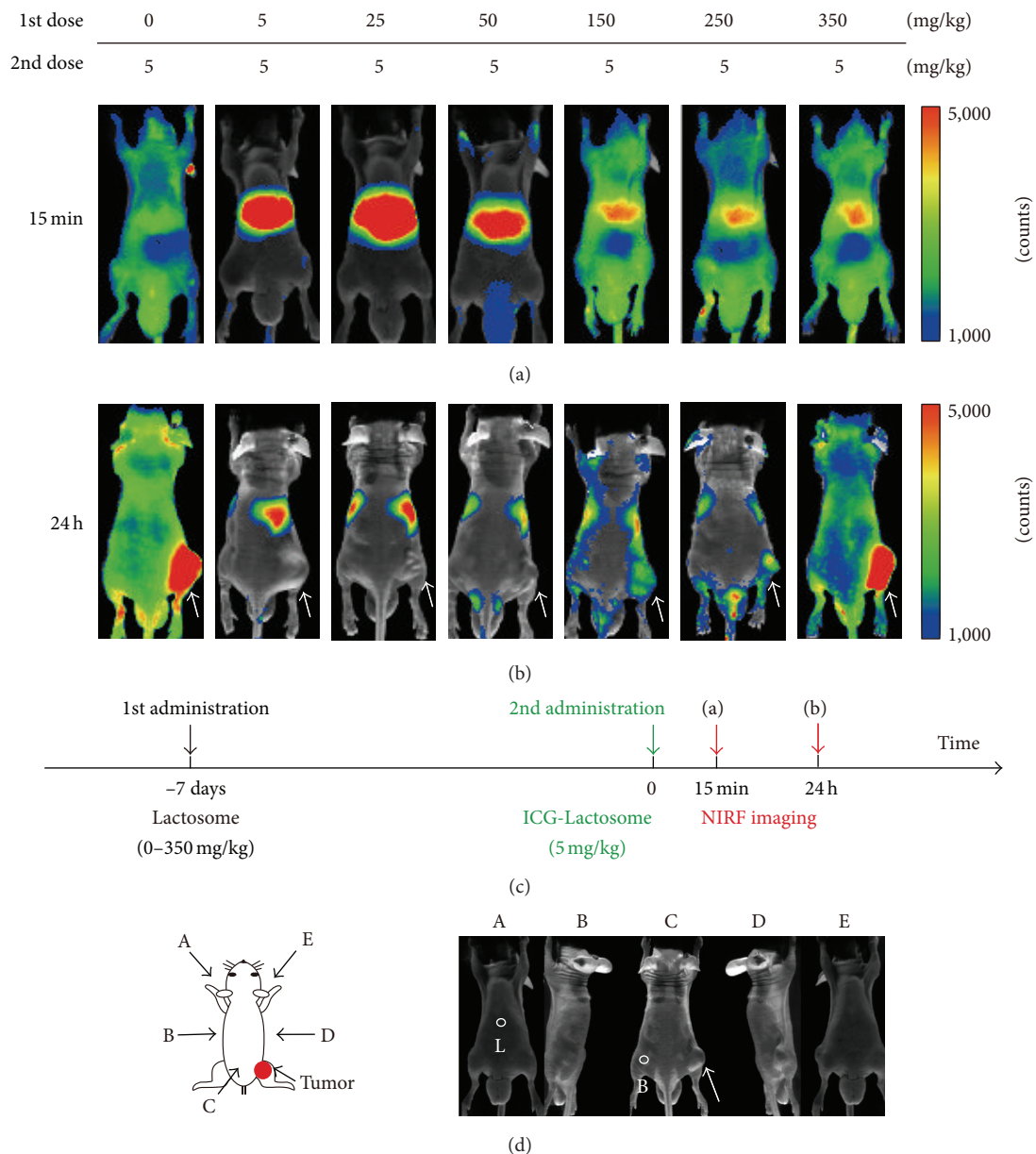


FIGURE 6: Effect of the first Lactosome dose on the Lactosome ABC phenomenon. NIRF images of mice at (a) 15 min (view from A in Figure 6(d)) and (b) 24 h (view from C in Figure 6(d)) after ICG-Lactosome of 2nd dose. Lactosomes (5, 25, and 50 mg/kg/100 μ L and 150, 250, and 350 mg/kg/200 μ L) were injected into the mice 7 days before the ICG-Lactosome administration. SUIT-2/pEF/luc cells were transplanted at the right femoral region of mice, in which tumor sites are indicated by white arrows. The fluorescein signal ranges were set to be the same for all the images from max count 5000 to min count 1000. (c) Time schedule for the NIRF imaging. Black and green arrows indicate the injection time points of Lactosome and ICG-Lactosome, respectively. NIRF imaging was performed at red arrows. (d) NIRF images were taken using Shimadzu Clairvivo OPT, which can take five images from different directions (A–E) with one time shot. The white circles indicate positions of ROI (L: liver; B: background). Reprinted from *Biochimica et Biophysica Acta (BBA)-General Subjects*, 2013, 1830, 4046–4052., E. Hara, A. Makino, K. Kurihara, M. Sugai, A. Shimizu, I. Hara, E. Ozeki, and S. Kimura. “Evasion from accelerated blood clearance of nanocarrier named as “Lactosome” induced by excessive administration of Lactosome.” Copyright (2013), with permission from Elsevier B.V.

could be suppressed by induced immunological tolerance (Figure 6). Further, even if anti-Lactosome IgM is once produced, the Lactosome ABC phenomenon can be evaded by dosing Lactosome over 50 mg/kg. Importantly, acute toxicity was not observed at the Lactosome dosage amount [56].

Recently the production of anti-Lactosome IgM has been found to be suppressed by increasing the local density of poly(sarcosine) chains on the micelle surface. Higher local density of the surrounding hydrophilic polymer chains should be related with prevention of the interaction between micelles and B cell receptors [57].

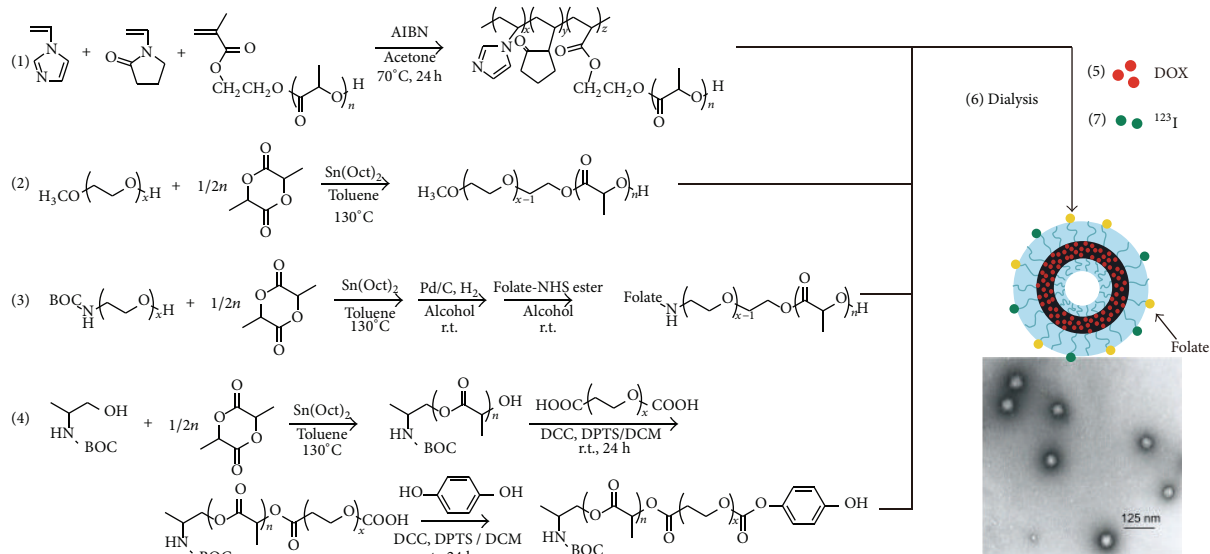


FIGURE 7: Representation of multifunctional hollow nanoparticles and their TEM image. Reprinted from Biomaterials, 2011, 32, 2213-2221., P. L. Lu, Y. C. Chen, T. W. Ou, H. H. Chen, H. C. Tsai, C. J. Wen, C. L. Lo, S. P. Wey, K. J. Lin, T. C. Yen, and G. H. Hsiue. "Multifunctional hollow nanoparticles based on graft-diblock copolymers for doxorubicin delivery." Copyright (2011), with permission from Elsevier.

Further, it is still unclear whether the ABC phenomenon is a general phenomenon for nanoparticles. However, to develop repeatedly injectable nanoordered carriers is essential for its general usages.

3. Vesicular Assemblies

The number of examples using vesicular assemblies as a carrier for DDS in nuclear medicinal field is relatively limited. It may be because of more difficult preparation of vesicular assemblies than polymeric micelles.

Lu et al. prepared multifunctional hollow nanoparticle from a mixture of doxorubicin hydrochloride (DOX-HCl), mPEG₅₀₀₀-*b*-poly(D,L-lactic acid)₁₅₁₀ (mPEG₅₀₀₀-*b*-PLA₁₅₁₀), folate-PEG₅₀₀₀-*b*-PLA₁₂₀₀, phenolic ester-PEG₅₀₀₀-*b*-PLA₆₅₀, and poly(*N*-vinylimidazole-*co*-*N*-vinylpyrrolidone)₉₆₀₀-*g*-PLA₄₉₀₀ (Figure 7) [58]. The hollow nanoparticle is designed to show sensitivity against intracellular pH changes by using pH sensitive character of *N*-vinylimidazole (NVI) (pKa values of NVI are around 6.0). Depending on the pH changes of the dispersion, its diameter was reversibly changed between 90 nm (pH 7.4) and 80 nm (pH 5.0), and rate of encapsulated DOX-HCl release could be accelerated under weak acidic conditions. Extracellular matrix of the tumor region is known to be in a weakly acidic condition, and therefore, the DOX-HCl is expected to be released selectively at the tumor region. Folate-PEG₅₀₀₀-*b*-PLA₁₂₀₀ provided the nanoparticle with a tumor-targeting ability, and phenolic ester-PEG₅₀₀₀-*b*-PLA₆₅₀ was used for modification of the nanoparticle with ^{125}I by the iodogen method.

To the tumor transplanted mice, the multifunctional hollow nanoparticle was administrated, and the time course of tumor growth was observed. Dynamics of the nanoparticle at 0.5–6 h from the administration were noninvasively

visualized by SPECT. Shortly after the administration, the nanoparticle was accumulated at the tumor region with a high level due to the folate-binding protein effect. Compared with the case of free DOX-HCl, the tumor growth was effectively suppressed with a minimum body weight loss.

4. Conclusion

In particular in these ten years, application of polymeric nanoparticles as a carrier for tumor-targeted drug delivery system (DDS) is expanded to nuclear medicinal fields. It is a tremendous advantage to apply polymeric nanoparticles for DDS, because *in vivo* pharmacokinetics can be well controlled by suitable selections about their size, shape, and surface characters and can be free from the loading imaging or therapeutic compounds. Therefore, when the same nanoparticle is used as a carrier for imaging and therapeutic purposes, diagnostic outcomes can directly predict the treatment efficiency of the loading therapeutic agent on the nanoparticle. Further, imaging results before and after chemotherapy can be used for prediction and evaluation of the therapeutic effect, respectively. In order to improve personal medical treatment, it is essential to dose the therapeutic agent properly to each patient. Polymeric micelles and vesicles endowed with two functions for diagnosis and therapy are expected to be potential materials for future personalized medicine, and these research areas are especially named as "nanotheranostics."

However, there are many research problems to be dissolved. For example, almost all types of nanoparticles are designed to evade from undesired capture by reticuloendothelial system (RES) and to show a prolonged blood circulation behavior. Radioactivity is decreased with distinct half-life of each radionuclide, and time period, which can

be effectively used, is limited. Therefore, radionuclides with relatively long half-life period such as ^{64}Cu for PET and ^{111}In for SPECT are mainly selected for radiolabeling of polymer nanoparticles. Further, how to control radiation exposure is also extremely important in nuclear medicinal fields. For these reasons, purpose of polymer nanoparticle DDS is mainly diagnosis, which can be performed by relatively low radioactivity, and research trials on inner radiotherapy are small in number. To accomplish practical usages of polymer nanoparticles as carriers for inner radiotherapy, (1) further improvement of drug delivery efficiency and (2) reduction of radiation exposure at radiosensitive organs such as bone marrow are essential by controlling the nanoparticles *in vivo* dynamics. It has already been revealed that to create synergetic therapeutic effect is possible by combined usages of therapeutic nanoparticle with conventional therapies, and therefore, therapeutic nanoparticles are now in an early phase of development.

Another problem for the view point of commercialization is how to ensure the quality of the nanoparticle. The number of examples utilizing polymeric nanoparticles as carriers for DDS in human clinical practice is limited. Therefore, to make rules for polymer nanoparticle production and their clinical studies is also considered to be important and started in government regulatory agencies [59].

There are many problems to be dissolved; however, application and commercialization researches on theranostic nanoparticles are expected surely to make future progresses in nuclear medicinal fields.

Conflict of Interests

The authors declare that there is no conflict of interests regarding the publication of this paper.

Acknowledgment

This study was partially supported by Coordination, Support and Training Program for Translational Research by MEXT, Japan.

References

- [1] R. Hao, R. J. Xing, Z. C. Xu, Y. L. Hou, S. Goo, and S. H. Sun, "Synthesis, functionalization, and biomedical applications of multifunctional magnetic nanoparticles," *Advanced Materials*, vol. 22, no. 25, pp. 2729–2742, 2010.
- [2] P. Horcajada, R. Gref, T. Baati et al., "Metal-organic frameworks in biomedicine," *Chemical Reviews*, vol. 112, no. 2, pp. 1232–1268, 2012.
- [3] D. Peer, J. M. Karp, S. Hong, O. C. Farokhzad, R. Margalit, and R. Langer, "Nanocarriers as an emerging platform for cancer therapy," *Nature Nanotechnology*, vol. 2, no. 12, pp. 751–760, 2007.
- [4] M. Ferrari, "Cancer nanotechnology: opportunities and challenges," *Nature Reviews Cancer*, vol. 5, no. 3, pp. 161–171, 2005.
- [5] R. K. Jain and T. Stylianopoulos, "Delivering nanomedicine to solid tumors," *Nature Reviews Clinical Oncology*, vol. 7, no. 11, pp. 653–664, 2010.
- [6] Z. Jiao, X. Wang, and Z. Chen, "Advance of amphiphilic block copolymeric micelles as drug delivery," *Asian Journal of Chemistry*, vol. 25, no. 4, pp. 1765–1769, 2013.
- [7] M. Elsabahy and K. L. Wooley, "Design of polymeric nanoparticles for biomedical delivery applications," *Chemical Society Reviews*, vol. 41, no. 7, pp. 2545–2561, 2012.
- [8] Z. Ge and S. Liu, "Functional block copolymer assemblies responsive to tumor and intracellular microenvironments for site-specific drug delivery and enhanced imaging performance," *Chemical Society Reviews*, vol. 42, no. 17, pp. 7289–7325, 2013.
- [9] S. Ganta, H. Devalapally, A. Shahiwala, and M. Amiji, "A review of stimuli-responsive nanocarriers for drug and gene delivery," *Journal of Controlled Release*, vol. 126, no. 3, pp. 187–204, 2008.
- [10] J. H. Park, S. Lee, J.-H. Kim, K. Park, K. Kim, and I. C. Kwon, "Polymeric nanomedicine for cancer therapy," *Progress in Polymer Science*, vol. 33, no. 1, pp. 113–137, 2008.
- [11] J. Fang, H. Nakamura, and H. Maeda, "The EPR effect: unique features of tumor blood vessels for drug delivery, factors involved, and limitations and augmentation of the effect," *Advanced Drug Delivery Reviews*, vol. 63, no. 3, pp. 136–151, 2011.
- [12] A. K. Iyer, G. Khaled, J. Fang, and H. Maeda, "Exploiting the enhanced permeability and retention effect for tumor targeting," *Drug Discovery Today*, vol. 11, no. 17–18, pp. 812–818, 2006.
- [13] H. Maeda, J. Wu, T. Sawa, Y. Matsumura, and K. Hori, "Tumor vascular permeability and the EPR effect in macromolecular therapeutics: a review," *Journal of Controlled Release*, vol. 65, no. 1–2, pp. 271–284, 2000.
- [14] L. Brannon-Peppas and J. O. Blanchette, "Nanoparticle and targeted systems for cancer therapy," *Advanced Drug Delivery Reviews*, vol. 64, pp. 206–212, 2012.
- [15] S. P. Egusquiaguirre, M. Igartua, R. M. Hernández, and J. L. Pedraz, "Nanoparticle delivery systems for cancer therapy: advances in clinical and preclinical research," *Clinical and Translational Oncology*, vol. 14, no. 2, pp. 83–93, 2012.
- [16] H. Tanisaka, S. Kizaka-Kondoh, A. Makino, S. Tanaka, M. Hiraoka, and S. Kimura, "Near-infrared fluorescent labeled peptosome for application to cancer imaging," *Bioconjugate Chemistry*, vol. 19, no. 1, pp. 109–117, 2008.
- [17] Y. Chen and X. Li, "Near-infrared fluorescent nanocapsules with reversible response to thermal/PH modulation for optical imaging," *Biomacromolecules*, vol. 12, no. 12, pp. 4367–4372, 2011.
- [18] A. Makino, S. Kizaka-Kondoh, R. Yamahara et al., "Near-infrared fluorescence tumor imaging using nanocarrier composed of poly(L-lactic acid)-block-poly(sarcosine) amphiphilic polydepsipeptide," *Biomaterials*, vol. 30, no. 28, pp. 5156–5160, 2009.
- [19] R. Weissleder, "A clearer vision for in vivo imaging," *Nature Biotechnology*, vol. 19, no. 4, pp. 316–317, 2001.
- [20] D. L. Bailey and K. P. Willowson, "Quantitative SPECT/CT: SPECT joins PET as a quantitative imaging modality," *European Journal of Nuclear Medicine and Molecular Imaging*, vol. 41, no. 1, pp. 17–25, 2013.
- [21] Y. Li, S. M. A. Rizvi, J. M. Blair et al., "Antigenic expression of human metastatic prostate cancer cell lines for in vitro multiple-targeted α -therapy with ^{213}Bi -conjugates," *International Journal of Radiation Oncology Biology Physics*, vol. 60, no. 3, pp. 896–908, 2004.
- [22] B. Cornelissen, S. Darbar, R. Hernandez et al., "ErbB-2 blockade and prenyltransferase inhibition alter epidermal growth factor

- and epidermal growth factor receptor trafficking and enhance ^{111}In -DTPA-hEGF auger electron radiation therapy,” *Journal of Nuclear Medicine*, vol. 52, no. 5, pp. 776–783, 2011.
- [23] D. L. Costantini, C. Chan, Z. L. Cai, K. A. Vallis, and R. M. Reilly, “ ^{111}In -labeled trastuzumab (Herceptin) modified with nuclear localization sequences (NLS): an auger electron-emitting radiotherapeutic agent for HER2/neu-amplified breast cancer,” *The Journal of Nuclear Medicine*, vol. 48, no. 8, pp. 1357–1368, 2007.
- [24] B. Cambien, P. R. Franken, A. Lamit et al., “(TcO_4^-)- Tc -99m-, auger-mediated thyroid stunning: dosimetric requirements and associated molecular events,” *PLoS ONE*, vol. 9, no. 3, Article ID e92729, 2014.
- [25] W. D. Bloomer and S. J. Adelstein, “5-125I-iododeoxyuridine as prototype for radionuclide therapy with Auger emitters,” *Nature*, vol. 265, no. 5595, pp. 620–621, 1977.
- [26] R. Rossin, D. P. J. Pan, K. Qi et al., “ ^{64}Cu -labeled folate-conjugated shell cross-linked nanoparticles for tumor imaging and radiotherapy: synthesis, radiolabeling, and biologic evaluation,” *Journal of Nuclear Medicine*, vol. 46, no. 7, pp. 1210–1218, 2005.
- [27] K. Qi, Q. Ma, E. E. Remsen, C. G. Clark Jr., and K. L. Wooley, “Determination of the bioavailability of biotin conjugated onto shell cross-linked (SCK) nanoparticles,” *Journal of the American Chemical Society*, vol. 126, no. 21, pp. 6599–6607, 2004.
- [28] J. Sudimack and R. J. Lee, “Targeted drug delivery via the folate receptor,” *Advanced Drug Delivery Reviews*, vol. 41, no. 2, pp. 147–162, 2000.
- [29] E. D. Pressly, R. Rossin, A. Hagooley et al., “Structural effects on the biodistribution and positron emission tomography (PET) imaging of well-defined ^{64}Cu -labeled nanoparticles comprised of amphiphilic block graft copolymers,” *Biomacromolecules*, vol. 8, no. 10, pp. 3126–3134, 2007.
- [30] M. Allmeroth, D. Moderegger, D. Gündel et al., “PEGylation of HPMA-based block copolymers enhances tumor accumulation in vivo: a quantitative study using radiolabeling and positron emission tomography,” *Journal of Controlled Release*, vol. 172, no. 1, pp. 77–85, 2013.
- [31] M. Allmeroth, D. Moderegger, D. Gündel et al., “HPMA-LMA copolymer drug carriers in oncology: an in vivo PET study to assess the tumor line-specific polymer uptake and body distribution,” *Biomacromolecules*, vol. 14, no. 9, pp. 3091–3101, 2013.
- [32] Z. Yang, S. Zheng, W. J. Harrison et al., “Long-circulating near-infrared fluorescence core-cross-linked polymeric micelles: synthesis, characterization, and dual nuclear/optical imaging,” *Biomacromolecules*, vol. 8, no. 11, pp. 3422–3428, 2007.
- [33] R. Zhang, C. Xiong, M. Huang et al., “Peptide-conjugated polymeric micellar nanoparticles for Dual SPECT and optical imaging of EphB4 receptors in prostate cancer xenografts,” *Biomaterials*, vol. 32, no. 25, pp. 5872–5879, 2011.
- [34] Y. Hong, H. Zhu, J. Hu et al., “Synthesis and radiolabeling of ^{111}In -core-cross linked polymeric micelle-octreotide for near-infrared fluorescence and single photon emission computed tomography imaging,” *Bioorganic and Medicinal Chemistry Letters*, vol. 24, no. 12, pp. 2781–2785, 2014.
- [35] R. Zhang, W. Lu, X. Wen et al., “Annexin A5-conjugated polymeric micelles for dual SPECT and optical detection of apoptosis,” *Journal of Nuclear Medicine*, vol. 52, no. 6, pp. 958–964, 2011.
- [36] A. I. Jensen, T. Binderup, P. Kumar Ek, A. Kjær, P. H. Rasmussen, and T. L. Andresen, “Positron emission tomography based analysis of long-circulating cross-linked triblock polymeric micelles in a U87MG mouse xenograft model and comparison of DOTA and CB-TE2A as chelators of copper-64,” *Biomacromolecules*, vol. 15, no. 5, pp. 1625–1633, 2014.
- [37] M. Okada, “Chemical syntheses of biodegradable polymers,” *Progress in Polymer Science*, vol. 27, no. 1, pp. 87–133, 2002.
- [38] B. Hoang, H. Lee, R. M. Reilly, and C. Allen, “Noninvasive monitoring of the fate of ^{111}In -labeled block copolymer micelles by high resolution and high sensitivity microSPECT/CT imaging,” *Molecular Pharmaceutics*, vol. 6, no. 2, pp. 581–592, 2009.
- [39] H. Lee, B. Hoang, H. Fonge, R. M. Reilly, and C. Allen, “In vivo distribution of polymeric nanoparticles at the whole-body, tumor, and cellular levels,” *Pharmaceutical Research*, vol. 27, no. 11, pp. 2343–2355, 2010.
- [40] R. M. Reilly, R. Kiarash, R. G. Cameron et al., “ ^{111}In -labeled EGF is selectively radiotoxic to human breast cancer cells overexpressing EGFR,” *Journal of Nuclear Medicine*, vol. 41, no. 3, pp. 429–438, 2000.
- [41] H. Fonge, H. Lee, R. M. Reilly, and C. Allen, “Multifunctional block copolymer micelles for the delivery of ^{111}In to EGFR-positive breast cancer cells for targeted Auger electron radiotherapy,” *Molecular Pharmaceutics*, vol. 7, no. 1, pp. 177–186, 2010.
- [42] B. Hoang, R. M. Reilly, and C. Allen, “Block copolymer micelles target auger electron radiotherapy to the nucleus of HER2-positive breast cancer cells,” *Biomacromolecules*, vol. 13, no. 2, pp. 455–465, 2012.
- [43] B. Hoang, S. N. Ekdawi, R. M. Reilly, and C. Allen, “Active targeting of block copolymer micelles with trastuzumab fab fragments and nuclear localization signal leads to increased tumor uptake and nuclear localization in HER2-overexpressing xenografts,” *Molecular Pharmaceutics*, vol. 10, no. 11, pp. 4229–4241, 2013.
- [44] C.-C. Cheng, C.-F. Huang, A.-S. Ho et al., “Novel targeted nuclear imaging agent for gastric cancer diagnosis: glucose-regulated protein 78 binding peptide-guided ^{111}In -labeled polymeric micelles,” *International Journal of Nanomedicine*, vol. 8, pp. 1385–1391, 2013.
- [45] C.-L. Peng, Y.-H. Shih, P.-C. Lee, T. M.-H. Hsieh, T.-Y. Luo, and M.-J. Shieh, “Multimodal image-guided photothermal therapy mediated by ^{188}Re -labeled micelles containing a cyanine-type photosensitizer,” *ACS Nano*, vol. 5, no. 7, pp. 5594–5607, 2011.
- [46] C.-L. Peng, Y.-H. Shih, K.-S. Liang et al., “Development of in situ forming thermosensitive hydrogel for radiotherapy combined with chemotherapy in a mouse model of hepatocellular carcinoma,” *Molecular Pharmaceutics*, vol. 10, no. 5, pp. 1854–1864, 2013.
- [47] D. H. Yu, Q. Lu, J. Xie, C. Fang, and H. Z. Chen, “Peptide-conjugated biodegradable nanoparticles as a carrier to target paclitaxel to tumor neovasculature,” *Biomaterials*, vol. 31, no. 8, pp. 2278–2292, 2010.
- [48] S. Sumitani, M. Oishi, T. Yaguchi et al., “Pharmacokinetics of core-polymerized, boron-conjugated micelles designed for boron neutron capture therapy for cancer,” *Biomaterials*, vol. 33, no. 13, pp. 3568–3577, 2012.
- [49] S. Sumitani and Y. Nagasaki, “Boron neutron capture therapy assisted by boron-conjugated nanoparticles,” *Polymer Journal*, vol. 44, no. 6, pp. 522–530, 2012.
- [50] A. Makino, E. Hara, I. Hara et al., “Control of in vivo blood clearance time of polymeric micelle by stereochemistry of

- amphiphilic polydepsipeptides,” *Journal of Controlled Release*, vol. 161, no. 3, pp. 821–825, 2012.
- [51] F. Yamamoto, R. Yamahara, A. Makino et al., “Radiosynthesis and initial evaluation of 18F labeled nanocarrier composed of poly(L-lactic acid)-block-poly(sarcosine) amphiphilic polydepsipeptide,” *Nuclear Medicine and Biology*, vol. 40, no. 3, pp. 387–394, 2013.
- [52] E. Hara, A. Makino, K. Kurihara et al., “Radionuclide therapy using nanoparticle of 131I-Lactosome in combination with percutaneous ethanol injection therapy,” *Journal of Nanoparticle Research*, vol. 15, Article ID 2131, 2013.
- [53] E. Hara, A. Makino, K. Kurihara, F. Yamamoto, E. Ozeki, and S. Kimura, “Pharmacokinetic change of nanoparticulate formulation “Lactosome” on multiple administrations,” *International Immunopharmacology*, vol. 14, no. 3, pp. 261–266, 2012.
- [54] T. Ishida and H. Kiwada, “Accelerated blood clearance (ABC) phenomenon upon repeated injection of PEGylated liposomes,” *International Journal of Pharmaceutics*, vol. 354, no. 1-2, pp. 56–62, 2008.
- [55] A. S. Abu Lila, H. Kiwada, and T. Ishida, “The accelerated blood clearance (ABC) phenomenon: clinical challenge and approaches to manage,” *Journal of Controlled Release*, vol. 172, no. 1, pp. 38–47, 2013.
- [56] E. Hara, A. Makino, K. Kurihara et al., “Evasion from accelerated blood clearance of nanocarrier named as “lactosome” induced by excessive administration of Lactosome,” *Biochimica et Biophysica Acta—General Subjects*, vol. 1830, no. 8, pp. 4046–4052, 2013.
- [57] E. Hara, M. Ueda, A. Makino, I. Hara, E. Ozeki, and S. Kimura, “Factors influences *in vivo* disposition of polymeric micelles on multiple administrations,” *ACS Medicinal Chemistry Letters*, vol. 5, no. 8, pp. 873–877, 2014.
- [58] P.-L. Lu, Y.-C. Chen, T.-W. Ou et al., “Multifunctional hollow nanoparticles based on graft-diblock copolymers for doxorubicin delivery,” *Biomaterials*, vol. 32, no. 8, pp. 2213–2221, 2011.
- [59] M. G. Wacker, “Nanotherapeutics—product development along the nanomaterial discussion,” *Journal of Pharmaceutical Sciences*, vol. 103, no. 3, pp. 777–784, 2014.

Review Article

Radioimmunotherapy: A Specific Treatment Protocol for Cancer by Cytotoxic Radioisotopes Conjugated to Antibodies

Hidekazu Kawashima

Department of Radiopharmaceutical Chemistry, Faculty of Pharmaceutical Sciences, Health Sciences University of Hokkaido, 1757 Kanazawa, Tobetsu-cho, Ishikari-gun, Hokkaido 061-0293, Japan

Correspondence should be addressed to Hidekazu Kawashima; kawashima@hoku-iryo-u.ac.jp

Received 27 June 2014; Accepted 4 August 2014; Published 14 October 2014

Academic Editor: Masahiro Ono

Copyright © 2014 Hidekazu Kawashima. This is an open access article distributed under the Creative Commons Attribution License, which permits unrestricted use, distribution, and reproduction in any medium, provided the original work is properly cited.

Radioimmunotherapy (RIT) represents a selective internal radiation therapy, that is, the use of radionuclides conjugated to tumor-directed monoclonal antibodies (including those fragments) or peptides. In a clinical field, two successful examples of this treatment protocol are currently extended by ^{90}Y -ibritumomab tiuxetan (Zevalin) and ^{131}I -tositumomab (Bexxar), both of which are anti-CD20 monoclonal antibodies coupled to cytotoxic radioisotopes and are approved for the treatment of non-Hodgkin lymphoma patients. In addition, some beneficial observations are obtained in preclinical studies targeting solid tumors. To date, in order to reduce the unnecessary exposure and to enhance the therapeutic efficacy, various biological, chemical, and treatment procedural improvements have been investigated in RIT. This review outlines the fundamentals of RIT and current knowledge of the preclinical/clinical trials for cancer treatment.

1. What Is Radioimmunotherapy (RIT)?

Antibodies (Abs) are glycoproteins secreted from plasma B cell and are used by immune system to identify and remove foreign pathogens such as bacteria and viruses. Because it is considered that Abs also have cytotoxic potency against some malignant tumor cells, the therapeutic efficacy in cancer has been examined. However, intact Abs are insufficient to improve patient survival rate dramatically. As a one approach to enhance the therapeutic response by using immunological technique, cytotoxic radioisotopes (α - or β -particle emitters) are conjugated to Abs or the fragments. This strategy is employed to deliver radioisotopes to the targeting tissue by appropriate vehicle. After the radiolabeled Abs bind to receptors/tumor antigens expressed on the surface of cancerous tissue, cells within an anatomic region of the α - or β -range will be killed.

In a clinical field, systemic radiotherapy using naked radioisotope (iodine-131: ^{131}I) was first performed by Hertz to patient of Graves' disease in 1941 [1]. Then, investigations on the use of Abs coupled with adequate radioisotopes subsequently emerged in the early 1950s [2, 3]. Though direct

radioiodinated Abs were mainly used in the initial clinical studies, progress in chelation chemistry has enabled the utilization of many therapeutic metal radioisotopes that possess inherent radiation properties. Various combinations of Abs and radioisotopes have been examined, which results in the adaptation in different clinical situations [4, 5]. RIT involves the application of radiolabeled monoclonal Abs (mAbs) to molecular targeted therapy [6]. Both the use of directly labeled mAbs and in vivo label of tumor-binding mAbs by conjugation-pretargeting method have been developed.

Irradiated cells absorb high amounts of energy in the form of photons or charged particles, which promote the direct macromolecular damage as well as the generation of reactive oxygen and/or nitrogen species [7]. Both free radicals and molecular oxygen damage DNA strand [8, 9], and the damage induces not only apoptosis [10] but also programmed necrosis [11]. Because the ranges in tissue of ionizing radiations are rather large compared with a typical cell size, uniform binding of the radioimmunoconjugates is not a prerequisite for its efficacy. In other words, adjacent cells not expressing the receptors/tumor antigens can also be killed

TABLE 1: Radioisotopes used in RIT.

Radioisotope	Energy _{max} (MeV)	Range	Half-life
β -Particle emitter			
⁶⁷ Cu	0.58	2.1 mm	2.6 d
⁹⁰ Y	2.28	12.0 mm	2.7 d
¹³¹ I	0.61	2.0 mm	8.0 d
¹⁷⁷ Lu	0.50	1.5 mm	6.7 d
¹⁸⁶ Re	1.07	4.5 mm	3.7 d
¹⁸⁸ Re	2.12	10.4 mm	16.9 hr
α -Particle emitter			
²¹¹ At	6.8	80 μ m	7.2 hr
²¹³ Bi	8.3	84 μ m	46 min
²²⁵ Ac	6.0~8.0	60~90 μ m	10.0 d
Auger-electron emitter			
¹²⁵ I		2~500 nm	60.5 d

by the physical cross-fire effect. This means continuous low-dose irradiation from radiolabeled Abs cause lethal effects on nearby normal cells. Moreover, it is reported that RITs also evoke the normalization of tumor vasculature [12], presumably owing to facilitation of immune cell migration towards the malignant lesions [13].

For therapy, therefore, α - or β -particle emitters are preferable. Vehicles coupled with radioisotopes emitting Auger electrons are also available; however, they need to be localized close to DNA due to the very short range of these radiations [14–16]. Simultaneous emission of γ (X) rays, which are suitable for imaging, will help measure pharmacokinetic parameters and calculate dosimetry of the radioimmunoconjugates. Table 1 shows radioisotopes commonly used for RIT.

Among them, relatively well-studied and practical radioisotopes are the β -emitters ¹³¹I, yttrium-90 (⁹⁰Y), and lutetium-177 (¹⁷⁷Lu). Radioisotope to use is selected by consideration of those radiophysical properties (energy and half-life) as well as the labeling chemistry. For example, ⁹⁰Y possesses a higher β -particle E_{\max} and a shorter half-life when compared with ¹³¹I. On the other hand, metal ⁹⁰Y should be conjugated to Ab via chelating agent, whereas ¹³¹I can form a carbon-iodine bond directly. Lutetium-177 has radiophysical properties similar to ¹³¹I and radiolabeling chemistry similar to ⁹⁰Y.

Investigations of RIT using α -particle emitters also have been developed. Because α -particle gives its energy to the surrounding molecules within a narrow range (<100 μ m, equivalent to a few cell diameters), it leads to high linear energy transfer (high LET) within the target and less bystander effect to nontarget tissues compared to Abs labeled with β -emitters. In addition to the high LET, which leads to the high relative biological effectiveness (RBE) [17], recent studies have shown that cytotoxic efficacy of α -particle is independent of the local oxygen concentration and cell cycle state [18]. Bismuth-213 (²¹³Bi), astatine-211 (²¹¹At), and actinium-225 (²²⁵Ac) are well investigated in α -particle RIT [19–22].

Compared to external beam radiation therapy, one of the most potent advantages of RIT is the ability to attack not only the primary tumor but also lesions systemically metastasizing. In addition, targeted radiotherapy using specific vehicle agents is extremely valuable in cases of (1) residual micrometastatic lesions, (2) residual tumor margins after surgical resection, (3) tumors in the circulating blood including hematologic malignancy, and (4) malignancies that present as free-floating cells [23].

Brief data on current RITs provided in this review paper is summarized in Table 2.

2. Direct Method

The success of RIT depends on the selective accumulation of cytotoxic radioisotopes at affected areas. Fundamental properties required for vehicles against a particular biomarker are (1) high binding affinity to the intended target, (2) high specificity, (3) high tumor to background ratio, (4) high metabolic stability, and (5) low immunogenicity [24, 25]. From the viewpoint of those molecular characteristics, Abs have been considered as suitable agent for the delivery of therapeutic radioisotopes. Moreover, the development of hybridoma technology in 1975 allowed taking advantage of mAbs in RIT [26].

“Direct method” requires direct conjugation of cytotoxic radioisotopes to various antitumor mAbs (or their fragments) via an appropriate chelator and the single-step administration to patients. Consequently, many antigenic determinants (mostly on the cell surface) have been targeted by Abs. On the other hand, one of the most critical obstacles to achieve high background ratio in this application is the slow clearance of Abs from the blood and nontarget tissues due to their high molecular weight [27, 28]. Abs will disappear from plasma very slowly, which encourages higher tumor uptake; however, a longer duration is needed to reach the maximum tumor to normal radioactivity ratio. Radiation dose for treating patient increases time-dependently, which results in the exposure of radioactive bone marrow leading to the hematologic toxicity. Therefore, structural diversification of Abs has been attempted to improve the pharmacokinetic properties. Lower molecular weight fragments of conventional Abs including F(ab')₂, Fab or its multivalent conjugate, minibody, diabody, and single chain variable fragments (scFv) could be utilized, which retain the essential antigen binding properties and obtain more rapid clearance rates than intact mAbs. Those smaller types of constructs can traverse the vascular channels, resulting in a more rapid tumor uptake and a faster blood clearance than parental Abs [29, 30], possessing potencies to achieve superior tumor to background ratios. In general, however, affinities of small Ab forms to tumor antigen are lower than those of Abs, and, moreover, too fast blood clearance of peptides yields less time to interact with the target. Therefore, absolute tumor uptake for these constructs is lower than those of Abs. Further development of the engineered forms holding both favorable pharmacokinetics

TABLE 2: Anticancer RITs reported in this century.

Cancer	Target molecule	mAb	Radioisotope	Subject	Reference
Non-Hodgkin lymphoma	CD20	Direct method	Y-90 I-131 I-131 Y-90 Bi-213 Ga-67 Y-90 At-211 I-131 I-131 I-131 Y-90 Pb-212 In-111 At-211 Y-90 Y-90 Lu-177 Bi-213 Bi-213	Human (in clinical use)	[33]
		Ibritumomab		Human (in clinical use)	[31, 33, 34]
		Tositumomab		Human (phase II)	[35-37]
		Rituximab		Human (phase II)	[32, 38, 39]
Myeloid leukemia	CD33	Epratuzumab	Y-90	Human (phase II)	[40, 41]
		Lintuzumab	Bi-213	Human (phase II)	[42]
Raji B-lymphoma	CD74	L243	Ga-67	Cell	[54, 55]
		cT84.66	Y-90	Human (phase I)	[62]
Colorectal cancer	Carcinoembryonic antigen (CEA) A33 glycoprotein	huA33	At-211	Mouse xenograft model	[58]
		F6 F(ab') ₂	I-131	Human (phase II)	[63, 64]
Colorectal cancer (liver metastases)	CEA	Labetuzumab	I-131	Human (phase II)	[48]
		A5B7	I-131	Human (phase I)	[66]
Gastrointestinal cancer	CEA-related cell adhesion molecule CEA	Trastuzumab	Y-90	Mouse xenograft model	[68]
		HER-2	Pb-212	Human (phase I)	[67]
Breast cancer	HER-2	NLS-trastuzumab	In-111	Cell	[73]
		MX35 F(ab') ₂	At-211	Human (phase I)	[75, 76]
Ovarian cancer	Na-dependent phosphate transporter MUC-1	mi70	Y-90	Human (phase I)	[77]
		J591	Y-90	Human (phase I)	[78]
Prostate cancer	MUC-1	Anti CD138 Ab	Lu-177	Human (phase I)	[79]
		Indirect method	Bi-213	Mouse xenograft model	[20]
Multiple myeloma	CD138	TF4 (HSG)	Y-90	Mouse xenograft model	[100, 101]
		IF5(scFv) ₄ (streptavidin)	Y-90	Mouse xenograft model	[102]
Non-Hodgkin lymphoma	CD20, CD22, HLA-DR CEA	Corresponding Abs (streptavidin)	Y-90	Mouse xenograft model	[103]
		hBS14 (HSG)	Y-90	Mouse xenograft model	[96]
Colon cancer	Ep-CAM TAG-72	MNI4 (MORF)	Re-188	Mouse xenograft model	[98]
		NR-LU-10 (HSG)	Y-90	Human (phase II)	[87]
Gastrointestinal cancer	Tenascin	CC49-(scFv) ₄ (streptavidin)	Y-90	Human (phase I)	[104]
		BC4 (biotin)	Y-90	Human (phase II)	[105]

and tumor uptake is desired. Radiolabeled peptides targeting intended tumor can be available due to the preferable pharmacokinetics and low antigenicity. In this approach, control of the affinity (specific accumulation) of radiolabeled conjugates to tumor tissue is also important.

2.1. Hematological Cancers. It is reported that anticancer responses occur at relatively low radiation-absorbed doses (i.e., less than 10 Gy) in non-Hodgkin lymphoma (NHL) [31, 32]. ⁹⁰Y-ibritumomab tiuxetan (Zevalin) and ¹³¹I-tositumomab (Bexxar) are the two FDA-approved radiolabeled anti-CD20 murine Abs that have been administered to patients with NHL [33, 34]. However, neither treatment is applied to patients with more than 25% bone marrow involvement because these patients might suffer from more severe hematologic toxicity. Several other radiolabeled Abs have been tested in hematological cancers. A ¹³¹I-labeled anti-CD20 mAb (¹³¹I-rituximab) [35–37] and an ⁹⁰Y-labeled anti-CD22 mAb (⁹⁰Y-epratuzumab tetraxetan) [32, 38, 39] are in advanced clinical trials.

Shorter-range radioisotopes (α -particle emitters) can be a better option for the treatment of patients with hematological cancer. In previous investigations, RIT using ²¹³Bi-labeled anti-CD33 IgG was performed in myeloid leukemia [40, 41]; however, short physical half-life of ²¹³Bi poses a problem for conjugate preparation. Thus, longer-lived emitters, such as ²¹¹At or ²²⁵Ac, which can emit four daughter α -particles during its decay, might be available. RITs using Auger-emitters, such as iodine-125 (¹²⁵I), gallium-67 (⁶⁷Ga), and indium-111 (¹¹¹In), could be suitable for micrometastatic disease. Potential cytotoxicity of ⁶⁷Ga-labeled anti-CD74 Ab was observed in a study using Raji B-lymphoma cells [42].

Due to the expression of these targeting antigens, normal B cells also have potencies to bind to the radiolabeled Abs. Thus, at low protein doses, the radioimmunoconjugates would be trapped to spleen rapidly, where a considerable number of B cells exist. To avoid this issue, unconjugated Ab is sometimes added to the system, which blocks the unfavorable distribution [43–45]. In addition, these Abs can enhance a tumor cell's sensitivity to radiation and chemotherapy [46–48], and thus, therapeutic responses would be achieved by a combination of the unconjugated Ab and targeted radiation.

2.2. Solid Cancers. RIT as a treatment protocol could be useful in the therapy for nonhematological cancers as well; however, convincing therapeutic outcomes have not been obtained yet in patients with solid cancer. One of the most obvious issues with RITs in solid cancers is that, unlike lymphoma, most of the Abs used are unable to affect tumor growth. To elicit clinical benefits for patients with advanced and/or disseminated solid cancers, several designs of the treatment are being undertaken: improvement of Ab uptake and enhancement of radiosensitization of cancer cells [49–51].

Here, some examples of RITs targeting solid cancer are shown.

2.2.1. Colorectal Cancer. Owing to the early characterization and ubiquitous expression in colorectal cancer, carcinoembryonic antigen (CEA) [52] has been the most common target for RIT in this disease. cT84.66, a chimeric IgG against the A3 epitope of CEA, possesses highly selective affinity to cancer cells expressing CEA [53]. RIT using ⁹⁰Y-cT84.66 was performed by Wong et al. [54, 55], with minor responses in tumor regression. Several other murine anti-CEA RIT agents have been evaluated, including ¹³¹I-NP-4 F(ab')₂, ¹³¹I-F6 F(ab')₂, ¹³¹I-A5B7, ¹³¹I-COL-1, and ¹⁸⁶Re-NR-CO-02 F(ab')₂ [50, 56–60].

A33, one of the glycoproteins, is expressed homogeneously in more than 95% of all colorectal cancers [61] and thus the humanized Ab (huA33) has been developed. Preclinical studies using ²¹¹At-labeled huA33 indicate that the uptake in tumor was found to be specific to the presence of A33 antigen [62].

In a trial study performed by Liersch et al., patients having undergone liver resection for metastatic colorectal cancer were treated with ¹³¹I-labeled humanized anti-CEACAM5 IgG [63]. Median survival of patients having received RIT was significantly longer than that of control subjects [64].

2.2.2. Breast Cancer/Ovarian Cancer. Trastuzumab is a humanized IgG mAb directed against the extracellular domain of the human epidermal growth factor receptor 2 (HER-2)/neu that is commonly overexpressed in breast, ovarian, and gastrointestinal tumors [65]. This Ab has been labeled with several radioisotopes such as ⁹⁰Y [66] and ¹¹¹In [67], for clinical study of breast cancer. Phase I study of intraperitoneal ²¹²Pb-trastuzumab for patients with advanced ovarian cancer is also ongoing [68].

MUC-1, a mucin epitope, is commonly expressed on the surface of breast cancer cells. Schrier et al. reported on a phase I study using the murine Ab labeled with ⁹⁰Y (⁹⁰Y-MX-DTPA-BrE-3) and autologous stem cell rescue in patients with breast cancer [69]. One-half of the patients exhibited objective partial response to the therapy. To overcome the limitation of repeated dosing, an ⁹⁰Y-labeled humanized Ab has also been evaluated for use with stem cell support [70].

Cell-surface sodium-dependent phosphate transport protein 2b, which is highly expressed on ovarian cancer cells, is recognized by the murine IgG MX35 [71, 72]. The potential usefulness of this Ab has been established in preclinical models, and then intraperitoneal administration of ²¹¹At-MX35 F(ab')₂ was undertaken to a phase I trial to determine the pharmacokinetics, dosimetry, and toxicity [73].

2.2.3. Prostate Cancer. MUC-1, described above for its use in breast cancer, has also been shown to be upregulated in androgen-independent prostate cancer cells, making it a good target for RIT [74]. m170, a murine mAb, was labeled with ⁹⁰Y, which was examined in patients with metastatic,

androgen-independent prostate cancer [75]. Many patients who complain of pain at the entry of study reported a significant reduction in pain following therapy. A phase I study of ^{90}Y -2IT-BAD-m170 combined with low-dose paclitaxel was also performed by the same group [76].

J591 is an IgG mAb against the extracellular domain of prostate-specific membrane antigen (PSMA). Several J591 constructs labeled with ^{90}Y [77], ^{177}Lu [78], and ^{213}Bi [79] have also been evaluated in patients with prostate cancer.

3. Indirect Method

In “indirect method,” directly radiolabeled mAbs are not used; that is, mAbs and radioactive effector molecules are administered separately and they will be conjugated in vivo. This technique can improve target to nontarget ratio to achieve high imaging contrast and/or therapeutic efficacy. In a field of RIT, this strategy is referred to as pretargeted radioimmunotherapy (PRIT) and was developed to avoid the issues associated with the prolonged residence times of radiolabeled Ab in 1980s [80, 81].

PRIT is a technique that enables the Ab localization phase to be temporally separated from the radioisotope administration in the form of a small molecular hapten. This approach involves the sequential administration of (1) a bispecific mAb derivative (bs-mAb) capable of binding a tumor antigen and a chelate and (2) a small molecular weight radiolabeled effector species. The radiolabeled species is administered following a scheduled lag period to allow the bs-mAbs to accumulate to the target site and any residual bs-mAbs are cleared from the circulation. The bs-mAb is not radiolabeled directly, and thus no exposure would occur during “unlabeled” bs-mAbs localize to the tumor by themselves. In some cases, an additional “clearing molecule,” which removes unbound bs-mAb from the circulation, is administered prior to the radiolabeled effector. Consequently, improvement of tumor to background ratios has been achieved [82, 83]. Summarized scheme is shown in Figure 1.

A key to successful implementation of the pretargeting method consists of the high target specificity and affinity offered by bs-mAb and the superior pharmacokinetic characteristics of a low molecular weight compound. The small size and inert properties of the radiolabeled effector allow it to distribute easily in the fluidic volume and then to be eliminated rapidly, thereby decreasing the overall radiation burden to nontarget organs and tissues such as bone marrow [84]. Also, PRIT increases the dose rate to the cancer as compared with a RIT by using directly radiolabeled IgG that takes 1-2 days to reach maximum distribution.

To ensure the two parts (bs-mAb and radiolabeled effector) bind to each other strongly upon interaction at cancerous region, each must be suitably modified with complementary reactive species. One of the approaches is based on avidin or streptavidin in conjunction with biotin in a variety of configurations [85]. Avidins could bind as many as four biotin molecules with very high binding constant (10^{-15} M), and, thus, some avidin/biotin-based PRIT were examined clinically [86–88]. In this protocol, clearing agent was injected

to remove residual streptavidinated Abs from the blood. The primary issue with PRIT depending on avidin (streptavidin) is the immunogenicity of these foreign proteins [89, 90].

Conjugation of radioisotopes to bs-mAb is controlled by another constituent. The approach has been utilized with a bs-mAb to histamine-succinyl-glycine (HSG) [91, 92]. By joining two haptens via a short peptide, uptake and retention of the radiolabeled effector (divalent hapten-peptide) would be enhanced locally within the cancer compared with those of the monovalent form [93–95]. Di-HSG-peptide structures have been developed for binding several radioisotopes, including ^{90}Y and $^{99\text{m}}\text{Tc}$ [96, 97]. Other methods employ complementary synthetic low immunogenic DNA analogs, morpholinos, as bridging agents [98, 99].

3.1. PRIT for Hematological Cancers. In preclinical studies, pretargeting method showed better responses with much less hematologic toxicity and thus represents a significant improvement over the RIA using anti-CD20 IgG agents radiolabeled directly [100].

Among the hematological cancers, NHL therapy has been examined in detail by pretargeting. In conventional NHL model mice, PRIT with a tri-Fab fragment followed by ^{90}Y -labeled effector led to dramatic cure rates compared to RIT with direct ^{90}Y -veltuzumab, which is a radiolabeled anti-CD20 Ab [101]. Similar therapeutic responses were also achieved using the streptavidin-biotin format of PRIT in the Ramos lymphoma model, using a combination of anti-CD20 Ab-streptavidin fusion protein 1F5(scFv)₄SA and ^{90}Y -DOTA-biotin [102]. Pagel et al. compared therapeutic efficacy between direct RIT and PRIT in xenograft models of lymphoma using CD20, CD22, and MHC class II cell surface receptor (HLA-DR) as the targets. In this study, PRIT by the streptavidin-biotin conjugation showed higher therapeutic indices and superior tumor regression [103].

3.2. PRIT for Solid Cancers. A phase II trial was examined with ^{90}Y -DOTA-biotin pretargeted with a NR-LU-10, an anti-Ep-CAM (epithelial glycoprotein-2) IgG-streptavidin conjugate in advanced colorectal cancer [87]; however, no significant responses were observed. More recently, a recombinant protein of streptavidin with four CC49 (anti-tumor-associated glycoprotein 72: anti-TAG-72) single chains and ^{90}Y -labeled biotin pair has been tested in patients with gastrointestinal malignancy [104].

In a field of brain tumor, patients with grade III glioma and glioblastoma were pretargeted with ^{90}Y -labeled biotin, resulting in a significant extension of survival in the PRIT subjects [105].

4. Concluding Remarks

Because Ab-based targeted radiation is considered to mediate direct cytotoxic effects, RIT (PRIT) could provide us with opportunities for safer and more efficient cancer treatment. Indeed, these techniques have been extensively used as conventional anticancer strategies. Especially, RIT (PRIT) has been effective in hematological cancers. There are also

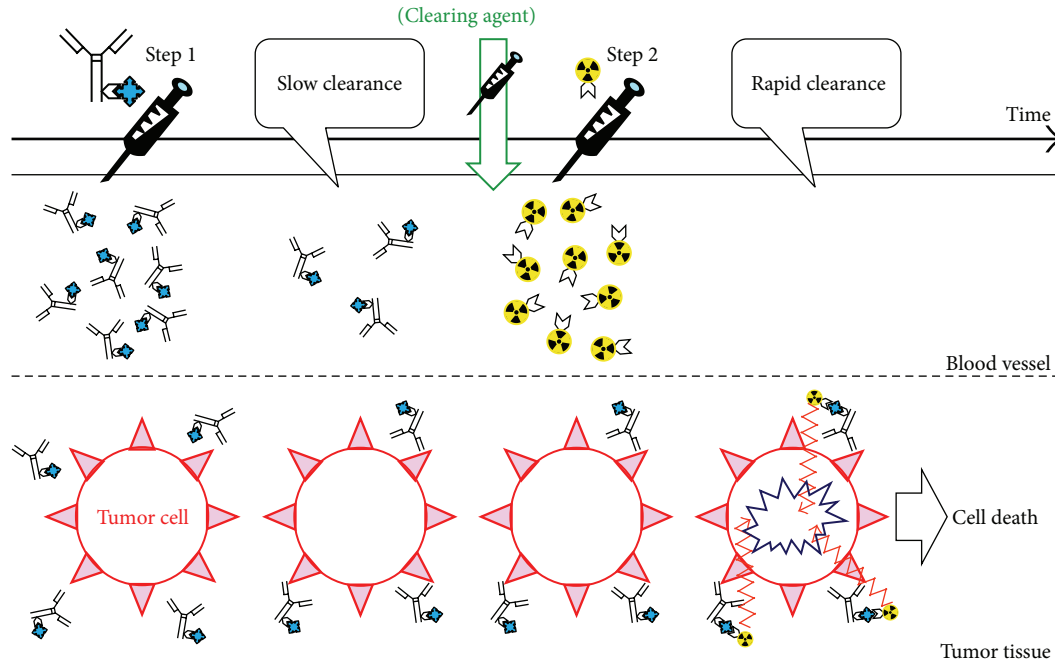


FIGURE 1: Schematic diagram of pretargeting approach.

developments of new immunostimulant for lymphoma that is combined with RIT (PRIT), which can enhance the overall therapeutic response.

On the contrary, responses to RIT (PRIT) are generally low in solid cancer and it might be due to the unconventional microenvironments. Oxygen concentrations less than 0.02% decrease the vulnerability of cancer cells to ionizing radiation [106], and even milder hypoxia produces a substantial level of resistance to irradiation [107]. Strategies to radiosensitize the lesions by means of an increased supply of oxygen or treatment of nitroimidazole analog [108] would help enhance the efficacy of RIT (PRIT).

RIT (PRIT) is a valuable treatment modality which can detect and quantify the accumulation of therapeutic agents readily. Thus, molecular imaging approach can be adapted to select patients, to decide the treatment strategy, and to assess the therapeutic benefit. Developments of novel Ab-based targeted therapeutics and the combination with other interventions should support cancer therapy in future.

Conflict of Interests

The author declares that there is no conflict of interests regarding the publication of this paper.

References

- [1] P. Fragu, "How the field of thyroid endocrinology developed in France after World War II," *Bulletin of the History of Medicine*, vol. 77, no. 2, pp. 393–414, 2003.
- [2] D. Pressman and L. Korngold, "The in vivo localization of anti-Wagner-osteogenic-sarcoma antibodies," *Cancer*, vol. 6, no. 3, pp. 619–623, 1953.
- [3] R. W. Wissler, P. A. Barker, M. H. Flax et al., "A study of the preparation, localization, and effects of antitumor antibodies labeled with I^{131} ," *Cancer Research*, vol. 16, no. 8, pp. 761–773, 1956.
- [4] O. A. Gansow, M. W. Brechbiel, S. Mirzadeh, D. Colcher, and M. Roselli, "Chelates and antibodies: current methods and new directions," *Cancer Treatment and Research*, vol. 51, pp. 153–171, 1990.
- [5] M. K. Moi, S. J. DeNardo, and C. F. Meares, "Stable bifunctional chelates of metals used in radiotherapy," *Cancer Research*, vol. 50, no. 3, pp. S789–S793, 1990.
- [6] D. M. Goldenberg and R. M. Sharkey, "Advances in cancer therapy with radiolabeled monoclonal antibodies," *The Quarterly Journal of Nuclear Medicine and Molecular Imaging*, vol. 50, no. 4, pp. 248–264, 2006.
- [7] K. M. Prise and J. M. O'Sullivan, "Radiation-induced bystander signalling in cancer therapy," *Nature Reviews Cancer*, vol. 9, no. 5, pp. 351–360, 2009.
- [8] J. A. Bertout, S. A. Patel, and M. C. Simon, "The impact of O_2 availability on human cancer," *Nature Reviews Cancer*, vol. 8, no. 12, pp. 967–975, 2008.
- [9] P. Vaupel and A. Mayer, "Hypoxia in cancer: significance and impact on clinical outcome," *Cancer and Metastasis Reviews*, vol. 26, no. 2, pp. 225–239, 2007.
- [10] G. Kroemer, L. Galluzzi, and C. Brenner, "Mitochondrial membrane permeabilization in cell death," *Physiological Reviews*, vol. 87, no. 1, pp. 99–163, 2007.
- [11] L. Cabon, P. Galán-Malo, A. Bouharrour et al., "BID regulates AIF-mediated caspase-independent necroptosis by promoting BAX activation," *Cell Death and Differentiation*, vol. 19, no. 2, pp. 245–256, 2012.
- [12] R. Ganss, E. Ryschich, E. Klar, B. Arnold, and G. J. Hämmerling, "Combination of T-cell therapy and trigger of inflammation induces remodeling of the vasculature and tumor eradication," *Cancer Research*, vol. 62, no. 5, pp. 1462–1470, 2002.

- [13] E. Tartour, H. Pere, B. Maillere et al., "Angiogenesis and immunity: a bidirectional link potentially relevant for the monitoring of antiangiogenic therapy and the development of novel therapeutic combination with immunotherapy," *Cancer and Metastasis Reviews*, vol. 30, no. 1, pp. 83–95, 2011.
- [14] R. W. Howell, "Auger processes in the 21st century," *International Journal of Radiation Biology*, vol. 84, no. 12, pp. 959–975, 2008.
- [15] M. J. Mattes, "Radionuclide-antibody conjugates for single-cell cytotoxicity," *Cancer*, vol. 94, no. 4, pp. 1215–1223, 2002.
- [16] G. L. Ong, S. E. Elsamra, D. M. Goldenberg, and M. Jules Mattes, "Single-cell cytotoxicity with radiolabeled antibodies," *Clinical Cancer Research*, vol. 7, no. 1, pp. 192–201, 2001.
- [17] A. K. Claesson, B. Stenerlöv, L. Jacobsson, and K. Elmroth, "Relative biological effectiveness of the α -particle emitter ^{211}At for double-strand break induction in human fibroblasts," *Radiation Research*, vol. 167, no. 3, pp. 312–318, 2007.
- [18] E. J. Hall and A. J. Giaccia, *Radiology for the Radiologist*, Lippincott Williams & Wilkins, Philadelphia, Pa, USA, 7th edition, 2007.
- [19] M. R. McDevitt, G. Sgouros, R. D. Finn et al., "Radioimmunotherapy with α -emitting nuclides," *European Journal of Nuclear Medicine*, vol. 25, no. 9, pp. 1341–1351, 1998.
- [20] M. Chérel, S. Gouard, J. Gaschet et al., " ^{213}Bi radioimmunotherapy with an anti-mCD138 monoclonal antibody in a murine model of multiple myeloma," *The Journal of Nuclear Medicine*, vol. 54, no. 9, pp. 1597–1604, 2013.
- [21] G. Vaidyanathan and M. R. Zalutsky, "Astatine radiopharmaceuticals: prospects and problems," *Current Radiopharmaceuticals*, vol. 1, no. 3, pp. 177–196, 2008.
- [22] M. Miederer, D. A. Scheinberg, and M. R. McDevitt, "Realizing the potential of the Actinium-225 radionuclide generator in targeted alpha particle therapy applications," *Advanced Drug Delivery Reviews*, vol. 60, no. 12, pp. 1371–1382, 2008.
- [23] M. L. Sautter-Bihl, G. Herbold, and H. Bihl, "Minimal residual disease: a target for radioimmunotherapy with ^{131}I -labeled monoclonal antibodies? Some dosimetric considerations," *Recent Results in Cancer Research*, vol. 141, pp. 67–75, 1996.
- [24] K. Chen and X. Chen, "Design and development of molecular imaging probes," *Current Topics in Medicinal Chemistry*, vol. 10, no. 12, pp. 1227–1236, 2010.
- [25] K. Chen and P. S. Conti, "Target-specific delivery of peptide-based probes for PET imaging," *Advanced Drug Delivery Reviews*, vol. 62, no. 11, pp. 1005–1022, 2010.
- [26] G. Köhler and C. Milstein, "Continuous cultures of fused cells secreting antibody of predefined specificity," *Nature*, vol. 256, no. 5517, pp. 495–497, 1975.
- [27] J. L. Murray, M. G. Rosenblum, L. Lamki et al., "Clinical parameters related to optimal tumor localization of indium-111-labeled mouse antimelanoma monoclonal antibody ZME-018," *The Journal of Nuclear Medicine*, vol. 28, no. 1, pp. 25–33, 1987.
- [28] S. F. Rosebrough, Z. D. Grossman, J. G. McAfee et al., "Thrombus imaging with Indium-111 and Iodine-131-labeled fibrin-specific monoclonal antibody and its $\text{F}(\text{ab}')_2$ and Fab fragments," *The Journal of Nuclear Medicine*, vol. 29, no. 7, pp. 1212–1222, 1988.
- [29] A. M. Wu and P. D. Senter, "Arming antibodies: prospects and challenges for immunoconjugates," *Nature Biotechnology*, vol. 23, no. 9, pp. 1137–1146, 2005.
- [30] L. A. Maleki, B. Baradaran, and J. Majidi, "Future prospects of monoclonal antibodies as magic bullets in immunotherapy," *Human Antibodies*, vol. 22, no. 1-2, pp. 9–13, 2013.
- [31] G. Sgouros, S. Squeri, A. M. Ballangrud et al., "Patient-specific, 3-dimensional dosimetry in non-Hodgkin's lymphoma patients treated with ^{131}I -anti-B1 antibody: assessment of tumor dose-response," *The Journal of Nuclear Medicine*, vol. 44, no. 2, pp. 260–268, 2003.
- [32] R. M. Sharkey, A. Brenner, J. Burton et al., "Radioimmunotherapy of non-Hodgkin's lymphoma with ^{90}Y -DOTA humanized anti-CD22 IgG (^{90}Y -Epratuzumab): do tumor targeting and dosimetry predict therapeutic response?" *The Journal of Nuclear Medicine*, vol. 44, no. 12, pp. 2000–2018, 2003.
- [33] S. J. Goldsmith, "Radioimmunotherapy of lymphoma: bexxar and zevalin," *Seminars in Nuclear Medicine*, vol. 40, no. 2, pp. 122–135, 2010.
- [34] M. S. Kaminski, M. Tuck, J. Estes et al., " ^{131}I -tositumomab therapy as initial treatment for follicular lymphoma," *The New England Journal of Medicine*, vol. 352, no. 5, pp. 441–449, 2005.
- [35] M. F. Leahy and J. H. Turner, "Radioimmunotherapy of relapsed indolent non-Hodgkin lymphoma with ^{131}I -rituximab in routine clinical practice: 10-year single-institution experience of 142 consecutive patients," *Blood*, vol. 117, no. 1, pp. 45–52, 2011.
- [36] J. H. Turner, A. A. Martindale, J. Boucek, P. G. Claringbold, and M. F. Leahy, " ^{131}I -anti CD20 radioimmunotherapy of relapsed or refractory non-Hodgkins lymphoma: a phase II clinical trial of a nonmyeloablative dose regimen of chimeric rituximab radiolabeled in a hospital," *Cancer Biotherapy & Radiopharmaceuticals*, vol. 18, no. 4, pp. 513–524, 2003.
- [37] T. M. Illidge, M. Bayne, N. S. Brown et al., "Phase I/2 study of fractionated ^{131}I -rituximab in low-grade B-cell lymphoma: the effect of prior rituximab dosing and tumor burden on subsequent radioimmunotherapy," *Blood*, vol. 113, no. 7, pp. 1412–1421, 2009.
- [38] F. Morschhauser, F. Kraeber-Bodéré, W. A. Wegener et al., "High rates of durable responses with anti-CD22 fractionated radioimmunotherapy: results of a multicenter, phase I/II study in non-Hodgkin's lymphoma," *Journal of Clinical Oncology*, vol. 28, no. 23, pp. 3709–3716, 2010.
- [39] G. L. Griffiths, S. V. Govindan, R. M. Sharkey, D. R. Fisher, and D. M. Goldenberg, " ^{90}Y -DOTA-hLL2: an agent for radioimmunotherapy of non-Hodgkin's lymphoma," *The Journal of Nuclear Medicine*, vol. 44, no. 1, pp. 77–84, 2003.
- [40] G. Sgouros, Å. M. Ballangrud, J. G. Jurcic et al., "Pharmacokinetics and dosimetry of an α -particle emitter labeled antibody: ^{213}Bi -HuM195 (anti-CD33) in patients with leukemia," *The Journal of Nuclear Medicine*, vol. 40, no. 11, pp. 1935–1946, 1999.
- [41] J. G. Jurcic, S. M. Larson, G. Sgouros et al., "Targeted α particle immunotherapy for myeloid leukemia," *Blood*, vol. 100, no. 4, pp. 1233–1239, 2002.
- [42] R. B. Michel, M. W. Brechbiel, and M. J. Mattes, "A comparison of 4 radionuclides conjugated to antibodies for single-cell kill," *The Journal of Nuclear Medicine*, vol. 44, no. 4, pp. 632–640, 2003.
- [43] M. S. Kaminski, K. R. Zasadny, I. R. Francis et al., "Iodine-131-anti-B1 radioimmunotherapy for B-cell lymphoma," *Journal of Clinical Oncology*, vol. 14, no. 7, pp. 1974–1981, 1996.
- [44] P. McLaughlin, A. J. Grillo-López, B. K. Link et al., "Rituximab chimeric anti-CD20 monoclonal antibody therapy for relapsed indolent lymphoma: half of patients respond to a four-dose treatment program," *Journal of Clinical Oncology*, vol. 16, no. 8, pp. 2825–2833, 1998.
- [45] T. E. Witzig, C. A. White, G. A. Wiseman et al., "Phase I/II trial of IDEC-Y2B8 radioimmunotherapy for treatment of relapsed

- or refractory CD20⁺ B-cell non-Hodgkin's lymphoma," *Journal of Clinical Oncology*, vol. 17, no. 12, pp. 3793–3803, 1999.
- [46] Y. Du, J. Honeychurch, M. S. Cragg et al., "Antibody-induced intracellular signaling works in combination with radiation to eradicate lymphoma in radioimmunotherapy," *Blood*, vol. 103, no. 4, pp. 1485–1494, 2004.
- [47] N. S. Kapadia, J. M. Engles, and R. L. Wahl, "In vitro evaluation of radioprotective and radiosensitizing effects of rituximab," *The Journal of Nuclear Medicine*, vol. 49, no. 4, pp. 674–678, 2008.
- [48] A. Ivanov, S. Krysov, M. S. Cragg, and T. Illidge, "Radiation therapy with tositumomab (B1) anti-CD20 monoclonal antibody initiates extracellular signal-regulated kinase/mitogen-activated protein kinase-dependent cell death that overcomes resistance to apoptosis," *Clinical Cancer Research*, vol. 14, no. 15, pp. 4925–4934, 2008.
- [49] R. F. Meredith, M. B. Khazaeli, W. E. Plott et al., "Phase II study of dual ¹³¹I-labeled monoclonal antibody therapy with interferon in patients with metastatic colorectal cancer," *Clinical Cancer Research*, vol. 2, no. 11, pp. 1811–1818, 1996.
- [50] T. Meyer, A. M. Gaya, G. Dancey et al., "A phase I trial of radioimmunotherapy with ¹³¹I-A5B7 anti-CEA antibody in combination with combretastatin-A4-phosphate in advanced gastrointestinal carcinomas," *Clinical Cancer Research*, vol. 15, no. 13, pp. 4484–4492, 2009.
- [51] F. Kraeber-Bodéré, C. Bodet-Milin, C. Niaudet et al., "Comparative toxicity and efficacy of combined radioimmunotherapy and antiangiogenic therapy in carcinoembryonic antigen-expressing medullary thyroid cancer xenograft," *The Journal of Nuclear Medicine*, vol. 51, no. 4, pp. 624–631, 2010.
- [52] P. Gold and S. O. Freedman, "Demonstration of tumor-specific antigens in human colonic carcinomata by immunological tolerance and absorption techniques," *The Journal of Experimental Medicine*, vol. 121, pp. 439–462, 1965.
- [53] J. D. Beatty, R. B. Duda, L. E. Williams et al., "Preoperative imaging of colorectal carcinoma with ¹¹¹In-labeled anticarcinoembryonic antigen monoclonal antibody," *Cancer Research*, vol. 46, no. 12, pp. 6494–6502, 1986.
- [54] J. Y. C. Wong, S. Shibata, L. E. Williams et al., "A phase I trial of ⁹⁰Y-anticarcinoembryonic antigen chimeric T84.66 radioimmunotherapy with 5-fluorouracil in patients with metastatic colorectal cancer," *Clinical Cancer Research*, vol. 9, no. 16, pp. 5842–5852, 2003.
- [55] J. Y. C. Wong, D. Z. Chu, L. E. Williams et al., "A phase I trial of ⁹⁰Y-DOTA-anti-CEA chimeric T84.66 (cT84.66) radioimmunotherapy in patients with metastatic CEA-producing malignancies," *Cancer Biotherapy and Radiopharmaceuticals*, vol. 21, no. 2, pp. 88–100, 2006.
- [56] T. M. Behr, R. M. Sharkey, M. E. Juweid et al., "Phase I/II clinical radioimmunotherapy with an iodine-131-labeled anticarcinoembryonic antigen murine monoclonal antibody IgG," *The Journal of Nuclear Medicine*, vol. 38, no. 6, pp. 858–870, 1997.
- [57] M. E. Juweid, R. M. Sharkey, T. Behr et al., "Radioimmunotherapy of patients with small-volume tumors using iodine-131-labeled anti-CEA monoclonal antibody NP-4 F(ab')₂," *The Journal of Nuclear Medicine*, vol. 37, no. 9, pp. 1504–1510, 1996.
- [58] M. Ychou, D. Azria, C. Menkarios et al., "Adjuvant radioimmunotherapy trial with iodine-131-labeled anticarcinoembryonic antigen monoclonal antibody F6 F(ab')₂ after resection of liver metastases from colorectal cancer," *Clinical Cancer Research*, vol. 14, no. 11, pp. 3487–3493, 2008.
- [59] B. Yu, J. Carrasquillo, D. Milenic et al., "Phase I trial of iodine 131-labeled COL-1 in patients with gastrointestinal malignancies: influence of serum carcinoembryonic antigen and tumor bulk on pharmacokinetics," *Journal of Clinical Oncology*, vol. 14, no. 6, pp. 1798–1809, 1996.
- [60] H. B. Breitz, P. L. Weiden, J.-L. Vanderheyden et al., "Clinical experience with rhenium-186-labeled monoclonal antibodies for radioimmunotherapy: results of Phase I trials," *The Journal of Nuclear Medicine*, vol. 33, no. 6, pp. 1099–1112, 1992.
- [61] P. Garin-Chesa, J. Sakamoto, S. Welt, F. X. Real, W. J. Rettig, and L. J. Old, "Organ-specific expression of the colon cancer antigen A33, a cell surface target for antibody-based therapy," *International Journal of Oncology*, vol. 9, no. 3, pp. 465–471, 1996.
- [62] Y. Almqvist, A. C. Steffen, H. Lundqvist, H. Jensen, V. Tolmachev, and A. Sundin, "Biodistribution of ²¹¹At-labeled humanized monoclonal antibody A33," *Cancer Biotherapy and Radiopharmaceuticals*, vol. 22, no. 4, pp. 480–487, 2007.
- [63] T. Liersch, J. Meller, B. Kulle et al., "Phase II trial of carcinoembryonic antigen radioimmunotherapy with ¹³¹I-labretuzumab after salvage resection of colorectal metastases in the liver: five-year safety and efficacy results," *Journal of Clinical Oncology*, vol. 23, no. 27, pp. 6763–6770, 2005.
- [64] T. Liersch, J. Meller, M. Bittrich, B. Kulle, H. Becker, and D. M. Goldenberg, "Update of carcinoembryonic antigen radioimmunotherapy with ¹³¹I-labretuzumab after salvage resection of colorectal liver metastases: comparison of outcome to a contemporaneous control group," *Annals of Surgical Oncology*, vol. 14, no. 9, pp. 2577–2590, 2007.
- [65] P. Carter, L. Presta, C. M. Gorman et al., "Humanization of an anti-p185HER2 antibody for human cancer therapy," *Proceedings of the National Academy of Sciences of the United States of America*, vol. 89, no. 10, pp. 4285–4289, 1992.
- [66] D. M. Crow, L. Williams, D. Colcher, J. Y. C. Wong, A. Raubitschek, and J. E. Shively, "Combined radioimmunotherapy and chemotherapy of breast tumors with Y-90-labeled anti-Her2 and anti-CEA antibodies with taxol," *Bioconjugate Chemistry*, vol. 16, no. 5, pp. 1117–1125, 2005.
- [67] D. L. Costantini, K. Bateman, K. McLarty, K. A. Vallis, and R. M. Reilly, "Trastuzumab-resistant breast cancer cells remain sensitive to the Auger electron-emitting radiotherapeutic agent ¹¹¹In-NLS-trastuzumab and are radiosensitized by methotrexate," *The Journal of Nuclear Medicine*, vol. 49, no. 9, pp. 1498–1505, 2008.
- [68] R. F. Meredith, "Safety study of ²¹²Pb-TCMC-trastuzumab radioimmunotherapy," <http://clinicaltrials.gov/ct2/show/NCT-01384253>.
- [69] D. M. Schrier, S. M. Stemmer, T. Johnson et al., "High-dose ⁹⁰Y Mx-diethylenetriaminepentaacetic acid (DTPA)-BrE-3 and autologous hematopoietic stem cell support (AHSCS) for the treatment of advanced breast cancer: a phase I trial," *Cancer Research*, vol. 55, no. 23, pp. 5921s–5924s, 1995.
- [70] P. J. Cagnoni, R. L. Ceriani, W. C. Cole et al., "Phase I study of high-dose radioimmunotherapy with 90-Y-hu-BrE-3 followed by autologous stem cell support (ASCS) in patients with metastatic breast cancer," *Cancer Biotherapy & Radiopharmaceuticals*, vol. 13, no. 4, p. 328, 1998.
- [71] M. Welshinger, B. W. T. Yin, and K. O. Lloyd, "Initial immunological characterization of MX35 ovarian cancer antigen," *Gynecologic Oncology*, vol. 67, no. 2, pp. 188–192, 1997.

- [72] B. W. T. Yin, R. Kiyamova, R. Chua et al., "Monoclonal antibody MX35 detects the membrane transporter NaPi2b (SLC34A2) in human carcinomas," *Cancer Immunity*, vol. 8, article 3, 2008.
- [73] H. Andersson, E. Cederkrantz, T. Bäck et al., "Intraperitoneal α -particle radioimmunotherapy of ovarian cancer patients: pharmacokinetics and dosimetry of ^{211}At -MX35 F(ab')₂: A Phase I Study," *The Journal of Nuclear Medicine*, vol. 50, no. 7, pp. 1153–1160, 2009.
- [74] S. J. DeNardo, C. M. Richman, H. Albrecht et al., "Enhancement of the therapeutic index: from nonmyeloablative and myeloablative toward pretargeted radioimmunotherapy for metastatic prostate cancer," *Clinical Cancer Research*, vol. 11, no. 19, pp. 7187s–7194s, 2005.
- [75] R. T. O'Donnell, S. J. DeNardo, A. Yuan et al., "Radioimmunotherapy with $^{111}\text{In}/^{90}\text{Y}$ -2IT-BAD-m170 for metastatic prostate cancer," *Clinical Cancer Research*, vol. 7, no. 6, pp. 1561–1568, 2001.
- [76] C. M. Richman, S. J. DeNardo, R. T. O'Donnell et al., "High-dose radioimmunotherapy combined with fixed, low-dose paclitaxel in metastatic prostate and breast cancer by using a MUC-1 monoclonal antibody, m170, linked to indium-111/yttrium-90 via a cathepsin cleavable linker with cyclosporine to prevent human anti-mouse antibody," *Clinical Cancer Research*, vol. 11, no. 16, pp. 5920–5927, 2005.
- [77] M. I. Milowsky, D. M. Nanus, L. Kostakoglu, S. Vallabhajosula, S. J. Goldsmith, and N. H. Bander, "Phase I trial of yttrium-90-labeled anti-prostate-specific membrane antigen monoclonal antibody J591 for androgen-independent prostate cancer," *Journal of Clinical Oncology*, vol. 22, no. 13, pp. 2522–2531, 2004.
- [78] N. H. Bander, M. I. Milowsky, D. M. Nanus, L. Kostakoglu, S. Vallabhajosula, and S. J. Goldsmith, "Phase I trial of ^{177}Lu -labeled J591, a monoclonal antibody to prostate-specific membrane antigen, in patients with androgen-independent prostate cancer," *Journal of Clinical Oncology*, vol. 23, no. 21, pp. 4591–4601, 2005.
- [79] M. R. McDevitt, E. Barendswaard, D. Ma et al., "An α -particle emitting antibody (^{213}Bi]J591) for radioimmunotherapy of prostate cancer," *Cancer Research*, vol. 60, no. 21, pp. 6095–6100, 2000.
- [80] D. T. Reardan, C. F. Meares, D. A. Goodwin et al., "Antibodies against metal chelates," *Nature*, vol. 316, no. 6025, pp. 265–268, 1985.
- [81] D. A. Goodwin, C. F. Meares, M. McTigue, and G. S. David, "Monoclonal antibody hapten radiopharmaceutical delivery," *Nuclear Medicine Communications*, vol. 7, no. 8, pp. 569–580, 1986.
- [82] D. A. Goodwin, C. F. Meares, M. J. McCall, M. McTigue, and W. Chaovapong, "Pre-targeted immunoscintigraphy of murine tumors with indium-111-labeled bifunctional haptens," *The Journal of Nuclear Medicine*, vol. 29, no. 2, pp. 226–234, 1988.
- [83] D. M. Goldenberg, R. M. Sharkey, G. Paganelli, J. Barbet, and J. Chatal, "Antibody pretargeting advances cancer radioimmunodetection and radioimmunotherapy," *Journal of Clinical Oncology*, vol. 24, no. 5, pp. 823–834, 2006.
- [84] B. M. Zeglis, K. K. Sevak, T. Reiner et al., "A pretargeted PET imaging strategy based on bioorthogonal diels-alder click chemistry," *The Journal of Nuclear Medicine*, vol. 54, no. 8, pp. 1389–1396, 2013.
- [85] D. J. Hnatowich, F. Virzi, and M. Rusckowski, "Investigations of avidin and biotin for imaging applications," *The Journal of Nuclear Medicine*, vol. 28, no. 8, pp. 1294–1302, 1987.
- [86] H. B. Breitz, P. L. Weiden, P. L. Beaumier et al., "Clinical optimization of pretargeted radioimmunotherapy with antibody-streptavidin conjugate and ^{90}Y -DOTA-biotin," *The Journal of Nuclear Medicine*, vol. 41, no. 1, pp. 131–140, 2000.
- [87] S. J. Knox, M. L. Goris, M. Tempero et al., "Phase II trial of yttrium-90-DOTA-biotin pretargeted by NR-LU-10 antibody/streptavidin in patients with metastatic colon cancer," *Clinical Cancer Research*, vol. 6, no. 2, pp. 406–414, 2000.
- [88] J. Schultz, Y. Lin, J. Sanderson et al., "A tetravalent single-chain antibody-streptavidin fusion protein for pretargeted lymphoma therapy," *Cancer Research*, vol. 60, no. 23, pp. 6663–6669, 2000.
- [89] G. Paganelli and M. Chinol, "Radioimmunotherapy: is avidin-biotin pretargeting the preferred choice among pretargeting methods?" *European Journal of Nuclear Medicine and Molecular Imaging*, vol. 30, no. 5, pp. 773–776, 2003.
- [90] D. M. Goldenberg, C. H. Chang, R. M. Sharkey et al., "Radioimmunotherapy: is avidin-biotin pretargeting the preferred choice among pretargeting methods?" *European Journal of Nuclear Medicine and Molecular Imaging*, vol. 30, no. 5, pp. 777–780, 2003.
- [91] E. Janevik-Ivanovska, E. Gautherot, M. Hillairet de Boisferon et al., "Bivalent hapten-bearing peptides designed for iodine-131 pretargeted radioimmunotherapy," *Bioconjugate Chemistry*, vol. 8, no. 4, pp. 526–533, 1997.
- [92] E. A. Rossi, D. M. Goldenberg, T. M. Cardillo, W. J. McBride, R. M. Sharkey, and C. Chang, "Stably tethered multifunctional structures of defined composition made by the dock and lock method for use in cancer targeting," *Proceedings of the National Academy of Sciences of the United States of America*, vol. 103, no. 18, pp. 6841–6846, 2006.
- [93] J.-M. le Doussal, M. Martin, E. Gautherot, M. Delaage, and J. Barbet, "In vitro and in vivo targeting of radiolabeled monovalent and divalent haptens with dual specificity monoclonal antibody conjugates: enhanced divalent hapten affinity for cell-bound antibody conjugate," *The Journal of Nuclear Medicine*, vol. 30, no. 8, pp. 1358–1366, 1989.
- [94] D. A. Goodwin, C. F. Meares, M. McTigue et al., "Pretargeted immunoscintigraphy: effect of hapten valency on murine tumor uptake," *The Journal of Nuclear Medicine*, vol. 33, no. 11, pp. 2006–2013, 1992.
- [95] O. C. Boerman, M. H. G. C. Kranenborg, E. Oosterwijk et al., "Pretargeting of renal cell carcinoma: improved tumor targeting with a bivalent chelate," *Cancer Research*, vol. 59, no. 17, pp. 4400–4405, 1999.
- [96] H. Karacay, P. Brard, R. M. Sharkey et al., "Therapeutic advantage of pretargeted radioimmunotherapy using a recombinant bispecific antibody in a human colon cancer xenograft," *Clinical Cancer Research*, vol. 11, no. 21, pp. 7879–7885, 2005.
- [97] R. M. Sharkey, T. M. Cardillo, E. A. Rossi et al., "Signal amplification in molecular imaging by pretargeting a multivalent, bispecific antibody," *Nature Medicine*, vol. 11, no. 11, pp. 1250–1255, 2005.
- [98] G. Liu, S. Dou, G. Mardirossian et al., "Successful radiotherapy of tumor in pretargeted mice by ^{188}Re -radiolabeled phosphorodiamidate morpholino oligomer, a synthetic DNA analogue," *Clinical Cancer Research*, vol. 12, no. 16, pp. 4958–4964, 2006.
- [99] G. Liu, S. Dou, P. H. Pretorius, X. Liu, M. Rusckowski, and D. J. Hnatowich, "Pretargeting CWR22 prostate tumor in mice with MORF-B72.3 antibody and radiolabeled cMORE," *European Journal of Nuclear Medicine and Molecular Imaging*, vol. 35, no. 2, pp. 272–280, 2008.

- [100] R. M. Sharkey, H. Karacay, C. R. Johnson et al., "Pretargeted versus directly targeted radioimmunotherapy combined with anti-CD20 antibody consolidation therapy of non-Hodgkin lymphoma," *The Journal of Nuclear Medicine*, vol. 50, no. 3, pp. 444–453, 2009.
- [101] R. M. Sharkey, H. Karacay, S. Litwin et al., "Improved therapeutic results by pretargeted radioimmunotherapy of non-Hodgkin's lymphoma with a new recombinant, trivalent, anti-CD20, bispecific antibody," *Cancer Research*, vol. 68, no. 13, pp. 5282–5290, 2008.
- [102] D. J. Green, J. M. Pagel, A. Pantelias et al., "Pretargeted radioimmunotherapy for B-cell lymphomas," *Clinical Cancer Research*, vol. 13, no. 18, pp. 5598s–5603s, 2007.
- [103] J. M. Pagel, N. Orgun, D. K. Hamlin et al., "A comparative analysis of conventional and pretargeted radioimmunotherapy of B-cell lymphomas by targeting CD20, CD22, and HLA-DR singly and in combinations," *Blood*, vol. 113, no. 20, pp. 4903–4913, 2009.
- [104] S. Shen, A. Forero, A. F. LoBuglio et al., "Patient-specific dosimetry of pretargeted radioimmunotherapy using CC49 fusion protein in patients with gastrointestinal malignancies," *The Journal of Nuclear Medicine*, vol. 46, no. 4, pp. 642–651, 2005.
- [105] C. Grana, M. Chinol, C. Robertson et al., "Pretargeted adjuvant radioimmunotherapy with Yttrium-90-biotin in malignant glioma patients: a pilot study," *British Journal of Cancer*, vol. 86, no. 2, pp. 207–212, 2002.
- [106] B. G. Wouters and L. D. Skarsgard, "Low-dose radiation sensitivity and induced radioresistance to cell killing in HT-29 cells is distinct from the 'adaptive response' and cannot be explained by a subpopulation of sensitive cells," *Radiation Research*, vol. 148, no. 5, pp. 435–442, 1997.
- [107] O. Trédan, C. M. Galmarini, K. Patel, and I. F. Tannock, "Drug resistance and the solid tumor microenvironment," *Journal of the National Cancer Institute*, vol. 99, no. 19, pp. 1441–1454, 2007.
- [108] J. Overgaard, H. S. Hansen, M. Overgaard et al., "A randomized double-blind phase III study of nimorazole as a hypoxic radiosensitizer of primary radiotherapy in supraglottic larynx and pharynx carcinoma. Results of the Danish Head and Neck Cancer Study (DAHANCA) Protocol 5–85," *Radiotherapy and Oncology*, vol. 46, no. 2, pp. 135–146, 1998.

Review Article

Radiolabeled Probes Targeting Hypoxia-Inducible Factor-1-Active Tumor Microenvironments

Masashi Ueda¹ and Hideo Saji²

¹ Department of Pharmaceutical Analytical Chemistry, Graduate School of Medicine, Dentistry, and Pharmaceutical Sciences, Okayama University, 1-1-1 Tsushima-naka, Kita-ku, Okayama 700-8530, Japan

² Department of Patho-Functional Bioanalysis, Graduate School of Pharmaceutical Sciences, Kyoto University, Kyoto 606-8501, Japan

Correspondence should be addressed to Masashi Ueda; mueda@cc.okayama-u.ac.jp

Received 27 June 2014; Accepted 6 August 2014; Published 18 August 2014

Academic Editor: Takahiro Higuchi

Copyright © 2014 M. Ueda and H. Saji. This is an open access article distributed under the Creative Commons Attribution License, which permits unrestricted use, distribution, and reproduction in any medium, provided the original work is properly cited.

Because tumor cells grow rapidly and randomly, hypoxic regions arise from the lack of oxygen supply in solid tumors. Hypoxic regions in tumors are known to be resistant to chemotherapy and radiotherapy. Hypoxia-inducible factor-1 (HIF-1) expressed in hypoxic regions regulates the expression of genes related to tumor growth, angiogenesis, metastasis, and therapy resistance. Thus, imaging of HIF-1-active regions in tumors is of great interest. HIF-1 activity is regulated by the expression and degradation of its α subunit (HIF-1 α), which is degraded in the proteasome under normoxic conditions, but escapes degradation under hypoxic conditions, allowing it to activate transcription of HIF-1-target genes. Therefore, to image HIF-1-active regions, HIF-1-dependent reporter systems and injectable probes that are degraded in a manner similar to HIF-1 α have been recently developed and used in preclinical studies. However, no probe currently used in clinical practice directly assesses HIF-1 activity. Whether the accumulation of ¹⁸F-FDG or ¹⁸F-FMISO can be utilized as an index of HIF-1 activity has been investigated in clinical studies. In this review, the current status of HIF-1 imaging in preclinical and clinical studies is discussed.

1. Introduction

Insufficient blood supply to a rapidly growing solid tumor leads to hypoxia—oxygen tension that is below physiological levels. The median value of partial oxygen pressure (pO₂) is reportedly 10 mmHg in breast cancers but is 65 mmHg in normal breast tissue [1]. Hypoxic regions are not only critically important in tumor physiology and treatment, but also strongly associated with malignant progression, therapeutic resistance, and poor prognosis [2–4]. In such regions, the transcription factor hypoxia-inducible factor-1 (HIF-1) is overexpressed. HIF-1, one of the critical components of hypoxic responses, is a master transcriptional activator of various genes related to malignant tumor phenotypes [5–7]. Therefore, the development of techniques to noninvasively detect HIF-1-active hypoxic tumor cells has received considerable interest. Such techniques will provide useful information that can be applied to qualitative diagnosis of tumors and development of therapeutic strategies for cancer.

2. HIF-1 Biology

HIF-1 is a heterodimeric transcription factor that consists of α and β subunits (HIF-1 α and HIF-1 β , resp.) [8]. HIF-1 β is a constitutively expressed nuclear protein; however, HIF-1 α expression is regulated at both the translational and posttranslational levels. Growth signaling through receptor tyrosine kinases activates PI3K/Akt/mTOR and Ras/MEK/ERK signaling pathways and increases HIF-1 α translation (Figure 1) [9–11]. In contrast, HIF-1 α expression is maintained at low levels in most normoxic tissues via a posttranslational regulation mechanism—oxygen-dependent proteasomal degradation. Under normoxic conditions, Pro⁴⁰² and Pro⁵⁶⁴ in the HIF-1 α oxygen-dependent degradation domain (ODD) are hydroxylated by proline hydroxylases [12–14]. The von Hippel-Lindau tumor suppressor protein (pVHL) specifically recognizes these hydroxylated prolines and interacts with HIF-1 α . pVHL forms a complex with Elongin BC, Cul2, and Rbx1 [15], and this complex, which acts as a ubiquitin ligase, polyubiquitinates

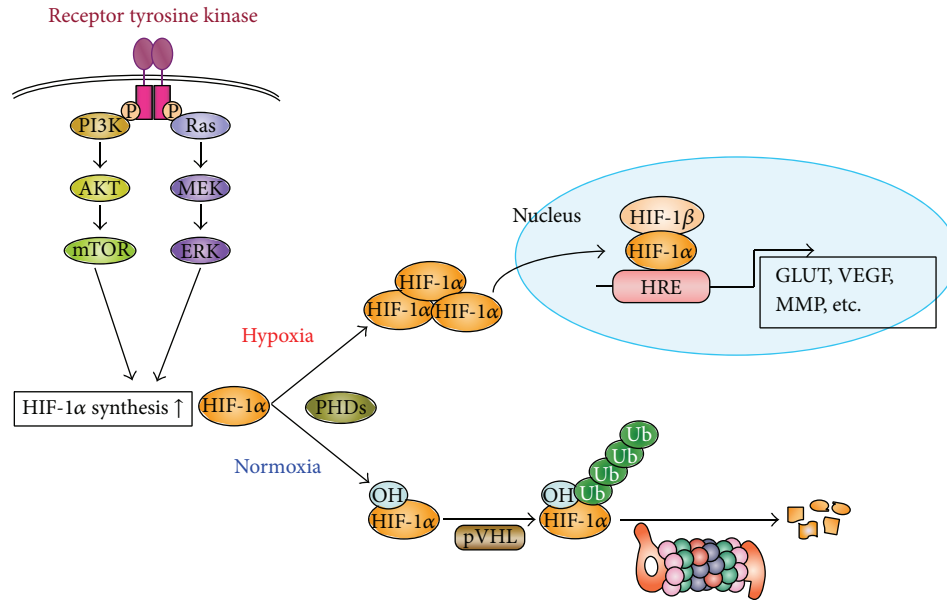


FIGURE 1: Regulatory mechanism of hypoxia-inducible factor (HIF-1) expression. Growth factor stimulation induces HIF-1 α subunit (HIF-1 α) protein synthesis by activating PI3K/Akt/mTOR and Ras/MEK/ERK kinase pathways. Under normoxic conditions, HIF-1 α is hydroxylated by proline hydroxylases (PHDs), triggering its interaction between von Hippel-Lindau tumor suppressor protein (pVHL), leading to its polyubiquitination and subsequent proteasomal degradation. In contrast, under hypoxic conditions, HIF-1 α remains stable, enters the nucleus, and, together with HIF-1 β , binds to hypoxia-responsive elements (HREs), upregulating the expression of target genes such as glucose transporters (GLUTs), vascular endothelial growth factors (VEGFs), and matrix metalloproteinases (MMPs). Ub: ubiquitin.

HIF-1 α , leading to its degradation in the 26S proteasome [16, 17]. However, proline residue hydroxylation does not occur under hypoxic conditions, allowing HIF-1 α to escape degradation and move into the nucleus where it associates with HIF-1 β and exerts its transcriptional activity by binding to hypoxia-responsive elements (HREs) (Figure 1) [18, 19]. Because HIF-1 β is constitutively expressed in the nucleus, the transcriptional activity of HIF-1 is regulated by HIF-1 α expression and degradation.

HIF-1 α expression is reported to increase dramatically in conditions where pO_2 is less than 6% (40 mmHg) [20]. However, the pO_2 threshold values that lead to HIF-1 α stabilization vary among different organs [21]. Because pulmonary cells are consistently exposed to relatively high pO_2 , the values that these cells perceive as abnormal are relatively high [11]. In contrast, the bone marrow is the only tissue that expresses HIF-1 α protein under normal physiological conditions [22]. Therefore, HIF-1 α is stably present in “biologically hypoxic regions,” where the tissues and/or cells themselves sense oxygen deficiency. These regions do not coincide completely with “physically hypoxic regions,” where pO_2 is less than 10 mmHg. Thus, HIF-1-dependent probes or reporter systems are required to directly visualize HIF-1 active hypoxic regions.

3. Monitoring HIF-1 Activity *In Vivo* by Using HIF-1-Dependent Reporter Gene Imaging

For the first time, nuclear medical molecular imaging of HIF-1 activity *in vivo* has been performed using a HIF-1-dependent

reporter system. In the field of molecular biology, reporter systems are commonly used to monitor the expression of a gene of interest. To directly monitor HIF-1 activity, cell lines that stably contain a reporter gene suitable for *in vivo* imaging downstream of HRE repeats have been established. When implanted into animals, these cells express the reporter protein in a HIF-1-dependent manner, and the amount of reporter protein expression can be measured using a molecular probe that binds to or is metabolized by these proteins.

Serganova et al. [23] and Wen et al. [24] performed positron emission tomography (PET) imaging to detect HIF-1 activity in tumors, using herpes simplex virus type 1 thymidine kinase (HSV1-TK) as a reporter gene; a PET reporter of *in vivo* gene expression has been widely used [25, 26]. Although endogenous TKs are normally present in mammalian cells, their substrate specificity differs from that of HSV-1TK. Because HSV1-TK has broader specificity than mammalian TKs, a probe that is selectively phosphorylated by viral TKs can be used to visualize HSV1-TK expression [27]. Serganova et al. [23] constructed a retroviral vector bearing the HRE-HSV1-TK reporter gene and transfected it into C6 glioma cells. The reporter system showed that dose-dependent patterns in the temporal dynamics of HIF-1 transcriptional activity were induced by decreased pO_2 . PET imaging using 2'-[^{18}F]fluoro-2'-deoxy-1 β -D-arabinofuranosyl-5-ethyl-uracil (^{18}F -FEAU), a radioactive probe selectively metabolized and retained in HSV1-TK-expressing cells, clearly visualized tumors. The spatial heterogeneity of HIF-1 transcriptional activity as a function

of tumor size was shown in a study of reporter xenografts in mice. With increasing tumor diameter (>3 mm), HIF-1 transcriptional activity markedly increased in the tumor core regions. This marked one of the earliest successes in nuclear medical molecular imaging for HIF-1 activity *in vivo*. Since then, several approaches for noninvasive imaging of HIF-1 activity have been reported, including those using different combinations of reporter genes and radiolabeled probes such as sodium-iodide symporter and ^{99m}Tc -pertechnetate [28], glycosylphosphatidylinositol-anchored avidin and ^{67}Ga -DOTA-biotin [29], and HSV1-TK and 9-(4-[^{18}F]fluoro-3-hydroxymethyl-butyl)guanine (^{18}F -FHBG) [30]. Brader et al. [31] constructed RH7777 Morris hepatoma cells bearing a triple reporter gene (HRE-HSV1-TK/green fluorescent protein/firefly luciferase) and prepared an orthotopic liver tumor model. They performed ^{18}F -FEAU-PET and luciferase bioluminescence imaging and succeeded in hypoxia-driven reporter imaging using both techniques.

HIF-1-dependent reporter systems are also useful for comparing HIF-1 activity and exogenous markers of tumor hypoxia. Wen et al. [24] generated rat prostate adenocarcinoma cells containing HRE-HSV1-TK fused to enhanced green fluorescent protein as a reporter. PET imaging was performed using 2'-fluoro-2'-deoxy- β -D-arabinofuranosyl-5-[^{124}I]iodouracil (^{124}I -FIAU), and the distributions of ^{124}I -FIAU and the exogenous hypoxic cell marker [^{18}F]fluoromisonidazole (^{18}F -FMISO) were compared. ^{124}I -FIAU PET imaging of hypoxia-induced reporter gene expression was feasible, and the intratumoral distributions of ^{124}I -FIAU and ^{18}F -FMISO were similar. Similar results were obtained for human colorectal HT29 cancer cells bearing the same reporter system [32]. However, no significant correlation between the ^{18}F -FMISO PET and HIF-1-dependent reporter readouts has also been reported [33]. The reasons for the discrepancy between these findings remain unclear and warrant further investigation. Notably, these described reporter systems did not include the ODD in the expressed reporter proteins. The degradation of HIF-1 α is reported to occur within a few minutes under normoxic conditions [34]. Thus, although reporter protein expression was regulated by HIF-1, it is necessary to acknowledge that the reporter proteins may not necessarily reflect real-time HIF-1 activity once the expression was completed.

4. Molecular Imaging of HIF-1-Active Tumor Microenvironments by Using Probes with Oxygen-Dependent Degradation

HIF-1-dependent reporter imaging systems are excellent tools not only for obtaining spatiotemporal information regarding HIF-1 expression, but also for evaluating the effectiveness of hypoxia-targeting therapies *in vivo*. However, these systems require exogenous gene transfection and are difficult to apply to humans. To overcome this limitation, a number of injectable probes containing ODD that degrade in an oxygen-dependent manner have been developed [35–41].

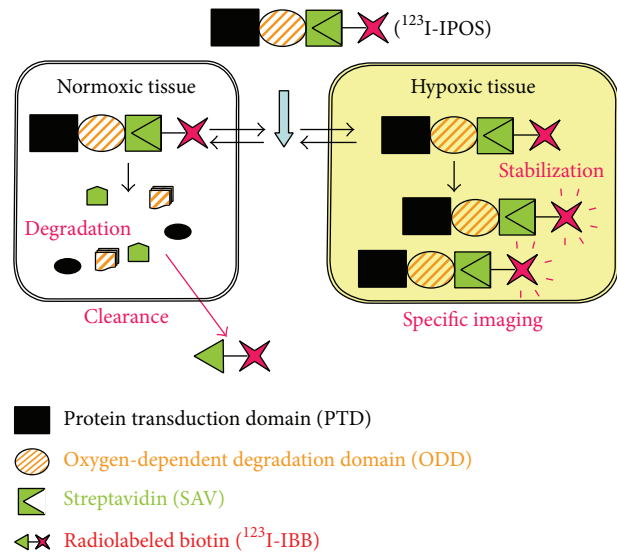


FIGURE 2: Principle underlying the imaging of HIF-1-active tumor microenvironments, using ^{123}I -IPOS. The PTD enables ^{123}I -IPOS to be delivered to all tissues. In normoxic tissues, oxygen-dependent POS degradation occurs and ^{123}I -IBB loses its binding partner and is cleared. In contrast, in hypoxic tissues, ^{123}I -IPOS escapes degradation and is retained within cells owing to its molecular size. Thus, ^{123}I -IPOS allows for specific imaging of HIF-1-active hypoxic microenvironments.

4.1. Chimeric Fusion Protein Probes Containing Oxygen-Dependent Degradation Domains. To design a probe that degraded in a manner similar to HIF-1 α , Kudo et al. [35] selected HIF-1 α _{548–603}, the region of ODD that is essential for oxygen-dependent degradation [42], as the core structure of the probe. An amino acid sequence that increases cell membrane permeability—the protein transduction domain (PTD) [43]—was included in the probe to facilitate its transport into cells. PTD-ODD was fused to monomeric streptavidin (SAV), generating the chimeric protein PTD-ODD-SAV (POS). POS was then labeled with the radioiodinated biotin derivative (3-[^{123}I]iodobenzoyl)norbiotinamide (^{123}I -IBB) to produce ^{123}I -IBB-POS (^{123}I -IPOS) [35]. The principle behind the imaging of HIF-1-active hypoxic microenvironments by using ^{123}I -IPOS is outlined schematically in Figure 2.

^{125}I -IPOS showed more than 2-fold greater accumulation in cells incubated under hypoxic conditions (0.1% O_2) than under normoxic conditions (20% O_2). Size-exclusion high-performance liquid chromatography (HPLC) analysis revealed that more than 80% of intracellular radioactivity was derived from intact ^{125}I -IPOS in the hypoxic cells. Reoxygenation analysis showed that the intracellular radioactivity of the reoxygenated group decreased by approximately 40%, compared to that under hypoxic conditions, and the radioactivity excreted into the medium were mostly attributable to ^{125}I -IBB and other small molecules [35]. These findings suggest that ^{125}I -IPOS is stable under hypoxic conditions but is degraded under normoxic conditions and that ^{125}I -IBB is excreted from cells. Biodistribution analysis showed that radioactivity accumulation in tumors 24 h after ^{125}I -IPOS

administration was $1.4 \pm 0.3\%$ of the injected dose per gram of tissue, and the tumor-to-blood ratio, which serves as an index of favorable image contrast, was 5.1. Forty-eight hours after ^{125}I -IPOS administration, radioactivity in the tumor decreased, but the tumor-to-blood ratio increased [35]. Single-photon emission computed tomography (SPECT)/X-ray computed tomography imaging with ^{125}I -IPOS clearly visualized the tumors. Autoradiographic study showed that the intratumoral distribution of ^{125}I -IPOS is heterogeneous and corresponds to HIF-1 α -positive regions detected using immunostaining [38]. Moreover, a positive and significant correlation was observed between ^{125}I -IPOS accumulation and HIF-1-dependent luciferase bioluminescent signals in the identical tumor [35]. These findings indicate that ^{125}I -IPOS is a promising probe for imaging HIF-1-active hypoxic microenvironments in tumors.

4.2. Rapid Detection of HIF-1-Active Tumor Microenvironments by Using POS: A Pretargeting Approach. Although PET is used less widely than SPECT in nuclear medical molecular imaging, it allows for higher sensitivity and resolution, as well as high-quality quantitative imaging. Thus, PET imaging of HIF-1-active tumors can provide precise information for determining appropriate therapeutic strategies and predicting prognoses of patients. Fluorine-18 is one of the most widely used radionuclides for PET imaging because of its ease of production, low positron energy, and adequate half-life (110 min). However, the half-life is too short to obtain signals 24 h after administration, at which time clear images can be obtained using ^{123}I -IPOS. Therefore, development of an imaging procedure that can be used to obtain high-contrast images during the early period after administration is required for successful PET imaging using ^{18}F .

A pretargeting approach uses a combination of tumor-targeting molecules and the prompt clearance of small radioactive compounds from the blood. One advantage of this method is that it can provide a high target:nontarget organ ratios shortly after injection. Therefore, we utilized a pretargeting approach based on the high-affinity and specific interaction between SAV and biotin for the PET imaging of HIF-1-active tumor microenvironments. The underlying principle of pretargeted imaging of HIF-1-active hypoxic microenvironments by using POS and (4- ^{18}F fluorobenzoyl)norbiotinamide (^{18}F -FBB) is outlined schematically in Figure 3.

Conjugation of *N*-succinimidyl-4- ^{18}F fluorobenzoate and norbiotinamine yielded ^{18}F -FBB, with a total synthesis time of 150 min, radiochemical yield of 23%, and radiochemical purity of >95%. An *in vitro* binding assay confirmed that ^{18}F -FBB bound to the SAV moiety of POS. Biodistribution analysis showed that ^{18}F -FBB was rapidly cleared from the body without POS pretargeting. The tumor-to-blood and tumor-to-muscle ratios were <1 at all investigated time points, indicating that ^{18}F -FBB itself does not show tumor accumulation. In contrast, ^{18}F -FBB accumulated in tumors in POS-pretargeted mice. ^{18}F -FBB was able to enter the tumor cells by passive diffusion owing to its lipophilicity

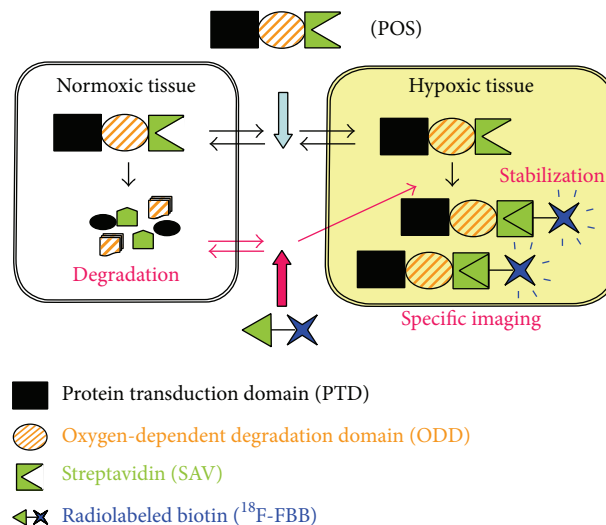


FIGURE 3: Principle underlying the imaging of HIF-1-active tumor microenvironments, using pretargeted POS and ^{18}F -FBB. The PTD enables the delivery of POS to all tissues. In normoxic tissues, POS degrades in a manner similar to HIF-1 α . In contrast, in hypoxic tissues, POS escapes degradation and is retained inside the cells. After allowing sufficient time for POS to degrade in normal tissues, ^{18}F -FBB is administered. ^{18}F -FBB enters cells by passive diffusion and binds to the SAV moiety of the POS retained in hypoxic cells; this does not occur in normoxic tissues. Therefore, pretargeting POS followed by ^{18}F -FBB administration enables specific imaging of HIF-1-active hypoxic microenvironments.

and bind to POS retained in tumor cells. Both tumor-to-blood and tumor-to-muscle radioactivity ratios increased over time [37]. Tumor-to-blood ratios comparable to those at 24 h after ^{123}I -IPOS administration can be obtained within 3 h of ^{18}F -FBB administration by using the pretargeting method. Pretreatment with excessive D-biotin significantly inhibited ^{18}F -FBB accumulation in POS-pretargeted tumors. Size-exclusion HPLC analyses revealed that 80% of intratumoral radioactivity is attributable to macromolecules. Taken together, these findings show that ^{18}F -FBB binds to POS *in vivo*, and PET imaging clearly delineated tumors within 3 h after injecting ^{18}F -FBB into POS-pretargeted mice. Therefore, the pretargeting approach makes it possible to reduce the time taken from probe administration to image acquisition by 8-fold, allowing imaging to be performed within the half-life of ^{18}F . In mice with tumors that had been transfected with a HIF-1-dependent luciferase reporter gene, ^{18}F -FBB accumulation positively correlated with HIF-1-dependent luciferase bioluminescent signals. The ^{18}F -FBB-distributed areas were consistent with HIF-1 α -positive areas in tumors pretargeted with POS [37]. Thus, these findings demonstrate that ^{18}F -FBB accumulation in the POS-pretargeted tumors reflects HIF-1-activity and the pretargeting approach with POS and ^{18}F -FBB is suitable for rapid imaging of HIF-1-active tumors.

4.3. Peptide Probes Containing Essential Amino Acids for Oxygen-Dependent Degradation. POS is a 34 kDa protein

generated in *Escherichia coli*. Although promising results for the imaging of HIF-1-active tumor microenvironments were obtained, as described above, clinical applications are limited by the possibility of immunogenicity. Peptide probes or small molecules are favorable for clinical applications because they can be easily synthesized with high purity and show no immunogenicity. Our research group succeeded in developing a peptide-based imaging probe that is degraded in a manner similar to HIF-1 α [41].

Based on the degradation mechanism of HIF-1 α , we selected HIF-1 α ₅₄₇₋₅₇₄ as the basic structure for the oxygen-sensitive peptide probe. For site-specific radiolabeling, a glycyl cysteine was introduced into the C-terminal of the HIF-1 α ₅₄₇₋₅₇₄ scaffold, yielding a peptide named OP30. OP30 was degraded when incubated with HeLa cell lysates but was unable to penetrate cell membranes. Thus, to increase its membrane permeability, the nine N-terminal amino acids of OP30 were replaced by L-lysine or D-lysine, producing peptides KOP30 and DKOP30, respectively. As expected, these modified peptides were also degraded in HeLa cell lysates and accumulated in the tumor cells. Degradation was inhibited by the addition of a proteasome inhibitor. Furthermore, by replacing the proline residues in KOP30 and DKOP30 that are essential for oxygen-dependent degradation with L-alanine, the resulting peptides (mKOP30 and mDKOP30, resp.) were not degraded in HeLa cell lysates. Taken together, these results indicate that the proline residues and proteasome function are required for the degradation of KOP30 and DKOP30, similar to HIF-1 α . Biodistribution analysis showed that ¹²⁵I-DKOP30 had better tumor accumulation and tumor-to-blood ratio than ¹²⁵I-KOP30. Therefore, we performed an additional study using ^{123/125}I-DKOP30. Tumors were visualized clearly by planar imaging using ¹²³I-DKOP30, and autoradiographic studies showed that the intratumoral distribution of ¹²⁵I-DKOP30 was consistent with the HIF-1 α -positive areas detected using immunohistochemical staining. Moreover, a positive and significant correlation was observed between ¹²⁵I-DKOP30 accumulation and HIF-1-dependent luciferase bioluminescent signals within the same tumor, whereas no correlation between ¹²⁵I-mDKOP30 accumulation and bioluminescent signals was observed. These findings indicate that ¹²³I-DKOP30 is a useful peptide probe for imaging HIF-1-active tumors.

Because many peptide probes have already been used in PET/SPECT imaging in humans [44–46], ¹²³I-DKOP30 has the most potential probe for imaging HIF-1-active tumors in clinical settings so far. Using planar imaging, the accumulation of ¹²³I-DKOP30 in tumors was found to be higher than the background radioactivity in the cervicofacial and thoracic regions; therefore, it is possible to detect HIF-1 activity in the head and neck, breast, and lung cancers. However, the high background radioactivity in the abdominal region would hamper the imaging of HIF-1-active abdominal tumors. To overcome this issue, a probe that demonstrates greater accumulation in tumors and/or faster clearance from blood and normal abdominal organs should be developed.

5. Molecular Imaging of HIF-1-Active Tumor Microenvironments in Clinical Practice

No probes currently used in clinical practice can directly detect HIF-1 activity. As described in Section 2, pO₂ values at which HIF-1 α is stable differ between organs. Thus, in principle, probes targeting physically hypoxic regions (pO₂ of ≤ 10 mmHg) are not suitable for the detection of HIF-1 expression or activity because the mechanisms underlying their hypoxic accumulation are independent of HIF-1 expression. However, HIF-1 α -positive regions reportedly overlap with pimonidazole-adducted regions in tumors. Although microscopic observation has shown that unmatched regions also exist [47, 48], the spatial resolution of nuclear medical imaging is not sufficiently high to distinguish these unmatched regions *in vivo*. Therefore, HIF-1 activity could potentially be evaluated indirectly by using probes targeting physically hypoxic regions. In fact, a number of clinical studies have been performed recently to evaluate HIF-1 expression in areas of [¹⁸F]fluoromisonidazole (¹⁸F-FMISO) or 2-deoxy-2-[¹⁸F]fluoro-D-glucose (¹⁸F-FDG) accumulation; however, the obtained results have been discrepant. Furthermore, it should be noted that neither ¹⁸F-FMISO nor ¹⁸F-FDG can be used to evaluate directly the HIF-1 activity, even if the probe accumulation is correlated with HIF-1 activity.

5.1. ¹⁸F-FMISO and Its Derivatives. Sato et al. [49] examined the relationship between ¹⁸F-FMISO PET results and HIF-1 α expression in patients with oral squamous cell carcinoma (OSCC). The maximum standardized uptake value (SUVmax) of ¹⁸F-FMISO PET was significantly higher in HIF-1 α -positive patients than in those negative for HIF-1 α . The authors concluded that ¹⁸F-FMISO uptake into the primary site of OSCC indicates the presence of a HIF-1 α -positive hypoxic environment. Kawai et al. [50] evaluated the correlations between ¹⁸F-FMISO uptake, HIF-1 α expression, and expression of vascular endothelial growth factor (VEGF), a HIF-1 target gene, in newly diagnosed and recurrent malignant gliomas. In contrast to the findings reported by Sato et al. [49], HIF-1 α expression in the tumors did not correlate with ¹⁸F-FMISO uptake in either newly diagnosed or recurrent glioma patients. A significant but weak correlation between VEGF expression and ¹⁸F-FMISO uptake was observed in newly diagnosed glioma patients, but not in those with recurrent glioma. Hu et al. [51] investigated the relationship between [¹⁸F]fluoroerythronitroimidazole (¹⁸F-FETNIM) uptake and expression of HIF-1 α , VEGF, and glucose transporter 1 (GLUT-1) in nonsmall cell lung cancer. A positive correlation existed between the tumor-to-muscle ratio of ¹⁸F-FETNIM and the expression of each of these HIF-1 α targets.

5.2. ¹⁸F-FDG. Sato et al. [49] examined the relationship between the SUVmax of ¹⁸F-FDG and HIF-1 α expression in OSCC, and no significant correlation was observed. This finding is in accordance with that reported by Cheng et al. [52] who found no correlation between ¹⁸F-FDG uptake

and HIF-1 α expression in breast cancer patients. Conversely, Takebayashi et al. [53] investigated the relationship between the SUVmax of ^{18}F -FDG, HIF-1 α expression, and GLUT-1 expression in gastric cancer patients. The SUVmax was correlated with HIF-1 α expression, but, interestingly, not with GLUT-1 expression. In this case, ^{18}F -FDG accumulation could indicate tissue hypoxia rather than glucose transport activity in aggressive cancer growths.

6. Conclusion

In this paper, the current status of nuclear medical molecular imaging strategies for HIF-1-active tumor microenvironments was discussed. At the preclinical level, HIF-1 activity has been directly evaluated by using HIF-1-dependent reporter systems and injectable probes that degrade in a manner similar to HIF-1 α . However, these techniques have not yet been applied clinically. At the clinical level, whether the accumulation of ^{18}F -FDG or ^{18}F -FMISO can be utilized as an index of HIF-1 activity has been investigated but results obtained in these studies varied substantially. To address this issue, the development of radiolabeled probes that directly evaluate HIF-1 activity in humans is required.

Conflict of Interests

The authors declare that there is no conflict of interests regarding the publication of this paper.

References

- [1] J. M. Arbeit, J. M. Brown, K. S. C. Chao et al., "Hypoxia: importance in tumor biology, noninvasive measurement by imaging, and value of its measurement in the management of cancer therapy," *International Journal of Radiation Biology*, vol. 82, no. 10, pp. 699–757, 2006.
- [2] H. Rundqvist and R. S. Johnson, "Tumour oxygenation: Implications for breast cancer prognosis," *Journal of Internal Medicine*, vol. 274, no. 2, pp. 105–112, 2013.
- [3] M. R. Horsman, L. S. Mortensen, J. B. Petersen, M. Busk, and J. Overgaard, "Imaging hypoxia to improve radiotherapy outcome," *Nature Reviews Clinical Oncology*, vol. 9, no. 12, pp. 674–687, 2012.
- [4] Y. Yoo, M. Hayashi, J. Christensen, and L. E. Huang, "An essential role of the HIF-1 α -c-Myc axis in malignant progression," *Annals of the New York Academy of Sciences*, vol. 1177, pp. 198–204, 2009.
- [5] D. M. Gilkes, G. L. Semenza, and D. Wirtz, "Hypoxia and the extracellular matrix: drivers of tumour metastasis," *Nature Reviews Cancer*, vol. 14, no. 6, pp. 430–439, 2014.
- [6] G. L. Semenza, "HIF-1 mediates metabolic responses to intratumoral hypoxia and oncogenic mutations," *The Journal of Clinical Investigation*, vol. 123, pp. 3664–3671, 2013.
- [7] J. Pouyssegur, F. Dayan, and N. M. Mazure, "Hypoxia signalling in cancer and approaches to enforce tumour regression," *Nature*, vol. 441, no. 7092, pp. 437–443, 2006.
- [8] G. L. Wang and G. L. Semenza, "Purification and characterization of hypoxia-inducible factor," *The Journal of Biological Chemistry*, vol. 270, no. 3, pp. 1230–1237, 1995.
- [9] D. P. Stiehl, W. Jelkmann, R. H. Wenger, and T. Hellwig-Bürgel, "Normoxic induction of the hypoxia-inducible factor 1 α by insulin and interleukin-1 β involves the phosphatidylinositol 3-kinase pathway," *FEBS Letters*, vol. 512, no. 1–3, pp. 157–162, 2002.
- [10] M. Pedersen, T. Löfstedt, J. Sun, L. Holmquist-Mengelbier, S. Pählman, and L. Rönnstrand, "Stem cell factor induces HIF-1 α at normoxia in hematopoietic cells," *Biochemical and Biophysical Research Communications*, vol. 377, no. 1, pp. 98–103, 2008.
- [11] S. Kizaka-Kondoh, S. Tanaka, H. Harada, and M. Hiraoka, "The HIF-1-active microenvironment: an environmental target for cancer therapy," *Advanced Drug Delivery Reviews*, vol. 61, no. 7–8, pp. 623–632, 2009.
- [12] M. Ivan, K. Kondo, H. Yang et al., "HIF α targeted for VHL-mediated destruction by proline hydroxylation: implications for O₂ sensing," *Science*, vol. 292, no. 5516, pp. 464–468, 2001.
- [13] P. Jaakkola, D. R. Mole, Y. M. Tian et al., "Targeting of HIF- α to the von Hippel-Lindau ubiquitylation complex by O₂-regulated prolyl hydroxylation," *Science*, vol. 292, no. 5516, pp. 468–472, 2001.
- [14] N. Masson, C. Willam, P. H. Maxwell, C. W. Pugh, and P. J. Ratcliffe, "Independent function of two destruction domains in hypoxia-inducible factor- α chains activated by prolyl hydroxylation," *EMBO Journal*, vol. 20, no. 18, pp. 5197–5206, 2001.
- [15] F. Okumura, M. Matsuzaki, K. Nakatsukasa, and T. Kamura, "The role of Elongin BC-containing ubiquitin ligases," *Frontiers in Oncology*, vol. 2, article 10, 2012.
- [16] L. E. Huang, J. Gu, M. Schau, and H. F. Bunn, "Regulation of hypoxia-inducible factor 1 α is mediated by an O₂-dependent degradation domain via the ubiquitin-proteasome pathway," *Proceedings of the National Academy of Sciences of the United States of America*, vol. 95, no. 14, pp. 7987–7992, 1998.
- [17] P. H. Maxwell, M. S. Wlesener, G. W. Chang et al., "The tumour suppressor protein VHL targets hypoxia-inducible factors for oxygen-dependent proteolysis," *Nature*, vol. 399, no. 6733, pp. 271–275, 1999.
- [18] S. M. Wood, J. M. Gleadle, C. W. Pugh, O. Hankinson, and P. J. Ratcliffe, "The role of the aryl hydrocarbon receptor nuclear translocator (ARNT) in hypoxic induction of gene expression: studies in ARNT-deficient cells," *The Journal of Biological Chemistry*, vol. 271, no. 25, pp. 15117–15123, 1996.
- [19] B. Jiang, E. Rue, G. L. Wang, R. Roe, and G. L. Semenza, "Dimerization, DNA binding, and transactivation properties of hypoxia-inducible factor 1," *Journal of Biological Chemistry*, vol. 271, no. 30, pp. 17771–17778, 1996.
- [20] B. H. Jiang, G. L. Semenza, C. Bauer, and H. H. Marti, "Hypoxia-inducible factor 1 levels vary exponentially over a physiologically relevant range of O₂ tension," *The American Journal of Physiology—Cell Physiology*, vol. 271, no. 4, pp. C1172–C1180, 1996.
- [21] D. M. Stroka, T. Burkhardt, I. Desbaillets et al., "HIF-1 is expressed in normoxic tissue and displays an organ-specific regulation under systemic hypoxia," *The FASEB Journal*, vol. 15, no. 13, pp. 2445–2453, 2001.
- [22] K. L. Talks, H. Turley, K. C. Gatter et al., "The expression and distribution of the hypoxia-inducible factors HIF-1 α and HIF-2 α in normal human tissues, cancers, and tumor-associated macrophages," *American Journal of Pathology*, vol. 157, no. 2, pp. 411–421, 2000.

- [23] I. Serganova, M. Doubrovin, J. Vider et al., "Molecular imaging of temporal dynamics and spatial heterogeneity of hypoxia-inducible factor-1 signal transduction activity in tumors in living mice," *Cancer Research*, vol. 64, no. 17, pp. 6101–6108, 2004.
- [24] B. Wen, P. Burgman, P. Zanzonico et al., "A preclinical model for noninvasive imaging of hypoxia-induced gene expression; comparison with an exogenous marker of tumor hypoxia," *European Journal of Nuclear Medicine and Molecular Imaging*, vol. 31, no. 11, pp. 1530–1538, 2004.
- [25] S. Soghomonyan, A. Hajitou, R. Rangel et al., "Molecular PET imaging of HSV1-tk reporter gene expression using [¹⁸F]FEAU," *Nature Protocols*, vol. 2, no. 2, pp. 416–423, 2007.
- [26] S. S. Yaghoubi and S. S. Gambhir, "PET imaging of herpes simplex virus type 1 thymidine kinase (HSV1-tk) or mutant HSV1-sr39tk reporter gene expression in mice and humans using [¹⁸F]FHBG," *Nature Protocols*, vol. 1, no. 6, pp. 3069–3075, 2007.
- [27] I. Serganova and R. Blasberg, "Reporter gene imaging: potential impact on therapy," *Nuclear Medicine and Biology*, vol. 32, no. 7, pp. 763–780, 2005.
- [28] J. Y. Chan, J. Chung, H. K. Joo et al., "Visualization of hypoxia-inducible factor-1 transcriptional activation in C6 glioma using luciferase and sodium iodide symporter genes," *Journal of Nuclear Medicine*, vol. 49, no. 9, pp. 1489–1497, 2008.
- [29] S. Lehmann, E. G. Garayoa, A. Blanc, R. Keist, R. Schibli, and M. Rudin, "Recording intracellular molecular events from the outside: glycosylphosphatidylinositol-anchored avidin as a reporter protein for in vivo imaging," *Journal of Nuclear Medicine*, vol. 52, no. 3, pp. 445–452, 2011.
- [30] C. Hsieh, J. Kuo, Y. Lee, C. Chang, J. G. Gelovani, and R. Liu, "Construction of mutant TKGFP for real-time imaging of temporal dynamics of HIF-1 signal transduction activity mediated by hypoxia and reoxygenation in tumors in living mice," *Journal of Nuclear Medicine*, vol. 50, no. 12, pp. 2049–2057, 2009.
- [31] P. Brader, C. C. Riedl, Y. Woo et al., "Imaging of hypoxia-driven gene expression in an orthotopic liver tumor model," *Molecular Cancer Therapeutics*, vol. 6, no. 11, pp. 2900–2908, 2007.
- [32] F. He, X. Deng, B. Wen et al., "Noninvasive molecular imaging of hypoxia in human xenografts: comparing hypoxia-induced gene expression with endogenous and exogenous hypoxia markers," *Cancer Research*, vol. 68, no. 20, pp. 8597–8606, 2008.
- [33] S. Lehmann, D. P. Stiehl, M. Honer et al., "Longitudinal and multimodal in vivo imaging of tumor hypoxia and its downstream molecular events," *Proceedings of the National Academy of Sciences of the United States of America*, vol. 106, no. 33, pp. 14004–14009, 2009.
- [34] A. Y. Yu, M. G. Frid, L. A. Shimoda, C. M. Wiener, K. Stenmark, and G. L. Semenza, "Temporal, spatial, and oxygen-regulated expression of hypoxia-inducible factor-1 in the lung," *The American Journal of Physiology—Lung Cellular and Molecular Physiology*, vol. 275, no. 4, pp. L818–L826, 1998.
- [35] T. Kudo, M. Ueda, Y. Kuge et al., "Imaging of HIF-1-active tumor hypoxia using a protein effectively delivered to and specifically stabilized in HIF-1-active tumor cells," *Journal of Nuclear Medicine*, vol. 50, no. 6, pp. 942–949, 2009.
- [36] M. Ueda, T. Kudo, Y. Kuge et al., "Rapid detection of hypoxia-inducible factor-1-active tumours: pretargeted imaging with a protein degrading in a mechanism similar to hypoxia-inducible factor-1 α ," *European Journal of Nuclear Medicine and Molecular Imaging*, vol. 37, no. 8, pp. 1566–1574, 2010.
- [37] T. Kudo, M. Ueda, H. Konishi et al., "PET imaging of hypoxia-inducible factor-1-active tumor cells with pretargeted oxygen-dependent degradable streptavidin and a novel ¹⁸F-labeled biotin derivative," *Molecular Imaging and Biology*, vol. 13, no. 5, pp. 1003–1010, 2011.
- [38] M. Ueda, T. Kudo, Y. Mutou et al., "Evaluation of [¹²⁵I]IPOS as a molecular imaging probe for hypoxia-inducible factor-1-active regions in a tumor: Comparison among single-photon emission computed tomography/X-ray computed tomography imaging, autoradiography, and immunohistochemistry," *Cancer Science*, vol. 102, no. 11, pp. 2090–2096, 2011.
- [39] H. Fujii, M. Yamaguchi, K. Inoue et al., "In vivo visualization of heterogeneous intratumoral distribution of hypoxia-inducible factor-1 α activity by the fusion of high-resolution SPECT and morphological imaging tests," *Journal of Biomedicine and Biotechnology*, vol. 2012, Article ID 262741, 6 pages, 2012.
- [40] M. Ueda, "Development of a method for high-contrasted nuclear medical imaging of hypoxia-inducible factor-1-active tumor by using a pretargeting approach," *Yakugaku Zasshi*, vol. 132, no. 5, pp. 595–600, 2012.
- [41] M. Ueda, K. Ogawa, A. Miyano, M. Ono, S. Kizaka-Kondoh, and H. Saji, "Development of an oxygen-sensitive degradable peptide probe for the imaging of hypoxia-inducible factor-1-active regions in tumors," *Molecular Imaging and Biology*, vol. 15, no. 6, pp. 713–721, 2013.
- [42] H. Harada, M. Hiraoka, and S. Kizaka-Kondoh, "Antitumor effect of TAT-oxygen-dependent degradation-caspase-3 fusion protein specifically stabilized and activated in hypoxic tumor cells," *Cancer Research*, vol. 62, no. 7, pp. 2013–2018, 2002.
- [43] S. Kizaka-Kondoh, S. Itasaka, L. Zeng et al., "Selective killing of hypoxia-inducible factor-1-active cells improves survival in a mouse model of invasive and metastatic pancreatic cancer," *Clinical Cancer Research*, vol. 15, no. 10, pp. 3433–3441, 2009.
- [44] R. Haubner, S. Maschauer, and O. Prante, "PET radiopharmaceuticals for imaging integrin expression: tracers in clinical studies and recent developments," *BioMed Research International*, vol. 2014, Article ID 871609, 17 pages, 2014.
- [45] D. Zeng, B. M. Zeglis, J. S. Lewis, and C. J. Anderson, "The growing impact of bioorthogonal click chemistry on the development of radiopharmaceuticals," *Journal of Nuclear Medicine*, vol. 54, no. 6, pp. 829–832, 2013.
- [46] S. Balogova, J. Talbot, V. Nataf et al., "¹⁸F-Fluorodihydroxyphenylalanine vs other radiopharmaceuticals for imaging neuroendocrine tumours according to their type," *European Journal of Nuclear Medicine and Molecular Imaging*, vol. 40, pp. 943–966, 2013.
- [47] S. Sobhanifar, C. Aquino-Parsons, E. J. Stanbridge, and P. Olive, "Reduced expression of hypoxia-inducible factor-1 α in perinecrotic regions of solid tumors," *Cancer Research*, vol. 65, no. 16, pp. 7259–7266, 2005.
- [48] X. Li, S. Carlin, M. Urano, J. Russell, C. C. Ling, and J. A. O'Donoghue, "Visualization of hypoxia in microscopic tumors by immunofluorescent microscopy," *Cancer Research*, vol. 67, no. 16, pp. 7646–7653, 2007.
- [49] J. Sato, Y. Kitagawa, Y. Yamazaki et al., "¹⁸F-fluoromisonidazole PET uptake is correlated with hypoxia-inducible factor-1 α expression in oral squamous cell carcinoma," *Journal of Nuclear Medicine*, vol. 54, no. 7, pp. 1060–1065, 2013.
- [50] N. Kawai, W. Lin, W. D. Cao, D. Ogawa, K. Miyake, and R. Haba, "Correlation between F-fluoromisonidazole PET and expression of HIF-1 α and VEGF in newly diagnosed

and recurrent malignant gliomas," *European Journal of Nuclear Medicine and Molecular Imaging*. In press.

- [51] M. Hu, L. Xing, D. Mu et al., "Hypoxia imaging with ¹⁸F-fluoroerythronitroimidazole integrated PET/CT and immunohistochemical studies in non-small cell lung cancer," *Clinical Nuclear Medicine*, vol. 38, no. 8, pp. 591–596, 2013.
- [52] J. Cheng, L. Lei, J. Xu et al., "¹⁸F-fluoromisonidazole PET/CT: a potential tool for predicting primary endocrine therapy resistance in breast cancer," *Journal of Nuclear Medicine*, vol. 54, no. 3, pp. 333–340, 2013.
- [53] R. Takebayashi, K. Izuishi, Y. Yamamoto et al., "Fluorodeoxyglucose accumulation as a biological marker of hypoxic status but not glucose transport ability in gastric cancer," *Journal of Experimental and Clinical Cancer Research*, vol. 32, no. 1, article 34, 2013.

Review Article

Why Are We Failing to Implement Imaging Studies with Radiolabelled New Molecular Entities in Early Oncology Drug Development?

Azeem Saleem,¹ Philip Murphy,² Christophe Plisson,¹ and Michael Lahn³

¹ Imanova Ltd., Centre for Imaging Sciences, Imperial College Hammersmith Hospital, Du Cane Road, London W12 0NN, UK

² GlaxoSmithKline Global Imaging Unit, Stockley Park West, 1-3 Ironbridge Road, Uxbridge, Middlesex UB11 1BT, UK

³ Early Phase Oncology Clinical Investigation, Eli Lilly Corporate Center, Building 31/4, 893 S. Delaware Street, Indianapolis, IN 46285, USA

Correspondence should be addressed to Azeem Saleem; azeem.saleem@imanova.co.uk

Received 6 June 2014; Accepted 18 July 2014; Published 18 August 2014

Academic Editor: Masahiro Ono

Copyright © 2014 Azeem Saleem et al. This is an open access article distributed under the Creative Commons Attribution License, which permits unrestricted use, distribution, and reproduction in any medium, provided the original work is properly cited.

In early drug development advanced imaging techniques can help with progressing new molecular entities (NME) to subsequent phases of drug development and thus reduce attrition. However, several organizational, operational, and regulatory hurdles pose a significant barrier, potentially limiting the impact these techniques can have on modern drug development. Positron emission tomography (PET) of radiolabelled NME is arguably the best example of a complex technique with a potential to deliver unique decision-making data in small cohorts of subjects. However, to realise this potential the impediments to timely inclusion of PET into the drug development process must be overcome. In the present paper, we discuss the value of PET imaging with radiolabelled NME during early anticancer drug development, as exemplified with one such NME. We outline the multiple hurdles and propose options on how to streamline the organizational steps for future studies.

1. Background

Access to and achieving therapeutic drug levels in the target tissue are a basic prerequisite for the successful development of a new molecular entity (NME). Conventionally, in drug development, plasma drug pharmacokinetics supplemented by preclinical data relating plasma to tissue pharmacokinetics is used as surrogate for target pharmacokinetics. However, increased realisation about interspecies differences and variable drug access in tumours and in sanctuary tissue sites, such as the brain, has led to the exploration of other methods that can provide confidence in tissue drug biodistribution and kinetics. One methodology that can provide such supportive information noninvasively is positron emission tomography (PET) imaging of radiolabelled NMEs. Radiolabelling of NME with a positron-emitting radionuclide to enable imaging does not change its biochemical properties and allows quantification of the NME at picomolar levels *in vivo* in tissue [1]. PET imaging continues to be used broadly in

neurosciences to evaluate drug access to the target during early stages of clinical development [2, 3]. In oncology, PET imaging studies can provide valuable information on drug access to tumour tissue, which can be affected by a number of factors such as the P-glycoprotein (PgP) and breast cancer resistance protein (BCRP) [4, 5] drug efflux mechanisms and aberrant tumour vasculature [6] (Table 1). Despite this valuable tool, there have been no prospective studies which used PET imaging for early decision-making in oncology trials. Consequently, the full potential of such studies had not been fully harnessed.

NMEs can be radiolabelled with short-lived positron-emitting radioisotopes (e.g., carbon-11, half-life 20 mins; Fluorine-18, half-life 119 mins) or with longer half-lives (e.g., Zirconium-89, half-life 3.3 days; Iodine-124, half-life 100 hours). Since the longer half-life of Zirconium-89 (⁸⁹Zr) and Iodine-124 (¹²⁴I) matches the circulation half-lives of monoclonal antibodies (mAbs), these isotopes have been used in the radiolabelling and evaluation of mAbs (Immuno-PET).

TABLE 1: Examples of some the clinical PET biodistribution studies performed with radiolabelled anticancer agents.

Drug	References
5-Fluorouracil	[10, 11]
Temozolomide	[12, 13]
N-[(2'-dimethylamino)ethyl]acridine-4-carboxamide (XR5000)	[14, 15]
Antisense oligonucleotide to Survivin (LY2181308)	[16, 17]
Docetaxel	[18]
Paclitaxel	[19]
Lapatinib	[20]
Erlotinib	[21–23]
Anti-CD44v6 chimeric monoclonal antibody, U36	[24]
Trastuzumab	[25, 26]
Some radiolabelled molecular entities under evaluation in ongoing imaging studies (NIH trial database)	
[⁸⁹ Zr]-Bevacizumab, [⁸⁹ Zr]-RO5323441 (placental growth factor antibody), [¹⁸ F]-SKI-249380 (dasatinib derivative), [¹²⁴ I]-PUH71, MMT0530A (a monoclonal antibody), [¹⁸ F]-Paclitaxel, [¹¹ C]-Erlotinib, and [⁸⁹ Zr]-Cetuximab	

Crucial developments including commercial availability of ⁸⁹Zr and ¹²⁴I, development and implementation of simplified radiolabelling techniques, and availability of radiolabelling protocols have allowed broad-scale clinical application of ⁸⁹Zr- and ¹²⁴I-immuno-PET in clinical mAb development studies [7]. However, such radiolabelling methods are not suited for other NMEs, which require development of molecule-specific radiochemistry. Moreover, the higher radiation doses associated with longer-lived PET radioisotopes limit its use in healthy volunteers and in performing repeat scans in the same subject.

In this paper, we have specifically focused on imaging studies of NMEs radiolabelled with short-lived radioisotopes. We will discuss the barriers in the implementation of PET studies, which currently limit the value of this tool. Using an example, we outline the logistics involved in conducting such studies. Finally, we propose ways to overcome potential barriers to streamline the performance of PET imaging studies with a particular emphasis on the conduct of such studies in the United Kingdom (UK).

2. PET Imaging Studies with Radiolabelled NMEs Are Ethically Justified and Provide Potential Savings in Drug Development

Because approximately 92% of oncology NMEs will not be approved [8], hundreds of patients receive limited or no additional benefit from participating in trials with NMEs. Incorporation of PET imaging studies in proof of concept studies, such as First-in-Human Dose (FHD) studies, is therefore a way to reduce attrition and is ethically justified, because it may help exclude ineffective NMEs early. As only 8% of oncology drugs reach the market, there has been an impetus to reduce late phase attrition by performing early proof of concept studies [9]. Typically phase I FHD studies are about a tenth (~£ 10 m) as expensive of a phase III study (~£ 100 m) [8]. Therefore, if PET studies are able to support a futility decision on a NME in a phase I proof of concept study,

it will allow the drug developer to shift focus to other active NMEs. In the experience of the authors, the additional cost of a typical PET study in 6 to 10 patients including development of radiochemical synthesis methods, regulatory approvals, and data analysis can range between £ 0.5 and 1 million. Such studies may also reduce the number of subjects needed in a FHD study and thus offset the costs of the imaging study. All of the above may potentially lead to increased efficiency in drug development and lead to a significant reduction in the costs of drug development.

3. Pharmacological Information Obtained from Clinical PET Studies

PET is a highly sensitive technology allowing the quantification of picomolar tissue levels, thereby enabling studies to be performed at microdoses of the NME, typically defined as 1–100 µg or <1/100 of the therapeutic dose. For instance, microdose studies with the radiolabelled topoisomerases I and II inhibitor, DACA, and [¹¹C]DACA were performed at 1/1000th of the phase I starting dose [14], a significant advantage during early drug development. PET studies with radiolabelled NMEs can provide information on drug pharmacology and are especially valuable where standard pharmacokinetic evaluation cannot be extrapolated from plasma pharmacokinetic profile of the NME (e.g., brain). They can also provide key information on the drug pharmacokinetics when the NME has a complex structure and there is an uncertainty about the pharmacokinetic profile and its impact on the target site (e.g., antisense oligonucleotide; ASO). In the following we show the primary benefits of using PET. A potential caveat with PET pharmacokinetic studies with agents administered orally may result due to differences in bioavailability as PET studies are conducted with intravenous administration of the radiolabelled NME.

3.1. Direct Evidence of Drug Access to Tumour Tissue. PET studies can provide direct evidence of drug access to target and the relative uptake in tumours compared to

normal tissue. PET studies with radiolabelled temozolomide ($[^{11}\text{C}]$ temozolomide) performed during early development demonstrated higher uptake of $[^{11}\text{C}]$ temozolomide in gliomas compared to normal brain tissue suggestive of a potentially advantageous therapeutic index [12]; currently, temozolomide is an approved and frequently used agent in the routine management of brain tumours.

3.2. Access to Sanctuary Sites. In contrast to brain tumours or metastases wherein the blood-brain-barrier is generally disrupted, drug access to normal brain remains a challenge. This is particularly an issue for monoclonal antibodies because their size does not allow them to cross an intact blood-brain-barrier and thereby fail to prevent CNS recurrences [27]. Although small molecules may have improved brain access due to their lower molecular weight, a number of factors influence the penetration of small molecules to the brain, such as lipophilicity, electric charge, affinity to active transport systems, or being a substrate compound for drug efflux mechanisms [28, 29]. Since there are limited models able to predict blood-brain-barrier penetration, a clinical PET study can provide direct confirmation. For example, a recent study of radiolabelled lapatinib, a small molecule targeting Her-1 and Her-2 tyrosine kinase, suggested that the drug did not cross an intact blood-brain-barrier [20]. Such an imaging study in small number of subjects can provide important insights into the lack of access to a sanctuary site, such as the brain, and thus avoid an expensive large trial or help design an appropriate confirmatory clinical study.

3.3. Evidence of Target Engagement and Drug Activity. Target engagement is crucial with the arrival of novel cytostatic and targeted agents especially since conventional structural imaging methods may not show a decrease in tumour size despite target engagement. For instance, target engagement of the anticancer agent LY2181308 as evidenced by the biodistribution of $[^{11}\text{C}]$ LY2181308 in tumours was proven through an associated decrease in tumour glucose metabolism measured by FDG-PET uptake [16]. Such direct and early evidence of target engagement could not have been substantiated in the absence of a decrease in tumour size on CT readout [16]. While PET studies using an appropriate pharmacodynamic radiotracer can provide an early readout of target engagement, they can also suggest resistance and/or sensitivity mechanisms, that is, discrepancy between tumour uptake and response to treatment. Other PET pharmacodynamic (PD) markers assess glucose metabolism (FDG), proliferation (Fluorothymidine), perfusion (water), angiogenesis (Fluciclatide) and hypoxia (fluoromisonidazole, HX4). The appropriate use of such a PET PD biomarker is based on the biology of the drug action and its presumed target.

3.4. Target Engagement for Patient Stratification. Potential differences in tumour phenotypic expression may be exploited to help stratify and in personalisation of therapy as elegantly exemplified by clinical PET studies with $[^{11}\text{C}]$ erlotinib, a tyrosine kinase inhibitor of epidermal growth factor receptor (EGFR). In patients with nonsmall

cell lung cancer, higher uptake of $[^{11}\text{C}]$ erlotinib was observed in patients with exon 19 mutations compared to patients with wild type EGFR expression, potentially allowing for personalisation of therapy [21, 22]. There is an increasing interest in the radiolabelling tyrosine kinase inhibitor (TKI) to aid their clinical development as shown by studies with 7 of the 12 FDA-approved TKIs [30]. cMET is a protooncogene that encodes a protein known as hepatocyte growth factor receptor, whose abnormal activation in cancer correlates with poor prognosis. A cMET imaging radioligand is also under development that may be used to potentially identify cMET positive tumours prior to administration of a cMET inhibitor [31].

3.5. Indication of Normal Tissue Toxicity. PET studies can also provide crucial information on the differential uptake of the NME and its radiolabelled metabolites in various tissue organs. Although the presence of increased drug concentrations in normal tissue do not necessarily signify specific tissue toxicities, increased uptake, and retention in tissues such as the cardiac muscle, renal cortex, or the presence of enterohepatic circulation of radioactivity may alert to the need of a vigorous monitoring and management of potential normal tissue toxicities during drug development. Microdosing clinical studies with $[^{11}\text{C}]$ DACA, a drug that did not progress beyond phase II studies, demonstrated drug accumulation in the heart suggestive of a potential cardiotoxicity risk, which in the later phase II studies was fortunately not observed [32–34].

3.6. Drug Scheduling. PET studies may potentially help in the optimisation of drug scheduling strategies that are intended to maximize drug levels/exposure to the target tissue, while limiting exposure to healthy organs. Such studies can be conducted either during early or late drug development stages. By applying mathematical techniques to PET studies with $[^{11}\text{C}]$ temozolomide, it was possible to predict brain tumour and normal tissue temozolomide concentration profiles for different temozolomide dosing regimens [13]. This study suggested that the predicted biodistribution of temozolomide in tumour was better for the 200 mg/m²/day for 5 days q 28 days regimen compared to 100 mg/m²/day for 5 days q 28 days and 75 mg/m²/day for 7 weeks regimens, a finding consistent with current clinical practice.

3.7. Utility of PET Biodistribution Studies in Later Phase Clinical Development. Although in this paper we primarily focused on the utility of PET imaging in FHD or early proof of concept studies, information provided from such studies can also be helpful in later phase trials, in order to interrogate drug combinations, novel-novel-drug testing, schedule modification, and repositioning of the compound. Some of these studies are currently under way (Table 1).

4. Implementation Challenges for PET Imaging Exemplified by the FHD Study with Antisense Oligonucleotide (ASO) (LY2181308) Targeting the Apoptosis Inhibitor Protein Survivin

Having discussed the potential advantages of performing PET studies with radiolabelled NMEs in FHD studies, we shall now provide an overview of one such study illustrating the challenges during early cancer drug development. This is one of the few examples of an imaging study with a radiolabelled NME which was prospectively integrated in a FHD study [16].

4.1. Study Genesis and Aims. The compound, LY2181308 (Eli Lilly and Company), was radiolabelled because there was uncertainty on whether such an ASO would reach the tumour tissue. For such a biodistribution study, there were several advantages for an ASO and in particular for LY2181308: (a) the pharmacokinetics of the agent allowed a nearly full extrapolation from animals to humans [17]; (b) the manufacturing was well controlled with few impurities. Importantly, at the time of conception, there was neither pharmacokinetic nor biodistribution study data for any ASO performed in cancer patients; consequently additional information on distribution of the ASO to the tumour was needed prior to moving the NME into the next phase of clinical development. Therefore, normal tissue and tumour pharmacokinetics of this NME was determined and its antitumour effect in cancer patients was assessed.

4.2. Operational Setup and Study Organisation. Broadly, the process consisted of 3 main tasks (a) development of radiolabelling conditions to non-Good Manufacturing Practice (non-GMP) standards and performance of preclinical radiation dosimetry, (b) transfer of non-GMP radiochemistry to GMP standard, tracer validation for clinical use, and submission of a dossier detailing radiochemical manufacturing and quality control processes to the UK Medicines and Healthcare Regulatory Agency (MHRA) for approval, and (c) submission of the clinical study documents to the independent Research Ethics Committee (REC) and the Administration of Radioactive Substances Committee (ARSAC) for approval to conduct the study in cancer patients. This required multidisciplinary and multi-institutional collaborations between the Early Oncology Clinical Investigation Division at Eli Lilly and Company, the sponsor and owner of LY2181308, and the University of Washington, St. Louis, MO, USA (UW) for development of non-GMP radiochemistry and the University of Manchester Wolfson Molecular Imaging Centre, Manchester, UK (WMIC), for implementation of GMP radiochemistry and conducting the clinical study.

The initial step to perform feasibility evaluation of radiosynthesis of [¹¹C]LY2181308 and development of non-GMP production at UW took over 15 months. The time period for this step is variable and will depend on the ease of introduction of the PET isotope. The synthetic route to label the NME often differs from that of the corresponding

unlabelled drug since the short half-life of the isotope requires the radioisotope to be introduced as part of the final synthetic step. This means both precursor for labelling and the radiotracer may require development of their respective preparation route. Dosimetry studies were then conducted in nonhuman primates to estimate the human radiation effective dose [35]. Following this, technology transfer of the methods to WMIC was undertaken for implementation of GMP radiochemistry. Implementation of GMP radiochemistry and performance of validation runs were done to confirm the manufacturing and quality control processes of the tracer in accordance with the approved EU regulations. Validation runs were performed to ensure that the impurities and additives in the end-product were within acceptable levels for human administration and confirmed the sterility of the formulated [¹¹C]LY2181308 doses produced. Although the formulated [¹¹C]LY2181308 was going to be given to patients participating in the concurrent FHD study, the radioactive form of [¹¹C]LY2181308 required a separate and updated Investigational Medicinal Product Dossier (IMPD) for this substudy of the FHD. This requirement was based on the fact that [¹¹C]LY2181308 was prepared and formulated in a different way than the authorised drug product for the concurrent FHD study. The IMPD therefore included updates to the Chemistry, Manufacturing and Control (CMC) section. Medical sections had to also be updated in the IMPD for the FHD study to justify the PET biodistribution study.

4.3. Study Hurdles. A number of considerable delays were encountered as this was the first of its kind study at that time (2005-2006) after introduction of the new regulatory processes emanating from the EU clinical trial directive. The major delay related to compiling adequate and sometimes novel documentation for regulatory review. In the light of new guidelines by the European Medicines Agency (EMA) (EMA 2006; [36]), a formal site inspection for assessing the manufacturing and production of the radiolabeled agent was performed by the UK Medicines and Healthcare products Regulatory Agency (MHRA) which added to the timelines. In parallel to the MHRA submissions other regulatory submissions to the Research Ethics Committee (REC) and the Administration of Radioactive Substances Advisory Committee (ARSAC) were made. Delays were also encountered with ethics approval as there were concerns about administration of radioactivity and the REC was unfamiliar with this type of study. Overall, the time from early radiochemistry work and dosimetry studies to the initiation of the clinical study took about 3 years (Figure 1).

4.4. Scientific Information Provided by the Study. Despite the long wait, this study provided valuable information, demonstrating rapid biodistribution of the radiopharmaceutical in tissues (including the tumour), an unanticipated but positive finding. In addition, greater than anticipated accumulation of [¹¹C]LY2181308 was observed in the cortex of kidneys, a finding that differed from the preclinical data. Consequently, there was concern about ASO-related renal toxicity and this directed adequate monitoring strategies for phase II

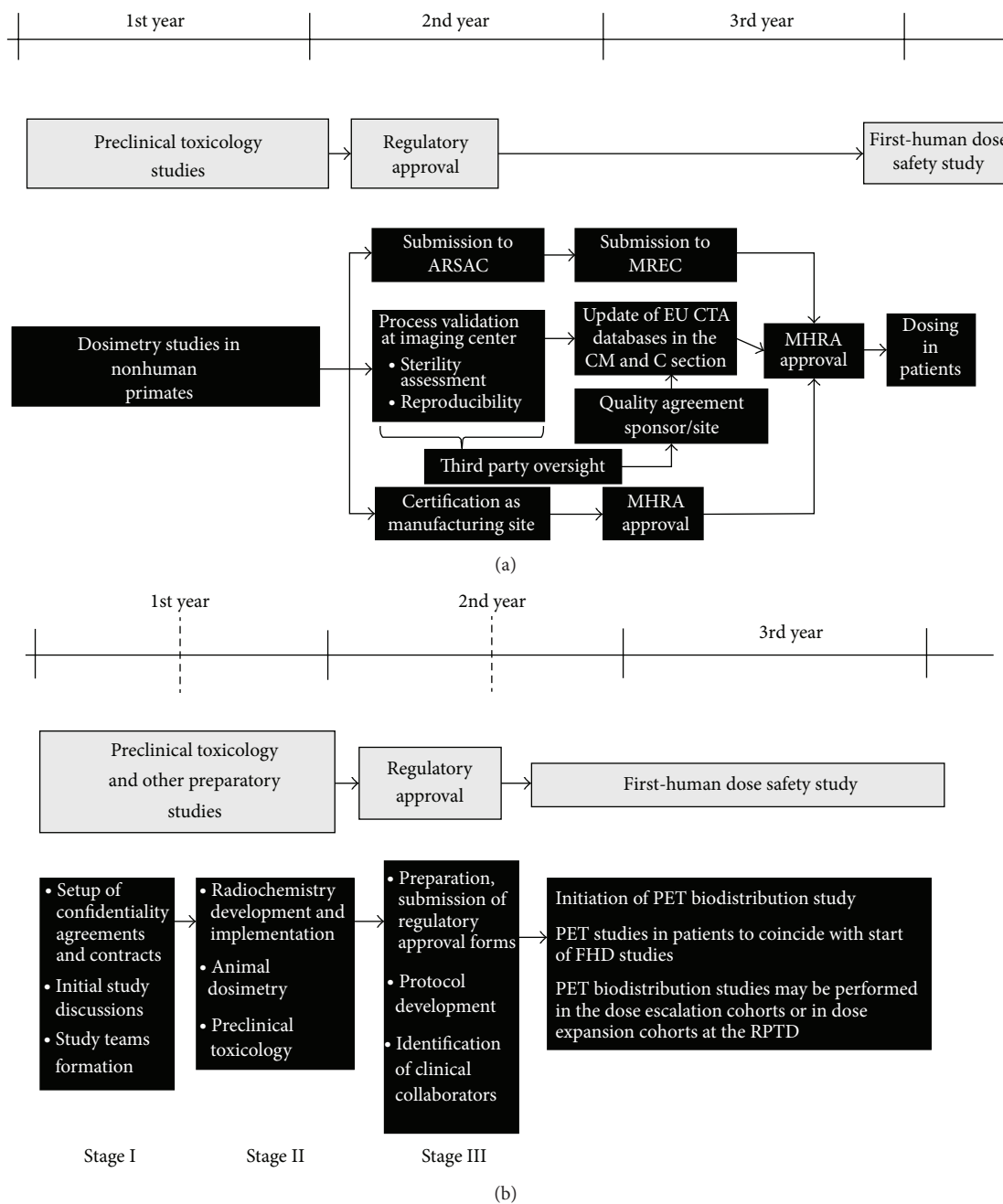


FIGURE 1: Summary of timelines and procedures performed in the PET biodistribution study of the ASO LY2181308 in relation to the FHD study (a). (b) Is proposed flowchart of future streamlined timelines of PET biodistribution studies in relation to FHD oncology studies with NMEs.

studies. Incidentally, the FHD study with LY2181308 [16, 17] included a patient in which the possible renal toxicity was of concern [37]; fortunately, this grade 2 toxicity was not dose-limiting and reversible. This unexpected finding during the biodistribution study shows another advantage of conducting such biodistribution studies early in drug development, because it detected an otherwise unappreciated toxicity risk. This study also demonstrated a decrease in tumour glucose metabolism as observed by a decrease in FDG-PET uptake, while simultaneously the target engagement was evaluated.

Complementing the otherwise favourable safety profile, this concomitant tumour response and target engagement justified the advancement of LY2181308 into phase II development [38–40].

5. Current Outlook and Future Considerations

Early drug development is a dynamic process with a focus on timelines to ensure the delivery of NMEs to the next development phase. Radiolabelling of an NME is often

commissioned late within a drug lifecycle and the impact of such data on key decisions can easily be lost. Delivery of a radiolabelled NME study needs to focus on providing the right data at the right time for the programme—and we argue that its greatest use is during early drug development.

Since the completion of the study with LY2181308, some of the processes have been positively streamlined in the UK. These include the implementation of the integrated research application system (IRAS) that allows for parallel submission to the various regulatory bodies including the Research Ethics Committee (REC), ARSAC, MHRA, and the hospital Research and Development (R&D) committees. Despite this, we feel that regulatory processes can be further streamlined in order to reduce timelines without sacrificing quality and patient's safety. For instance, although decisions from regulatory bodies such as REC, MHRA, and ARSAC are dictated by strict timelines, addressing multiple queries from RECs that either are unaware of or have not dealt with such biodistribution studies with radiolabelled NMEs may result in significant delays. Therefore, assignment of specialized RECs to review such PET studies would likely minimise delays.

In addition to the interaction with regulatory bodies, recruitment of patients to PET studies is dependent on the hospital R&D approval process, which is not time-bound. Discussions with the hospital R&D departments can lead to an impasse about study costs, extent of contractual obligations, intellectual property (IP) rights, and other legal interpretations of contracts. An early engagement with hospital R&D departments and the clinical investigators and/or mandating time-bound approval process may help reduce delays. The European Commission has also recognised that since the introduction of the EU Clinical Trials directive 2001/2/EC the number of clinical trial applications in the EU between 2007 and 2011 has fallen by 25%, whilst the costs for bureaucracy and resource requirements to handle paperwork have doubled, and delays have increased by 90%. The European Commission is therefore putting together new proposals that will reduce bureaucracy and include procedures to simplify and streamline the trial authorisation procedures. We hope that these proposals likely to come into effect in 2016 will improve the regulatory approval processes.

Currently PET clinical studies with radiolabelled NMEs are considered a clinical trial by the MHRA, requiring submission of an IMPD in the UK. As the MHRA now regularly audit imaging centres for PET studies, it is no longer a requirement that sites are reaudited before the initiation of every such biodistribution study. Guidelines for animal toxicity testing and for quality of all chemicals entering the manufacturing process and of the radiopharmaceutical (European commission GMP guidelines Annex 3, 2008 [41]) provide useful recommendations for the GMP implementation of radiopharmaceuticals for early phase clinical trials [42]. However, time and resources to conduct additional animal toxicology evaluation to enable PET imaging studies are minimal and consideration is given to include such studies in the standard animal toxicology evaluation if PET studies are planned in order not to add further time to the existing timelines.

Since animal dosimetry studies overestimate the radiation dose in humans and the radiation exposure for carbon-11 radiotracers is quite low (on average equivalent to about one year of background radiation exposure in the UK), we believe that dosimetry studies are not required, especially for carbon-11 labelled NMEs [43]. Even with Fluorine-18 radiolabelled radiotracers, the radiation exposure to the subject is on average similar to that obtained with a diagnostic FDG PET scan (or equivalent to about 3-year background radiation exposure) [44]; a case can be made for not performing animal dosimetry studies for radiolabelled NMEs, especially in a group of patients with limited life span and where the tracer is unlikely to be used as a diagnostic agent in the future.

Other processes may also lead to potential delays, including those related to transference of non-GMP to GMP methods. Radiolabelling feasibility of the NME and production of the radiopharmaceutical with good reproducibility may be highly variable. Hence, the feasibility evaluation process must consider the chemical structure and the ease of synthesis of the NME. The performance of the labelling feasibility work should be done on a similar automated platform as the one(s) to be used for the GMP implementation. This requires an appropriate PET radiochemistry infrastructure ideally with duplication of equipment, as R&D grade materials should not be used on equipment for GMP synthesis in accordance to EU guidelines. Involvement of the quality assurance department early in the development process will also make for an easy translation to the GMP settings. Finally, sourcing of a GMP-grade precursor, failure of validation runs, and delays in sterility analysis during validation may need to be addressed to avoid potential delays.

Therefore, good project management including a GMP implementation and risk management plan and regular interaction between the drug developers, radiochemists, and medicinal chemists during the development process will help focus on the timelines and address unforeseen issues. Project allocation to a team with expertise in R&D radiolabelling feasibility and translation to GMP will especially help avoid potential delays. Skilled leadership, effective communication and decision-making, formation of study teams consisting of members with the requisite skills, and identification of favoured suppliers to source precursors are likely to help prevent delays.

As the ultimate success of such studies is crucially dependent on patient recruitment, protocols should be patient-friendly. It is equally important that the small number of imaging centres work closely with the FHD study sites and the clinical investigators. Therefore, a well-established nexus of the imaging centre, phase I units, and clinical investigators that can deliver such studies will be attractive to the pharmaceutical industry.

On the basis of our experience, a period of up to 6 months is expected from initiation of a study proposal to confirmation of radiochemistry production feasibility. An additional 9 months is then required for the implementation of radiolabelling methods in accordance with the principles of GMP, regulatory submission, and approval until the initiation of the PET biodistribution study (Table 2). This period of 15 months for initiation of the PET study from study

TABLE 2: Sequential stages of activities, their timelines, potential causes for delays, and recommendations to reduce delays in PET biodistribution studies.

Activities	Approx. time (months)	Potential causes for delays	Comments and recommendations for improvement in timelines
Stage I (all activities can be done simultaneously): time 1-2 months			
Initial study discussion formulation of an outline research plan	2 months	Prevarication, and absence of key decision makers	Clear communication and clear goal setting by the respective team leaders
Confidentiality agreements completion	1-2 months	Legal issues	Preexistence of a master services agreements
Formation of study teams with clear definition of roles and responsibilities	1 month	Organisational issues Availability of experienced staff and agreement	Ensure inclusion of key staff, chemists, regulatory, clinical, biologists
Contract agreements	1-2 months	Disagreements on pricing and intellectual property rights	Early finance and legal involvement. Work with contract-based imaging services providers
Stage II (all activities can be done simultaneously): time 4-7 months			
Radiochemistry feasibility and production of radiolabelled NME (non-GMP or GMP) Implementation of GMP radiochemistry (RC) and its validation Preclinical dosimetry study Animal toxicology studies	4-7 months	Radiochemical method development issues Issues with procurement of precursor (GMP or non-GMP) Problems transferring from non-GMP to GMP settings	Selection of PET centre with good track record of developing and implementing radiopharmaceuticals for clinical use and management of drug maker expectations Preferred approved suppliers Duplication of equipment for straightforward transfer of methods, development of cassette based chemistry, good communication, and regular interactions Agreement of clear milestones and associated timelines for "Go-No Go" decisions
Stage III (all activities can be done simultaneously): time 3-6 months			
Preparation of IMPD dossier for submission to MHRA	1 month	Subject to delays in GMP implementation	Experienced personnel to complete CMC section
Identification of clinical collaborators Initiation of contracts with hospital	3 months	Identification and selection of appropriate clinicians Realistic assessment of recruiting potential	Initiate early in Stage III as can cause significant delays Preferred clinicians, imaging centre-linked clinical units
Development of research study protocol	2 months	Internal hierarchical and regulatory approval	
Preparation and submission of regulatory submission to the REC, MHRA, and ARSAC and to hospital R and D	2 months	CMC section completion due to RC implementation delays Delays in getting a date for an REC meeting	Done via the common IRAS However, MHRA and ARSAC require additional information to that provided by IRAS
Obtaining regulatory approvals and study initiation	2-3 months	Delays if there are queries or need for modifications Variable calibre of ethics committee to review such studies	Hospital R and D approval not time-bound Submission to or designation of ethics committees to review such studies

conception would fit well with the similar time required for standard initiation of a FHD clinical study from compound selection. We think that these streamlined timelines would allow for a greater integration of PET biodistribution studies during FHD clinical studies.

Despite the potential utility, anticipated improvements of organisational and regulatory interactions, and increased

interest in radiolabelling NMEs [45], there is a missing collection of examples supporting the value for early clinical biodistribution studies. This lack of supporting information, perceived high costs, timelines, and overall complexity of the technology [46], in a current climate of tightening budgets, prevents us from fully assessing the impact of biodistribution studies on clinical development and hampers uptake by

scientists and clinicians intimately involved in the drug development process. However, it is heartening to note that there are a few clinical PET biodistribution studies currently underway worldwide, as reflected in the NIH trial database (Table 1). While from this list it appears that NMEs are being evaluated in imaging studies, their value in the overall drug development is not clear. Nevertheless, we anticipate that results from such and other well-designed studies integrated into the drug development process will likely catalyse a wider use of this technology and an even greater focus on efficiency and timelines.

We would like to propose the following action points that would lead to greater implementation of such studies. Firstly, the key stakeholders from academia, industry, PET community, and imaging bodies should be brought together to act as a forum for discussion of proposals submitted by members who are new to this area. We envisage that this group would provide advice and guide in the setup and implementation of studies and also interact with the regulatory bodies. Because such specialized clinical imaging centres are limited, we would propose creating a network of accredited centres working closely with clinical investigators and clinical units that are able to implement all aspects of such studies. At the current stage, we do not expect more than 5 such studies to occur every year worldwide; however, this would likely increase if such studies prove their value in drug development.

Conflict of Interests

The authors declare that there is no conflict of interests regarding the publication of this paper.

References

- [1] M. Bergström, A. Grahnén, and B. Långström, "Positron emission tomography microdosing: a new concept with application in tracer and early clinical drug development," *European Journal of Clinical Pharmacology*, vol. 59, no. 5-6, pp. 357-366, 2003.
- [2] S. Kapur, R. Zipursky, C. Jones, G. Remington, and S. Houle, "Relationship between dopamine D2 occupancy, clinical response, and side effects: a double-blind PET study of first-episode schizophrenia," *The American Journal of Psychiatry*, vol. 157, no. 4, pp. 514-520, 2000.
- [3] P. M. Matthews, E. A. Rabiner, J. Passchier, and R. N. Gunn, "Positron emission tomography molecular imaging for drug development," *British Journal of Clinical Pharmacology*, vol. 73, no. 2, pp. 175-186, 2012.
- [4] K. Natarajan, Y. Xie, M. R. Baer, and D. D. Ross, "Role of breast cancer resistance protein (BCRP/ABCG2) in cancer drug resistance," *Biochemical Pharmacology*, vol. 83, no. 8, pp. 1084-1103, 2012.
- [5] R. K. Vadlapatla, A. D. Vadlapudi, D. Pal, and A. K. Mitra, "Mechanisms of drug resistance in cancer chemotherapy: coordinated role and regulation of efflux transporters and metabolizing enzymes," *Current Pharmaceutical Design*, vol. 19, no. 40, pp. 7126-7140, 2013.
- [6] A. Saleem and P. M. Price, "Early tumor drug pharmacokinetics is influenced by tumor perfusion but not plasma drug exposure," *Clinical Cancer Research*, vol. 14, no. 24, pp. 8184-8190, 2008.
- [7] G. A. M. S. Van Dongen and M. J. W. D. Vosjan, "Immunopositron emission tomography: shedding light on clinical antibody therapy," *Cancer Biotherapy and Radiopharmaceuticals*, vol. 25, no. 4, pp. 375-385, 2010.
- [8] S. M. Paul, D. S. Mytelka, C. T. Dunwiddie et al., "How to improve R&D productivity: the pharmaceutical industry's grand challenge," *Nature Reviews Drug Discovery*, vol. 9, no. 3, pp. 203-214, 2010.
- [9] B. Pagliara, "A record year for approvals," *MedNows*, vol. 7, no. 2, pp. 6-8, 2012.
- [10] E. O. Aboagye, A. Saleem, V. J. Cunningham, S. Osman, and P. M. Price, "Extraction of 5-fluorouracil by tumor and liver: a noninvasive positron emission tomography study of patients with gastrointestinal cancer," *Cancer Research*, vol. 61, no. 13, pp. 4937-4941, 2001.
- [11] A. Saleem, J. Yap, S. Osman et al., "Modulation of fluorouracil tissue pharmacokinetics by eniluracil: in-vivo imaging of drug action," *The Lancet*, vol. 355, no. 9221, pp. 2125-2131, 2000.
- [12] A. Saleem, G. D. Brown, F. Brady et al., "Metabolic activation of temozolomide measured in vivo using positron emission tomography," *Cancer Research*, vol. 63, no. 10, pp. 2409-2415, 2003.
- [13] L. Rosso, C. S. Brock, J. M. Gallo et al., "A new model for prediction of drug distribution in tumor and normal tissues: Pharmacokinetics of temozolomide in glioma patients," *Cancer Research*, vol. 69, no. 1, pp. 120-127, 2009.
- [14] A. Saleem, R. J. Harte, J. C. Matthews et al., "Pharmacokinetic evaluation of N-[2-(dimethylamino)ethyl]acridine-4-carboxamide in patients by positron emission tomography," *Journal of Clinical Oncology*, vol. 19, no. 5, pp. 1421-1429, 2001.
- [15] D. J. Propper, J. De Bono, A. Saleem et al., "Use of positron emission tomography in pharmacokinetic studies to investigate therapeutic advantage in a phase I study of 120-hour intravenous infusion XR5000," *Journal of Clinical Oncology*, vol. 21, no. 2, pp. 203-210, 2003.
- [16] A. Saleem, J. C. Matthews, M. Ranson et al., "Molecular imaging and pharmacokinetic analysis of carbon-11 labeled antisense oligonucleotide LY2181308 in cancer patients," *Theranostics*, vol. 1, pp. 290-301, 2011.
- [17] D. C. Talbot, M. Ranson, J. Davies et al., "Tumor survivin is downregulated by the antisense oligonucleotide LY2181308: a proof-of-concept, first-in-human dose study," *Clinical Cancer Research*, vol. 16, no. 24, pp. 6150-6158, 2010.
- [18] A. A. M. van der Veldt, N. H. Hendrikse, E. F. Smit et al., "Bio-distribution and radiation dosimetry of ¹¹¹C-labelled docetaxel in cancer patients," *European Journal of Nuclear Medicine and Molecular Imaging*, vol. 37, no. 10, pp. 1950-1958, 2010.
- [19] K. A. Kurdziel, J. D. Kalen, J. I. Hirsch et al., "Human dosimetry and preliminary tumor distribution of ¹⁸F-fluoropacitaxel in healthy volunteers and newly diagnosed breast cancer patients using PET/CT," *Journal of Nuclear Medicine*, vol. 52, no. 9, pp. 1339-1345, 2011.
- [20] A. Saleem, "Brain and tumor penetration of carbon-11-labeled lapatinib (¹¹C]Lap) in patients (pts) with HER2-overexpressing metastatic breast cancer (MBC): ASCO Annual Meeting 2013, Chicago, USA," *Journal of Clinical Oncology*, vol. 31, supplement, abstract 635, 2013.

- [21] I. Bahce, E. F. Smit, M. Lubberink et al., "Development of [¹¹C]erlotinib positron emission tomography for *in vivo* evaluation of EGF receptor mutational status," *Clinical Cancer Research*, vol. 19, no. 1, pp. 183–193, 2013.
- [22] D. J. Stewart and J. J. Erasmus, "Erlotinib accumulation in brain metastases from non-small cell lung cancer: visualization by positron emission tomography in a patient harboring a mutation in the epidermal growth factor receptor," *Journal of Thoracic Oncology*, vol. 6, no. 7, pp. 1149–1151, 2011.
- [23] A. A. Memon, B. Weber, M. Winterdahl et al., "PET imaging of patients with non-small cell lung cancer employing an EGF receptor targeting drug as tracer," *British Journal of Cancer*, vol. 105, no. 12, pp. 1850–1855, 2011.
- [24] P. K. E. Börjesson, Y. W. S. Jauw, R. De Bree et al., "Radiation dosimetry of ⁸⁹Zr-labeled chimeric monoclonal antibody U36 as used for immuno-PET in head and neck cancer patients," *Journal of Nuclear Medicine*, vol. 50, no. 11, pp. 1828–1836, 2009.
- [25] E. C. Dijkers, T. H. O. Munnink, J. G. Kosterink et al., "Biodistribution of ⁸⁹Zr-trastuzumab and PET imaging of HER2-positive lesions in patients with metastatic breast cancer," *Clinical Pharmacology and Therapeutics*, vol. 87, no. 5, pp. 586–592, 2010.
- [26] J. E. Mortimer, J. R. Bading, D. M. Colcher et al., "Functional imaging of human epidermal growth factor receptor 2-positive metastatic breast cancer using (64)Cu-DOTA-trastuzumab PET," *Journal of Nuclear Medicine*, vol. 55, no. 1, pp. 23–29, 2014.
- [27] J. C. Bendell, S. M. Domchek, H. J. Burstein et al., "Central nervous system metastases in women who receive trastuzumab-based therapy for metastatic breast carcinoma," *Cancer*, vol. 97, no. 12, pp. 2972–2977, 2003.
- [28] N. J. Abbott, A. A. Patabendige, D. E. Dolman, S. R. Yusof, and D. J. Begley, "Structure and function of the blood-brain barrier," *Neurobiology of Disease*, vol. 37, no. 1, pp. 13–25, 2010.
- [29] R. Nau, F. Sörgel, and H. Eiffert, "Penetration of drugs through the blood-cerebrospinal fluid/blood-brain barrier for treatment of central nervous system infections," *Clinical Microbiology Reviews*, vol. 23, no. 4, pp. 858–883, 2010.
- [30] P. Slobbe, A. J. Poot, A. D. Windhorst, and G. A. M. S. Van Dongen, "PET imaging with small-molecule tyrosine kinase inhibitors: TKI-PET," *Drug Discovery Today*, vol. 17, no. 21–22, pp. 1175–1187, 2012.
- [31] Ö. Lindhe, A. Thibblin, G. Antoni et al., "PET imaging of c-Met expression in non-human primates using [¹⁸F]AH113804," in *Proceedings of the 103rd Annual Meeting of the American Association for Cancer Research*, Chicago, Ill, USA, 2012.
- [32] C. Dittrich, V. Dieras, P. Kerbrat et al., "Phase II study of XR5000 (DACA), an inhibitor of topoisomerase I and II, administered as a 120-h infusion in patients with advanced ovarian cancer," *Investigational New Drugs*, vol. 21, no. 3, pp. 347–352, 2003.
- [33] C. Dittrich, B. Coudert, L. Paz-Ares et al., "Phase II study of XR 5000 (DACA), an inhibitor of topoisomerase I and II, administered as a 120-h infusion in patients with non-small cell lung cancer," *European Journal of Cancer*, vol. 39, no. 3, pp. 330–334, 2003.
- [34] F. Caponigro, C. Dittrich, J. B. Sorensen et al., "Phase II study of XR 5000, an inhibitor of topoisomerases I and II, in advanced colorectal cancer," *European Journal of Cancer*, vol. 38, no. 1, pp. 70–74, 2002.
- [35] C. S. Dence, R. Laforest, X. Sun, T. L. Sharp, M. J. Welch, and R. H. MacH, "Radiochemical synthesis, rodent biodistribution and tumor uptake, and dosimetry calculations of [¹¹C] methylated LY2181308," *Molecular Imaging and Biology*, vol. 12, no. 6, pp. 608–615, 2010.
- [36] European Medicines Agency, *Guideline on the Requirements to the Chemical and Pharmaceutical Quality Documentation Concerning Investigational Medicinal Products in Clinical Trials*, European Commission, London, UK, 2006, Edited by Committee for Medicinal Products for Human Use (CHMP).
- [37] W. G. Herrington, D. C. Talbot, M. M. Lahn et al., "Association of long-term administration of the survivin mRNA-targeted antisense oligonucleotide LY2181308 with reversible kidney injury in a patient with metastatic melanoma," *American Journal of Kidney Diseases*, vol. 57, no. 2, pp. 300–303, 2011.
- [38] H. P. Erba, H. Sayar, M. Juckett et al., "Safety and pharmacokinetics of the antisense oligonucleotide (ASO) LY2181308 as a single-agent or in combination with idarubicin and cytarabine in patients with refractory or relapsed acute myeloid leukemia (AML)," *Investigational New Drugs*, vol. 31, no. 4, pp. 1023–1034, 2013.
- [39] P. Wiechno et al., "Randomized phase II study with window-design to evaluate anti-tumor activity of the survivin antisense oligonucleotide (ASO) LY2181308 in combination with docetaxel for first-line treatment of castrate-resistant prostate cancer (CRPC)," in *Proceedings of the American Society of Clinical Oncology Annual Meeting*, Journal of Clinical Oncology, Chicago, Ill, USA, 2013.
- [40] D. Talbot, F. H. Blackhall, D. Kowalski et al., "A randomized open-label phase II study evaluating antitumor activity of the survivin antisense oligonucleotide LY2181308 (LY) in combination with docetaxel (DO) for second-line treatment of patients with non-small cell lung cancer (NSCLC) using change in tumor size (CTS)," in *Proceedings of the American Society of Clinical Oncology*, Chicago, Ill, USA, 2013.
- [41] E. A. I. Directorate-General, *EU Guidelines to Good Medical Practice Medicinal Products for Human and Veterinary Use*, Edited by: C. G. Pharmaceuticals, European Commission, Brussels, Belgium, 2008.
- [42] A. Verbruggen, H. H. Coenen, J. Deverre et al., "Guideline to regulations for radiopharmaceuticals in early phase clinical trials in the EU," *European Journal of Nuclear Medicine and Molecular Imaging*, vol. 35, no. 11, pp. 2144–2151, 2008.
- [43] P. Zanotti-Fregonara and R. B. Innis, "Suggested pathway to assess radiation safety of ¹¹C-labeled PET tracers for first-in-human studies," *European Journal of Nuclear Medicine and Molecular Imaging*, vol. 39, no. 3, pp. 544–547, 2012.
- [44] P. Zanotti-Fregonara, A. A. Lammertsma, and R. B. Innis, "Suggested pathway to assess radiation safety of ¹⁸F-labeled PET tracers for first-in-human studies," *European Journal of Nuclear Medicine and Molecular Imaging*, vol. 40, no. 11, pp. 1781–1783, 2013.
- [45] A. J. Poot, P. Slobbe, N. H. Hendrikse, A. D. Windhorst, and G. van Dongen, "Imaging of TKI-target interactions for personalized cancer therapy," *Clinical Pharmacology and Therapeutics*, vol. 93, no. 3, pp. 239–241, 2013.
- [46] T. Jones, P. Price, and B. Tavittian, "Realizing the full potential of PET for measuring the biodistribution of novel anticancer agents," *Journal of Nuclear Medicine*, vol. 52, no. 9, p. 1500, 2011.

Review Article

PET Quantification of Cerebral Oxygen Metabolism in Small Animals

**Takashi Temma, Kazuhiro Koshino, Tetsuaki Moriguchi,
Jun-ichiro Enmi, and Hidehiro Iida**

*Department of Investigative Radiology, National Cerebral and Cardiovascular Center Research Institute,
5-7-1 Fujishiro-dai, Suita, Osaka 565-8565, Japan*

Correspondence should be addressed to Takashi Temma; ttemma@ncvc.go.jp

Received 25 June 2014; Accepted 24 July 2014; Published 17 August 2014

Academic Editor: Masashi Ueda

Copyright © 2014 Takashi Temma et al. This is an open access article distributed under the Creative Commons Attribution License, which permits unrestricted use, distribution, and reproduction in any medium, provided the original work is properly cited.

Understanding cerebral oxygen metabolism is of great importance in both clinical diagnosis and animal experiments because oxygen is a fundamental source of brain energy and supports brain functional activities. Since small animals such as rats are widely used to study various diseases including cerebral ischemia, cerebrovascular diseases, and neurodegenerative diseases, the development of a noninvasive *in vivo* measurement method of cerebral oxygen metabolic parameters such as oxygen extraction fraction (OEF) and cerebral metabolic rate of oxygen (CMRO₂) as well as cerebral blood flow (CBF) and cerebral blood volume (CBV) has been a priority. Although positron emission tomography (PET) with ¹⁵O labeled gas tracers has been recognized as a powerful way to evaluate cerebral oxygen metabolism in humans, this method could not be applied to rats due to technical problems and there were no reports of PET measurement of cerebral oxygen metabolism in rats until an ¹⁵O-O₂ injection method was developed a decade ago. Herein, we introduce an intravenous administration method using two types of injectable ¹⁵O-O₂ and an ¹⁵O-O₂ gas inhalation method through an airway placed in the trachea, which enables oxygen metabolism measurements in rats.

1. Introduction

Since cerebral blood flow (CBF) and oxygen metabolism are fundamental for brain activity, the *in vivo* measurement of CBF, oxygen extraction fraction (OEF), and cerebral metabolic rate of oxygen (CMRO₂) is of great importance in clinical diagnosis and for animal experiments. In particular, small animals such as mice and rats are widely used for research in a variety of diseases such as cerebral ischemia [1], dementia [2], Alzheimer's disease [3], and neurodegenerative diseases [4]. Small animals are also useful for the elucidation of glial function in pathological conditions [5] and for understanding the functional relationship between the brain and peripheral organs [6]. Therefore, the development of a noninvasive *in vivo* measurement method of such cerebral metabolic parameters in small animals has been eagerly sought.

Positron emitters, such as ¹⁸F, ¹⁵O, ¹¹C, and ¹³N, emit positrons (β^+) from which pairs of photons are detected

by positron emission tomography (PET) to generate reconstructed images. This involves several corrections for random coincidence events, dead time count losses, detector inhomogeneity, photon attenuation, and scatter, among others. The annihilation radiation can noninvasively transmit through biological tissues. Thus positron-labeled compounds are used in combination with PET imaging to obtain biological information of living systems in research and clinical settings. For instance, ¹⁵O labeled O₂ gas PET has been used to estimate cerebral oxygen metabolism in patients for diagnostic purposes since the 1970s [7–12]. Although the ¹⁵O-O₂ gas PET technique also attracted researchers for the evaluation of cerebral oxygen metabolism in small animals, it was applied unsuccessfully due to technical challenges until the 1990s. To overcome these challenges, several methodological inventions have been tried, which have facilitated the evaluation of CMRO₂ and OEF in small animals in the current research setting.

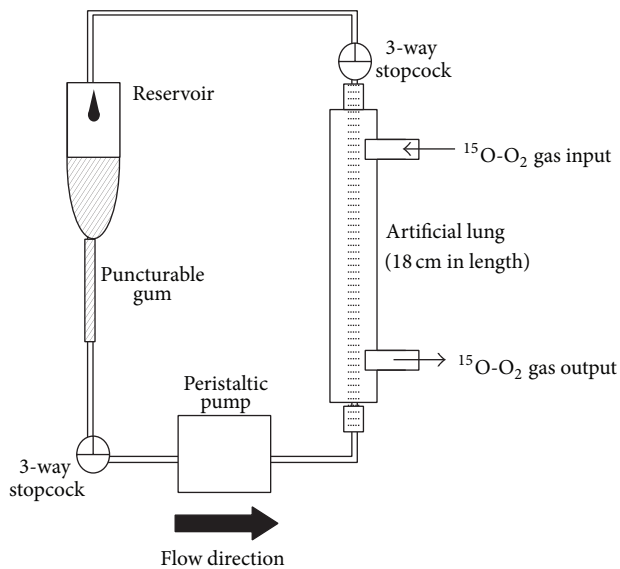


FIGURE 1: Injectable $^{15}\text{O}-\text{O}_2$ preparation system using an 18 cm long artificial lung. The length of the artificial lung was 6 cm in the original report [13] and was changed to 18 cm in the latter studies for improvement of labeling efficiency [14, 15, 17].

Herein, we introduce an intravenous administration method using injectable $^{15}\text{O}-\text{O}_2$ and an inhalation method of $^{15}\text{O}-\text{O}_2$ gas, both of which can measure CMRO_2 and OEF with PET in living rats under anesthesia.

2. Intravenous Administration Method

Although the importance of evaluating cerebral oxygen metabolism in small animals has been recognized, application of the inhalation method using $^{15}\text{O}-\text{O}_2$ gas in small animals could not be performed due to technical issues such as the potential influence of high radioactivity in the inhalation tube on the rat brain data acquisition. To overcome this situation, Magata et al. first developed an $^{15}\text{O}-\text{O}_2$ injection method, which made rat OEF measurement possible using PET [13]. They collected blood from several rats and labeled the blood with $^{15}\text{O}-\text{O}_2$ gas using an artificial lung (Figure 1). After 10 minutes of $^{15}\text{O}-\text{O}_2$ uptake into the red blood cells, they had ^{15}O labeled blood (72 MBq/mL) to use as an injectable for intravenous administration into normal rats for PET imaging. In fact, they performed two serial PET scans with ^{15}O -water and injectable $^{15}\text{O}-\text{O}_2$ and obtained 44 ± 4.5 mL/min/100 g of CBF and 0.54 ± 0.11 of OEF in normal rats under pentobarbital anesthesia. Subsequently, the same group evaluated the utility of the injectable $^{15}\text{O}-\text{O}_2$ PET system using brain infarction rats [14], hypertensive rats [15], and normal monkeys [16]. The results indicated that the injectable $^{15}\text{O}-\text{O}_2$ PET system could provide information on cerebral oxygen metabolism under normal and pathological conditions in rats as well as in larger animals. In particular, using the injectable $^{15}\text{O}-\text{O}_2$ PET technique in spontaneously hypertensive rats (SHR), this research group

clearly demonstrated that hypertension could intensify cerebral metabolic disturbances during the acute phase after the onset of stroke (Figure 2 [15]). This same group also applied the $^{15}\text{O}-\text{O}_2$ injection technique to miniature pigs to evaluate myocardial oxygen metabolism, which was also considered to be a difficult target for evaluation by $^{15}\text{O}-\text{O}_2$ gas inhalation because of the existence of radioactivity spillover from the gas volume in the lung to the myocardium due to limited spatial resolution [17]. Although the blood-based injectable $^{15}\text{O}-\text{O}_2$ system provided a strong option that enabled oxygen metabolism measurement in small animals under normal and pathological conditions, some drawbacks were addressed for further applications. Namely, the blood-based injectable $^{15}\text{O}-\text{O}_2$ system required that additional rats be sacrificed for blood collection and there was a possibility that the biological characteristics of the blood components might be damaged during the preparation process.

Tiwari et al. then reported on a different injectable $^{15}\text{O}-\text{O}_2$ system using hemoglobin-containing vesicles (HbV) to overcome these problems (Figure 3) [18]. The HbV, originally developed as an alternative oxygen carrier [19], was a liposome (about 300 nm in diameter) consisting of 1,2-dipalmitoyl-*sn*-glycero-3-phosphatidylcholine (DPPC), cholesterol, and 1,2-dipalmitoyl-*sn*-glycero-3-phosphoglycerol (DPPG) (5/5/1 at a molar ratio) and containing 10.8 g/dL hemoglobin molecules. The authors tested the feasibility of the HbV as an ^{15}O -oxygen carrier, optimized a preparation system to obtain $^{15}\text{O}-\text{O}_2$ -HbV with a high labeling yield, and performed a PET study in normal rats after intravenous administration of $^{15}\text{O}-\text{O}_2$ -HbV. As a result, they achieved optimization of the labeling procedure using a direct bubbling method of $^{15}\text{O}-\text{O}_2$ gas into the HbV solution containing L-cysteine using a vortex. They obtained 214 ± 7.8 MBq/mL $^{15}\text{O}-\text{O}_2$ -HbV, which is about 3-fold higher than the previous blood-based injectable $^{15}\text{O}-\text{O}_2$ [13]. They also measured CBF, OEF, and CMRO_2 values using the $^{15}\text{O}-\text{O}_2$ -HbV with PET imaging in normal rats. The same research group from the University of Fukui proceeded to lessen the invasiveness of the $^{15}\text{O}-\text{O}_2$ injection method in the next step. In fact, all of the manuscripts using the $^{15}\text{O}-\text{O}_2$ injection method described above adopted continuous arterial blood sampling during the PET scans for estimation of the input function to analyze cerebral metabolic parameters [13–16, 18]. Since the total volume of blood sampling is limited in small animals such as rats, they applied a steady-state method they originally developed for CBF measurement using ^{15}O -water PET in rats [20] to the $^{15}\text{O}-\text{O}_2$ -HbV PET to decrease the injection and blood sampling volumes [21]. They prepared ^{15}O -water, $^{15}\text{O}-\text{O}_2$ -HbV, and $^{15}\text{O}-\text{CO}$ -HbV obtained in a similar manner as the $^{15}\text{O}-\text{O}_2$ -HbV, and PET scans were performed with continuous intravenous administration of $^{15}\text{O}-\text{CO}$ -HbV, ^{15}O -water, and $^{15}\text{O}-\text{O}_2$ -HbV through a multiprogrammed syringe pump with gradual changes in the injection speed. They reported that the injection and sampling blood volumes were 1.65 and 0.65 mL in ^{15}O -water PET and 1.65 and 1.40 mL in $^{15}\text{O}-\text{O}_2$ -HbV PET, respectively,

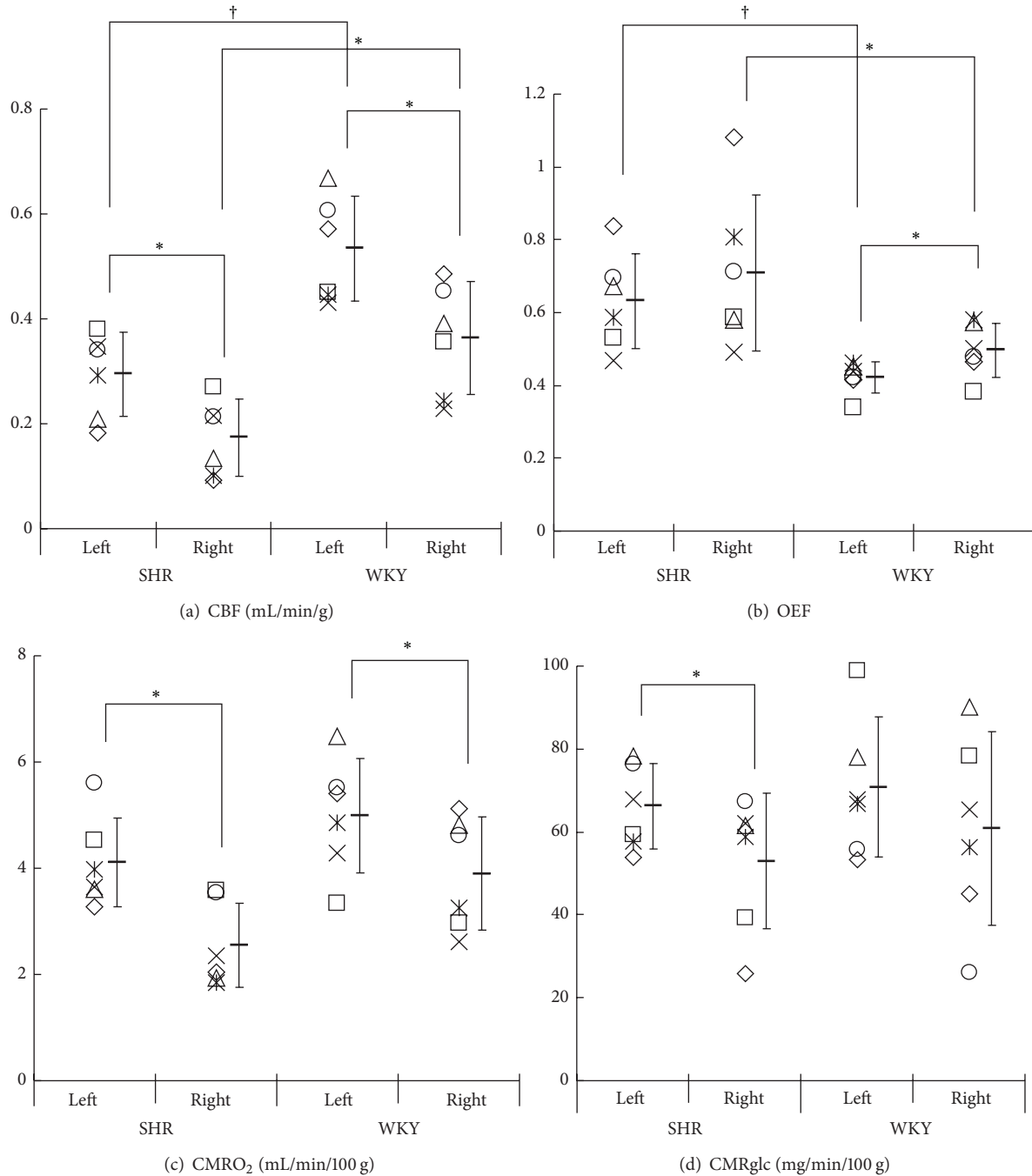


FIGURE 2: (Figure 1 in [15]) Quantitative values of CBF (a), OEF (b), CMRO₂ (c), and cerebral metabolic rate of glucose (CMRglc) (d). PET with ¹⁵O-water and injectable ¹⁵O-O₂ and an *ex vivo* autoradiography with ¹⁸F-FDG were performed one hour after the onset of a right middle cerebral artery occlusion using spontaneously hypertensive rats (SHR) and Wistar Kyoto rats (WKY). CBF, OEF, and CMRO₂ were obtained from PET and CMRglc was obtained from ARG. Each of the six marks indicates the hemispheric average of 4 slices in an individual. Bar-shaped marks show the average and the error bars represent SD. Significant differences between hemispheres and between SHR and WKY were determined using the Wilcoxon signed rank test, **P* < 0.05, and the Mann-Whitney *U* test, **P* < 0.05, †*P* < 0.01.

and achieved the measurement of CBF, OEF, CMRO₂, and cerebral blood volume (CBV) values in several cerebral regions using a high resolution PET system (SHR-41000; Hamamatsu Photonics, Hamamatsu, Japan). In addition, the

usefulness of the steady-state method was confirmed in a rat model of brain infarction. As such, in combination with the improvement in small animal PET systems and experimental procedures, the ¹⁵O-O₂ intravenous administration method

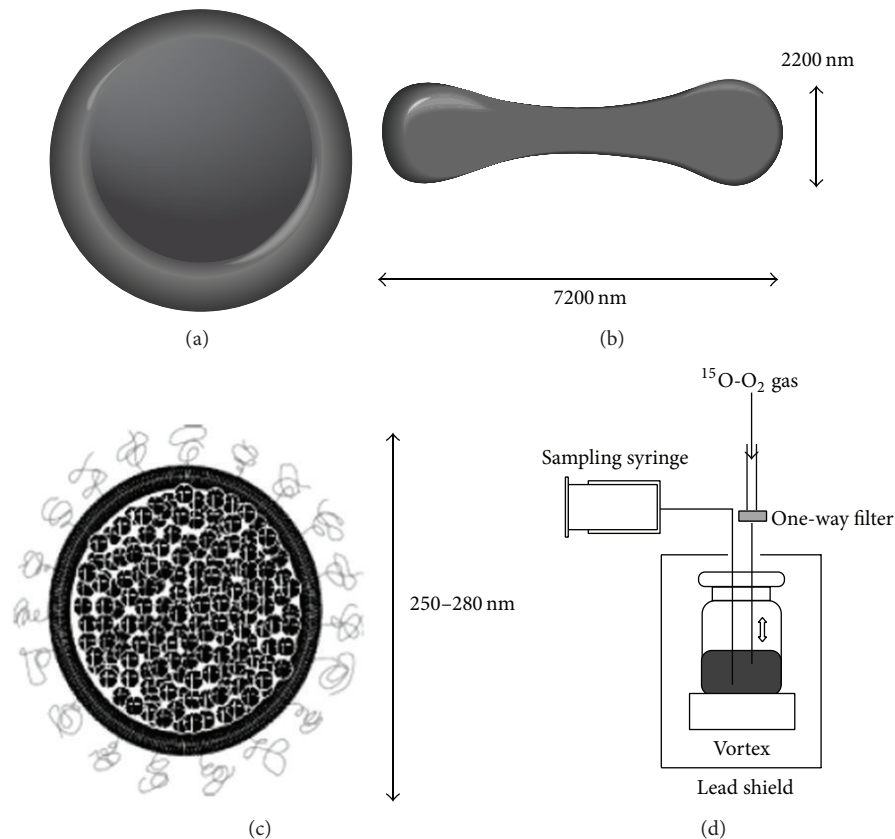


FIGURE 3: A schematic diagram of the $^{15}\text{O}-\text{O}_2\text{-HbV}$ preparation system. Normal human red blood cells (RBC) (a, b), hemoglobin-vesicle (HbV) structure (c) with shape and approximate diameters, and the final labeling setup with a lead shield for injectable $^{15}\text{O}-\text{O}_2\text{-HbV}$ preparation (d) are shown (courtesy of Dr. Kiyono, University of Fukui, Fukui, Japan).

made possible cerebral oxygen metabolism measurement of rats in normal and pathological conditions, with minimal invasiveness.

3. Inhalation Method

Aside from the intravenous administration method, researchers have also tried to develop an $^{15}\text{O}-\text{O}_2$ gas inhalation method for small animals such as rats. Yee et al. first performed a micro-PET experiment using normal rats with briefly inhaled $^{15}\text{O}-\text{O}_2$ gas [22]. In this report, the authors applied the one-step method using single inhalation of $^{15}\text{O}-\text{O}_2$ gas [23] to rats, and the $^{15}\text{O}-\text{O}_2$ gas contained in a syringe was administered by a bolus insufflation into the lung through a cannula surgically placed in the trachea. In addition, they omitted arterial blood sampling in consideration of the limited blood volume of rats. Instead, for the estimation of input function, the field of view (FOV) of a PET scan was positioned to cover the brain and the heart at the same time. The time activity curve data from the heart was corrected using the volume ratio of the pure arterial space inside the ROI as the arterial input function [24]. As a result, $5.00 \pm 0.36 \text{ mL/min/100 g}$ of CMRO_2 was calculated in 10 normal rats under α -chloralose anesthesia with continuous infusion. The study was successfully

performed to achieve rat CMRO_2 measurement with only one PET scan and without arterial blood sampling; however, a tracheotomy for tracer administration, animal size restriction for simultaneous brain-heart scan, and poor signal to noise ratio were mentioned as limitations.

Recently, Watabe et al. reported the application of a steady-state $^{15}\text{O}-\text{O}_2$ gas inhalation method for normal rats [25]. Namely, they performed a tracheotomy and placed a flexible tube into the trachea to serve as an administration route for the ^{15}O -gas tracers. They performed three serial PET scans using $^{15}\text{O}-\text{CO}_2$, $^{15}\text{O}-\text{O}_2$, and $^{15}\text{O}-\text{CO}$ gas, respectively, and measured CBF, OEF, CMRO_2 , and CBV values in the normal brains of rats under anesthesia according to the original ^{15}O gas steady-state inhalation method used in clinical settings [26–28]. A clinical PET camera (Headtome-V PET scanner; Shimadzu Corp.) was used and the feasibility of using the camera for small animal studies was evaluated by phantom experiments. After precise evaluation of partial volume effects, scatter correction from the high radioactivity in the pleural cavity, and application of a cross-calibration factor, the authors succeeded in obtaining quantitative and comparable values and functional images of CBF, OEF, CMRO_2 , and CBV in normal rats. In addition, they tested the applicability of the method to a small number of ischemia model rats ($n = 2$) and successfully showed decreased CBF

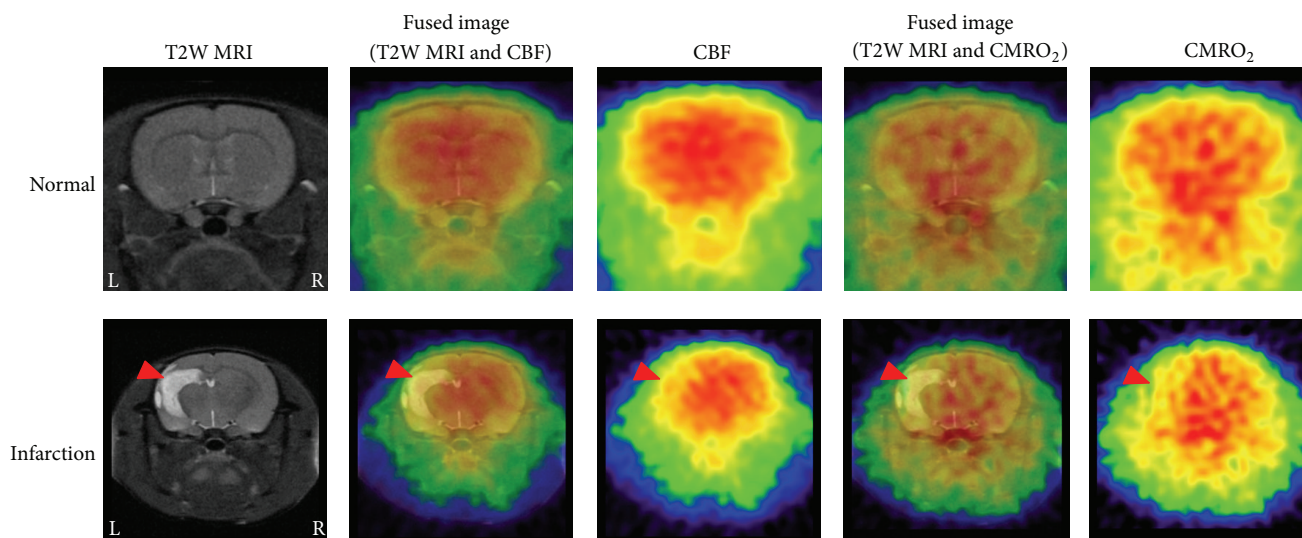


FIGURE 4: Functional images (“pseudo” CBF and $CMRO_2$) of normal and infarction rat brains (Wistar rats, male, 8 weeks old). T2 weighted MR images are shown as a position reference. PET scans were performed during continuous administration of $^{15}O\text{-CO}_2$ and $^{15}O\text{-O}_2$ gases by spontaneous respiration of rats under isoflurane anesthesia.

and $CMRO_2$ values and increased OEF value in the ipsilateral hemisphere. The total time was about 73 min for the entire PET experiment in each rat. The results clearly indicated that the steady-state ^{15}O -gas inhalation method used in clinical settings could be applied to rats with consideration of the appropriate care to avoid possible errors. However, tracheotomy was still required for gas tracer administration and the rats underwent arterial blood sampling during the PET scan, which might be considered a limitation in the above study.

On this basis, we are now developing an ^{15}O gas administration technique that uses the spontaneous respiration of rats under isoflurane anesthesia for micro-PET measurement of cerebral metabolic function without arterial blood sampling. As shown in Figure 4 (unpublished data), we can provide “pseudo” functional images of a rat brain under both normal and pathological conditions. We expect to successfully perform this technique in the near future.

Finally, regardless of the administration route of $^{15}O\text{-O}_2$, recirculating ^{15}O labeled water, which is a metabolic product of $^{15}O\text{-O}_2$, should be taken into consideration for estimating quantitative $CMRO_2$ and OEF in small animals. The recirculating ^{15}O -water could have a crucial impact on these parameters due to more rapid appearance after $^{15}O\text{-O}_2$ administration in small animals than in humans. In fact, most of the studies described above measured the contribution of recirculating ^{15}O -water as an input function by separating the plasma from the whole blood samples [13–15, 21, 25]. However, this procedure requires repetitive blood sampling during a PET study, which may alter physiological function due to the limited total blood volume in small animals. Recently, an alternative approach has been applied, in which the time activity curve of recirculating ^{15}O -water could be predicted from a whole blood radioactivity concentration curve by modeling the kinetics of the metabolic process

of oxygen molecules in the whole body [29]. Thus, the labor intensive procedure of frequent arterial blood sampling with centrifugation can be avoided, making the protocol applicable to many studies using clinical patients as well as experimental animals. It is of note that this method was shown to be applicable to a wide range of species from human to rats. Therefore, using the simplified method to predict the contribution of recirculating ^{15}O -water, in combination with less invasive techniques to obtain the time activity curve such as an online scintillation detector coupled to an arteriovenous shunt [30] or ROI analysis of the cardiac ventricle in PET images [22], the ^{15}O PET technique could be more widely applied to small animals under a broad range of conditions.

4. Conclusion

Since oxygen is a key molecule for energy production in living brains, the measurement of cerebral oxygen metabolism is important to understand brain function in normal and pathological conditions. With some technological innovations including the development of injectable $^{15}O\text{-O}_2$ preparations and the successful application of an $^{15}O\text{-O}_2$ gas inhalation method with appropriate corrections, measurement of cerebral oxygen metabolism (OEF and $CMRO_2$) has become possible in living rats, as compared to the difficult challenges faced more than a decade ago. However, there are several issues that remain unresolved for the ideal achievement of noninvasive quantification of OEF and $CMRO_2$ in living rats by PET using ^{15}O gas tracers; these include tracheotomy, arterial blood sampling, and long experimental time. In contrast, the total examination time in clinical settings has been dramatically reduced from more than 40 minutes [31] to about 10 minutes by recent technical innovations [9, 32]. Therefore, experiments involving small animal models would also benefit from further methodological progress

including faster and less invasive measurement (e.g., ^{15}O gas administration by spontaneous respiration, input function estimation from the heart or large arteries) with improvement of resolution and sensitivity by dedicated PET scanners for small animals and the development of a fully automated rapid measurement system for animal ^{15}O gas experiments. With such innovation, the ^{15}O PET technique could be more widely applied to studies in model animals including not only ischemia and infarction but also neurodegenerative and psychiatric diseases.

Conflict of Interests

The authors declare that there is no conflict of interests regarding the publication of this paper.

References

- [1] H. Yao and T. Nabika, "Standards and pitfalls of focal ischemia models in spontaneously hypertensive rats: with a systematic review of recent articles," *Journal of Translational Medicine*, vol. 10, no. 1, article 139, 2012.
- [2] J. Weaver, F. Y. Jalal, Y. Yang, J. Thompson, G. A. Rosenberg, and K. J. Liu, "Tissue oxygen is reduced in white matter of spontaneously hypertensive-stroke prone rats: a longitudinal study with electron paramagnetic resonance," *Journal of Cerebral Blood Flow & Metabolism*, vol. 34, no. 5, pp. 890–896, 2014.
- [3] Y. Lu, Y. Huang, C. Tang et al., "Brain areas involved in the acupuncture treatment of AD model rats: a PET study," *BMC Complementary and Alternative Medicine*, vol. 14, article 178, 2014.
- [4] C. Li, K. Yuan, and H. Schluesener, "Impact of minocycline on neurodegenerative diseases in rodents: a meta-analysis," *Reviews in the Neurosciences*, vol. 24, pp. 553–562, 2013.
- [5] G. P. Morris, I. A. Clark, R. Zinn, and B. Vissel, "Microglia: a new frontier for synaptic plasticity, learning and memory, and neurodegenerative disease research," *Neurobiology of Learning and Memory*, vol. 105, pp. 40–53, 2013.
- [6] J. J. Cone, J. E. McCutcheon, and M. F. Roitman, "Ghrelin acts as an interface between physiological state and phasic dopamine signaling," *The Journal of Neuroscience*, vol. 34, pp. 4905–4913, 2014.
- [7] A. Gupta, H. Baradaran, A. D. Schweitzer et al., "Oxygen extraction fraction and stroke risk in patients with carotid stenosis or occlusion: a systematic review and meta-analysis," *American Journal of Neuroradiology*, vol. 35, pp. 250–255, 2014.
- [8] M. Hokari, S. Kuroda, T. Shiga, N. Nakayama, N. Tamaki, and Y. Iwasaki, "Impact of oxygen extraction fraction on long-term prognosis in patients with reduced blood flow and vasoreactivity because of occlusive carotid artery disease," *Surgical Neurology*, vol. 71, no. 5, pp. 532–538, 2009.
- [9] N. Kudomi, Y. Hirano, K. Koshino et al., "Rapid quantitative CBF and CMRO₂ measurements from a single PET scan with sequential administration of dual ^{15}O -labeled tracers," *Journal of Cerebral Blood Flow and Metabolism*, vol. 33, no. 3, pp. 440–448, 2013.
- [10] T. Nezu, C. Yokota, T. Uehara et al., "Preserved acetazolamide reactivity in lacunar patients with severe white-matter lesions: ^{15}O -labeled gas and H₂O positron emission tomography studies," *Journal of Cerebral Blood Flow and Metabolism*, vol. 32, no. 5, pp. 844–850, 2012.
- [11] M. Tanaka, E. Shimosegawa, K. Kajimoto et al., "Chronic middle cerebral artery occlusion: a hemodynamic and metabolic study with positron-emission tomography," *The American Journal of Neuroradiology*, vol. 29, no. 10, pp. 1841–1846, 2008.
- [12] J. Baron and T. Jones, "Oxygen metabolism, oxygen extraction and positron emission tomography: historical perspective and impact on basic and clinical neuroscience," *NeuroImage*, vol. 61, no. 2, pp. 492–504, 2012.
- [13] Y. Magata, T. Temma, H. Iida et al., "Development of injectable O-15 oxygen and estimation of rat OEF," *Journal of Cerebral Blood Flow and Metabolism*, vol. 23, no. 6, pp. 671–676, 2003.
- [14] T. Temma, Y. Magata, Y. Kuge et al., "Estimation of oxygen metabolism in a rat model of permanent ischemia using positron emission tomography with injectable ^{15}O -O₂," *Journal of Cerebral Blood Flow and Metabolism*, vol. 26, no. 12, pp. 1577–1583, 2006.
- [15] T. Temma, Y. Kuge, K. Sano et al., "PET O-15 cerebral blood flow and metabolism after acute stroke in spontaneously hypertensive rats," *Brain Research*, vol. 1212, pp. 18–24, 2008.
- [16] T. Temma, Y. Magata, H. Iida et al., "Development of injectable O-15 oxygen and its application for estimation of OEF," *International Congress Series*, vol. 1265, pp. 262–265, 2004.
- [17] T. Temma, H. Iida, T. Hayashi et al., "Quantification of regional myocardial oxygen metabolism in normal pigs using positron emission tomography with injectable ^{15}O -O₂," *European Journal of Nuclear Medicine and Molecular Imaging*, vol. 37, no. 2, pp. 377–385, 2010.
- [18] V. N. Tiwari, Y. Kiyono, M. Kobayashi et al., "Automatic labeling method for injectable ^{15}O -oxygen using hemoglobin-containing liposome vesicles and its application for measurement of brain oxygen consumption by PET," *Nuclear Medicine and Biology*, vol. 37, no. 1, pp. 77–83, 2010.
- [19] Y. Ogata, "Characteristics and function of human hemoglobin vesicles as an oxygen carrier," *Polymers for Advanced Technologies*, vol. 11, no. 5, pp. 205–209, 2000.
- [20] M. Kobayashi, Y. Kiyono, R. Maruyama, T. Mori, K. Kawai, and H. Okazawa, "Development of an H₂ ^{15}O steady-state method combining a bolus and slow increasing injection with a multiprogramming syringe pump," *Journal of Cerebral Blood Flow and Metabolism*, vol. 31, no. 2, pp. 527–534, 2011.
- [21] M. Kobayashi, T. Mori, Y. Kiyono et al., "Cerebral oxygen metabolism of rats using injectable ^{15}O -oxygen with a steady-state method," *Journal of Cerebral Blood Flow and Metabolism*, vol. 32, no. 1, pp. 33–40, 2012.
- [22] S. H. Yee, K. Lee, P. A. Jerabek, and P. T. Fox, "Quantitative measurement of oxygen metabolic rate in the rat brain using microPET imaging of briefly inhaled ^{15}O -labelled oxygen gas," *Nuclear Medicine Communications*, vol. 27, no. 7, pp. 573–581, 2006.
- [23] S. Ohta, E. Meyer, C. J. Thompson, and A. Gjedde, "Oxygen consumption of the living human brain measured after a single inhalation of positron emitting oxygen," *Journal of Cerebral Blood Flow and Metabolism*, vol. 12, no. 2, pp. 179–192, 1992.
- [24] S. Yee, P. A. Jerabek, and P. T. Fox, "Non-invasive quantification of cerebral blood flow for rats by microPET imaging of ^{15}O labelled water: the application of a cardiac time-activity curve for the tracer arterial input function," *Nuclear Medicine Communications*, vol. 26, no. 10, pp. 903–911, 2005.
- [25] T. Watabe, E. Shimosegawa, H. Watabe et al., "Quantitative evaluation of cerebral blood flow and oxygen metabolism in normal anesthetized rats: ^{15}O -Labeled gas inhalation PET with

- MRI fusion,” *Journal of Nuclear Medicine*, vol. 54, no. 2, pp. 283–290, 2013.
- [26] T. Jones, D. A. Chesler, and M. M. Ter Pogossian, “The continuous inhalation of Oxygen-15 for assessing regional oxygen extraction in the brain of man,” *The British Journal of Radiology*, vol. 49, no. 580, pp. 339–343, 1976.
- [27] R. S. J. Frackowiak, G. L. Lenzi, T. Jones, and J. D. Heather, “Quantitative measurement of regional cerebral blood flow and oxygen metabolism in man using ^{15}O and positron emission tomography: theory, procedure, and normal values,” *Journal of Computer Assisted Tomography*, vol. 4, no. 6, pp. 727–736, 1980.
- [28] A. A. Lammertsma and T. Jones, “Correction for the presence of intravascular oxygen-15 in the steady-state technique for measuring regional oxygen extraction ratio in the brain. I. Description of the method,” *Journal of Cerebral Blood Flow and Metabolism*, vol. 3, no. 4, pp. 416–424, 1983.
- [29] N. Kudomi, T. Hayashi, H. Watabe et al., “A physiologic model for recirculation water correction in CMRO_2 assessment with $^{15}\text{O}_2$ inhalation PET,” *Journal of Cerebral Blood Flow and Metabolism*, vol. 29, no. 2, pp. 355–364, 2009.
- [30] T. Ose, H. Watabe, T. Hayashi et al., “Quantification of regional cerebral blood flow in rats using an arteriovenous shunt and micro-PET,” *Nuclear Medicine and Biology*, vol. 39, no. 5, pp. 730–741, 2012.
- [31] M. A. Mintun, M. E. Raichle, W. R. W. Martin, and P. Herscovitch, “Brain oxygen utilization measured with O-15 radiotracers and positron emission tomography,” *Journal of Nuclear Medicine*, vol. 25, no. 2, pp. 177–187, 1984.
- [32] N. Kudomi, T. Hayashi, N. Teramoto et al., “Rapid quantitative measurement of CMRO_2 and CBF by dual administration of ^{15}O -labeled oxygen and water during a single PET scan - A validation study and error analysis in anesthetized monkeys,” *Journal of Cerebral Blood Flow and Metabolism*, vol. 25, no. 9, pp. 1209–1224, 2005.